Open Research Online

The Open University's repository of research publications
and other research outputs

Creep and Anelastic Deformation in Austenitic Steels

Thesis

How to cite:

Rao, Ashwin (2010). Creep and Anelastic Deformation in Austenitic Steels. PhD thesis The Open University.

For guidance on citations see FAQs.

© 2010 The Author

https://creativecommons.org/licenses/by-nc-nd/4.0/

Version: Version of Record

Link(s) to article on publisher's website:
http://dx.doi.org/doi:10.21954/ou.ro.0000ed7f

Copyright and Moral Rights for the articles on this site are retained by the individual authors and/or other copyright owners. For more information on Open Research Online's data policy on reuse of materials please consult the policies page.

oro.open.ac.uk

UNRESTRICTED

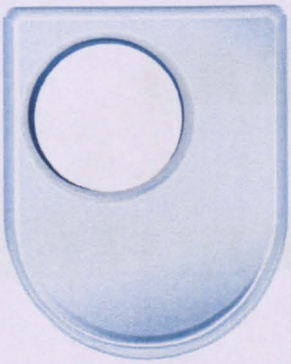

The Open University

Faculty of Mathematics, Computing and Technology

Materials Engineering Group

Creep and Anelastic Deformation in Austenitic Steels

Ashwin Rao

September 2010

A THESIS SUBMITTED TO THE DEPARTMENT OF MATERIALS ENGINEERING OF THE OPEN UNIVERSITY FOR THE DEGREE OF DOCTOR OF PHILOSOPHY

DATE OF SUBMISSION : 5 MAY 2010
DATE OF AWARD : 8 SEPT 2010

CREEP AND ANELASTIC DEFORMATION IN AUSTENITIC STEELS

Ashwin Rao

September 2010

A THESIS SUBMITTED TO THE DEPARTMENT OF MATERIALS ENGINEERING OF THE OPEN UNIVERSITY FOR THE DEGREE OF DOCTOR OF PHILOSOPHY

Photograph showing creep damage in a steam header made from austenitic stainless steel

PREFACE

This thesis is submitted for the degree of Doctor of Philosophy of The Open University. The work described in this dissertation was carried out in the Department of Materials Engineering of the Faculty of Technology, between January 2007 and April 2010, under the supervision of Prof. M. E. Fitzpatrick, Dr. Martin Rist and Prof. L. Edwards. It is an original work of the author except where reference is made to the work of others. None of this work is submitted or is in the process of submission in whole or part for a degree at any other university.

The work presented in this thesis has been published in the following papers:

1. A. Rao, P.J.Bouchard, M.E.Fitzpatrick, 'Anelasticity in Austenitic Steels', Advances in Materials Science for Environmental and Nuclear Technology, Ceramic Transactions, Vol. 222, Pg. 133.

The Open University
RESEARCH SCHOOL
28 SEP 2010

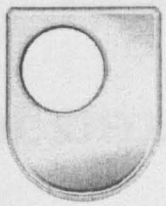

The Open University

EX12 Revised 27 January 2010

RESEARCH SCHOOL

Library Authorisation Form

Please return this form to the Research School with the two bound copies of your thesis to be deposited with the University Library. All candidates should complete parts one and two of the form. Part three only applies to PhD candidates.

Part One: Candidates Details

Name: ASHWIN RAO PI: Y3598922

Degree: PHD

Thesis title: Creep & Inelastic Deformation in Austenitic Steels

Part Two: Open University Library Authorisation

I confirm that I am willing for my thesis to be made available to readers by The Open University Library, and that it may be photocopied, subject to the discretion of the Librarian.

Signed: Ashwin Rao Date: 16/9/2010

Part Three: British Library Authorisation [PhD candidates only]

If you want like a copy of your PhD thesis to be available on loan to the British Library Thesis Service as and when it is requested, please tick Section A of this form.

The University has agreed that your participation in the British Library Thesis Service should be voluntary. Please tick either (a) or (b) to indicate your intentions.

(a) [✓] I am willing for The Open University to loan the British Library a copy of my thesis.

(b) [ ] I do not wish The Open University to loan the British Library a copy of my thesis.

Signed: Ashwin Rao Date: 16/9/2010

CREEP AND ANELASTICITY IN AUSTENITIC STEELS

Abstract

This study examines the creep behaviour of austenitic steels under service temperatures, to determine the effect of creep on material performance. Nuclear power plant components are in regular use at temperatures greater than 450°C, where creep deformation plays a dominant role in limiting the lifetime of the material. The prime aim of this study was to characterise the effect of load-reductions on the creep behaviour of austenitic steels (AISI type 316H).

In-service materials seldom operate at a constant load and/or temperature. The supply demand, maintenance operations, refuelling, etc. will result in large variation of load and temperature acting on the material. Experiments where load/temperature removals during a creep test were therefore conducted. These unloading procedures result in material recovery of the accumulated creep strain (anelasticity). This phenomenon will influence the material properties such as creep life and ductilities. Creep life was found to increase by 2-3 times whereas creep ductilities decreased by 50% when compared to steady-load creep data under identical conditions.

The occurrence of anelasticity suggested the presence of a material backstress. The origin and evolution of this internal stress was investigated using neutron diffraction and TEM microscopy. Lattice strain measurements were conducted in-situ using neutron diffraction during a creep test which consisted of load/unload cycles. Experimental results suggest that creep strain is equivalent to plastic strain at a granular level. The data also shows intergranular micro-stresses are introduced into the material by primary creep. Anisotropic behaviour of the individual crystal planes results in formation of tensile and compressive intergranular stresses in individual grain families. Residual compressive stresses drive this anelastic deformation.

TEM examinations of samples stopped during the unload show changes in dislocation and precipitate morphologies during the plastic strain recovery phase. Evidence of a changing dislocation substructure during the load-reduction period was found. Examinations have

also shown carbide densities change during the unload. Pipe diffusion is a possible mechanism which can be used to explain this occurrence. The changing precipitate and dislocation state will influence the strengthening mechanisms, which in-turn will affect the deformation characteristics. These microstructural observations were introduced into a damage mechanics model. Predictions of material behaviour using this model have shown good agreement with experimental data.

Outcomes of this project, have established that changes in creep deformation mechanisms will greatly influence material properties. Deformation history of the material will affect the intergranular stress state which in turn will affect the elastic and plastic response of the material. The effect of plastic strain history must be considered and incorporated accounted in any design and assessment procedure.

ACKNOWLEDGEMENTS

There are a number of people without whose support, I would not have been writing this thesis. Thanks are due to my supervisors, Prof. Mike Fitzpatrick, Prof. John Bouchard, Dr. Martin Rist and Prof. Lyndon Edwards (now at ANSTO) for firstly providing me an opportunity to carry out my PHD and then for their supervision and assistance during this period. The encouragement and enthusiasm during this period has been inspirational. Thanks also to Dr. Supriyo Ganguly (now at Cranfield University) for his help during these years. The financial assistance from the EPSRC sponsored Keeping the Nuclear Option Open (KNOO) programme is greatly acknowledged.

I am thankful to all my family members for their constant emotional (and sometimes financial!) support. Thank you mom, dad and all at home, Chikki, Pavan, Pooja and Murali Mama here in U.K, thanks to both my grandfathers who passed away during my PHD. I am sure you are looking over me all the time.

I am also grateful to the technical officers within the group for their assistance and advice. Pete Ledgard for his extraordinary workshop skills (sorry Pete- I lost count of the number of samples after 100), Gordon Imlach for his assistance on the electron microscopes and all the talks we had about Rangers F.C, Ian Norman for the laboratory supplies and walking routes in the U.K, Stan Hiller for assistance with optical microscopy and the discussions about food and culture, Colin Gagg for helping me with the 68 creep tests we conducted and more importantly for tolerating my constant annoyance, Heather Davies for her assistance with the TEM and for also teaching me the importance of keeping a workbench clean. Thanks also to the support staff at the OU particularly Courtney, Debbie and Angie.

Thanks also to the other academics at the OU for their support and encouragement. I also would like to acknowledge the assistance of members at ISIS, Rutherford Appleton Laboratories- Dr. Ania Paradowska for her help in the neutron diffraction experiments, David Dean and Mike Spindler of British Energy for their assistance.

I have had the pleasure of working with a number of students within the group. Their assistance during these years has been invaluable. Thanks to Dr. Moshiur Rahman, Dr. Mulyadi, Dr. Olivier 'Frenchman' Zanellato, Dr. Kashif Khan, Himanshu 'Saheb' Lalvani,

Sue Storer (thanks mom!), Murat Acar, Bama Perumal, Yuki Phillips, Shiv Sharma and all the others.

The music of Jimi Hendrix, Led Zeppelin, Eric Clapton, Neil Young, Bob Dylan, Chuck Shuldiner, Joe Satch and all the others have been my inspiration and solace during this period. Thanks for creating such wonderful 'noise'.

Thanks to all my friends for their emotional support and help. Leelu, Kulla, Rangu, Badri, Naga, Shreyas, Divya, Anu, Kundapur, Colin, Julia, Jen, Aga and the rest for putting up with me all these years. Dr. Mulla/Rao, please, the next time I see you all.

Lastly, thank you GOD (whatever form you exist in!)

Ashwin Rao

September 2010

TABLE OF CONTENTS

LIST OF FIGURES

LIST OF TABLES

NOMENCLATURE

ε-	*Strain*
$\dot{\varepsilon}$ -	*Strain rate*
$\dot{\varepsilon}_{ss}$ -	*Secondary or Steady state creep rate*
ε_{el}-	*Elastic strain*
ε_{an}-	*Anelastic strain*
εf-	*Rupture strain*
t-	*Time*
tr-	*Rupture time*
t_p-	*Time spent in primary creep*
t_s-	*Time spent in secondary creep*
t_t-	*Time spent in tertiary creep*
D_L-	*Lattice self diffusion constant*
σ-	*Applied stress*
Ω-	*Atomic volume*
d_{gb}-	*Average grain boundary diameter*
K-	*Universal gas constant*
T-	*Absolute Temperature (K)*
n-	*Stress exponent*
Q-	*Activation energy (KJ/mol)*
T_L-	*Dislocation line tension*
G-	*Shear modulus*
b-	*Burger's vector*
R-	*Bending radius of dislocation*
τ-	*Shear stress*
τ_r -	*Resolved shear stress*
F-	*Applied force*
A-	*Area of cross-section*
λ-	*Wavelength*
d-	*Distance between crystals*
θ-	*Incident angle of neutron beam*
v-	*Velocity of thermal neutrons*
d_o-	*D-spacing of stress-free reference sample*
ρ_d -	*Dislocation density*

N_d- *Number of dislocation intersections*

L- *Length of test line*

S- *Specimen thickness*

ρ_c - *Carbide density*

N_c- *Number of carbides within sampling area*

S- *State variable describing microstructural changes occurring during deformation*

H- *Hardening parameter*

L- *Recovery co-efficient*

ω- *State variable to describe creep cavitation*

K_c- *Material constant which describes particle coarsening*

The rabbit-hole went straight on like a tunnel for some way, and then dipped suddenly down, so suddenly that Alice had not a moment to think about stopping herself before she found herself falling down a very deep well.

Down, down, down. Would the fall NEVER come to an end!

An expert is a man who has made all the mistakes, which can be made, in a very narrow field - Niels Bohr

CHAPTER 1: INTRODUCTION

1.1 Background and Aims

Power generation by coal fired, gas fired, and nuclear power plants account for a significant proportion of total electricity generated. The increased global need for energy has resulted in higher demands on power plants. Increasing the efficiency of power plants will help in bridging the gap between supply and demand. More efficient plants also have significant environmental benefits. One of the key techniques to achieve better efficiencies is to increase the operating temperatures of power plant.

Increasing the operating temperatures would mean operating near the limits of performance of some materials. In the current scenario where there has been a substantial increase in the number of power plants being constructed, this has to be accounted for and materials used in the construction of nuclear power plants have to be characterised for a number of conditions (stress, temperature, loading cycles, etc). The increased energy demand has also led to extending the life of nuclear power plants. The impact of any of these individual conditions on material properties has been well understood but a combination of these presents highly complex scenarios where a number of deformation mechanisms can influence the material performance. Thus it is important to study material behaviour under complex loading conditions.

The overall aim of this research project is to characterise the high temperature response of austenitic steels. This category of steels has been extensively used in power plant construction owing to their corrosion resistance and high temperature properties. Elevated temperature performance involves deformation through creep. Failure due to creep is a key reason which limits the operating temperature of a component. The creep behaviour of

austenitic steels has been studied under a variety of loading conditions. When power plants are being life extended, the prior deformation will affect the future response of the material. Deformation through its lifetime would have occurred through a combination of complex loading cycles. This project specifically looks at understanding material behaviour under loading conditions seen during power plant shut downs and start-ups. This scenario would involve a combination of creep deformation and a very low cycle fatigue effects as well. The assessment codes used to determine the lifetime must take into account such situations.

1.2 Project Details

The project was a part of the Keeping the Nuclear Option Programme (KNOO) programme funded by EPSRC. KNOO is a four-year initiative set-up to address the challenges related to increasing the safety, reliability and sustainability of nuclear power. It involves a number of universities and industrial partners and addresses various facets of nuclear power generation. The KNOO programme represents the single largest commitment to nuclear fission in the UK in the last 30 years.

The programme was divided into four work packages, each looking at a different area of nuclear fission power research. This project came under work package II which has looked at material performance under extreme conditions.

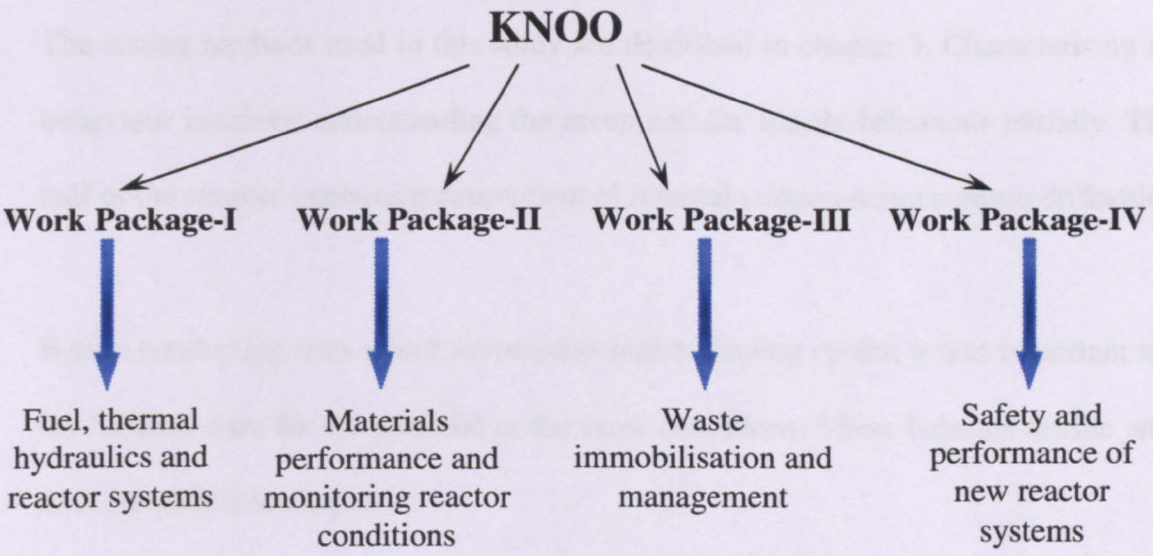

Fig. 1.1 Schematic of KNOO programme

1.3 Outline of Thesis

The thesis presents research carried out to understand the effect of anelasticity on creep behaviour of austenitic steels. Anelasticity can be defined as a recoverable plastic strain seen when a sample is unloaded during a creep test. Various experimental techniques including creep testing, TEM metallography and neutron diffraction were used for this purpose. The structure of the thesis is as follows:

Chapter 2 presents some basic concepts regarding high temperature behaviour. An introduction to austenitic steels has been given. The fundamentals of creep have then been explained. Deformation of any sort will involve changes to dislocation structures. The interactions of dislocations with other dislocations and precipitates have been described. High temperature behaviour involves formation and growth of precipitates. Some of the commonly found precipitates have been explained. Finally, the basics of residual and intergranular stresses have been presented.

The testing methods used in this study are described in chapter 3. Characterising material behaviour involved understanding the creep and the tensile behaviour initially. The latter half of the chapter explains measurement of internal stresses using neutron diffraction.

Before conducting tests which involved complex loading cycles, it was important to obtain the baseline data for the material at the same conditions. These baseline tensile and creep tests are shown in chapter 4.

Chapter 5 presents the results from the creep tests where the loads were taken off and reapplied to simulate reactor shut downs/ start-ups. A number of such tests were conducted and involved unloading for different time periods. Comparisons with the baseline creep data showed significant deviations.

To understand the microstructural changes, two techniques were used: TEM examination and neutron diffraction. The observations from the TEM have been presented in chapter 6. Changes in the dislocation and precipitate densities were observed which have been shown in that chapter. Chapter 7 presents results from an experiment where the intergranular stresses were measured in-situ using neutron diffraction.

Some of these microstructural changes observed during the anelastic phase were incorporated into material models based on damage mechanics. Predictions of material behaviour using this model were performed. Results from these have been presented in chapter 8.

Chapter 9 presents a discussion of the results obtained and how some of the results obtained may be interlinked at a microstructural level. Future areas where this work can be extended have also been mentioned.

CHAPTER 2: LITERATURE REVIEW

Steels form the most important class of metallic alloys in today's world. The manufacture of ferrous alloys has been undertaken since ancient times. 'Stainless' steels form an important category among steels and are used in a wide range of industries including construction, weapons and cutlery to name a few. The enhanced resistance they offer to corrosion is one of their attractive properties.

The initial part of this chapter introduces austenitic stainless steels which is the main material used in this project. The latter parts describe the phenomenon called 'creep' which dominates material deformation at high temperature. The physical mechanisms responsible for creep and the effect of high temperature on material properties are briefly described.

2.1 Introduction to Stainless Steels

Stainless steels are a group of alloy steels which are based on Fe-Cr or Fe-Cr-C/Fe-Cr-Ni systems. They are generally termed as stainless if they display enhanced resistance to corrosion. Chemically to be called 'stainless' they must contain a minimum of 10.5wt% chromium. This level of chromium forms a thin passivation layer of chromium oxide when exposed to air. It is impervious to water and air, protecting the metal beneath. The chromium content assists these steels to exhibit good resistance to oxidation, even at high temperatures (heat-resistance). The improved resistance to corrosion by adding chromium was first studied by Pierre Berthier. The first reported commercial 'stainless steel' is attributed to Harry Brearly who invented it in 1912.

2.1.1 Classification of Stainless Steels

Stainless steels are classified based on the dominant phase within the matrix. Fig. 2.1 shows the Fe-Cr phase diagram. This diagram serves as an initial point to understand the solubility of chromium in iron and also the phase stability of the steel. The γ phase represents the austenitic structure which has a non-magnetic face centred cubic structure. The α and the δ represent the ferrite structure (magnetic and body centred cubic structure).

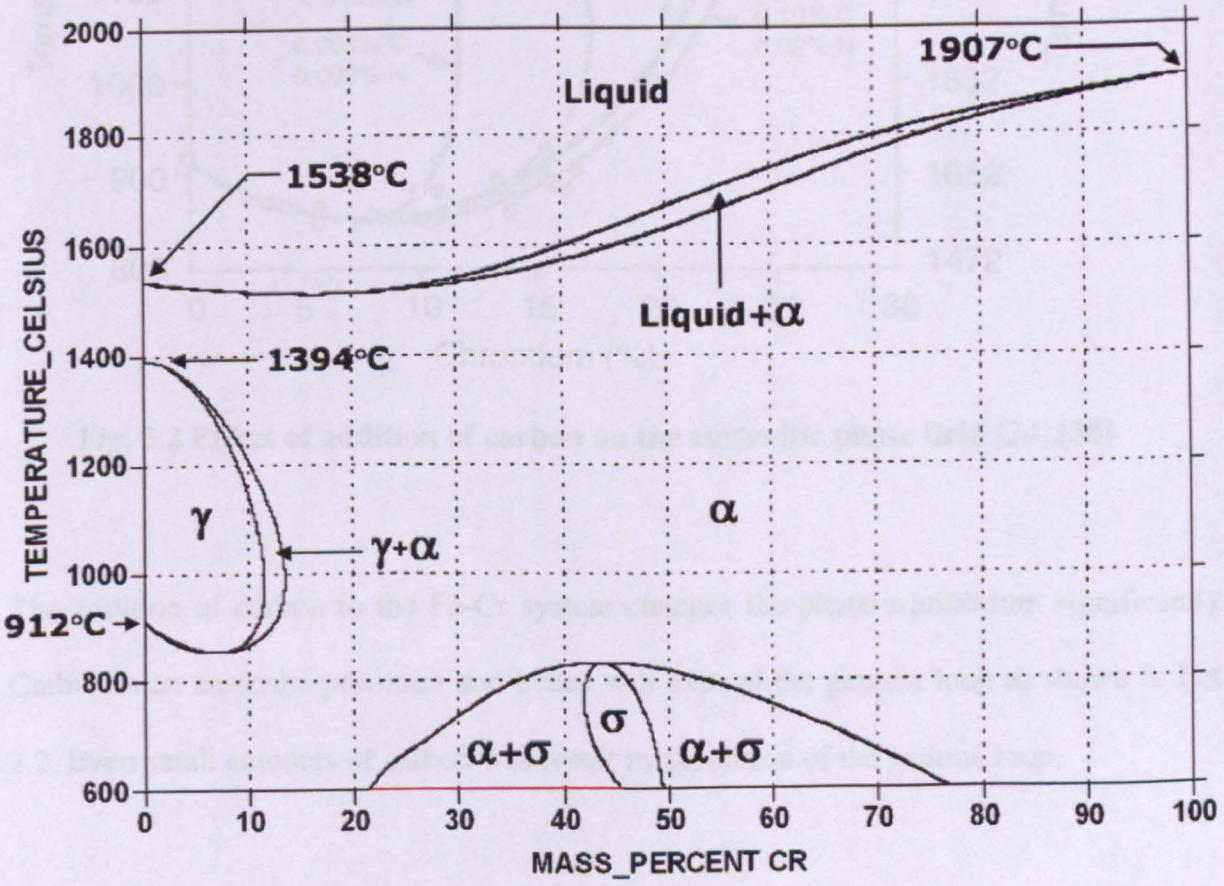

Fig. 2.1 Fe-Cr phase diagram [35, 36]

At low chromium concentrations (<12%), a loop of austenite is formed in the temperature range of 912°C to 1394°C (the gamma loop). Alloys with more than 12.7 wt %Cr will exist as ferrite at elevated temperatures whereas alloys which have less than 12 wt% will form austenite at temperatures within the gamma loop.

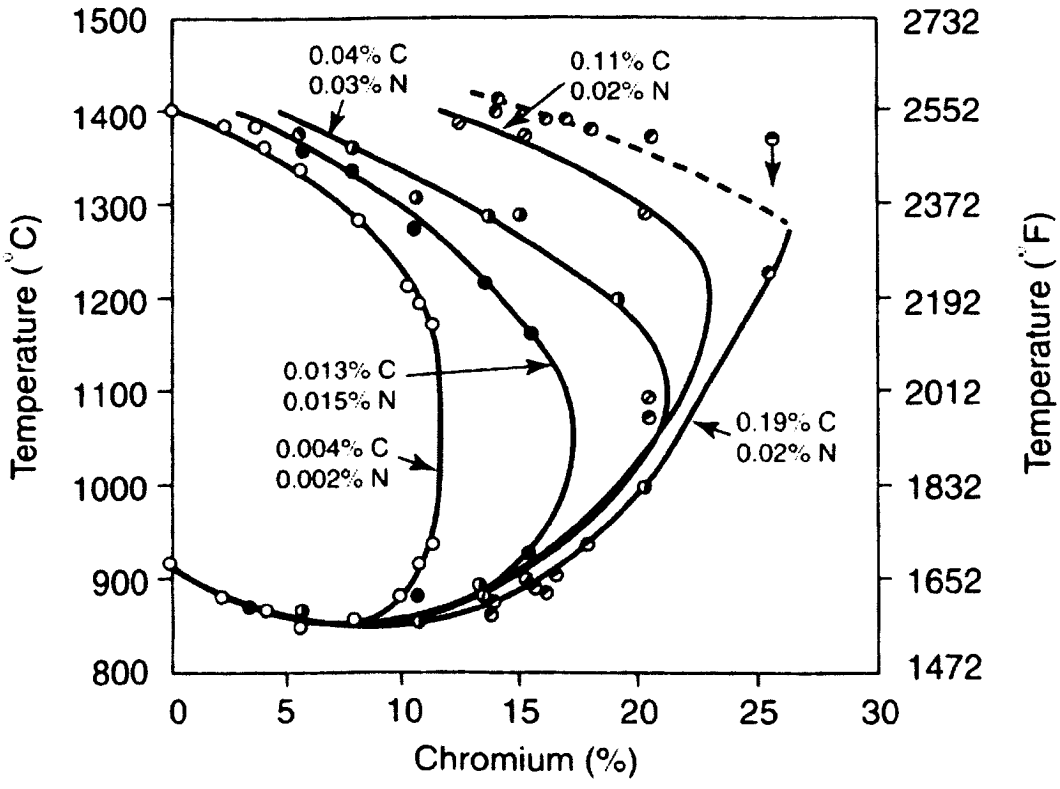

Fig. 2.2 Effect of addition of carbon on the austenitic phase field [34],[38]

The addition of carbon to the Fe-Cr system changes the phase equilibrium significantly. Carbon is an austenite promoter and hence will expand the gamma loop as shown in Fig. 2.2. Even small amounts of carbon will result in expansion of the gamma loop.

2.1.2 Types of Stainless Steel

Stainless steels are of many different types. Their classification is based on their internal microstructure and the predominant crystal structure. Some of the main types of stainless steels are described below. Table 2.1 shows the chemical composition of some of the important grades of stainless steels.

ASTM Designation	C (wt%)	Si(wt%)	Mn(wt%)	P(wt%)	S(wt%)	N(wt%)	Cr(wt%)	Mo(wt%)	Ni(wt%)
301	0.05-0.15	<2	<2	0.045	<0.015	0.11	16-19	0.8	6-9.5
304	<0.07	<1.00	<2.00	0.045	<0.015	0.11	17-19.5	-	8-10.5
304L	<0.03	<1.0	<2.0	0.045	<0.015	<0.11	17-19	-	8-10
310S	<0.1	<1.5	<2.0	0.045	<0.015	<0.11	24-26	-	19-22
314	<0.20	1.5-2.0	<2.0	0.045	<0.015	<0.11	24-26	-	19-22
316	<0.07<1.0	<2.0	<2.0	0.045	<0.015	<0.11	16.5-18.5	2-2.50	10-13
316LN	<0.03	<1.0	<2.0	0.045	<0.015	0.12-0.22	16.5-18.5	2-2.5	10-12.0
321	<0.08	<1.0	<2.0	0.045	<0.015	-	17-19		9-12
405	<0.08	<1.0	<1.0	0.04	<0.015	-	12-14	-	-
409	<0.03	<1.0	<1.0	0.04	<0.015	-	10.5-12.5	-	-
410S	<0.08	<1.0	<1.0	0.04	<0.015	-	12-14	-	-
439	<0.05	<1.0	<1.0	0.04	<0.015	-	16-18	-	-
410	0.08-0.15	<1.0	<1.5	0.04	<0.015	-	11.5-13.5	-	-
420	0.16-0.25	<1.0	<1.5	0.04	<0.015	-	12-14	-	-
630 (*)	<0.07	<0.7	<1.5	0.04	<0.015	-	15-17	<0.6	3-5
631(+)	<0.09	<0.7	<1.5	0.04	<0.015	-	16-18	-	6.5-7.8

Table 2.1 Composition of common stainless steels from ASTM A240/A240M-99a
***- can contain copper (up to 5%) and niobium**
+ can contain aluminium (up to 1.5%)

Austenitic Stainless Steels

These steels represent the largest of the general groups of stainless steels and have austenite (face centred cubic crystal) as their primary phase. This class of steel contains iron, 18wt% chromium, and 8wt% nickel. Type 304 is the most commonly used austenitic grade. Other grades contain alloying elements like nitrogen, manganese, etc. The yield strengths are comparable to mild steels (210MPa). They also exhibit good high temperature strength and can be used in service temperatures of up to 450-500°C. They have got good low-temperature impact properties making them useful in cryogenic applications.

Ferritic Stainless Steels

Their main metallurgical phase is ferrite which has a body centred cubic crystal structure. They are used in applications where corrosion resistance rather than mechanical properties is the main requirement. Ferritic steels containing lower chromium (10-12 wt%) are used in environments such as automobile exhaust systems. Steels with higher chromium (up to 25%) can be used to enhance corrosion resistance (e.g. marine applications).

The microstructure of ferritic steels can be significantly changed by the presence of other elements either as intentional additions or as impurities. Nitrogen and carbon which can be present as impurities are austenite promoters [38]. In order to achieve a stable microstructure, it is necessary to keep the nitrogen and carbon concentrations low or add other elements which promote the ferrite state. Chromium is the primary ferrite stabiliser. In addition to chromium, elements like silicon, titanium, molybdenum are also ferrite promoters. Aluminium is added to improve oxidation resistance at higher temperatures.

Martensitic Stainless Steels

The martensitic microstructure was first observed by German microscopist Adolf Martens around 1890. The composition is such that the austenite in these steels is able to transform into martensite. Martensite is a distorted form of ferrite and has a body centred tetragonal structure. The magnitude of tetragonal distortion depends on the degree of supersaturation with carbon.

The phase change occurring from austenite to martensite can be exploited to enhance mechanical properties. Typical heat-treatments consist of austenitisation at a temperature high enough to dissolve carbides followed by quenching to obtain martensite. Tempering is used to impart ductility and toughness to the steel. Tempering consists of heating the steel and holding the steel at that temperature so that the carbon trapped in the martensite diffuses. This diffusion can lead to the formation of either pearlite (cementite+ferrite) or bainite (similar to pearlite but with smaller lamellar structure).

Martensitic steels have carbon contents of up to 2 wt%. 410 is the basic grade and has chromium in the range of 12wt%- 14wt %. As a result of this, corrosion resistance is less when compared to austenitic or higher ferritic grades.

These steels can be designed so as to have a wide range of strengths. In an annealed state, these steels can have yield strengths of 275MPa but in a tempered and quenched condition, yield strengths increase to 1000MPa. The hardness values are also high and the material has good wear and abrasion resistance.

The applications of this class of steel are in gas and jet engine turbine blades, steam piping and hydroturbines. They are generally not used in operating conditions in excess of 650°C

as their mechanical properties and corrosion resistance are degraded at higher temperatures.

Precipitation Hardened Steels

These steels are designed to derive a significant part of their hardness from precipitation reactions. The elements which are used in these steels form fine precipitates when heat treated. Copper, aluminium, titanium, niobium, and molybdenum are added to achieve the precipitation. They are denoted by a suffix PH and are subclassified based on their dominant phase in their microstructure.

Tensile strengths in excess of 1500MPa can be achieved in these steels [41]. Proper heat treatments will also result in the material having good ductility and toughness. Their service temperatures are limited to 300°C but austenitic PH grades can be used in environments at higher temperatures (600°C). Corrosion resistance properties approach those of 304 grade stainless steel.

Typical applications include pressure vessels, turbine blades, nuclear waste casks etc. As many of these alloys are martensitic and precipitation strengthened, fabrication of such steels is difficult and requires specialised heat treatments. As a result, they can be more expensive than other grades of steel.

Duplex Stainless Steels

Duplex stainless steels have a mixed microstructure of austenite and ferrite. Duplex steels show greater strength than austenitic stainless steels and also improved resistance to localised corrosion, particularly pitting, crevice corrosion and stress corrosion cracking. They have a higher thermal conductivity and a lower thermal expansion rate. The steels in

this category are generally ferromagnetic. They are mainly used in areas where corrosion resistance is important and have been used instead of austenitic steels in applications where stress corrosion cracking and pitting are issues.

They are stronger than austenitic steels with yield strengths of over 400MPa. They are also harder thus offering good abrasion resistance. Toughness and ductility are also comparable but they undergo a ductile to brittle transformation at lower temperatures. They are susceptible to embrittlement at temperatures in excess of 250°C [34] and thus are not used in service above such temperatures. They are more expensive than austenitic steels due to their processing cost.

Their biggest use has been in the oil and gas industry where they are used in the construction of pipelines (both onshore and offshore). Due to their thermal expansion being close to low alloy steels, they are used in situations where they are coupled with low alloy steels.

2.2 Effect of Alloying Elements

Stainless steels can contain a number of elements which are added to improve the mechanical properties and corrosion resistance. These will influence some of the precipitation reactions which are discussed later. The principle alloying elements to the iron base are carbon and chromium in martensitic/PH steels and nickel for austenitic/duplex grades. This section examines the effect of some of the alloying elements.

Chromium

Chromium provides corrosion resistance to steel. The addition of chromium promotes the formation of an oxide layer ($(Fe,Cr)_2O_3$) on the surface. It increases the stability of this compound as it has a higher affinity to oxygen than iron. Chromium is also a ferrite promoter. Thus in ferritic stainless steels, it is the main element which stabilises the microstructure. Chromium also assists in formation of precipitates. The most common chromium rich carbide is $M_{23}C_6$ where 'M' is generally 'Cr' but can also be 'Fe' or 'Mo'. This carbide is found in almost all steels.

Chromium is also influential in the formation of intermediate phases (eg: σ phase). Such phases increase embrittlement in steels. The sigma phase can form in most grades of austenitic steels but is more common in high-Cr austenites. Chromium is also found in the 'chi' and the laves phases.

Nickel

The main function of nickel is to promote austenite. Addition of nickel enables the austenitic loop (Fig. 2.1) to greatly expand such that austenite is stable at room temperature and below. Nickel does not promote the formation of carbides or intermetallics although it can influence precipitation reactions [42]. It has also been associated with a reduction in stress corrosion cracking resistance [43]. It is a good solid solution strengthener and improves toughness in both ferritic and martensitic grades. Addition of nickel can also lead to a reduction in the ductile-to-brittle transition temperature [44].

Manganese

Manganese is added to almost all grades of steel. In terms of composition about 1-2 wt% is added to austenitic steels but for ferritic and martensitic grades, it is less than 1%.

Manganese is an austenite promoter but this depends on its amount and also on the level of nickel. It assists in stabilisation of austenite at lower temperatures to prevent formation of martensite. It can also increase the solubility of nitrogen in the austenite phase [45]. Historically, it has been added to prevent hot cracking during solidification. Hot cracking is a solidification cracking process associated with iron sulphide compounds. Manganese addition forms stable manganese sulphide which reduces the risk of hot cracking.

Silicon

Silicon like manganese is added to all grades of stainless steels mainly to prevent deoxidation during melting. It ranges from 0.3-0.6 wt%. Higher levels of silicon (4-5wt %) can improve corrosion resistance. Silicon can also provide oxide scaling resistance. In austenitic steels silicon up to 1wt% has no effect on the phase balance but levels higher than this can lead to ferrite promotion. Silicon is generally regarded as a ferrite promoter.

Silicon forms iron silicides (FeSi, Fe_2Si, Fe_5Si_3) and other intermetallics, all of which can lead to embrittlement. It also expands the composition range over which the sigma phase can be formed. It also tends to segregate during solidification which results in formation of low melting point eutectic constituents by combining with nickel. For all these reasons, its composition is held below 1wt%.

Molybdenum

The function of molybdenum depends on the particular grade. For ferritic and duplex grades, amounts of up to 6 wt% can improve pitting and crevice corrosion. In austenitic steels, addition of molybdenum greatly improves high temperature strength. However, higher amounts of molybdenum will make the material difficult to hot work. Molybdenum in martensitic steels can act as a carbide former. Small amounts (up to 0.5wt%) of it

increase the secondary hardening characteristics resulting in higher room temperature yield and better strength at high temperatures. Molybdenum is also a ferrite promoter. Potentially in martensitic grades, this can be a problem as ferrite will be retained in the microstructure resulting in reduced toughness and ductility.

Carbon

Carbon is an interstitial atom and is present in all steels. Generally, in stainless steels the carbon content is controlled to within 0.1wt%. In solution, carbon provides an interstitial strengthening effect, particularly at elevated temperatures. At elevated temperatures, carbon combines with other elements and forms carbides. These precipitates increase the capacity of the material to stop dislocation motion, thereby imparting high temperature strength. $M_{23}C_6$ rich areas can lead to degradation in corrosion resistance.

Nitrogen

Nitrogen is generally present as an impurity but sometimes is added intentionally to some austenitic and all duplex grades. Small additions can lead to increased strength in austenitic steels [48]. The effect is more prominent at cryogenic temperatures.

Both carbon and nitrogen are powerful austenite promoters and their levels must be controlled if a precise microstructure is required. Other than these, a number of other elements like niobium, titanium, vanadium, etc. are added to enhance carbide formation. Niobium and titanium in austenitic steels provide stabilisation of carbon and hence retard intergranular corrosion. Tungsten and vanadium provide elevated temperature strength by forming finely dispersed carbides.

2.3 Austenitic Stainless Steels

As mentioned before, austenitic steels form the largest group in terms of production of stainless steels. During production of such steels, it is necessary to preserve the austenite structure at room temperature. This is done by adding elements like nickel which promote austenite in large quantities (>8wt %). Higher nickel favours better ductility. Other austenite promoting elements include carbon, nitrogen and copper. Carbon also imparts high temperature strength. Nitrogen can increase the room and cryogenic temperature strengths.

Although chromium favours the formation of ferrite it is required to retain the corrosion resistance of the material. However, when chromium is added to a steel containing nickel it retards the kinetics of the austenite to ferrite transformation, thus helping to retain austenite at room temperature [1]. This explains the existence of the common 18% Cr 8% Ni (known as the 304 alloy) austenitic stainless steel alloys. The more chromium used in the steel (for higher corrosion resistance) the more nickel is required to retain the austenite at room temperature.

These steels have good ductility and toughness. During a tensile test, they exhibit high elongation (about 30-40% strain). Their cost is quite high compared to ferritic and martensitic grades due to the higher alloy content but they offer distinct advantages with regards to weldability and formability which can offset these costs.

There is a wide variety of austenitic grades available. Most of these are based on the 300 series. Steels falling under this series are the most widely used. They are based on 18Cr-8Ni steel with additional alloying to provide unique or enhanced properties. These steels

are used in a wide range of applications including structural supports, pressure vessels, piping systems, surgical equipment, etc.

2.4 316 Austenitic Steels

The 316 grade steel is a modification of the basic stainless steels (18% Cr 8% Ni- Grade 304). Molybdenum (2-3%) is present which substantially improves the general corrosion resistance of the alloy, in particular resistance to pitting corrosion [2]. Consequently more nickel is also required to help retain the austenitic structure of the alloy. The carbon content within this alloy is also adjusted to produce 316L and 316H grades. 316L is a low carbon alloy containing a maximum of 0.03%C. This is useful for welding applications, reducing formation of carbides and hence intergranular corrosion. 316H has a higher carbon content (0.04-0.1%C). Higher carbon content results in an improvement of the high temperature creep properties of the alloy.

A more detailed description of the material properties of this grade of steel is given in chapter 4.

2.5 High Temperature Deformation

The strength of a material can change significantly with temperature. Materials which operate in high temperature environments will typically see a reduction in their yield strength. Temperature increases the mobility of atoms which enables diffusion controlled mechanisms to play a greater role in influencing the material characteristics. The motion of dislocations will also increase and dislocation climb influences material behaviour as temperature increases. Deformation mechanisms may change with temperature with

different slip systems getting activated. Temperature will also affect the microstructural stability of the material.

It is evident that applications at high temperature involve a number of possible problems. While predicting material behaviour at high temperatures, it is important that the material properties are considered with respect to a time scale. While conducting a tensile test at elevated temperatures, factors like strain rate and time of exposure will affect the results. The phenomenon called 'creep' plays an important role in the material properties.

Creep can be defined as the time-dependent deformation of the material when exposed to a stress. This deformation is generally more pronounced at elevated temperatures. The mechanisms controlling creep are influenced by both stress and temperature [3]. Theoretically, creep is a thermally driven process and will occur at all temperatures above absolute zero, but the dimensional changes due to creep at lower temperatures are extremely small and can be ignored.

Creep becomes more prominent when the operating temperature is more than 0.3 T_m [4], where T_m is the melting point of the material. Many of the internal mechanisms of the material which affect the creep behaviour are thermally activated processes. A further description of some of these mechanisms is given in the following sections. Diffusion controlled processes will be affected by temperature thus contributing to higher creep rates. Dislocation motion is also affected by temperature. A higher temperature gives more energy to dislocations. This helps them to 'climb' over obstacles which means they are not constrained to move in their own slip planes. Other mechanisms like recrystallisation are also influenced by temperature. Depending on the crystal and atomic structures, each of

these mechanisms will have an activation energy associated with it. These values will vary from material to material.

2.6 The Creep Curve

Creep tests are generally load controlled tests. Specimens are subject to a constant load at a fixed temperature. The strain in the material is measured at fixed time intervals and a graph of strain against time is plotted. This curve is called the creep curve. Fig. 2.3 shows a typical creep curve.

Creep can be split into separate stages: primary, secondary and tertiary. The extent to which these three stages are distinguishable is dependent on applied stress and temperature [7].

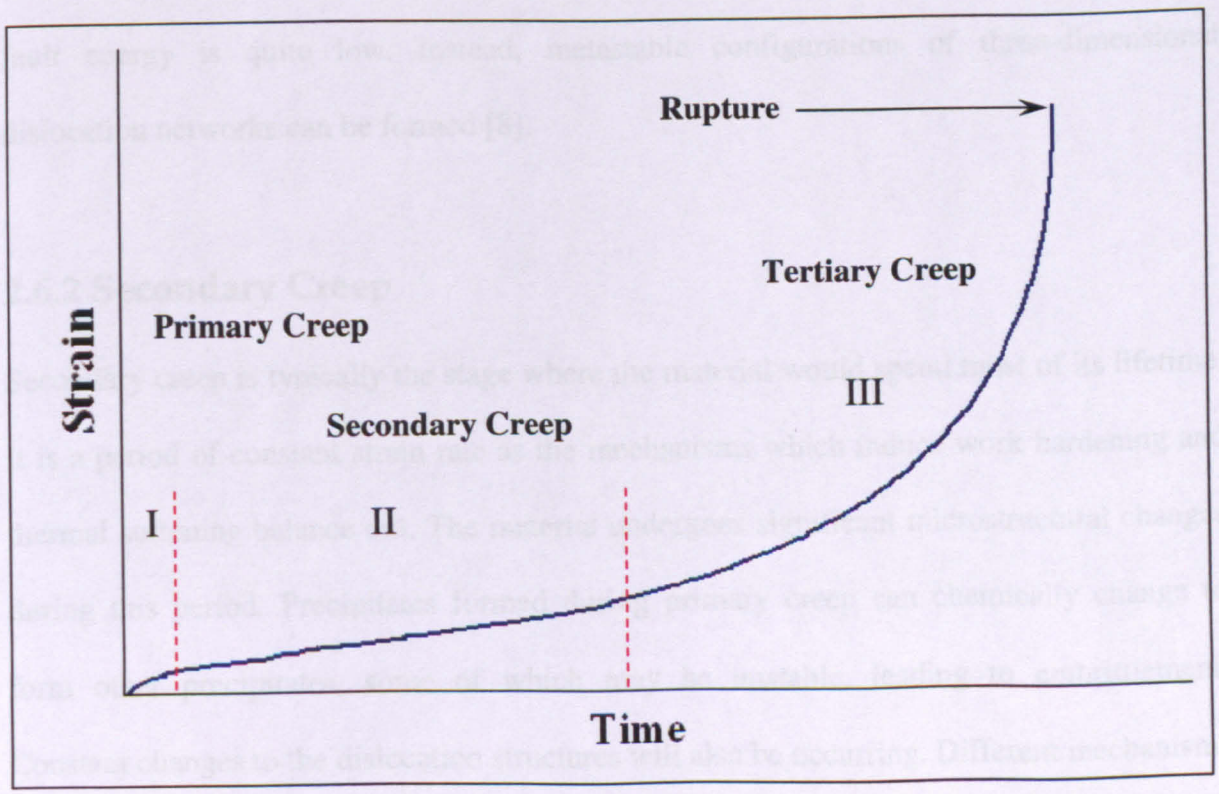

Fig. 2.3 A typical creep curve

2.6.1 Primary Creep

Primary creep is the initial stage of creep after the load has been applied. This process consists of strain hardening of the material. It is a period of decreasing strain rate. Although most creep experimentation is concentrated around the secondary stage, some power plant components may spend a considerable amount of time in the primary stage. Primary creep is influenced by microstructural changes. Dislocation structures accumulate and this results in hardening. This induces a decrease in strain rate as primary creep progresses. Thermomechanical pre-treatments can also influence the primary creep behaviour [8].

Primary creep is the principal stage for stress-induced generation of dislocations. At the same time, dislocations form low energy networks of sub-boundaries. This process decreases the available mobile dislocations causing a decrease in flow rate. Sub-boundary formation in austenitic steels can sometimes be retarded for long times as their stacking fault energy is quite low. Instead, metastable configurations of three-dimensional dislocation networks can be formed [8].

2.6.2 Secondary Creep

Secondary creep is typically the stage where the material would spend most of its lifetime. It is a period of constant strain rate as the mechanisms which induce work hardening and thermal softening balance out. The material undergoes significant microstructural changes during this period. Precipitates formed during primary creep can chemically change to form other precipitates, some of which may be unstable, leading to embrittlement. Constant changes to the dislocation structures will also be occurring. Different mechanisms are prevalent during this stage. This include diffusional (Nabarro-Herring Creep, Coble

Creep) and dislocation creep (power law creep). These are explained further in the following sections.

2.6.3 Tertiary Creep

Tertiary creep is the final stage in creep leading to rupture. It is a period of increasing strain rate as the cavities which are formed in the material will coalesce and form creep cracks leading to failure. The total time elapsed and the accumulated strain at the end of this stage would give the rupture life and ductility. These parameters are important factors in design and assessment [9]. Fracture in creep tests is generally intergranular. Examples of intergranular cracks are shown in Fig. 2.4 and 2.5.

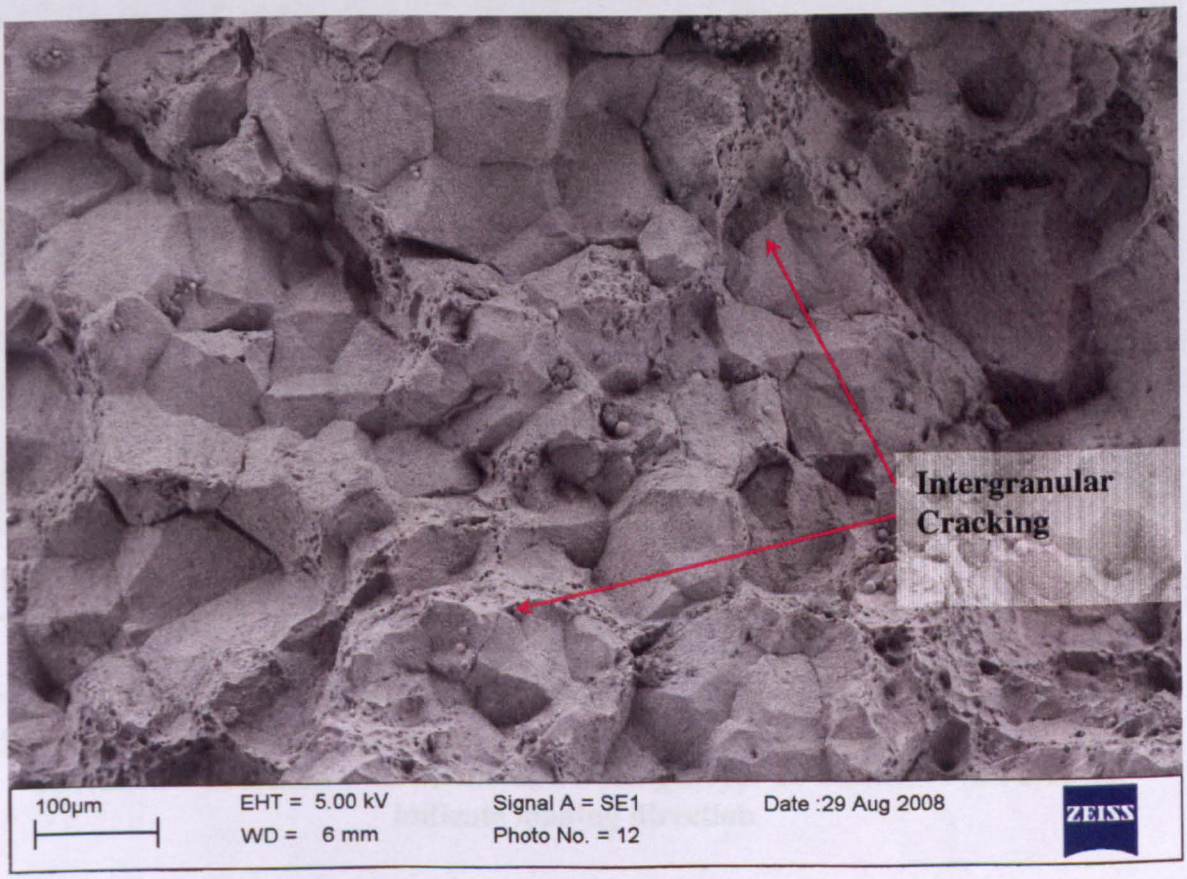

Fig. 2.4 Electron microscope image showing a creep rupture surface (axial direction) in a 316H steel specimen with test conditions 650°C 180MPa

The different stages identified during this process are [1].

- Formation of cavities
- Nucleation of cavities
- Intergranular wedge cracks
- Nucleation of cracks
- Stable growth of cracks
- Unstable growth of cracks leading to final fracture.

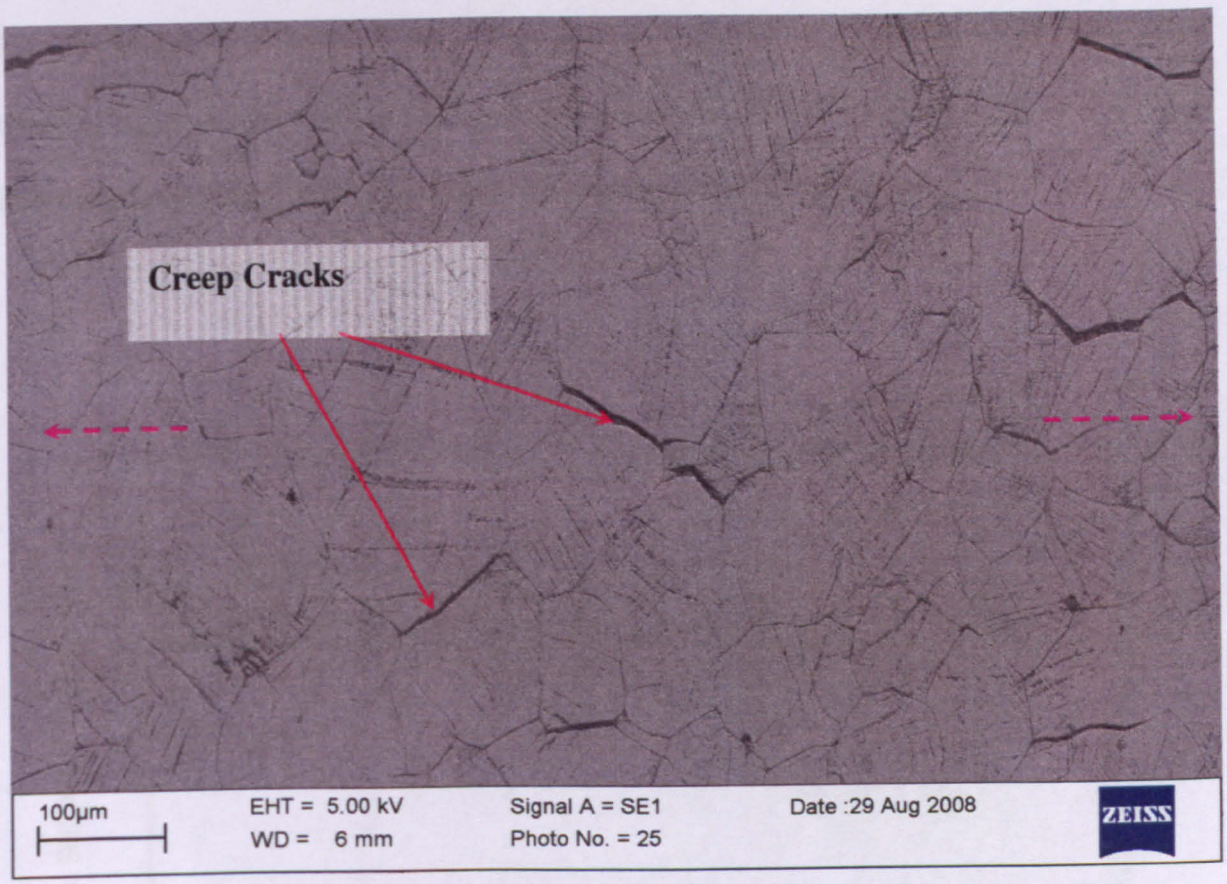

Fig. 2.5 Electron microscope image showing intergranular creep cracks (transverse direction to loading) in a 316H steel specimen with test conditions 650°C 180MPa. Specimen was etched with Murakami's Reagent for 20 seconds. Pink arrows indicate loading direction

2.7 Mechanisms in Secondary Creep

As mentioned in the previous section, secondary creep can consist of either diffusion creep mechanisms and/or dislocation creep mechanisms depending on the stress-temperature conditions. A useful way to represent these mechanisms are creep deformation mechanism maps. A map showing the different mechanisms in AISI316 steel is shown in Fig. 2.6. The boundaries of each region are calculated by using the appropriate equations for a given mechanism at different combinations of stress and temperature. The stresses and temperatures are normalised to σ/G (where G is the shear modulus) and T/T_m respectively. The advantage of normalisation is that materials of the same crystal class and similar bonding type can be reduced to a single map. The effect of strain rate can also be introduced into these maps by plotting contours of constant strain rate.

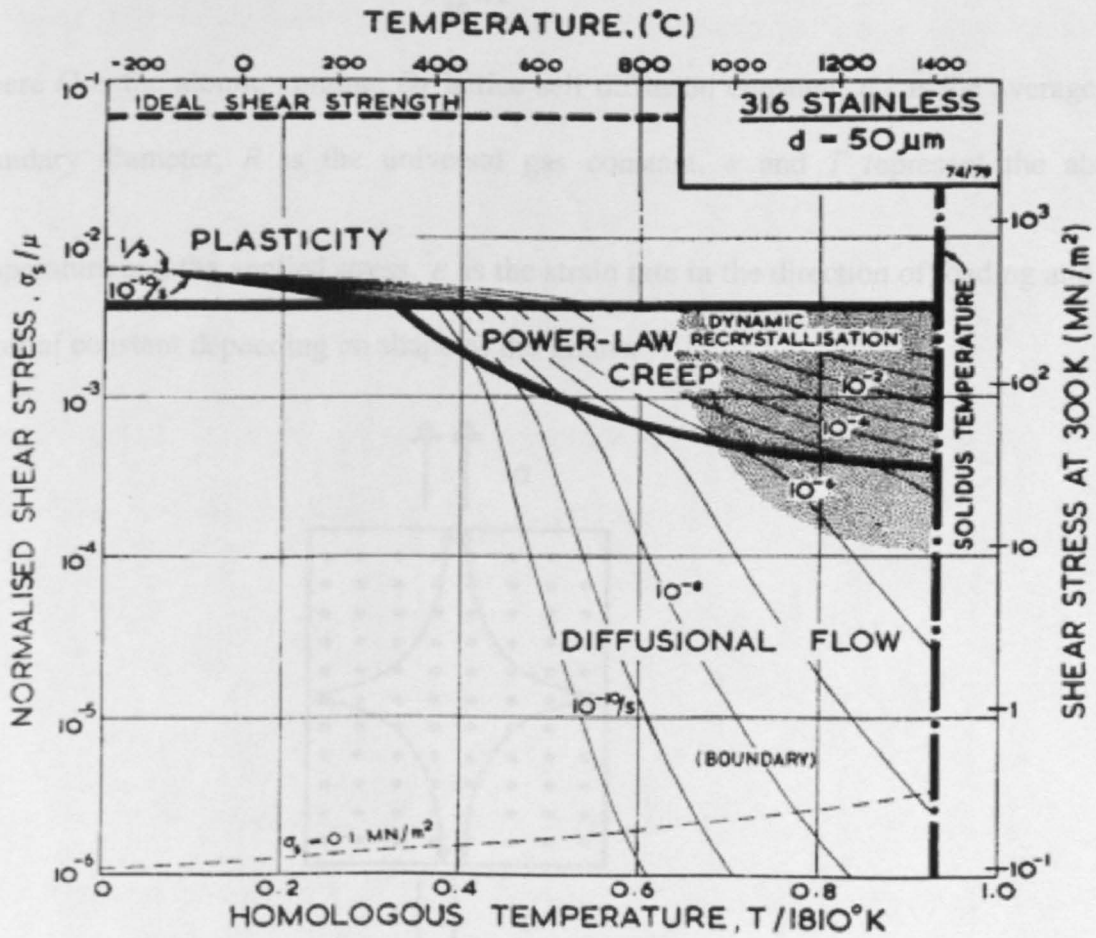

Fig. 2.6 Creep deformation map for 316 Steel with a grain size of 50 microns [33]

2.7.1 Diffusion Creep Mechanisms

An external stress applied to the material can direct the diffusion of point defects through a crystal or around ground boundaries. This concept was first proposed by Nabarro [10] and Herring [11]. A schematic showing atomic flow through the crystal lattice is shown in Fig. 2.7. They proposed relationships for the through-grain diffusion and its relation to strain. Free surfaces and grain boundaries are usually sources and sinks of vacancies. Vacancy formation is enhanced in these regions due to reduced energies needed to form vacancies resulting from imperfections (e.g. mismatch in the grain boundaries between two neighbouring grains). If these concentrations are not uniform, diffusion causes the vacancies to migrate which results in deformation of the crystal with activation energy equal to self diffusion. This process for pure crystals can be represented by [11, 12]:

$$\dot{\varepsilon} = \frac{\alpha D_L \sigma \Omega}{d_{gb}^2 RT} \qquad 2.1$$

Where Ω is the atomic volume, D_L lattice self diffusion constant, d_{gb} is the average grain boundary diameter, R is the universal gas constant, σ and T represent the absolute temperature and the applied stress. $\dot{\varepsilon}$ is the strain rate in the direction of loading and α is a material constant depending on shape of the grains.

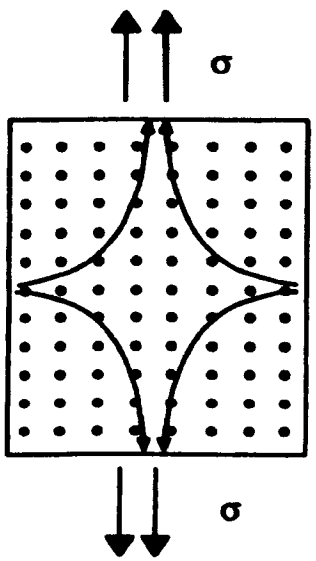

Fig 2.7 Schematic of Nabarro-Herring creep. Atomic flow through the crystal causes deformation [14]

Coble creep is another diffusional creep mechanism but can be considered as a special case of Nabarro-Herring creep. Coble creep can be represented by [4, 5]

$$\dot{\varepsilon} = \frac{141 D_{gb} \delta \sigma \Omega}{{d_{gb}}^3 KT} \qquad 2.2$$

Where D_{gb} is the grain boundary self diffusion constant and δ is the grain boundary thickness. The major difference between Coble creep and Nabarro Herring creep is that creep rate is dependent on the grain size and also the activation energies for bulk diffusion and grain boundary diffusion [15]. Generally grain boundary diffusion has a lesser activation energy. For this reason, Coble creep can become more enhanced at temperatures lower than what is required for Nabarro-Herring creep.

2.7.2 Dislocation Creep

Diffusion creep in the previous section has been described by motion of vacancies from one sink (grain boundaries, material bulk, etc.) to another. Dislocation motion will also influence deformation to a large extent. Strain rates seen in this type of creep can be described as

$$\dot{\varepsilon} \propto \sigma^{(n>1)} \qquad 2.3$$

Where n is called the stress exponent and is between 2-10 for steel in a majority of cases. Dislocations can propagate through the material by either 'glide' or 'climb'.

Dislocation Glide

This type of dislocation motion occurs when a dislocation line moves parallel to its Burgers vector. A schematic of this process is shown in Fig. 2.8. It requires only a small displacement without transfer of matter. Vacancy diffusion is the primary method for this mechanism. This motion is also termed as conservative [17] and is defined as 'the motion

of a dislocation line when it moves on the cylinder defined by its initial position and its Burgers vector' [18], [19]. The stress exponent is generally less than 4 [16].

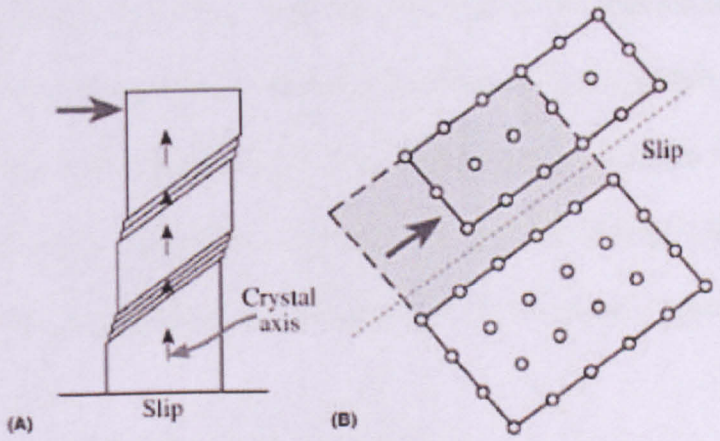

Fig. 2.8 Schematic of dislocation glide (a) macroscopic (b) atomic ([22])

Dislocation Climb

Dislocation motion where the movement is perpendicular to their Burgers vector is termed as dislocation climb. At elevated temperatures, if a dislocation is held up by an obstacle, a small 'climb' in the perpendicular direction might enable it to overcome the obstacle. This process will get repeated the next time it meets an obstacle. This process has been schematically illustrated in Fig. 2.9. The glide motion controls most of the strain but the velocity is controlled by the climb step. This process requires diffusion of vacancies or interstitials. Thus, the main rate controlling process would be atomic diffusion. The stress exponent for this process is between 4-7 [7].

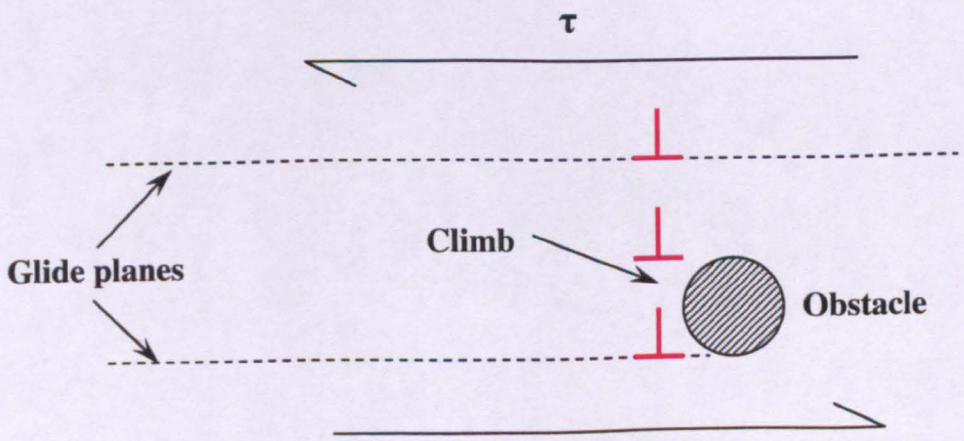

Fig. 2.9 Schematic of dislocation climb and glide [22]

In high temperature creep, dislocation climb and glide can be thought of as successive motions of dislocations. The time taken for a dislocation to climb over an obstacle depends on the flux of thermal vacancies. Typically, the higher the applied stress, the higher this rate will be and also the distance which the dislocation has to climb will be smaller. The time taken to glide to the next obstacle will depend on the balance of forces between the applied stress and the internal stresses in the material which will oppose the glide. Typically, secondary creep rate can be described by an Arrhenius type equation

$$\dot{\varepsilon} = A\sigma^n \exp\left(\frac{-Q}{RT}\right) \qquad 2.4$$

Where σ is the stress, n is the stress exponent, Q is the activation energy, T is the absolute temperature, R is the universal gas constant and A is a material constant.

2.8 Influence of Stress on Creep Behaviour

As explained in the previous section, creep has a power-law relationship with the applied stress. The stress exponent n lies between 1-7. There are exceptions to these numbers as n can have a thermal dependence.

$$\dot{\varepsilon} = A\sigma^n \qquad 2.5$$

At higher temperatures were diffusion flow dominates, metals behave in a viscous manner and n has a value of 1 i.e. the creep rate varies linearly with stress. During power law creep stress indices of 3-5 can be accounted for theoretically by dislocation climb. As mentioned earlier work hardening results in the piling up of dislocations and recovery occurs by dislocation climb. During secondary creep the two processes are equal and so the creep

rate is controlled by climb. As stresses are increased, the power law relationship breaks down and an exponential relationship can be found [23].

$$\dot{\varepsilon} = A_1 \exp(\beta\sigma) \qquad 2.6$$

Where A_1 and β are material parameters independent of applied stress but can have a thermal dependence.

2.9 Influence of Temperature on Creep Behaviour

It has already been stated that creep generally becomes significant above $0.3\text{-}0.4T_m$, however while the melting point has a large influence on the creep properties of the material, it is only one of many important factors to be considered. The crystallographic and metallurgical structures also have a great influence on the temperature at which creep will become significant and these factors are particularly important in the case of steels. For body-centred cubic (bcc) ferritic steels creep becomes important above 300°C. However, for face-centred cubic (fcc) austenitic steel, creep only becomes significant above 500°C despite both steels having a similar melting point due to differences between the rates of self-diffusion in ferrite and austenite.

An Arrhenius type equation can be used to understand the effect of temperature on creep deformation.

$$\dot{\varepsilon} = A \exp\left(\frac{-Q}{RT}\right) \qquad 2.7$$

Thus, creep rate will increase exponentially with applied temperature. Theories [24, 25] explaining creep behaviour are generally based on diffusion controlled processes. Metals generally deform when the crystallographic planes slip over each other by motion of dislocations. Below a homologous temperature of around 0.4, these dislocations can move

freely by the action of self-diffusion through the lattice until they pile up (work hardening) at some internal obstacle i.e. precipitates, particles, grain boundaries or the stress fields of other dislocations. The back stresses generated by the pile-up of dislocations will eventually balance the external stress, so deformation will stop (the end of primary creep). However, at higher homologous temperatures (0.4-0.6), dislocations have a considerably higher thermal activity giving them increased mobility. First of all the mobility is confined to the screw component of the dislocation. This means that the dislocations can pass obstacles by moving out of their original planes by a mechanism called cross slip. At higher temperatures dislocations can climb over the obstacle by diffusion. It is through these mechanisms that recovery can occur, removing the effects of earlier work hardening. This is the beginning of secondary creep, where work hardening and recovery are balanced. The creep rate now becomes proportional to the climbing rate, which in turn is controlled by the rate of atomic diffusion. At even higher temperatures, it is possible for creep to occur by pure diffusion. However, this temperature is usually out of the range of engineering interest.

2.10 Precipitation During Creep in Austenitic Stainless Steels

Stainless steel, due to its alloying elements can form different types of precipitates during creep. The formation of precipitates is influenced by the aging temperature and also the duration of aging. The ratios of the alloying elements will determine the nature of the precipitates formed. To impart creep resistance, one would ideally want a finer distribution of carbides as this means the dislocations will get pinned more quickly thus affecting their motion. Some of the commonly found precipitates are described below.

$M_{23}C_6$ Carbide

This carbide is the predominant carbide seen in many austenitic grades. This carbide is predominantly chromium carbide but other alloying elements can substitute chromium. Thus, generically it is termed $M_{23}C_6$. It has an fcc structure with a lattic parameter of 10.57-10.68 Å [1]. Precipitation of this carbide occurs rapidly on the ferrite-austenite interface followed by precipitation on inclusions, grain boundaries and twin boundaries [26]. The formation of this carbide seems to occur throughout the material's lifetime. Lai [49] has found that in creep specimens which were exposed for times greater than 80,000 hours, there was an increase in the carbide densities. Also, it is probable that at longer exposure hours, carbide growth occurred predominantly in the grain boundaries [50].

An excess of $M_{23}C_6$ can lead to degradation in intergranular corrosion resistance and reduction in tensile properties like ductility and toughness [1]. Except in the intragranular form, this carbide is not desirable for good creep properties. It causes a local depletion in chromium and possibly local loss of the stainless property.

M_6C Carbide

This is formed in stainless steels containing molybdenum or niobium. It has an fcc structure with a lattice parameter of 11Å. In 316 steels, it is formed after longer aging times and from $M_{23}C_6$ [28].

$$M_{23}C_6 \xrightarrow[\sim 650^\circ C]{+Mo} (FeCr)_{21}Mo_2C_6 \xrightarrow{+Mo} M_6C$$

It has also been theorised that a continuous grain boundary layer of M_6C could promote intergranular embrittlement.

MC Carbides

It is generally found in steels which are stabilised (eg: Grades 321- titanium stabilised, 347- niobium stabilised) to prevent intergranular corrosion. These steels are given a heat treatment to improve their intergranular corrosion resistance. Such treatments precipitate NbC or TiC carbides. The effect of these precipitates on material properties seems to be minimal. These can precipitate intragranularly and also on dislocations and stacking faults.

Sigma Phase

The σ phase formed in austenitic steels is a hard, brittle phase. Its occurrence is generally associated with embrittlement. It can precipitate along triple points and grain boundaries. In creep-resistant steels, it has a detrimental effect when precipitated on grain boundaries but little effect when precipitated intragranularly [26]. The sigma phase formation occurs due to transformation of delta ferrite after prolonged exposure to elevated temperatures (>450°C). The phase formation has very slow kinetics and can take several hundred or sometimes thousands of hours to form.

Laves Phase

It is a minor constituent in 316 steels and generally occurs when the aging temperature is over 600°C. It precipitates intragranularly but can also be found along grain boundaries. The effect of this phase on creep properties is still uncertain. It does promote the occurrence of M_6C particularly in niobium stabilised steels which can cause embrittlement.

2.11 Interaction of Dislocations

Dislocation interaction is one of the main factors influencing the material properties. Dislocations can interact with a number of entities within the material and these include precipitates, other dislocations and grain/sub-grain boundaries. One of the examples is

during primary creep, stress-induced generation of dislocations occurs and dislocations tend to pile up which increases the strength of the material initially.

2.11.1 Interaction with Other Dislocations

Dislocation motion will affect the overall substructure within the material. The direction of dislocation motion will result in dislocations repelling dislocations and hence cancelling each other if their motions are in an opposite sense to each other. Similarly, dislocations in the same glide plane can attract other dislocations moving in the same directions. A schematic is shown in Fig. 2.10. Edge dislocations with identical or opposite Burgers vector *b* on neighbouring glide planes may attract or repulse each other, depending on the precise geometry. The blue double arrows in the picture below thus may signify repulsion or attraction.

Fig. 2.10 Schematic of (a) Dislocation Repulsion/ (b) Attraction

Dislocations tend to shorten their link lengths in order to minimise their energy. The force exerted is similar to a tensile force applied along a line. This is due to atoms near the core of a dislocation having a higher energy due to distortion. The force on the dislocation is the strain energy per unit length and is given by [29].

$$T_L \approx \frac{1}{2} G b^2 \qquad 2.8$$

Where T_L is the line tension, G is the shear modulus and b is the Burgers vector.

2.11.2 Polygonisation and Subgrain Formation

A material after deformation can be in a metastable, high energy state due to an increase in its internal energy. In order to achieve stability, it will try to lower its internal energy. An external source of energy (e.g. temperature) might be needed to achieve this [51]. Recovery is the earliest onset of re-arrangement of crystal defects in the deformed microstructure at elevated temperature, where some restoration of the original structure and properties may occur through annihilation of point defects and dislocations and spatial re-arrangement of dislocations [52]. Consequently, the metal will soften. In the case of deformed metals, point defects and dislocations are created during deformation. However, point defects anneal out at lower temperatures and do not usually constitute a separately identifiable stage of recovery.

Another recovery mechanism is polygonisation. It is generally associated with crystal structures that have been deformed plastically. A schematic of dislocation structures in a deformed crystal is shown in Fig. 2.11. Any crystal that has been plastically deformed will contain an excess of positive-edge dislocations that lie along certain slip planes. When dislocations of the same sign accumulate on the same slip planes, their strain fields are additive. However, dislocations can also be arranged so that the tensile strain field may overlap with the compressive field in which case their strain fields will cancel each other. Polygonisation can thus lead to lowering the strain energy. It also can cause the regrouping of edge dislocations into low-angle boundaries which approach the state of strain-free crystals. These low-angle boundaries are termed as sub-boundaries and the resultant crystals as sub-grains.

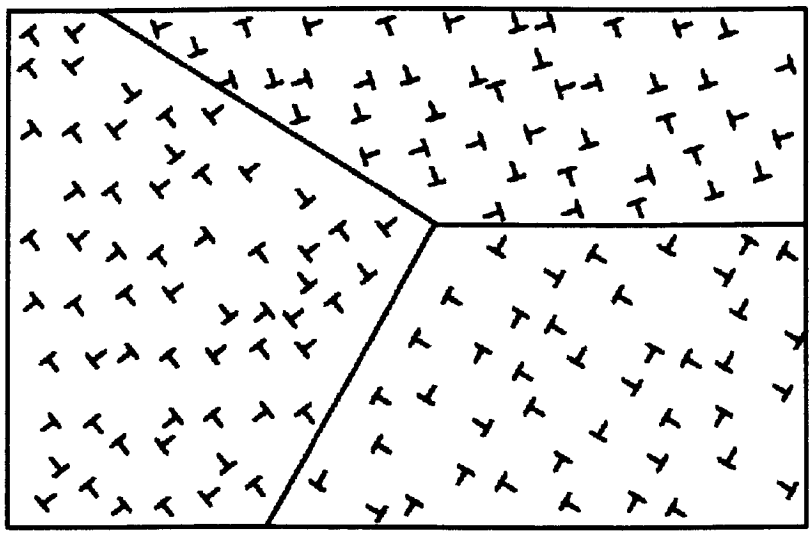

(a)

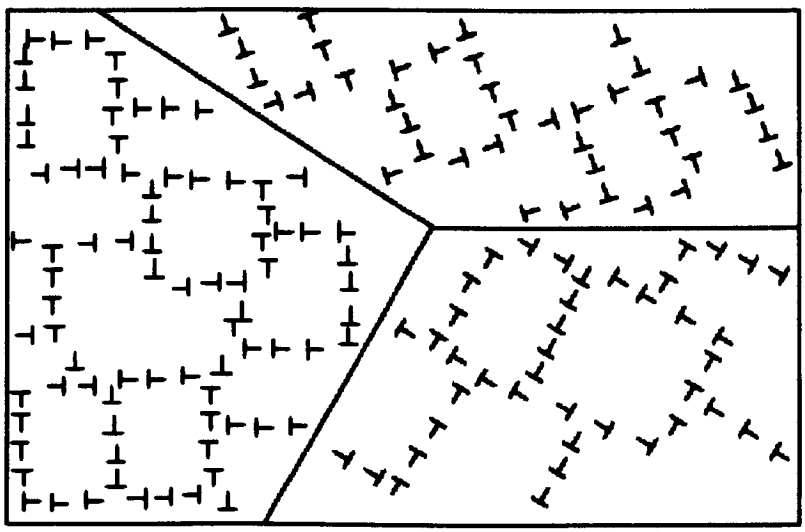

(b)

Fig. 2.11 Schematic representation of dislocation structures after (a) Deformation (b) Formation of subgrains and subgrain boundaries [51]

2.11.3 Interaction with Precipitates

When a dislocation encounters a precipitate, pinning of dislocations occurs where the dislocation is held by precipitates at the two ends and bending of the dislocation occurs.

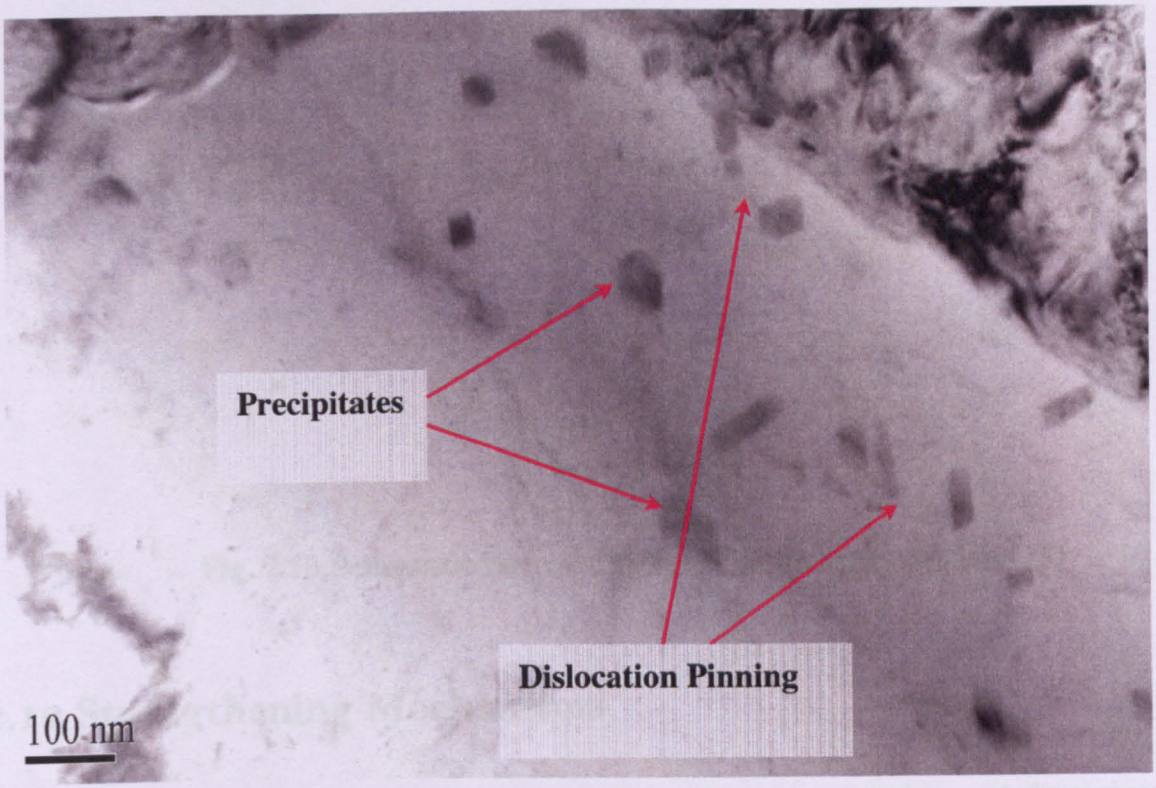

Fig. 2.12 An example of dislocations being pinned by precipitates. Precipitates seen here are mainly $M_{23}C_6$. Specimen is a 316H creep specimen tested at 650°C 180MPa for 100 hours

Dislocation bowing can be schematically described as in Fig. 2.13. The bending radius [31] can be shown to be

$$R = \frac{Gb}{\tau} \qquad 2.9$$

Where R is the bending radius and τ is the applied shear stress.

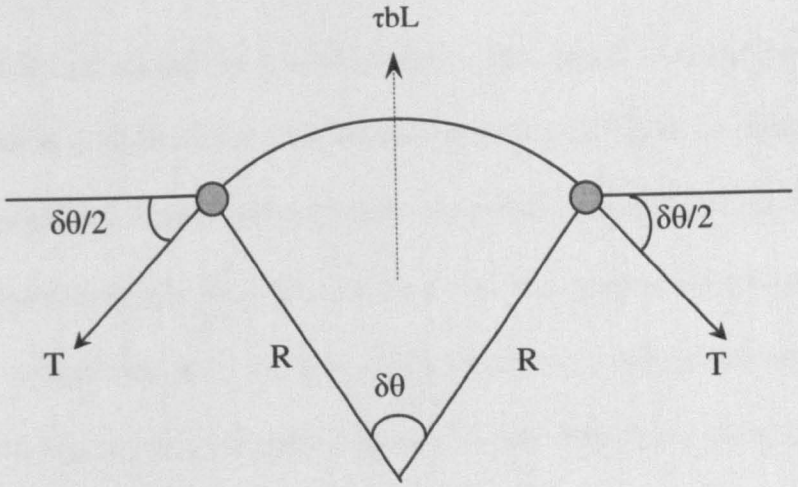

Fig. 2.13 Schematic representation of dislocation bowing [31]

2.12 Strengthening Mechanisms

When materials operate at high temperature, it is necessary to understand the processes through which the material retains its strength. Mechanisms include solid solution strengthening, grain boundary strengthening, precipitate strengthening and work hardening. These are described below.

2.12.1 Solution Strengthening

This process occurs when atoms of another element (solute) are added to a base element (solvent). In the case of steel, carbon and iron act as the solute and solvent respectively. The difference in sizes between the solute and the solvent atoms creates local stress fields which impede the motion of dislocations. Interstitial atoms cause a tetragonal distortion [7] which creates a shear stress field which will interact with edge or screw dislocations. Dislocations create internal stress fields within the crystal. The attraction or repulsion between the dislocations and the solute atoms increases the stress which is needed for the dislocation to propagate which results in increasing the yield strength of the material.

2.12.2 Precipitation Strengthening

Precipitates, which are secondary phase particles, can cause material strengthening by impeding the motion of dislocations. The process is shown in Fig. 2.14. When a dislocation encounters a precipitate, it will form a 'bend' around the precipitate. As the shear stress acting on the dislocation becomes greater than the line tension radius of this bend the dislocation can escape out. It is for this reason that a fine dispersion of precipitates is desired when looking at creep properties as this would reduce the distance a dislocation would move before it gets pinned again.

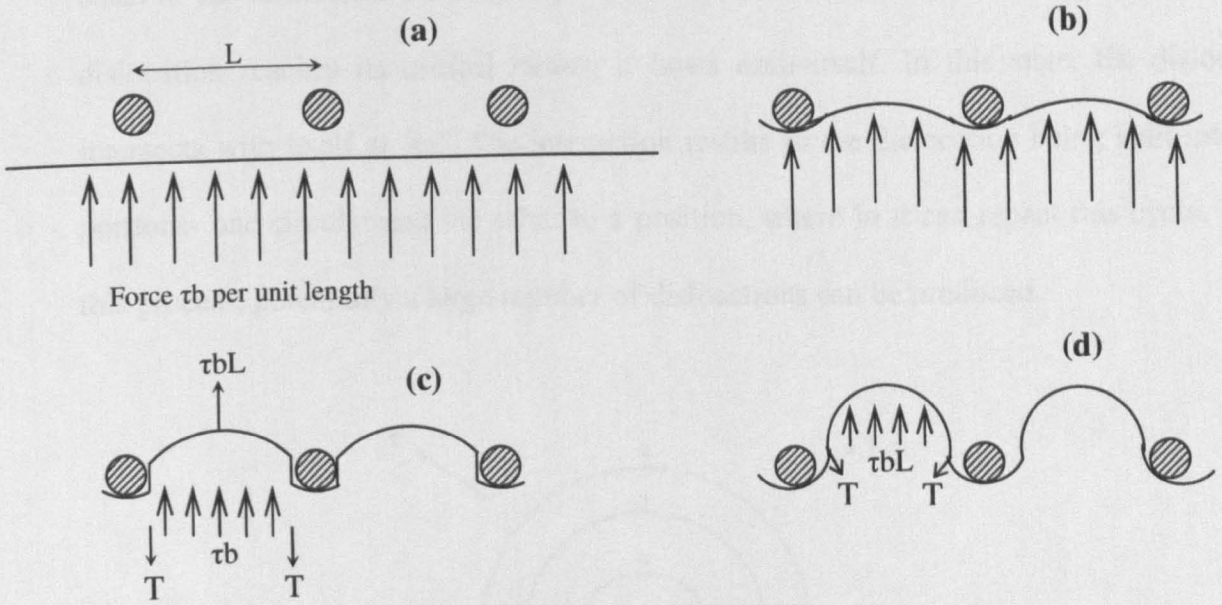

Fig. 2.14 Precipitate strengthening [32] (a) Approach situation (b) Sub-critical Situation (c) critical situation (d) Escape situation

2.12.3 Work Hardening

Strain hardening is caused by dislocations interacting with each other and also with obstacles to their motion. It generally involves interactions among a large number of dislocations. Dislocations generate stress fields. When they interact with each other, the stress fields can either be repulsive or attractive. When dislocations cross, entanglement can occur which causes opposition to dislocation motion. These entanglements and jogs act

as pinning points, which oppose dislocation motion. As both of these processes are more likely to occur when more dislocations are present, there is a correlation between dislocation density and yield strength.

Generation of Dislocations through the Frank-Reed Mechanism

Frank-Reed mechanism is mechanism which is used to explain increases in dislocation numbers. If a dislocation which is pinned between two carbides is considered, the shear stress acting on the slip will bow the pinned dislocation. Further application of the stress leads to the dislocation bowing to positions 'b' and 'c' shown in the Fig. 2.15. Once the dislocation reaches its critical radius, it bows onto itself. In this state, the dislocation intersects with itself at 'm'. The interaction results in the dislocation being split into two portions- one circular and the other to a position, where in it can repeat this cycle. Using this process, potentially a large number of dislocations can be produced.

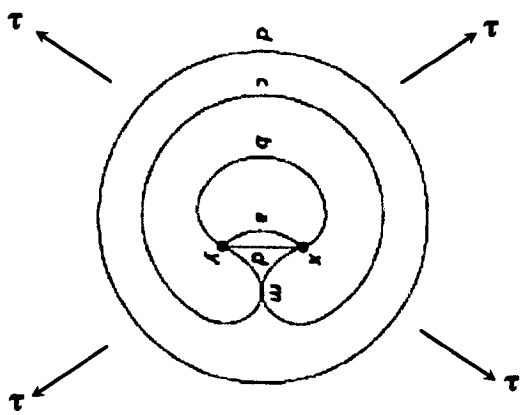

Fig. 2.15 Schematic of the Frank-Reed Mechanism [80]

2.13 Introduction to Residual Stress

Stresses acting within a material can either be reaction stresses or residual stresses. Reaction stresses occur when a body subjected to external loading equilibrates with the externally applied load.

Residual stresses are those stresses which are retained within a body when no external forces are acting. Residual stresses arise due to incompatibilities between different regions of the material, component or assembly. Residual stresses self-equilibrate over an area which depends upon the length scale over which they vary. Premature component failures may be possible due to residual stresses as they can superimpose with in-service stresses.

Residual stresses can be either beneficial [53], [54] or detrimental. Residual stresses can be used to extend the life of a component. An example of this would be cold hole expansion of fastener holes which is used in the aerospace industry [54], [55]. In the power plant industry, residual stresses are known to cause cracking in components [54]. The characterisation of residual stresses is vital as frequently they can cause failures. In safety critical systems, this would have to be accounted for. Fig. 2.16 shows processes which generate residual stresses at macroscopic and microscopic levels.

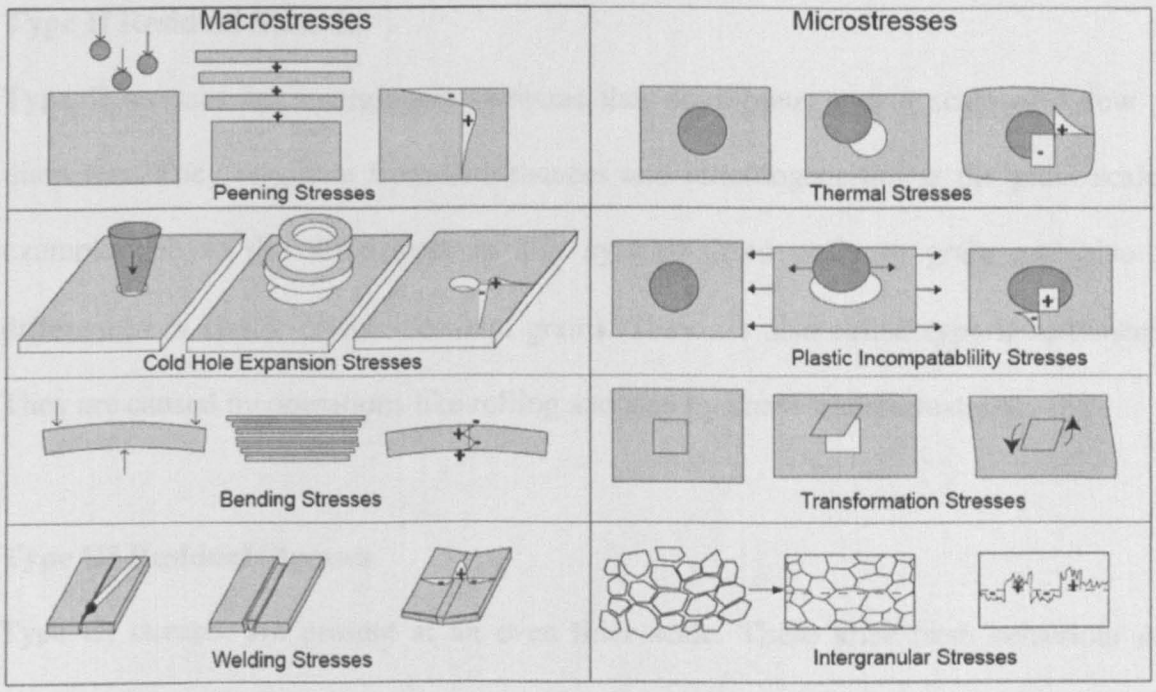

Fig. 2.16 Processes which generate residual stresses [55]

2.14 Classification of Residual Stresses

Residual stresses can act over a range of distances. Generally, residual stresses are classified on the basis of their length scales.

Type I Residual Stresses

Type I stresses are those which neglect the underlying microstructure. They are continuum level stresses which equilibrate over a length scale which is comparable to the extent of the component. They are also called macrostresses. The most important consideration in these stresses is that they can be described by continuum mechanics [55]. Since this type of stress spans a significant distance it encompasses a considerable aggregate of grains. Processes such as welding, cold expansion, plastic bending and shot peening cause such stresses [53], [57].

Type II Residual Stresses

Type II stresses are intergranular stresses that equilibrate over a scale of a few grain diameters. They originate from disturbances and inhomogeneities at the grain scale, for example due to the differences in slip systems from grain to grain and also from differences in elastic effects between grains. They are also called type II microstresses. They are caused by operations like rolling and also by phase transformations.

Type III Residual Stresses

Type III stresses are present at an even finer scale. These arise from behaviour at the atomic scale. They can occur due to line and point defects, dislocations, doping atoms of different sizes, etc.

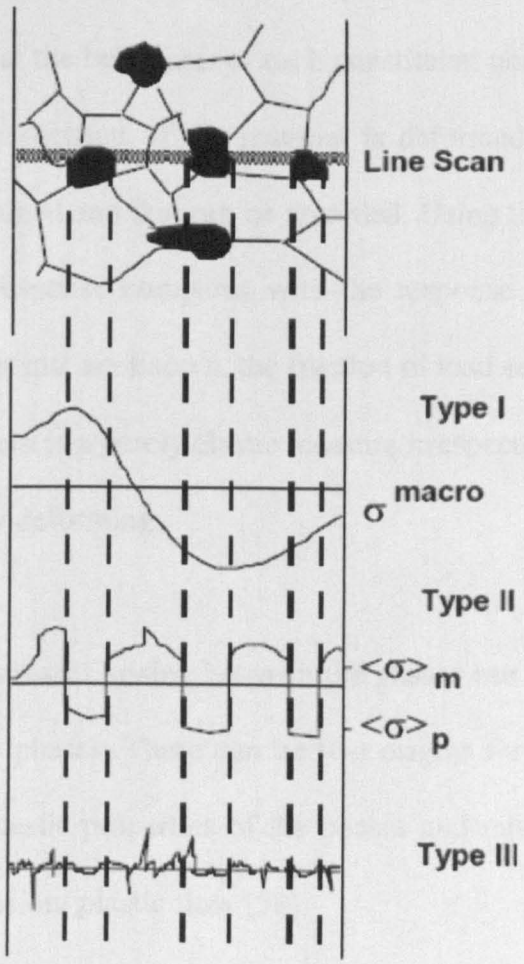

Fig. 2.17 Length scales of internal stresses [59]

Fig. 2.17 provides a schematic illustration of the different length scales that apply to internal stresses. Type I residual stresses vary on a long length scale. Stresses which are at a microstructural level are categorised as Type II stresses. An example will be the stresses between the carbides and the matrix in stainless steels. Grain orientations also influence the magnitude of these stresses. Type III stresses vary within the microstructural element (e.g. interactions between dislocation substructures). The total stress at any given position in the material is the sum of the three stress contributions.

2.15 Generation of Internal Stresses

The understanding of the internal mechanisms responsible for material behaviour in this study requires a background to internal stress and possible causes for it to occur. By using diffraction, one can look at the behaviour of each constituent phase, as each will produce a characteristic diffraction spectrum. If the material is deformed, the lattice parameter for each phase can be determined and this can be recorded. Using this technique, it is possible to study how the bulk response compares with the response of each individual phase. Assuming the elastic constants are known, the fraction of load each plane bears can also be calculated. The lattice strain is a purely elastic measure irrespective of whether the material is elastically or plastically deforming.

In multiphase materials, stresses arising between the phases can be considered to be due to shape misfit between the phases. There can be two origins for this: load transfer arising from differences in the elastic properties of the phases and misfits caused by effects like differential thermal expansion/ plastic flow [58].

When a material is loaded, differences in elastic properties between the phases or crystallographic planes can lead to internal stresses and load redistribution between the planes. As a result, subsequent plastic flow due to local differences in yield strength and hardening can cause local reaction stresses and lead to redistribution of stress [60].

2.16 Anisotropy in Crystals

When dealing with the smaller length scales, the behaviour of the different crystal planes will not be equal. Due to this reason, anisotropic strains and stress will occur. Anisotropy can have both elastic and plastic origins.

Elastic Anisotropy

When a single crystal of any material is considered, its elastic stiffness will depend on its orientation relative to the applied load. This elastic anisotropy will result in the variation in the internal strains (and thus internal stress) experienced by grains which will be oriented differently in a polycrystal due to an applied load. The lattice strains obtained would be representative of this. Hence, in neutron diffraction experiments, it is necessary to use 'diffraction elastic constants' when making measurements of stress.

Plastic Anisotropy

During plastic deformation, slip occurs along certain slip systems. Thus plastic strains will lead to a further level of misfit stresses which is dependent on the grain orientation. Daymond [59] suggests that a polycrystal can be considered as a composite in which every orientation of the grain has a slightly different yield stress which produces a complex stress-strain response.

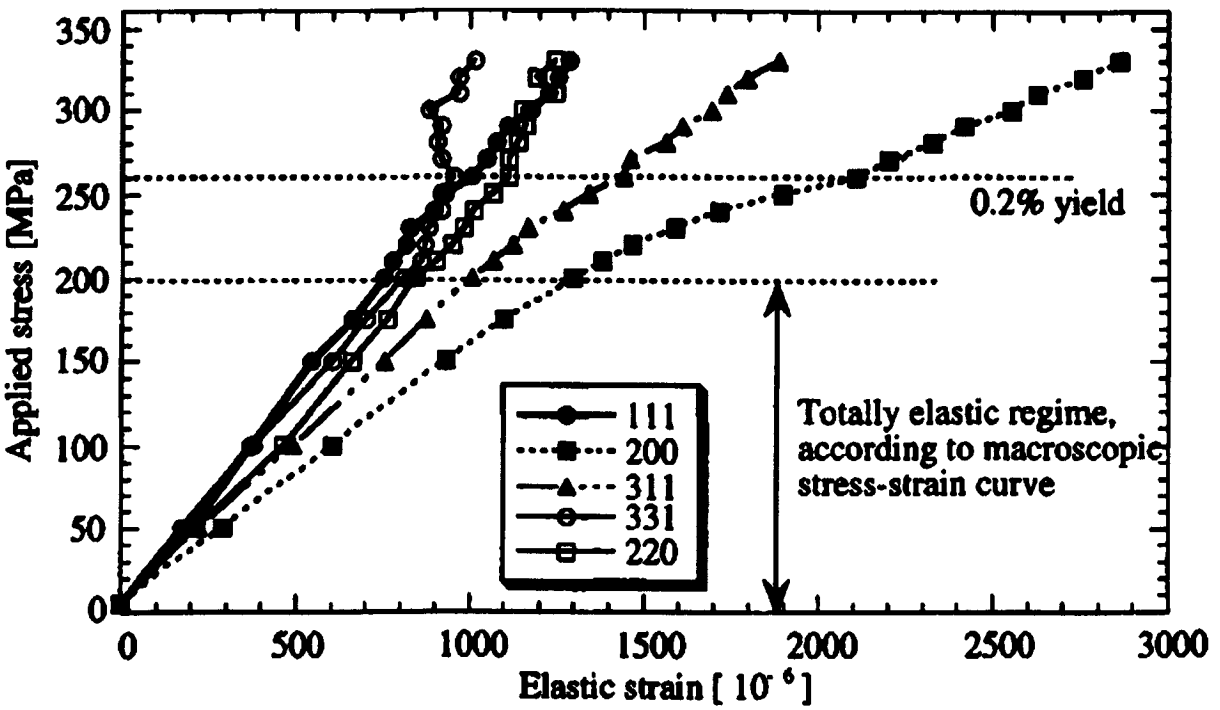

Fig. 2.18 Internal strains measured on different diffraction peaks in stainless steel undergoing tensile deformation [55]

An example of the strain response of the different grain families in shown in Fig. 2.18. It can be seen that as the material starts to plastically deform, deviations occur from the linear elastic region. In such a case, the yield of preferentially oriented grains may be relatively different to that of their neighbours which can generate internal stresses and also stress redistributions.

The main reason for plastic anisotropy is anisotropy of slip in a crystal. In iron which has a fcc structure, the slip plane is of type {111} and direction <110> [7]. Slip will occur along the plane which reaches the critically resolved shear stress first. The Schmid factor relates the applied stress and the critically resolved shear stress as below [52]

$$\tau_r = \frac{F}{A}\cos\phi\cos\lambda \qquad 2.10$$

Where τ_r is the resolved shear stress, φ is the angle between the tensile axis and the slip plane normal, λ is the angle between the slip plane direction and the tensile axis. F and A represent the applied force and the area of cross section respectively. The term $\cos\varphi\cos\lambda$ is the Schmid Factor.

To apply the same principles to polycrystals is much more complicated as determining the order the grains will take to reach yield is complex. The stress on each grain orientation will not be equal to the applied stress, because of elastic anisotropy. For example, the {111} plane is elastically stiff compared to the {200} plane which is highly compliant. Another reason is the constraint provided by the surrounding grains which would result in a non-uniaxial stress state.

2.17 Generation of Intergranular Stresses through Elastic/Plastic deformation

Creep behaviour of stainless steels, when subjected to complex loading cycles requires understanding the evolution of internal stresses. Diffraction from crystallographic planes for macroscopic stress measurement is a widely used technique [55, 67] and has been used in this study. If these stresses due to anisotropies are not accounted for, then the overall residual stresses measured will not be correct. As explained before, this additional stress may result in premature failure. When dealing with plastically deformed materials, it is important to understand the causes of these intergranular stresses and also to identify which subset(s) of grains may accumulate higher levels of intergranular stress.

Stainless steels are highly anisotropic both in their elastic and plastic behaviour. The elastic/plastic property of a single grain in a polycrystalline material is generally anisotropic and will also depend on grain orientation. When a material is subjected to a plastic deformation, strain incompatibilities between neighbouring grains will result in internal stresses being generated. Based on the classification presented in section 2.15, these stresses are Type-II stresses.

When deformation within a grain is compared, differences exist in the deformation when the grain interior and the grain boundary are compared [72, 73]. Interactions between adjacent grains and the development of a dislocation substructure will also lead to intergranular stresses. Grain scale effects can originate from dislocation pile-ups [74] wherein there is a larger concentration of dislocations and work hardening [75] which is caused by changes in the dislocation density. These grain to grain variations will lead to development of longer range internal stresses. The extent to which deformation mechanisms will be affected probably depends on the volume fraction of grain boundaries being affected but certainly at a grain level, these will affect the internal stresses which can be additional stresses along with the residual stresses.

In a broader sense, creep strain can be considered as an inelastic strain. Creep will occur at stresses which are below the yield stress of the material which means both elastic and plastic strains will contribute to the overall macro-strain of the material. A number of studies on stainless steels have been carried which have looked at the behaviour of internal stresses when the material was plastically strained. Some of these studies were carried out in-situ as the material was being deformed whilst others looked at the internal stresses in pre-strained materials. Studies most relevant to this project have been described below.

For materials which have a cubic structure, evolution of intergranular stresses has been reported by a number of studies [61-64]. A number of studies have been carried out to understand the effect of plastic strain (accumulated or pre-strained) on the intergranular stress levels. Internal stress evolution during in-situ tensile loading [66, 67, 70] has been measured using neutron diffraction. Clausen et al. [69] conducted tensile testing of stainless steels. They loaded the specimen to 330MPa and then unloaded from various levels of plastic strain. The accumulation of elastic loads does not happen at the same rate between different grain families. Interaction between slip systems can cause hardening of certain planes. Junctions between slip systems will develop dislocation kinks and jogs which can either promote or inhibit dislocation motion. The resultant dislocation substructure would thus change.

Studies have been carried out to understand the effects of plastic pre-straining on the creep and other material properties of austenitic steels. Wilshire and Willis [76] have reported that specimens which were pre-strained to 20% at room temperature saw an increase of 2-3 times in their creep lives when compared to as-received material. The creep ductility also reduces in this case. Willis and Hales [77] also conducted tests on 316 stainless steel and have reported similar results with regards to the strain at failure. Enami [78] has reported effects of both tensile and compressive pre-straining on the tensile fracture behaviour in steels which having bainitic and pearlitic based microstructure. A tensile pre-strain of 10 % on such materials reduces the ductility by about 15% whereas a compressive pre-strain of the same magnitude does not change the ductilities by much. He also mentions a nucleated void can grow more easily in a tensile stress field which may explain the ductility decrease. Prestraining can induce a restriction in the dislocation generation and movement particularly near precipitates. The increase in creep strength with increasing levels of pre-strain was due to the restriction of dislocation generation and movement at intragranular

carbide precipitates. Fujiwara [79] investigated pre-strain effects on 316 stainless steel that was solution treated at 1000°C and reported a decrease in creep strength with pre-strain. He attributes this to the increase in the number of grain boundary carbides.

Modelling of crystallographic behaviour can also be used to explain crystallographic behaviour. Modelling has been carried out using the finite element method [65] or using a self- consistent modelling approach [66, 67]. All these results point towards the anisotropy existing within the crystal. Both elastic and plastic anisotropies can lead to intergranular stresses. Texture of the grains can also influence the internal stresses.

2.18 Conclusions

- Austenitic steels form a very important class of steels and are used in a number of nuclear power plant applications.
- Behaviour of materials during high temperature deformation differs from room temperature behaviour. Creep affects the material properties significantly at elevated temperatures.
- Mechanisms responsible for creep depend on the stress/temperature conditions. Both diffusion and dislocation controlled processes can occur.
- Carbide precipitation will affect the material properties. Dislocation interactions with carbide and other entities will control the deformation rate.
- An introduction to residual stresses has been given. Primarily in this study, intergranular stresses play an important role. Generation of intergranular stresses can occur as a result of the changing plastic strain.

References

[1] P. Marshall. *Austenitic stainless steels: Microstructure and mechanical properties,* Elsevier applied science publishers, London, 1984.

[2] R.W.K.Honeycombe, *Steels: Microstructure and properties*, Edward Arnold, London, 1981.

[3] Evans and Wilshire, *Introduction to Creep*, Institute of Materials, 1993.

[4] Evans and Wilshire, *Creep of Metals and Alloys*, Inst. Of Mater., London, 1985.

[5] E. N. da C. Andrade, *On the Viscous Flow in Metals, and Allied Phenomena*, Proc. from the Royal Society of London, 84(567):1-12, June 1910.

[6] E. N. da C. Andrade, *The Flow in Metals under Large Constant Stresses*, Proc.from the Royal Society of London, 90(619):329-342, July 1914.

[7] G.E.Dieter, *Mechanical Metallurgy,* McGraw-Hill series in Materials Science and Engineering. McGraw Hill, 3rd edition, 1986.

[8] B.Illschner, *Creep in stainless steels*, CEGB Meeting, London, 1977.

[9] R5 Issue 3. Assessment Procedure for high temperature structures. British Energy Generation Limited, Gloucester, UK, 2003

[10] F.R.Nabarro , *Deformation of crystals by the motion of single ions*, Bristol Conf. on Strength of Solids, Phys. Soc., London, p.75, 1948

[11] C.Herring, *Diffusional Viscosity of Polycrystalline Solid*, J.Appl.Phys., Vol.21 (1950), pp.437,

[12] F.R.Nabarro, Phil. Mag., Vol.16 (1967), pp.231.

[14] T.G.Nieh, J.Wadsworth, O.D.Sherby, *Superplasticity in metals and ceramics*, Cambridge Solid State Science Series, 1997.

[15] J.P.Poirier, Creep *of crystals: High-temperature deformation processes in metals,* Cambridge Earth Science Series, 1985.

[16] J.Gittus, *Creep, viscoelasticity, and creep fracture in solids*, 1984.

[17] J.Friedel, *Dislocations*, Pergamon Press, 1964.

[18] W.T.Read, W.Shockley, *Dislocation models of crystal grain boundaries*, Phys. Rev, Vol.78 (1950), pp.275.

[19] J.S.Koehler, in Imperfections in Nearly Perfect Crystals, edited by W. Shockley et al. (Wiley, New York, 1952), pp. 197.

[20] F.Seitz, *The Theory of Plastic Flow in Single Crystals,* Adv. Phys., Vol.1 (1952), pp.43.

[21] F.Seitz, Phys. Rev., Vol.99 (1952), pp.722.

[22] C.B.Carter, M.G.Norton, *Ceramic materials: science and engineering*, Springer, 2007.

[23] F.Garofalo, O.Richmond, W.F.Domis, F. yon Gernmingen et al., Joint International Conference on Creep, London, Institute of Mechanical Engineering, pp.1-31, 1963.

[24] D.McLean. *Reports on progress in Physics*, Vol.29 (1966), pp.1-33.

[25] R.Lagneborg, *Development and Refinement of the Recovery-Creep Theory*, Metal Sci. Jour., Vol.3 (1969), pp.161-168.

[26] T.Sourmail, *Precipitation in creep resistant austenitic stainless steels,* Mat. Sci. Tech, Vol.17-1 (2001), pp. 1-14,.

[27] M.H.Lewis, B.Hattersley, *Precipitation of M23C6 in austenitic steels,* Acta Metall., Vol.13 (1965), pp.1159-1168.

[28] B.Weiss, R.Stickler, *Phase instabilities during high temperature exposure of 316 austenitic stainless steel,* Met. Trans., Vol.3 (1972), pp.851.

[29] D.Hull, D.J.Bacon, *Introduction to Dislocations*, Elsevier Science & Technology, 4th ed. ,2001

[30] H.M.Tawancy, A.Ul-Hamid, N.M.Abbas, Practical Eng. Failure Anal., Mechanical Engineering, CRC Press, 1 edition.

[31] W.O.Soboyejo, *Mechanical Properties of Engineered Materials*, CRC Press, 2002.

[32] M.F.Ashby and D.R.H.Jones, *Engineering Materials 1*, 2nd ed., 2002.

[33] H.Frost and M.Ashby, *Deformation-Mechanism Maps: The Plasticity and Creep of Metals and Ceramics*, Pergamon Pr; 1st edition, October 1982.

[34] J.C.Lippold, D.J.Kotecki, *Welding Metallurgy and Weldability of Stainless Steels*, Wiley Interscience, 2005.

[35] M.Hansen, *Constitution of Binary Alloys*, 2nd ed., McGraw Hill, 1958.

[36] ASM Metals Handbook, 8th ed., Vol. 8, ASM International.

[37] ASM. 1982. *Engineering Properties of Steels*, AMS International, Materials Park, OH.

[38] E.Baerlecken, , W.Fischer, K. Lorenz, Stahl und Eisen, 81(12) pp.768.

[39] J.J.Demo, *Structure and Composition of wrought ferritic steels* in Handbook of Stainless Steels., McGraw-Hill, 1977.

[40] H.Thielsch, *Physical and welding metallurgy of chromium stainless steels*, Welding Jour., 30(5), pp.209s-250s.

[41] AK Steel, 17-4 PH Stainless Steel Data Bulletin, AK Steel Corporation.

[42] D.Peckner, I.M.Bernstein, *Handbook of Stainless Steels*, McGraw Hill, 1977.

[43] H.R.Copson, *Physical Metallurgy of Stress Corrosion Fracture*, Interscience, 1959.

[44] S.Floreen, H.W.Hayden, Trans. of the American Society for Metals, Vol.61, pp. 489.

[45] H.Wentrup, O.Reif, Archiv fuer das Eisenhuettenwesen, 20, pp. 359,1949.

[46] O.Kubaschewski, Iron: Binary Phase Diagrams, Springer-Verlag, 1982.

[47] W.Dahl. C.Duren, 'Stahl und Eisen' 93, pp. 813, 1973.

[48] J.J.Irvine, Jour. of the Iron and Steel Institute, London, pp.153-161, 1961

[49] J.K.L.Lai, CEBG Report TRPD. L/2383, N82, 1983.

[50] C.F.Etienne, CEGB Informal Meetings on Creep in Stainless Steels, London, 1977.

[51] F.J.Humphreys and M.Hatherly, *Recrystallization and Related Annealing Phenomena*, 2nd ed. Elsevier Science, 2004.

[52] R.Reed-Hill, *Physical Metallurgy Principles*, Van Nostrand Company, 1964.

[53] P.J.Withers and H.K.D.H.Bhadeshia, *Residual stress, Part 1-Measurement techniques*, Mater. Sci. Tech. (2001), Vol. 17, pp. 355-365.

[54] J.R. Santisteban, L. Edwards, A. Steuwer and P.J. Withers, *Time-of-flight neutron transmission diffraction*, J. Appl. Cryst. **34** (2001), p. 289.

[55] P.J.Withers, *Residual stress and its role in failure*, Reports on Progress in Physics 70 (2007) pp.54.

[56] D. Stefanescu, A. Steuwer, R. A. Owen, B. Nadri, L. Edwards, M. E. Fitzpatrick and P. J. Withers, *Elastic Strains around cracked cold-expanded fastener holes measured using the synchrotron X-ray diffraction method*, J. Strain Analysis Vol.39 (2004) pp.459–469.

[57] E.Macherauch, K.H. Kloos: *Origin, Measurement and Evaluation of Residual Stresses*, Verlag, Germany, 1987.

[58] T.W.Clyne, P.J.Withers, *An Introduction to Metal Matrix Composites*, Cambridge University Press, 1993

[59] M.R.Daymond, *Internal Stresses in Deformed Crystalline Aggregates*, Reviews in Mineralogy and Geochemistry, Vol.63 (2006), pp.427.

[60] Daymond, M.R., Bourke, M.A.M., Von Dreele, R., Clausen, B. & Lorentzen, *Use of Rietveld Refinement for Elastic Macrostrain Determination and for the Evaluation of Plastic Strain History from Diffraction Spectra*, J. Appl. Phys., Vol.82 (1997), pp.1554-1562.

[61] S. MacEwen, J. Faber and A. Turner, *The use of time-of-flight neutron diffraction to study grain interaction stresses*, Acta Metall. Vol.31 (1983), pp.657–676.

[62] M.R. Daymond, C.N. Tomé, M.Bourke, *Measured and predicted intergranular strains in textured austenitic steel,* Acta Mater. Vol.48 (2000), pp.553–564.

[63] B. Clausen, T. Lorentzen, M.Bourke, M.R. Daymond, *Lattice Strain Evolution During Uniaxial Loading of Stainless Steel,* Mater. Sci. Eng. A (1999) 259.

[64] E.C. Oliver, M.R. Daymond and P.J. Withers, *Interphase and intergranular stress generation in carbon steels,* Acta Mater. Vol.52 (2004), pp.1937–1951.

[65] P. Dawson, D. Boyce, *Residual strains in HY100 polycrystals: comparisons of experiments and simulations*, S. MacEwen and R. Rogge, Metall. Mater. Trans. 31A (2000), pp.1543.

[66] J. Pang, T. Holden, J.S. Wright and T. Mason, *The generation of intergranular strains in 309H stainless steel under uniaxial loading, Acta Mater* **48** (2000), pp. 1131–1140

[67] Daymond, M.R., Tome, C.N. & Bourke, M.A.M., *Measured and predicted intergranular strains in textured austenitic steel,* Acta mater. 48 (2000) pp.553-564.

[68] S.R.MacEwen, J.Faber Jr, A.P.L.Turner, Acta Metall. Vol.31, (1983) pp.657.

[69] B. Clausen, T. Lorentzen, M.A.M. Bourke, M.R. Daymond, *Lattice strain evolution during uniaxial tensile loading of stainless steel,* Mater. Sci. Eng. A259 (1999) 17.

[70] R. Lin Peng, M. Odén, Y. D. Wang, S. Johansson, *Intergranular strains and plastic deformation of an austenitic stainless steel,* Mater. Sci. and Eng. A334 (2002) 215–222.

[71] X. Feaugas, *On the origin of the tensile flow stress in the stainless steel AISI 316L at 300 K: back stress and effective stress*, Acta Mater. Vol.47 (1999) pp.3617.

[72] J. Quinta da Fonseca, E.C. Oliver, P.S. Bate and P.J. Withers, *Evolution of intergranular stresses during in situ straining of IF steel with different grain sizes,* Materials Science and Engineering A 437 (2006) pp.26–32

[73] W. Boas and M. Hargreaves, Proc. Roy. Soc. 193 (1948) (1032), pp. 87–89.

[74] L. Evers, W. Brekelmans and M. Geers, *Scale dependent crystal plasticity framework with dislocation density and grain boundary effects,* Int. J. Sol. Struct. 41 (2004), pp. 5209–5230

[75] Z. Shen, R. Wagoner and W. Clark, *Dislocation and grain boundary interactions in metals,* Acta Metall. Vol.36 (1988), pp. 3231–3242.

[76] B.Wilshire, M.Willis, *Mechanisms of strain accumulation and damage development during creep of prestrained 316 stainless steels,* Metallurgical and Materials Transactions A, Vol. 35A, Feb 2004, pp. 563.

[77] M. Willis, A. McDonaugh-Smith and R. Hales, *Prestrain effects on creep ductility of a 316 stainless steel light forging,* International Journal of Pressure Vessels and Piping 76 (1999) pp.355–359.

[78] K. Enami, *The effects of compressive and tensile prestrain on ductile fracture initiation in steels,* Engineering Fracture Mechanics 72, (2005), pp.1089–1105.

[79] Fujiwara M, Uchida H, Ohta S. , *Effect of boron and carbon on creep strength of cold-worked type 316 stainless steel,* Journal of Materials Science Letters 1994; pp.13

[80] Reza Abbaschian and Robert E. Reed-Hill, *Physical Metallurgy Principles*, 4th ed., 2008

CHAPTER 3: TESTING METHODS AND EXPERIMENTAL TECHNIQUES

During this study, a number of experimental techniques have been used to characterise material behaviour. Macroscopic material properties like tensile strength, creep rupture life and ductility are generally determined by applying loads on the specimens and recording strain. Intergranular and residual stresses were measured using neutron diffraction techniques. Material microstructure was characterised using optical and electron microscopy. The electron microscopy results are described in chapter 6. This chapter presents an overview of the different experimental techniques used.

3.1 Specimen Design

The specimen design used for all the creep testing is shown in Fig. 3.1. The specimen was manufactured from a 316H steel blank which was 100mm long and 12.5mm in diameter. The length to diameter ratio of the gauge was 5. The specimen design conforms to standards prescribed by ASTM E139-06 [1], ASTM E-08 [2].

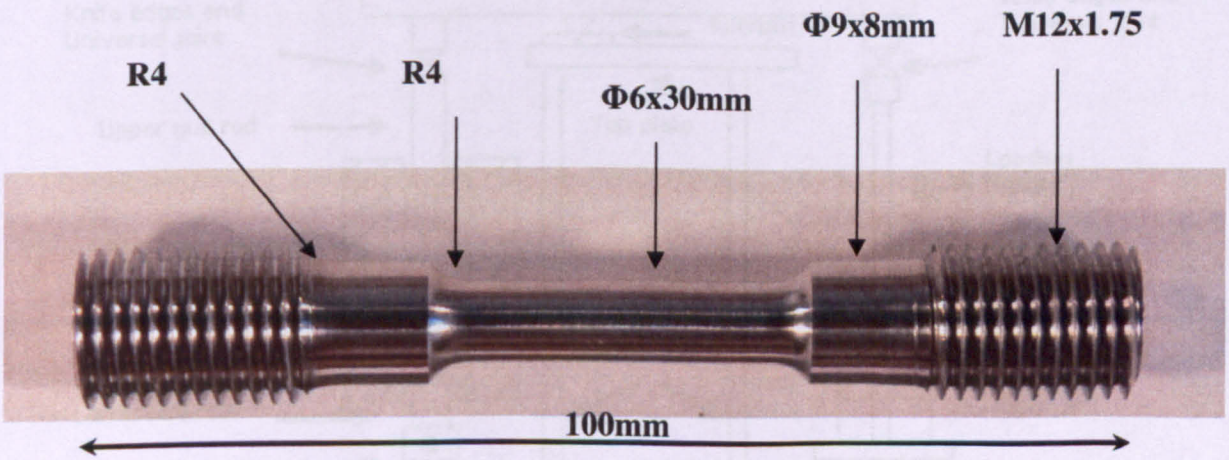

Fig. 3.1 Specimen design

3.2 Creep Testing

Creep and creep rupture properties are usually measured under simple tensile conditions. Most of the design/assessment procedures are based on this data. Tests with complex loading cycles are compared to monotonic creep rupture data to check the differences in the material behaviour. Monotonic creep rupture tests are carried out by applying a known tensile load to a sample held at a fixed temperature.

Fig. 3.2 is a schematic of the machines used to conduct the creep experiments. An example of the creep frame(s) used for in this study is shown in Fig. 3.3. Creep experiments can sometimes be purely rupture data where one measures only the rupture strain and time to failure and does not record the change of strain with time. However, in all tests conducted in this study, the strain was recorded continuously.

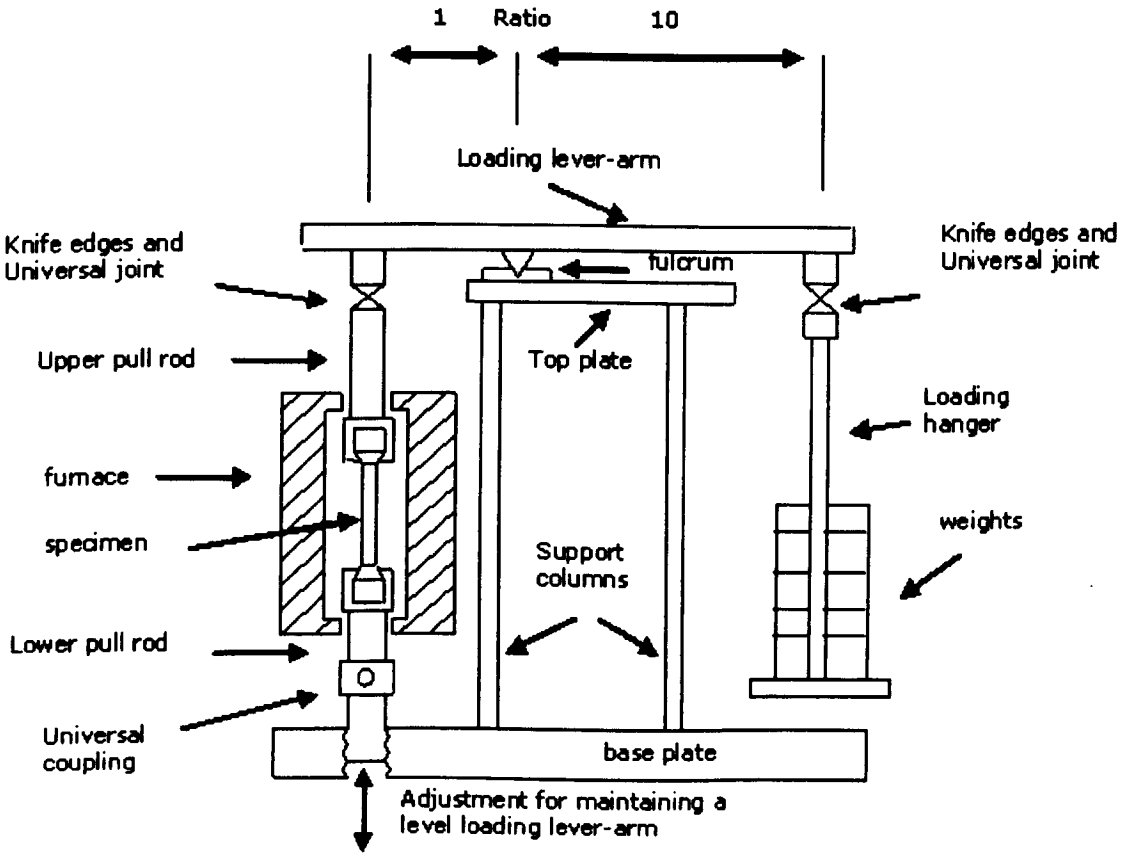

Fig. 3.2 Schematic of a creep frame

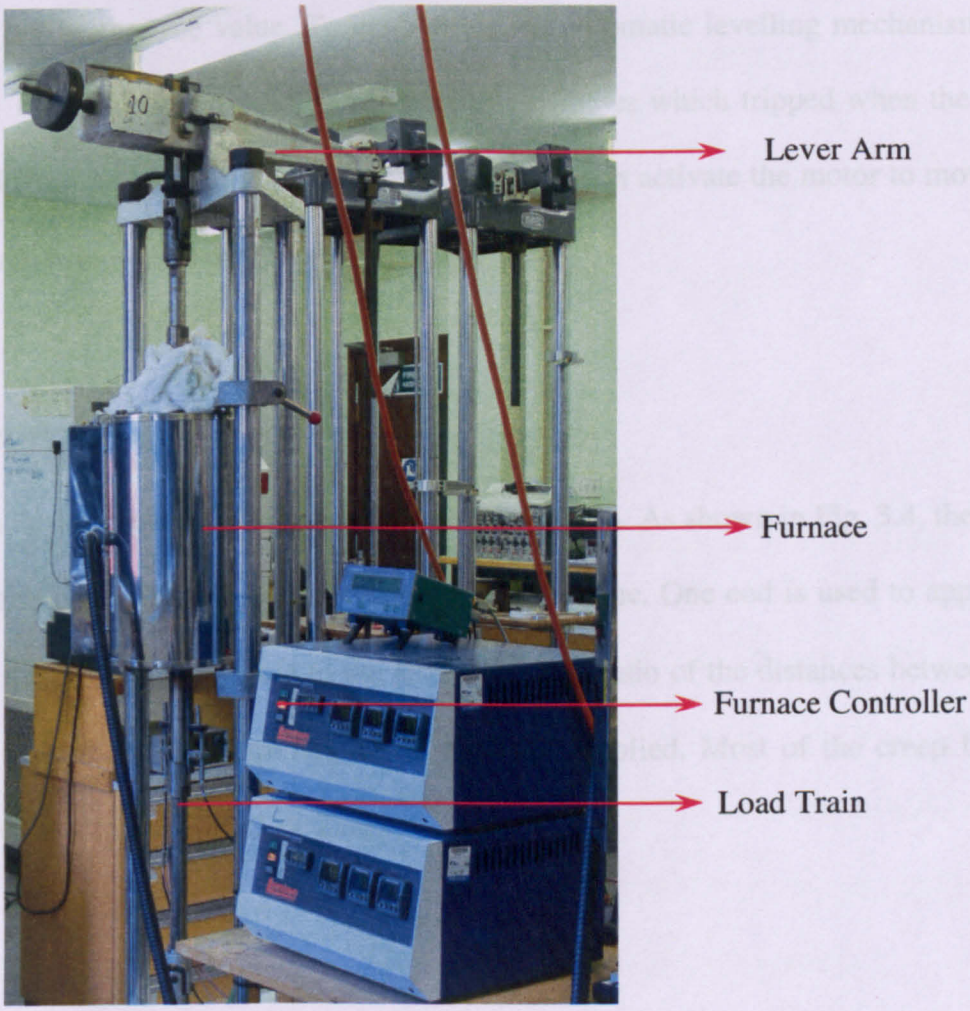

Fig. 3.3 Picture of creep frames used

3.2.1 Machine Frame and Drive System

The machine frame consists of a base to which columns are attached to support the lever arm assembly. Underneath the base, the drive system used to run the system is present. The drive system is required to move the pull rods up and down which are required for initial setup and also for balancing the lever arm. The drive system was essentially a motor assembly connected to a worm-wheel mechanism which moved the load train assembly up and down.

When applying the force, it is essential that the lever arm remains horizontal; else the force applied will not be the true value. To enable this, an automatic levelling mechanism was also present. The mechanism consists of two limit switches which tripped when the lever arm deviated from its horizontal position which would then activate the motor to move the load train up/down to make the lever arm horizontal.

3.2.2 Lever Arm

The force on the specimen was applied through a lever arm. As shown in Fig. 3.4, the lever arm has a knife edge which is used to place it on the frame. One end is used to apply the weights and the other is connected to the specimen. The ratio of the distances between the knife edges determines the amplification of the force applied. Most of the creep frames used had lever arm ratios of 10:1 or 25:1.

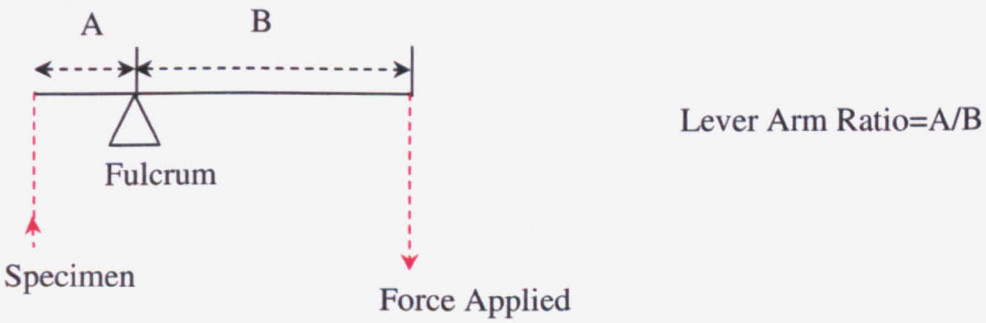

Fig. 3.4 Schematic of lever arm mechanism

3.2.3 Strain Monitoring and Recording

For a continuous creep test, strain has to be monitored constantly and recorded at regular time intervals. In most cases, displacement of the specimen is measured which is then converted to strain. In this study, displacement was measured using a Linear Variable Displacement Transformer (LVDT).

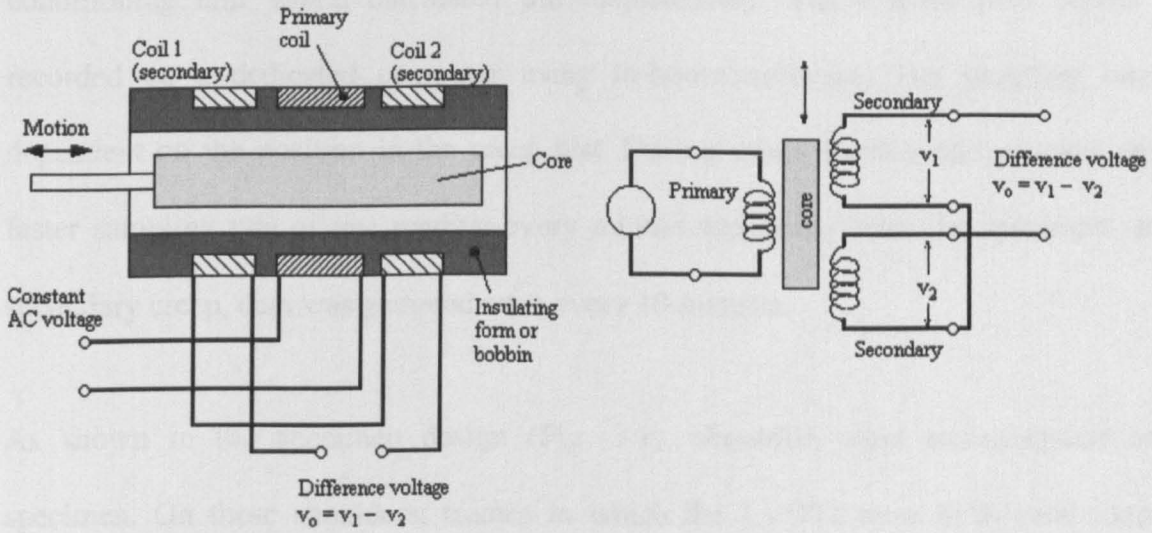

Fig. 3.5 (a) Sectional view of a LVDT. (b) Circuit diagram for an LVDT

A schematic and a circuit diagram of an LVDT are shown in Fig. 3.5. An LVDT consists of three symmetrically spaced coils wound onto an insulated bobbin. The magnetic core can move within the bobbin and provides a path for the magnetic flux linkage between the primary and the secondary coils. The motion (from a mechanical input) changes the characteristics of the flux path and the changes can be detected in the circuit.

The primary coil is excited by an a.c. signal and voltages are induced in the two secondary coils. The induced voltages depend on the position of the core inside the bobbin. The secondary coils are wired in a series-opposing circuit so that when the core is centred between them the voltages induced are opposite but equal. When the core is centred between the two secondary coils, the induced voltages v_1 and v_2 are equal but out of phase by 180 degrees, and they cancel to give a zero output voltage. When the core moves from the centre position, an output voltage v_1-v_2 is developed. If the displacement is within the working range of the LVDT, the voltage and displacement will be linearly related.

Two LVDTs were used for each sample, each measuring strain along one diameter. The LVDTs had a displacement resolution of one micron. The LVDTs were connected to a

conditioning unit which calculated the displacement. The displacement values were recorded on a dedicated computer using in-house software. The sampling rate was dependent on the position in the creep test. During initial loading and primary creep, a faster sampling rate of one reading every minute was used. Once the specimen reached secondary creep, data was gathered once every 10 minutes.

As shown in the specimen design (Fig. 3.1), shoulders were manufactured on the specimen. On these shoulders, frames in which the LVDTs were held were connected using screws. The frames and the screws used were manufactured from Inconel which is a nickel based alloy.

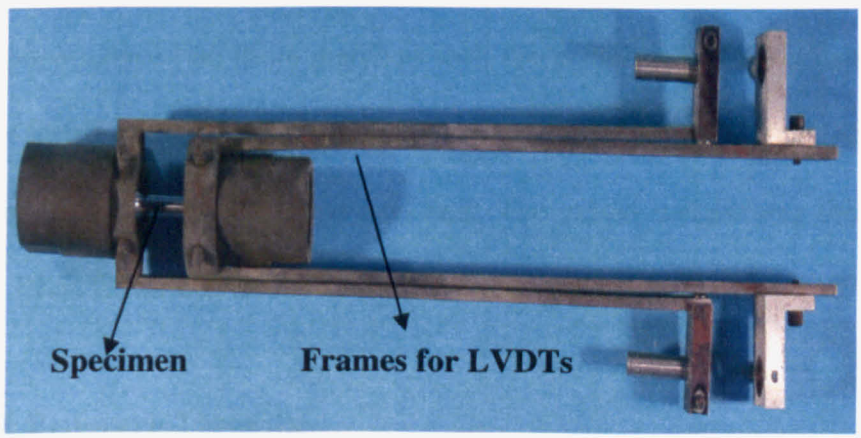

(a)

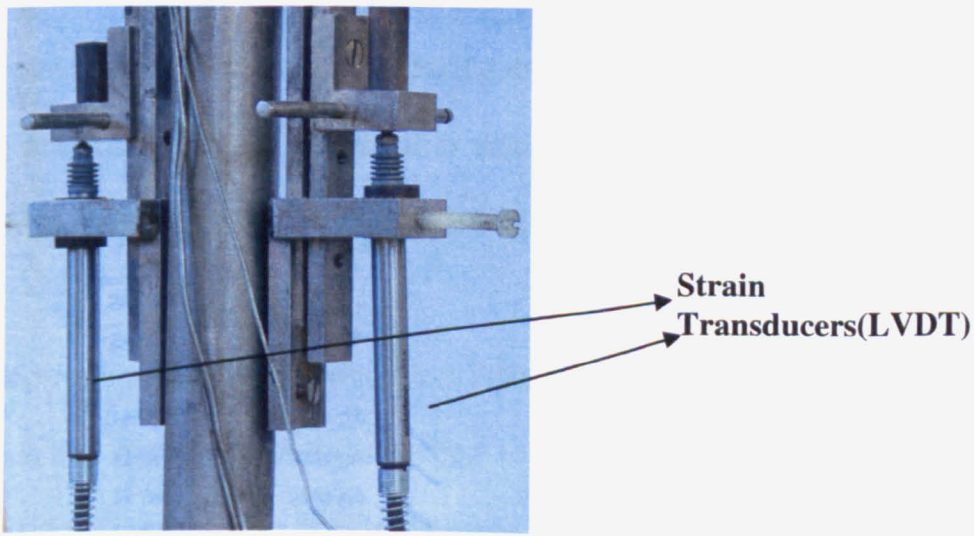

Fig. 3.6 Equipment for strain recording

3.2.4 Load Train and Pull Rods

The load train in the creep frames consisted of pull rods to which the specimen was attached. The assembly consisted of two rods which were attached using a connector piece. One of the rods was made from stainless steel (AISI316H) and the other was made from Alloy-X (nickel based alloy). A nose piece which held the sample was attached to the Alloy-X rod. A collet was used to hold the specimen in the nose piece. The other ends of this pull rod assembly were attached to universal joints.

Calibration of Weights

Before using any of the static weights for applying the loads, it had to be ensured that the weights displayed on them matched with the actual values. Small changes in the geometry of the frame can result in imbalances and can be a source of error. All weights used in each frame were measured using a load cell. The actual weight was then stuck on the weight used. Each frame had its own set of calibrated weights.

3.2.5 Furnace Details

As creep is temperature dependent, control of specimen temperature is very important. A good, stable temperature is required during the course of the testing. Testing standards [1], [2], [3] prescribe a thermal gradient less than 3°C across the gauge length and the sample temperature should be ±3°C of the required temperature.

All creep frames used in this study had their own dedicated furnaces. The furnaces were induction coil furnaces with three heating zones. Each of these zones could be controlled individually. Furnaces were controlled using Eurotherm 3200 controllers. These were PID

(Proportional Integral Derivative) controllers which offered better stability and lesser temperature offshoots. The furnace had a maximum rating of 1200°C.

As shown in Fig. 3.3, the furnace was attached to the columns in the frames. The furnaces could be moved so that the sample and load train assembly were central in the furnace. Ceramic plugs and wool were used at the end of the furnace tube to minimise heat loss and also for maintaining good temperature stability.

The furnace heating was controlled using three thermocouples. These were internal to the furnace and not attached to the specimen. Three N-type thermocouples (top, middle and bottom) were fixed on the sample gauge length to monitor the specimen temperature. The thermocouples were attached to a temperature logger which recorded the temperatures at fixed intervals.

3.3 Tensile Testing Apparatus

Other material characterisation tests were also carried out. These included tensile testing both at room and elevated temperatures and low-cycle fatigue testing.

Fig. 3.7 shows the test equipment. The equipment consisted of a 100kN capacity servo-electric test machine along with an Instron 8862 controller.

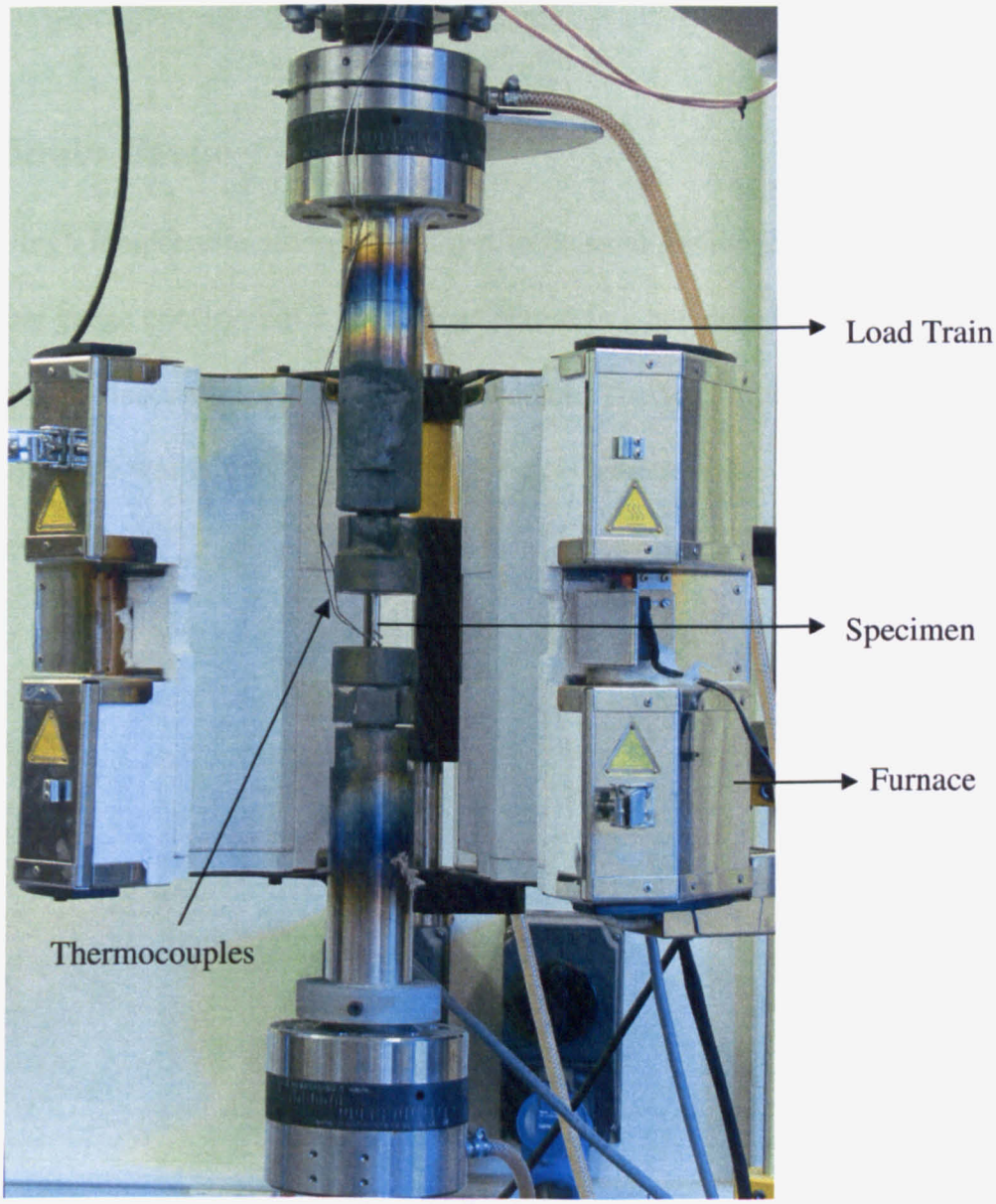

Fig. 3.7 Equipment used for conducting the room temperature and elevated temperature tensile tests

3.3.1 Furnace Details

The machine has a three zone furnace controlled by Eurotherm 3216 controllers. Each zone has its own controller which enables more accurate temperature control. The thermocouples attached to the specimen were plugged directly to the controllers. This was done to control the temperature directly from the specimen. The maximum attainable

temperature was 1100°C. Three n-type thermocouples were used to monitor the specimen temperature.

3.3.2 Strain Gauge

Special high temperature strain gauges had to be used for the elevated temperature tests. The strain gauge consisted of 2 quartz legs placed in a housing. The knife edges at the end of the quartz pieces were placed on the specimen. The length between the knife edges of the strain gauge was 25mm. Fig. 3.8 shows the placement of the strain gauge relative to the specimen.

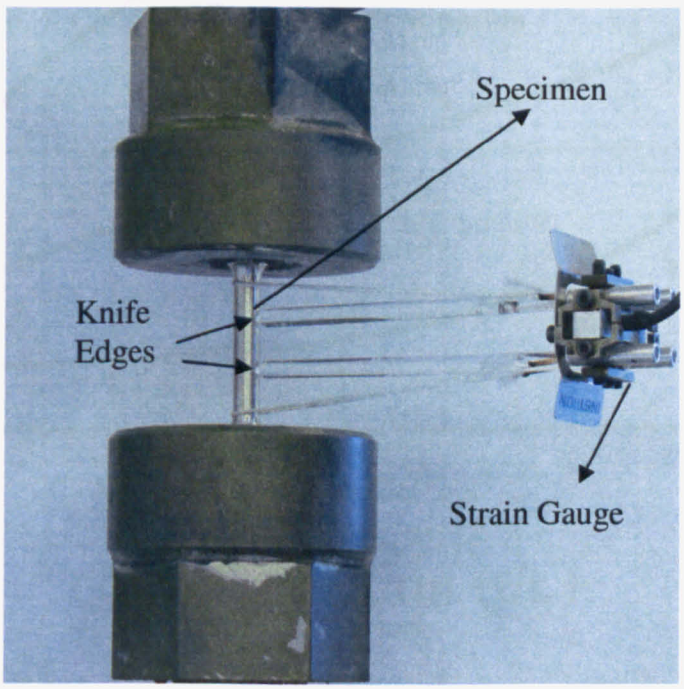

Fig. 3.8 Strain gauge used on the Instron 8862 machine

3.4 Representation of Creep Data

When creep tests are done over a wide range of temperatures and stresses, the shapes of the curves will be markedly different depending on the conditions applied. The stress and temperature will determine the prevalent creep mechanism which can be determined using

the deformation mechanism maps described in section 2.7. Ideally, one would expect to see the majority of the lifetime in secondary creep but in reality, there will be situations where either primary or tertiary creep will have a significant impact on the material behaviour. Fig. 3.9 shows a generic example of the different types of creep curves that can be obtained during creep rupture testing.

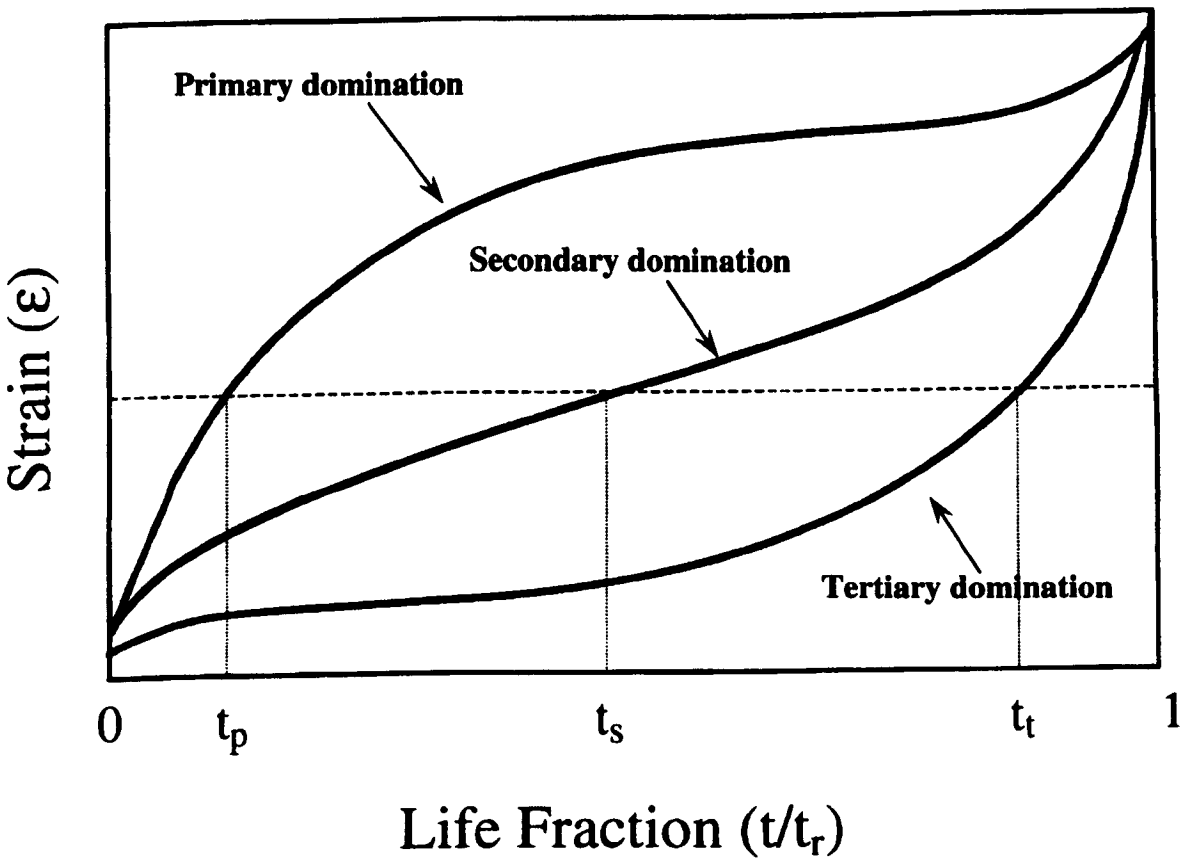

Fig. 3.9 Generic examples of creep curves with primary, secondary and tertiary domination

Creep curves are generally plotted as instantaneous strain against time. For design considerations, properties like strain rate and reduction in strength, along with rupture time and ductility may be important. Creep strain rate is calculated using the slope in the secondary regime as shown in Fig. 3.10

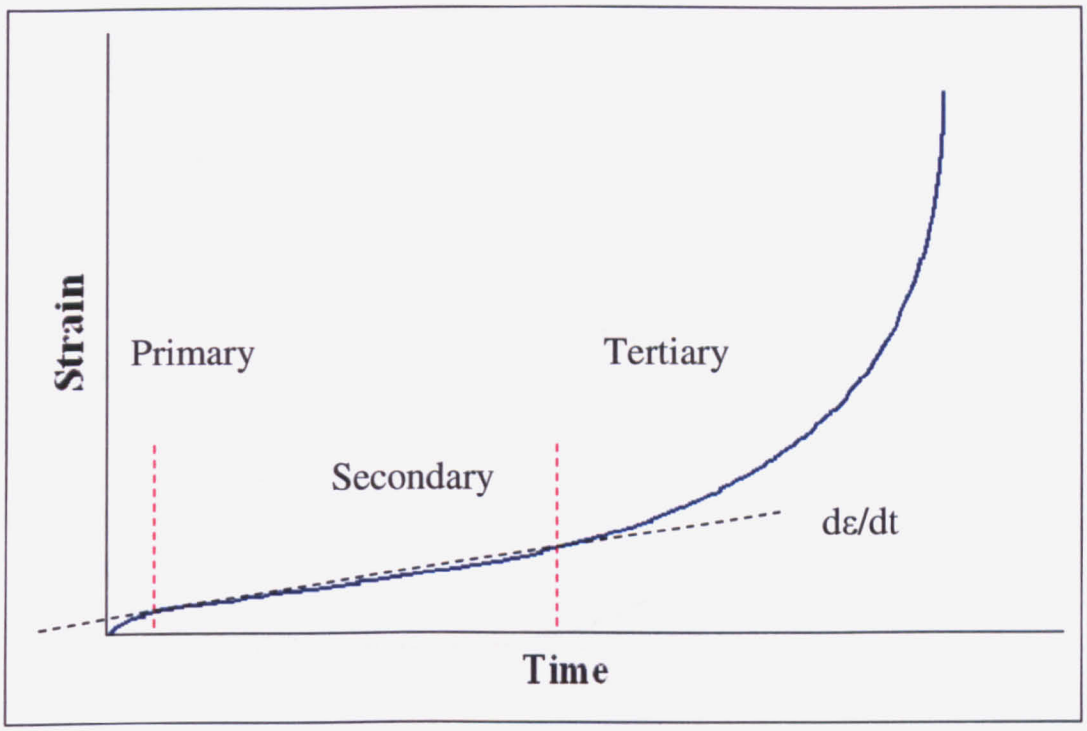

Fig. 3.10 Calculating secondary creep rate.

Secondary or minimum creep rate is also calculated by plotting the change in strain rate over time (Fig. 3.11). Primary creep is a period of rapid decrease in strain rate. The strain rate reaches a minimum during secondary creep and accelerates during tertiary. This method is also an effective way of looking at the onset of the different stages in creep.

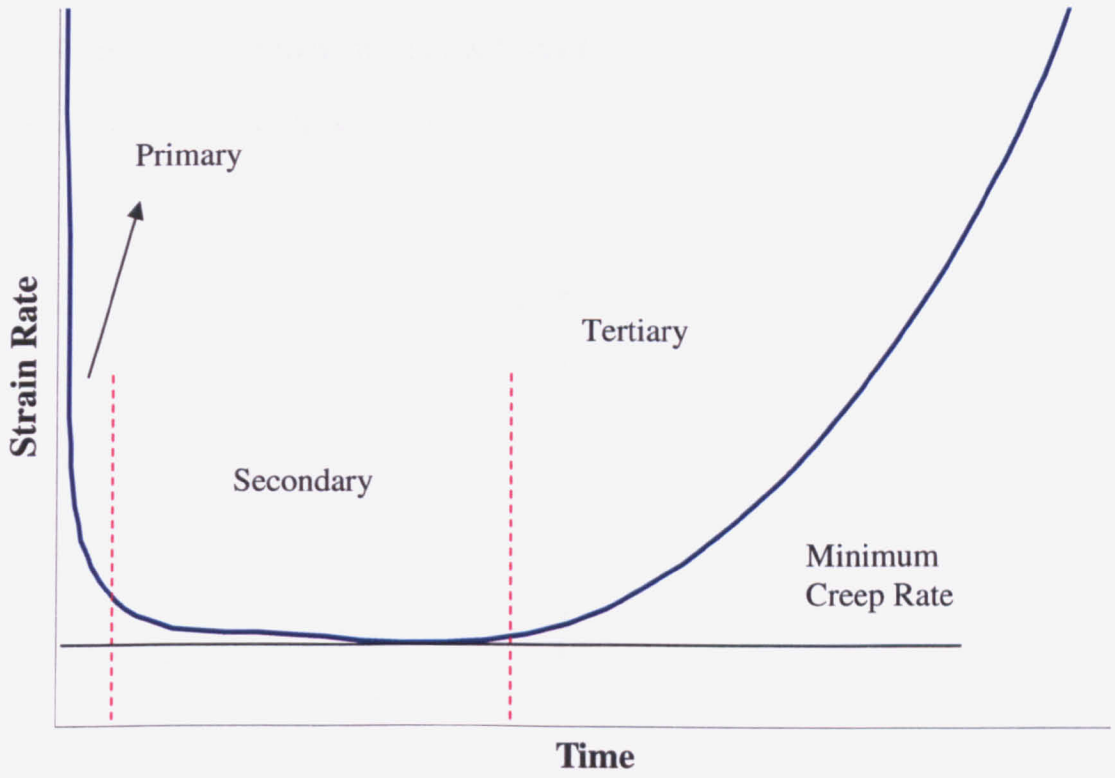

Fig. 3.11 Change in strain rate during the different stages of creep

The secondary creep rate is also needed to calculate the stress exponent n and the activation energy Q (section 2.7.2- Dislocation Creep). Secondary creep can be described using an Arrhenius type representation.

$$\dot{\varepsilon} = A\sigma^n \exp\left(\frac{-Q}{RT}\right) \qquad 3.1$$

Taking logarithms on both sides,

$$\ln(\dot{\varepsilon}) = \ln(A) + n\ln(\sigma) - \frac{Q}{RT} \qquad 3.2$$

By plotting the natural logarithm of strain rate against the inverse of temperature for the different tests, one can obtain the activation energy which will be the slope of the line. Similarly, plotting the natural logarithm of strain rate against natural logarithm of applied stress, the stress exponent can be determined.

If a large number of creep tests exist, different types of plots can be used to understand the data effectively. Apart from the standard way of plotting strain against time, some of the other popular ways are shown in Fig. 3.12

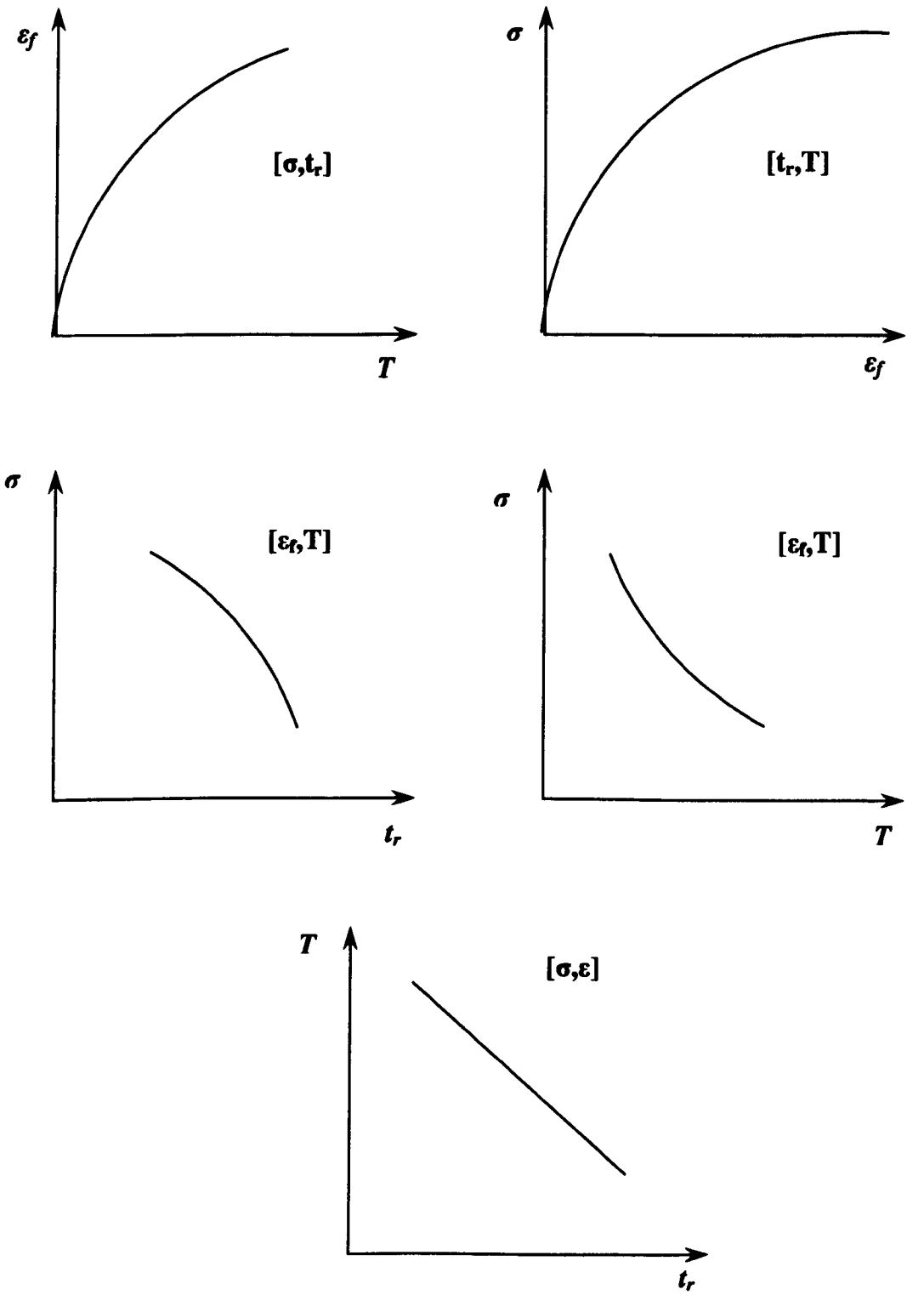

Fig. 3.12 Methods of presenting creep data

3.5 Diffraction Techniques

During this study, diffraction techniques have been used to characterise the material behaviour. Diffraction experiments (X-ray, neutron or synchrotron X-ray) are all based on Bragg's Law. Neutron diffraction was chosen for this study as the capacity of neutrons to penetrate into the material is higher compared to X-rays. A basic introduction to diffraction is given in this section.

3.5.1 Diffraction and Strain Measurement

Diffraction is a scattering phenomenon that occurs when waves are incident on a crystalline material having periodically arranged array of atoms. The atoms scatter the incident wave in all directions. Diffraction occurs for elastic scattering of the incident wave by the atoms when a number of scattered beams mutually reinforce each other [4]. Since diffraction occurs due to elastic scattering phenomena, the energy of the diffracted beam is the same as that of the incident beam [4]. Bragg's law (Fig. 3.13) of diffraction describes the condition for a crystalline material to diffract an incident beam. If a monochromatic beam of wavelength λ is incident on the surface of a crystalline material at an incidence angle θ, the spacing between the crystal planes (d) will be related to the wavelength as under

$$\lambda = 2d \sin\theta \qquad 3.3$$

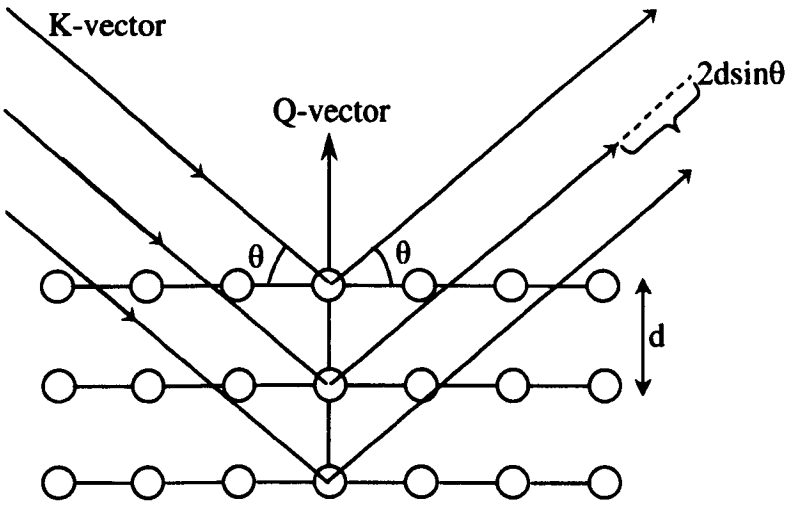

Fig. 3.13 Schematic of diffraction [22]

Therefore, from equation 3.3 the d-spacing for a particular lattice reflection can be determined if the wavelength of the incident radiation and the angular position of the diffracted beam peak is known.

The energy of a photon is given by $E= hc/\lambda$ where c is the speed of light, λ is the wavelength of the electromagnetic radiation and E is the energy of the photon. Substituting in equation 3.3

$$\frac{hc}{E} = 2d\sin\theta \qquad 3.4$$

Thus, using this, one can relate the energy to the inter-planar spacing. From this, if the wavelength of the incident radiation is constant, then the inter-planar spacing can be determined by looking at the energy spectrum.

De Broglie's wave-particle duality can be used to relate the velocity of thermal neutrons (v) and the wavelength (λ).

$$\lambda = \frac{h}{mv} \qquad 3.5$$

Where m is the mass of the neutrons and h is Planck's constant.

Substituting 3.5 into 3.3

$$\frac{h}{mv} = 2d \sin\theta \qquad 3.6$$

If the path length L travelled by the neutron and the time of flight t is known then

$$\frac{ht}{mL} = 2d \sin\theta \qquad 3.7$$

Therefore, at a constant diffraction angle, the inter-planar spacing for a particular lattice plane can be derived determining the peak time-of-flight as the velocity of the neutrons after interactions with the different crystal plane families will not be the same. Strain can be determined using equation 3.8

$$\varepsilon = \frac{d - d_o}{d_o} \qquad 3.8$$

Where d_o is the d-spacing of a reference stress free sample.

3.6 Neutron Diffraction

Neutron scattering is widely used for measurement of internal strain. Neutrons used for this purpose are thermal neutrons having kinetic energy of 10-100 meV and wavelength in the order of 1Å [6-8]. The neutrons are in thermodynamic equilibrium with the medium at room temperature and their wavelengths are close to the inter-planar spacing of many crystalline materials. The earliest references of neutron diffraction for stress measurement date back to the 1980s [7] and since then continuous development in the field has now led to the possibility of measuring real scale engineering components by dedicated strain

scanners (for example ENGIN-X at ISIS) [9]. The properties of neutrons that make them suitable for stress measurements can be summarised as follows [9, 10]:

- The motion of neutrons can be considered as waves which allow the use of De-Broglie's equation to derive the time-of-flight and hence the wavelength.

- Neutrons, being electrically neutral will not interact with electron cloud of an atom and will interact with the nucleus of any crystalline material, thus not changing the chemical state of the material being measured. However, the scattering/absorption between all elements will not be equal.

- Neutrons are highly penetrating which allows non-destructive measurement deep inside the bulk of a material and in common engineering materials they can probe to depths of many centimetres.

- The wavelength of thermal neutrons is of the order of the interplanar spacing. In diffraction experiments this results in a diffraction angle (2θ) close to 90°, which enables the use of a square geometry gauge volume.

Facilities with neutron diffraction capabilities can be split into reactor source and spallation source. Both the methods are explained briefly in the next section.

3.6.1 Reactor Neutron Source

In reactor neutron sources, neutrons are produced by nuclear fission [13]. Present reactor neutron sources consist of a compact core of uranium alloy plates enriched in U_{235}. The

neutrons produced are fast moving neutrons and have to be slowed. This is done by directing them to the required moderator by beam tubes held tangentially to the core. The thermal neutron beam collected from the moderator is polychromatic having a range of wavelengths. For strain measurement purposes the white beam is usually monochromated [13] by using a crystal monochromator where a single wavelength is selected by Bragg diffraction when the polychromatic beam is incident on the single crystal at a particular angle of incidence. A schematic is shown in Fig. 3.14.

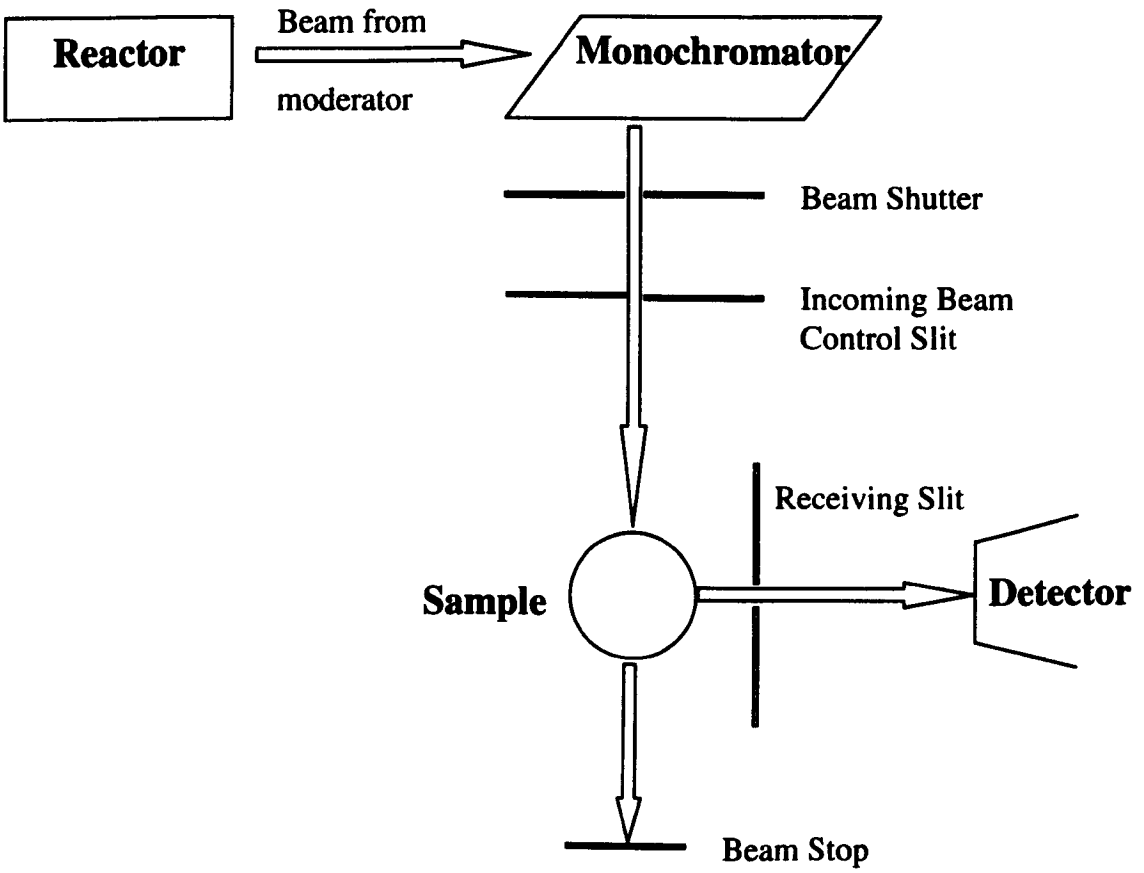

Fig. 3.14 Schematic of neutron production at a reactor source

The beam from the neutron tube first passes through a collimator and then through a pair of slits which determines the dimensions of the incoming beam. The slits are made up of a neutron-opaque material like cadmium. The diffracted beam is passed either through a collimator or receiving slits for precise location of measurement area. The incident and

receiving slits define the measurement area precisely for the spatial resolution needed for strain measurement purposes. The diffractometer consists of two co-axial rotating stages, the sample stage and the detector stage, the centres of which coincide. The sample and the detector are rotated to satisfy the Bragg diffraction condition (θ–2θ) for different wavelengths and lattice reflections. The variation of observed intensity plotted against 2θ is measured and the angular position of the peak is determined by fitting the peak profile with a mathematical function which depends on the shape of the profile. After determining the angular position, the d-spacing is calculated from equation 3.3.

3.6.2 Spallation Neutron Source

In a spallation neutron source, neutrons are produced in sharp pulses. High energy protons are accelerated in a synchrotron ring, and are made to impact a heavy atomic target (Pb, W, Ta or U) [6, 7, 14]. As a result of the collision, the target nuclei become excited and produce neutrons. The energy level of the neutrons produced is very high. The neutrons are passed through moderators surrounding the target [15]. The spallation process has the advantage of high neutron brightness in the pulse and also less heat generation. The pulse of neutrons produced in the process is characterised by a well defined spectrum of wavelengths.

From the De-Broglie relation of wave particle duality, the wavelength is inversely proportional to the velocity. Therefore, a single pulse of neutrons with different wavelengths will take different times to reach the sample at a fixed distance from the moderator. In spallation sources this time-of-flight of the neutrons is measured and the wavelength is deduced from the flight time over a known flight path [15]. In a spallation neutron source, therefore, unlike a continuous flux reactor neutron source, strain is measured by a polychromatic incident beam. In the strain measurement instrument,

ENGIN-X based at ISIS which is a Spallation neutron source, the detectors are positioned at a fixed angle of 90° with respect to the incident beam. The sample is placed with the scattering vector bisecting the incident beam and the diffracted beam. Figure.3.15 shows the schematic set up in a spallation neutron source.

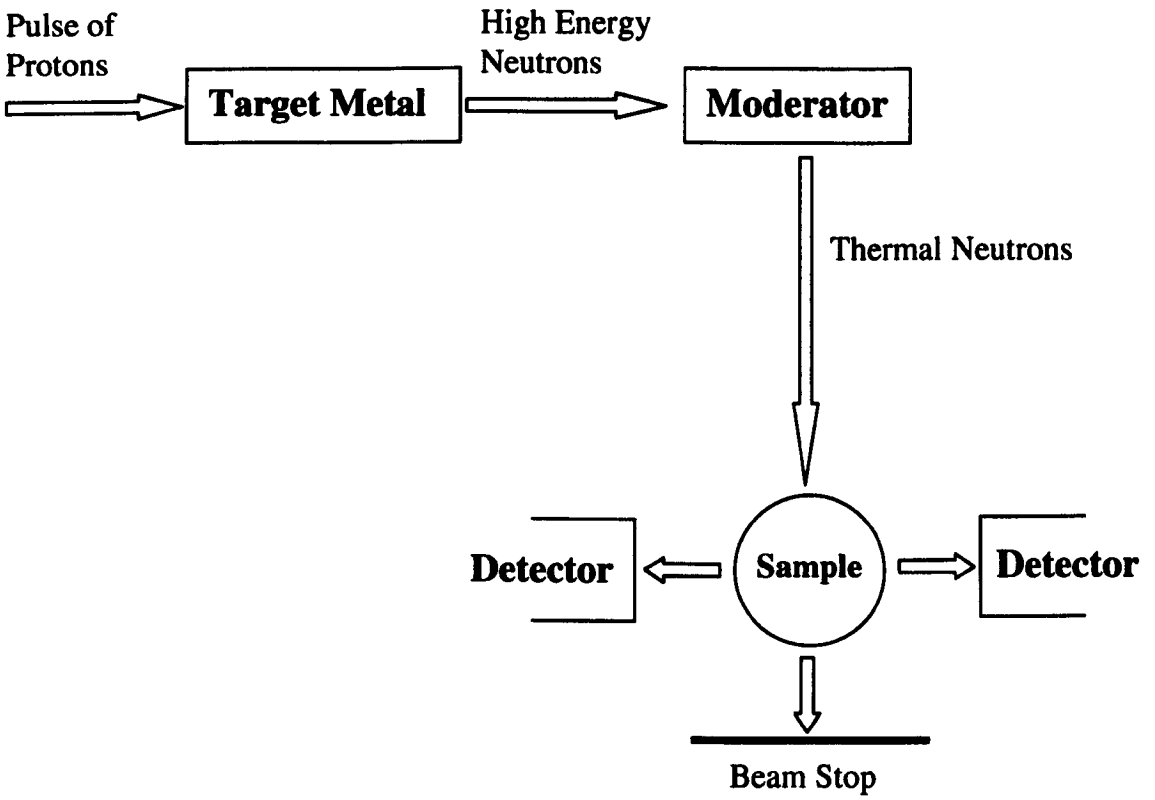

Fig 3.15 Principle of producing neutrons from a spallation source

The incident pulse of neutrons will be diffracted within the sample at different times depending upon the particular wavelength in a pulse satisfying the Bragg condition for the d-spacing of a particular family of crystallographic planes. The diffraction spectrum in a pulsed neutron source will therefore contain multiple diffraction peaks from various families of lattice reflections. An example is shown in Fig. 3.16. The data will contain information from all the crystal planes.

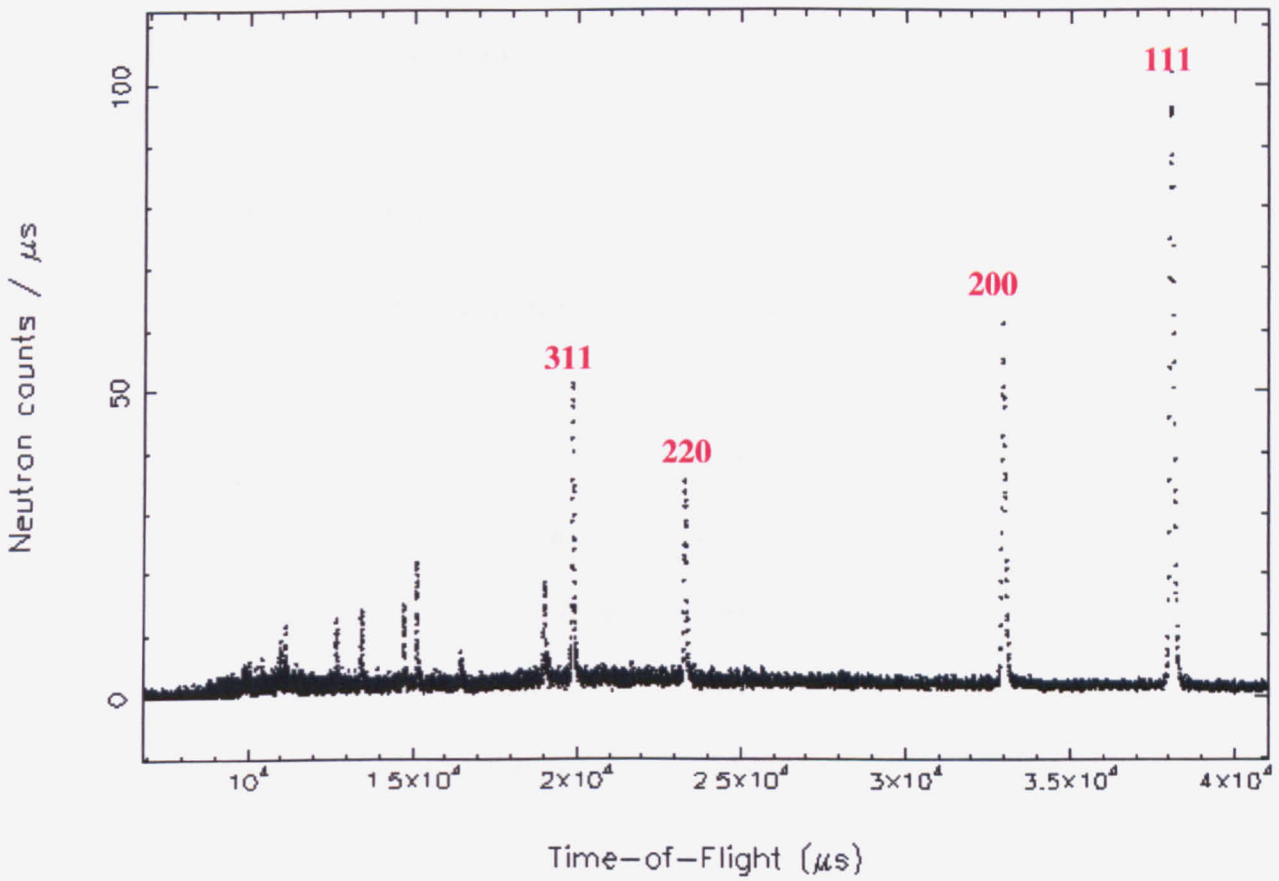

Fig. 3.16 Example of a diffraction spectrum for 316 steel. Each peak represents a specific family of planes.

The two detector banks at ENGIN-X consist of a large number of elements spanning an angular range of approximately 15°. There are time shifts between the diffraction spectra recorded in each detector element, since the path length and diffraction angle vary from element to element. To produce the final diffraction spectrum, the relative time shifts are subtracted and the intensity from all detectors are summed. This is known as time focussing [16]. The diffraction data is then refined and the lattice parameter of the unit cell of the polycrystalline material is determined using a Pawley or a Reitveld refinement of the data. Strain is determined by measuring the average lattice parameter of a stress-free reference and then by using equation 3.8. In pulsed neutron experiments, since many crystallographic planes show peaks in the diffraction profile, the average lattice parameter is generally used instead of the d-spacing of any particular lattice plane. The sample

mounting table is motorised and the sample can be scanned through the gauge volume in all directions to form a strain map.

3.7 Conclusions

- The experimental procedures used for creep and tensile testing have been described.
- There are various ways creep data can be represented. Depending on the study, different analysis methods can be used.
- Neutron diffraction techniques have been described.
- Neutron diffraction can either be fixed wavelength or time-of-flight. The working principles of both these methods have been explained.

References

[1] ASTM E8 / E8M - 08 Standard Test Methods for Tension Testing of Metallic Materials

[2] ASTM E21 - 09 Standard Test Methods for Elevated Temperature Tension Tests of Metallic Materials

[3] ASTM E139 - 06 Standard Test Methods for Conducting Creep, Creep-Rupture, and Stress-Rupture Tests of Metallic Materials

[4] P.J.Withers and H.K.D.H.Bhadeshia, *Residual stress, Part 1-Measurement techniques*, Mater. Sci. Tech. (2001), Vol. 17, pp. 355-365.

[5] S.G.Ganguly: PhD Thesis, *Non-Destructive Measurement of Residual Stresses in Welded Aluminium 2024 Airframe Alloy*, The Open University, 2004.

[6] N. Ananthaviravakumar: PhD Thesis, *Investigation of Residual Stresses in Engineering Components Using Neutron and Synchrotron X-ray Diffraction Techniques*, Division of Civil and Environmental Engineering, University of Salford, 2002

[7] P.A. Browne: PhD Thesis, *Determination of Residual Stress in Engineering Components Using Diffraction Techniques*, Division of Civil and Environmental Engineering, University of Salford, 2000.

[8] Dann, J.A., Daymond, M.R., Edwards, L., James, J. and Santisteban, J.R., *A comparison between Engin and Engin-X, a new diffractometer optimized for stress measurement* (2004). Physica B: Condensed Matter, 350(1-3), pp. 511–514.

[9] M. Dutta: PhD Thesis, *Residual Stress Measurement in Engineering Materials and Structures Using Neutron Diffraction*, Materials Engineering, The Open University, 1999.

[10] D.Q. Wang: Ph.D. thesis, *Strain Measurement Using Neutron Diffraction*, Dept. of Materials Engineering, The Open University, 1996.

[11] A.J. Allen, M.T. Hutchings, C.G. Windsor, and C. Andreani, *Neutron diffraction methods for the study of residual stress fields*, Advances in Physics, 1985, Vol. 34, 4, pp. 445-473

[12] C.H. de Novion: *The Use of Neutrons for Materials Characterisation*, in M.E.Fitzpatrick and A.Lodini (Eds), Analysis of Residual Stresses by Diffraction Using Neutron and Synchrotron Radiation, Taylor & Francis, London, 2003, pp 3-27.

[13] L. Pintschovius: *Neutron Diffraction Using a Constant Wavelength*, in M.E.Fitzpatrick and A.Lodini (Eds), Analysis of Residual Stresses by Diffraction Using Neutron and Synchrotron Radiation, Taylor & Francis, London, 2003, pp 133-145.

[14] E. Macherauch and K.H. Kloos: *Origin, Measurement and Evaluation of Residual Stresses*, Verlag, Germany, 1987.

[15] M.W. Johnson and M.R. Daymond: *Neutron Pulsed Source Instrumentation*, in M.E. Fitzpatrick and A.Lodini (Eds), Analysis of Residual Stresses by Diffraction Using Neutron and Synchrotron Radiation, Taylor & Francis, London, 2003, pp 146-169.

[16] E.C. Oliver: PhD Thesis, *The Generation of Internal Stresses in Single and Two Phase Materials*, Faculty of Science and Engineering, University of Manchester, 2003.

CHAPTER 4: CHARACTERISATION OF AS-RECEIVED AUSTENITIC STEEL (AISI 316H)

There are a number of materials which are used to manufacture components used in nuclear power plants. The operating environment and the material properties required will determine the selection of materials. For this thesis, austenitic stainless steel was chosen for study. Austenitic steels are used to manufacture a wide range of components within the power generation industry. They are used in the construction of piping systems, heat exchanger systems, steam headers, etc. Components like the reactor pressure vessel (RPV) are made from ferritic steel with austenitic steel liners. Their retention of strength at elevated temperatures and corrosion resistance properties are the primary reasons for their use.

Austenitic steels come in many different grades and varieties. AISI grade 316H steel was used for this project. The steel is a modification of the commonly used 316 grade steel. The carbon content is slightly higher than the 316 grade steel which improves high temperature performance.

4.1 Description of As Received Material

The 316H steel used in this study was sourced from Power Metal Suppliers, a company which supplies material to power plants. The test certificate has been attached in Appendix I.Some of the salient features were:

Grade: 316H (UNS S31609)

Melting Method: Electric Furnace

Surface: Cold Draw and Centreless Ground

Product Form: Bars

Size Supplied: 15m (5 rods of 3m each, 12.5mm diameter)

Standard: Tech. Agr. 151-2002

Specification: ASTM A: 479/A 479M-01 Cond-A-Annealed

182/A 182M-97c(Chemical and Mechanical Properties Only)

ASME SA: 479/SA-479M-96a Cond-A-Annealed, 182/SA-182M-95

Heat Treatment: Held at 1100°C for 90 minutes, then water quenched

		C	Mn	Si	P	S	Cr	Ni	Mo
Chemical Composition of as received bar (%)		0.078	0.63	0.29	0.32	0.015	18.46	10.17	2.12
Composition according to ASTM 240	**Min (% weight)**	0.04	-	-	-	-	16	10	2
	Max (% weight)	0.10	2	0.75	0.045	0.03	18	14	3

Table 4.1: Composition of as received 316H stainless steel barstock

4.2 Grain Size Calculation

For measurement of grain size, eight (four transverse and four longitudinal) specimens were cut from two different bars. The specimens were taken approximately 20 cm away from each end of the bar. The specimens were cut using the Electric Discharge Machining (EDM) process. Specimens from both transverse and longitudinal directions were cut.

4.2.1 Specimen Preparation

For grinding and polishing purposes, the specimens were placed in a hot mount resin made of bakelite. The objective was to get a fine mirror finish on the specimen surface. Both

grinding and polishing processes were used to obtain this. The following steps were performed:

Grinding was performed using grinding papers embedded with silicon carbide (SiC).

Grit Size(microns)	Grinding Time (seconds)	Force Applied (lbs)
200	120	7
800	300	8
1200	300	9
2500	600	9
4000	300	9

Table 4.2: Details of specimen preparation (grinding)

For further finishing, the specimens were polished using a soft NAP grade paper. Diamond abrasives of different sizes were used. Abrasive sizes of 9, 6, 3 and 1 micron were used. Each stage lasted for five minutes and a force of 10N was applied while polishing. For each paper, only one size of abrasive was used.

Etching Process

The etching process applied is dependent on the desired result. For characterising the grain size, grain boundaries have to be etched. In this study, the specimens were etched electrolytically. A 60% (aqueous) nitric acid solution was used for this purpose. A voltage of 2V was applied for 90-120 seconds. Specimens 1 and 2 were from two different bars. 'i' and 'ii' denote the two ends of the bar. The resulting optical micrographs are shown in Fig. 4.1 & 4.2.

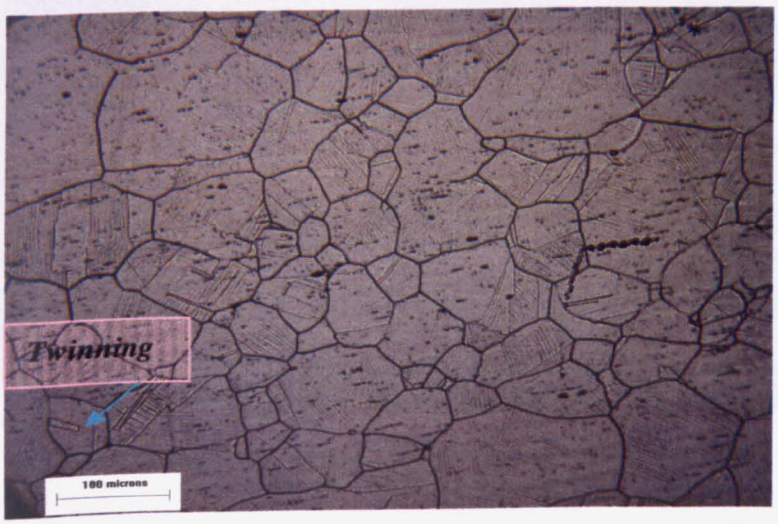

a

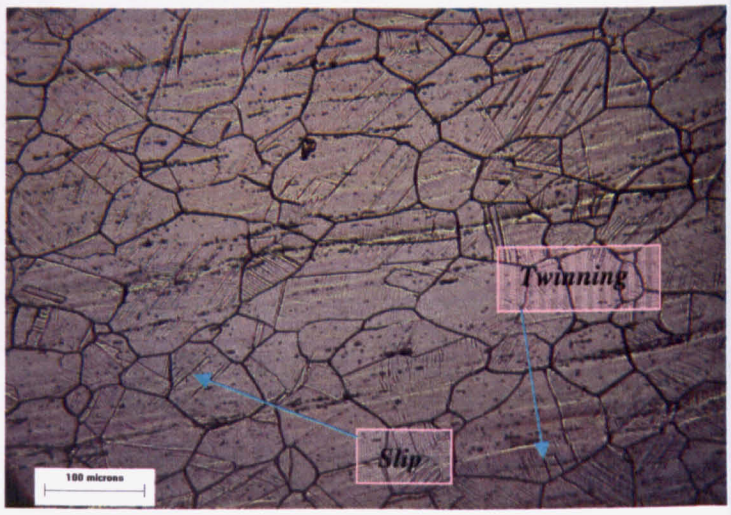

b

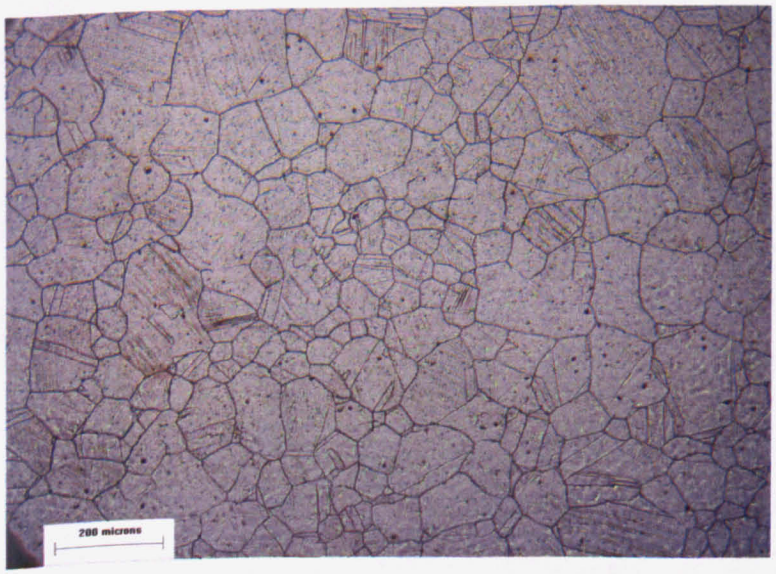

c

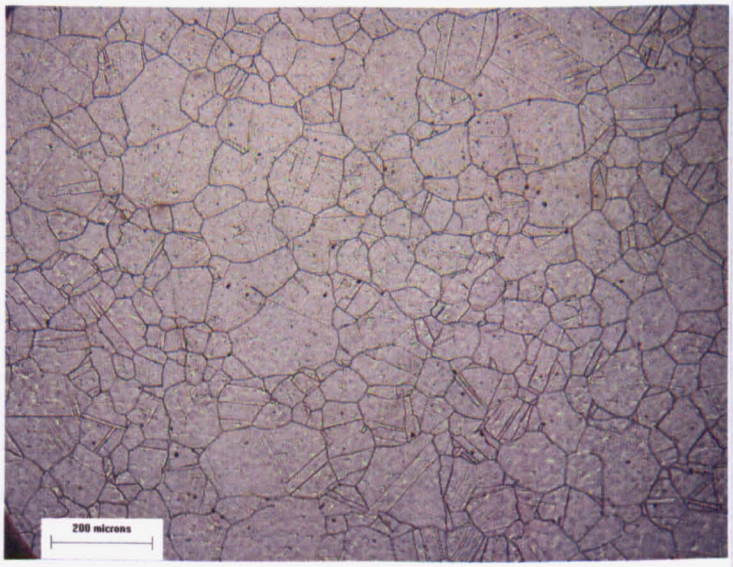

d

Fig. 4.1 **(a)** Longitudinal section of Specimen 1(i) **(b)** Longitudinal section of Specimen 1(ii) **(c)** Transverse section of Specimen 1(i) **(d)** Transverse section of Specimen 1(ii)

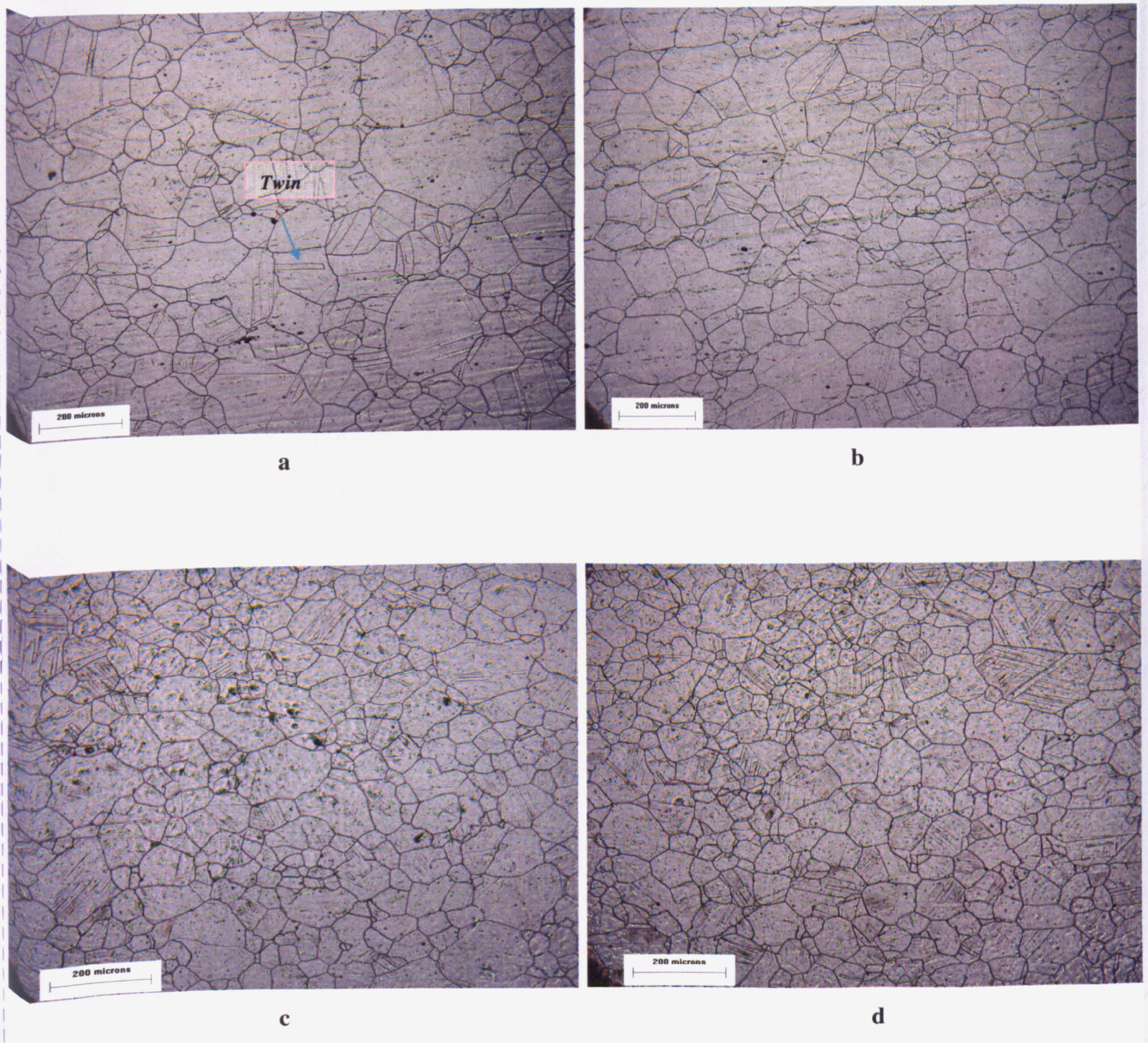

Fig. 4.2 (a) Longitudinal section of Specimen 2(i) **(b)** Longitudinal section of Specimen 2(ii) **(c)** Transverse section of Specimen 2(i) **(d)** Transverse section of Specimen 2(ii)

4.2.2 Linear Intercept Method for Estimation of Grain Sizes

The mean linear intercept length is one of the most commonly used methods to determine grain size. The full details of the procedure can be found in [5]. Grain size is determined by laying a series of uniformly distributed test lines on the planar section and counting the number of times that grain boundaries are intercepted.

For the specimens obtained, three lines were drawn for each specimen. The size of the lines was decided based on the magnification. For each sample, the size of the test lines was chosen so as to sample about 50 grains. Table 4.3 summarises the results.

Specimen	Section	Length of Test Line(microns)	Number of Intercepts	Grain Size in microns (Length of test line/ number of intercepts)	Average Grain Size(microns)
1(i)	Longitudinal	857	16	53	
		657	11	59	59
		514	8	64	
1(i)	Transverse	1000	19	52	
		1000	13	76	60
		1000	15	66	
1(ii)	Longitudinal	500	9	55	
		500	8	62	66
		500	8	62	
1(ii)	Transverse	1000	14	71	
		1000	16	62	75
		1000	15	66	
2(i)	Longitudinal	1000	15	66	
		1000	14	71	65
		1000	16	62	
2(i)	Transverse	1000	16	62	
		1000	15	66	66
		1000	19	52	
2(ii)	Longitudinal	1000	13	76	
		1000	14	71	60
		1000	13	76	
2(ii)	Transverse	1000	16	62	
		1000	13	76	64
		1000	18	55	

Table 4.3 Grain size calculations

The calculations show that the material has a fairly uniform grain size of about 60-75 microns. The optical photographs also show evidence of twinning and slip. As seen in Fig. 4.1, there are twins in the material. Most of the specimens show areas of slip as shown in Fig. 4.1 and 4.2. The slip systems may be a result of prior cold work on the material, most probably during the cold drawing process.

4.2.3 Influence of Grain Size

Grain size is an important factor which affects material properties. Generally, larger grains suppress diffusional flow [2]. Creep deformation maps similar to those described in section 2.7 are applicable for a specific grain size.

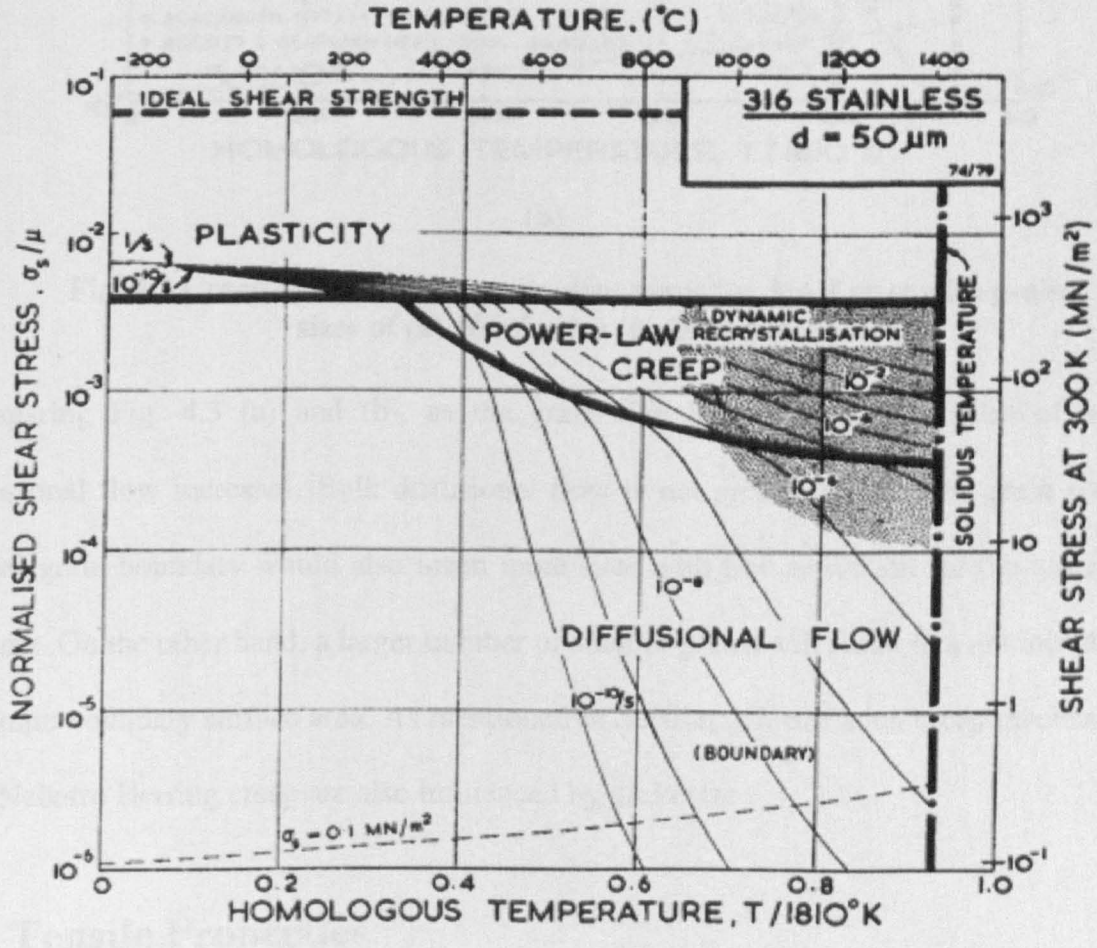

(a)

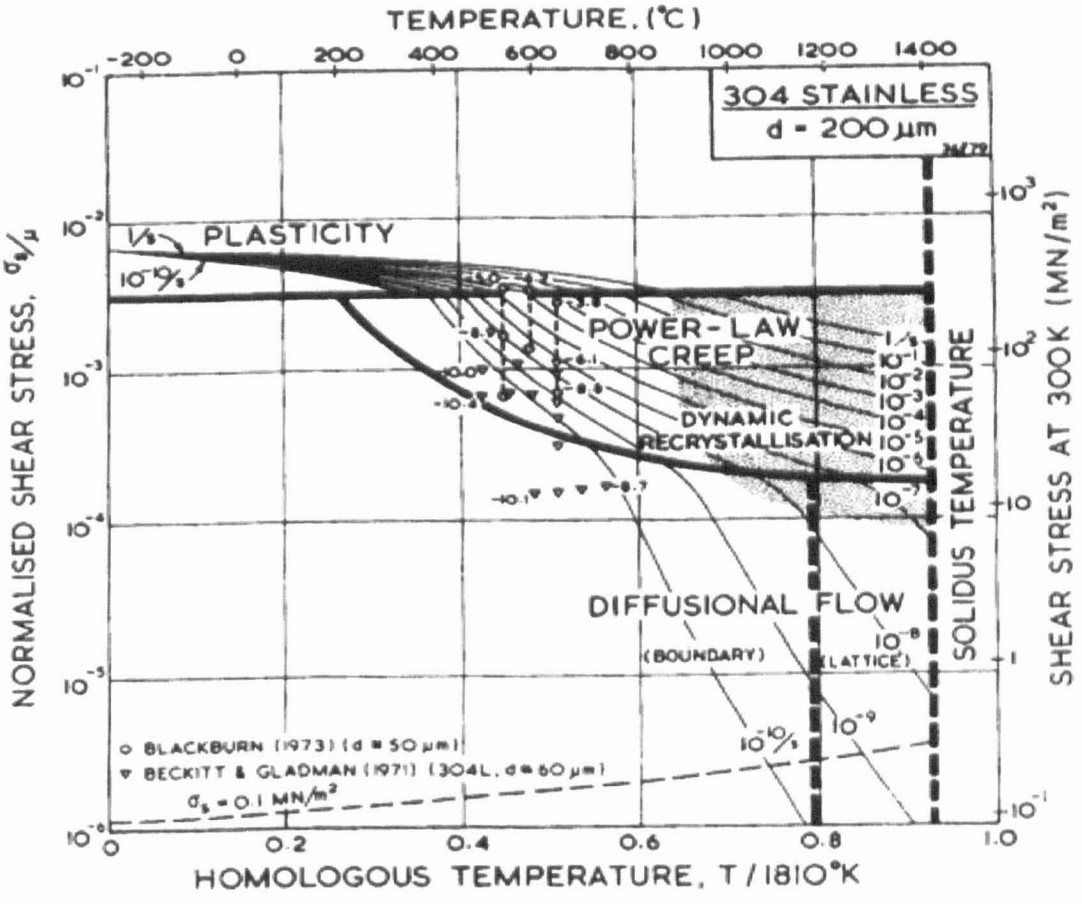

(b)

Fig. 4.3 Creep deformation mechanism maps for 316H steel with grain sizes of (a) 50 microns (b) 200 microns

Comparing Fig. 4.3 (a) and (b), as the grain size increases, the influence of lattice diffusional flow increases. Bulk diffusional flow is not greatly affected by grain size. A longer grain boundary would also mean more sites with low activation for the cavitation process. On the other hand, a larger number of smaller grains will result in a net increase in the grain boundary surface area. As mentioned in Section 2.7, diffusion creep mechanisms like Nabarro Herring creep are also influenced by grain size.

4.3 Tensile Properties

The first step in characterising the material was to determine the tensile strength of the as received material. Tensile testing was carried out on two different machines to check the amount of scatter in the data. Tensile tests were also done at room temperature, 550°C and

650°C to determine the yield strengths. The results obtained from the tensile tests were an input for the stress levels for the creep testing.

4.3.1 Room and Elevated Temperature Tensile Properties

Tests were conducted using displacement control. All the tests were performed at a displacement rate of 0.081mm/min. The results of the tensile tests are shown in Fig. 4.4. The proof stress values are summarised in Table 4.4.

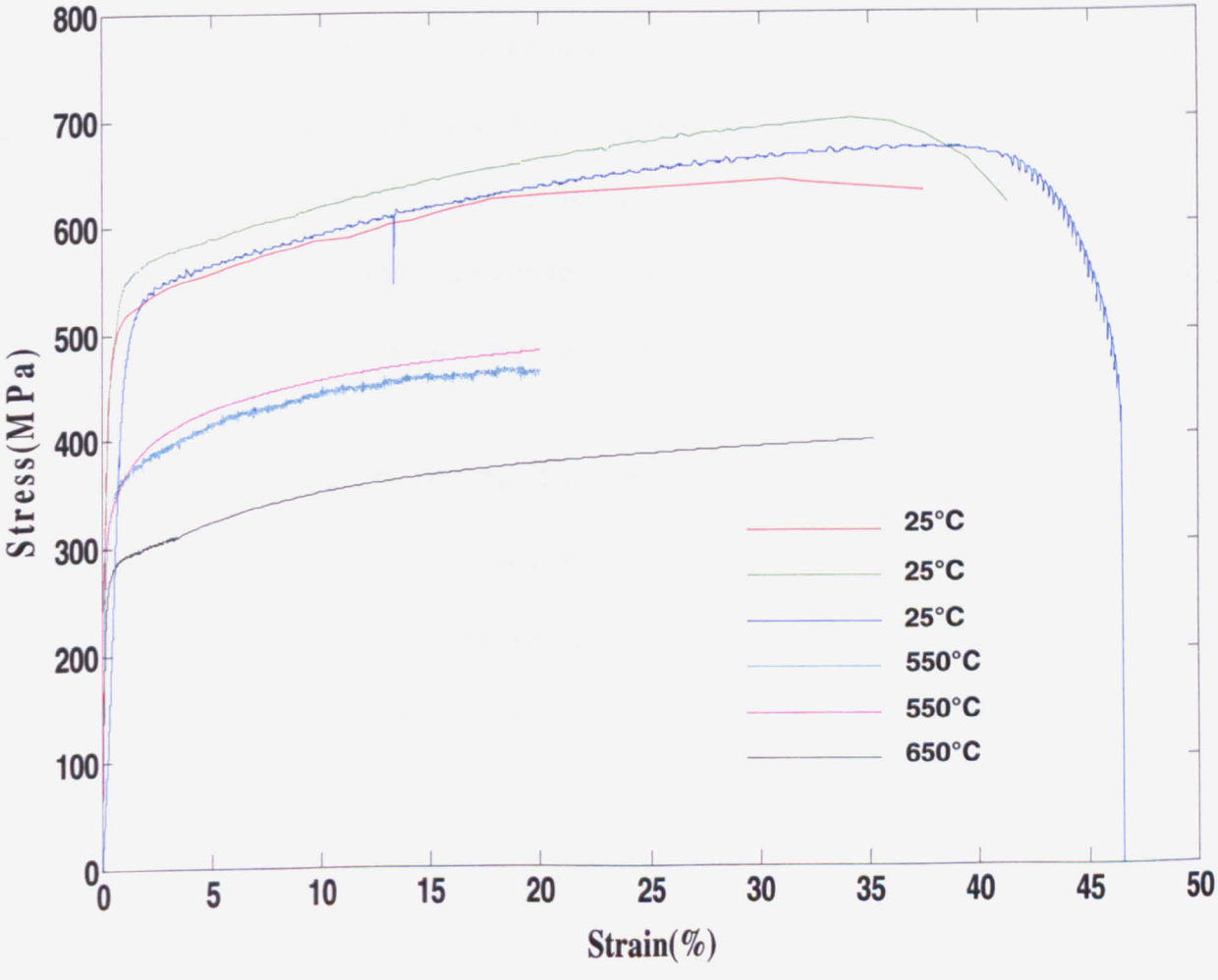

Fig. 4.4 Results of tensile testing: room temperature, 550°C and 650°C

Specimen	0.2% Proof Stress (MPa)	1% Proof Stress (MPa)
Room temperature	224, 219, 230	285, 292, 310
550°C	127, 118	157, 145
650°C	110	127

Table 4.4 Proof strength values at room temperature and elevated temperature for as received 316H steel

The room temperature yield stress of the material is around 220MPa. The value decreases as expected at elevated temperatures and is around 125MPa at 550°C and 110MPa at 650°C. The test certificate (Appendix I) for the material shows a proof stress of 30ksi (210MPa). This is assumed to be at room temperature and for 0.2%. The tests thus confirm the value given in the test certificate to an acceptable level.

4.4 Baseline Creep Rupture Testing

Creep rupture data is one of the most important data inputs for understanding high temperature behaviour. Creep rupture tests give the overall lifetime of the material and its failure strain. Other parameters like secondary strain rate can be calculated from the strain data obtained. Before conducting any of the tests which involved complex loading cycles, the baseline creep rupture data had to be generated.

4.4.1 Selection of Operating Conditions

Creep has a strong dependence on stress and temperature. Conditions for a creep test (stress and temperature) are chosen accounting for several factors including operating

conditions the component may experience and the prevalent mechanism of creep to be studied.

Generally for material testing, a large number of creep tests are done at a range of temperatures and stresses and a database is built. During this project, the material response was studied under a limited range of conditions, as it was not intended to build a large database and AISI 316H steel has in any case been widely characterised. Some of the creep databases available are listed in [6], [7], [8], [9] with which the results obtained can be compared.

A number of the current fleet of Advanced Gas Cooled Reactors (AGR) have had their lives extended. In order for safe life extension, it is necessary to determine the effects of prior operation. The stress and temperature conditions for this study were chosen such that they would represent the conditions seen in gas cooled nuclear power plants which have higher operating temperatures (between 550°C and 650°C) than the PWR (Pressurised Water Reactor) type which has operating temperatures around 300°C. Since temperature plays a major role in the mechanisms responsible for creep deformation, it was decided that the tests would be conducted at temperatures at which the components operate while increasing the stress so that the test would finish within a reasonable amount of time. The stress applied was decided based on the tensile testing results shown previously.

4.4.2 Results of Creep Rupture Testing

The temperatures used in this study were mainly 650°C and 550°C. Tests have also been done at 600°C, 700°C, 750°C and 800°C. The majority of the testing was done at 650°C.

Test Procedure

The tests were conducted using the equipment described in chapter 3. During the setup, the following points were followed:

- The whole lever arm assembly and the load train were balanced for weight before every test. An imbalance in the weight would result in the wrong load being applied.
- Three thermocouples were used at different points in the gauge for better control.
- The samples were heated to the required temperature and the furnace controllers were adjusted until a satisfactory temperature gradient (±3°C) was achieved.
- Temperature was recorded every 10 minutes.
- An initial load of 50N was applied to eliminate slack within the load train. After this procedure, the remaining load was applied.
- Displacement was recorded every minute for the first few hours and then was sampled every 10 minutes for the remainder of the test.

Figures 4.5-4.15 show a sample of the creep curves for tests conducted at temperatures ranging from 550-800°C. A summary of the results obtained is shown in Table 4.5.

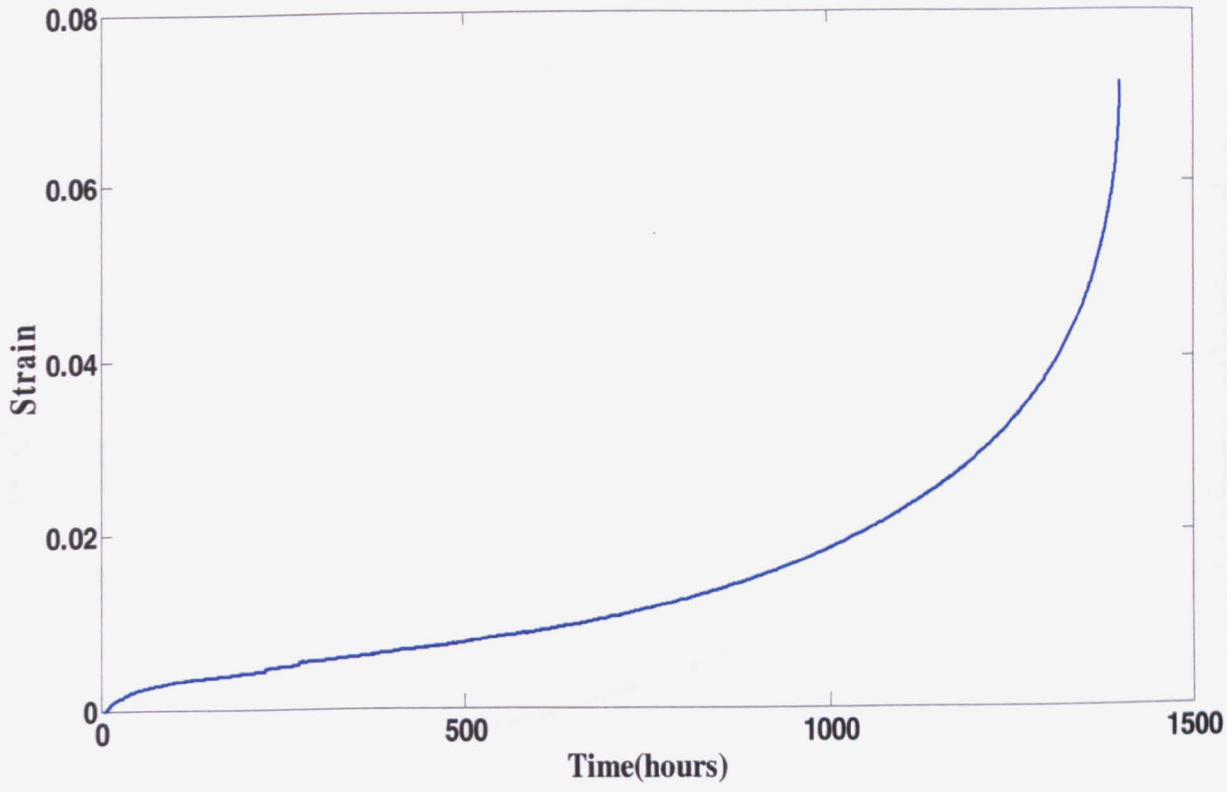

Fig. 4.5 Creep rupture test conducted at 650°C 160MPa

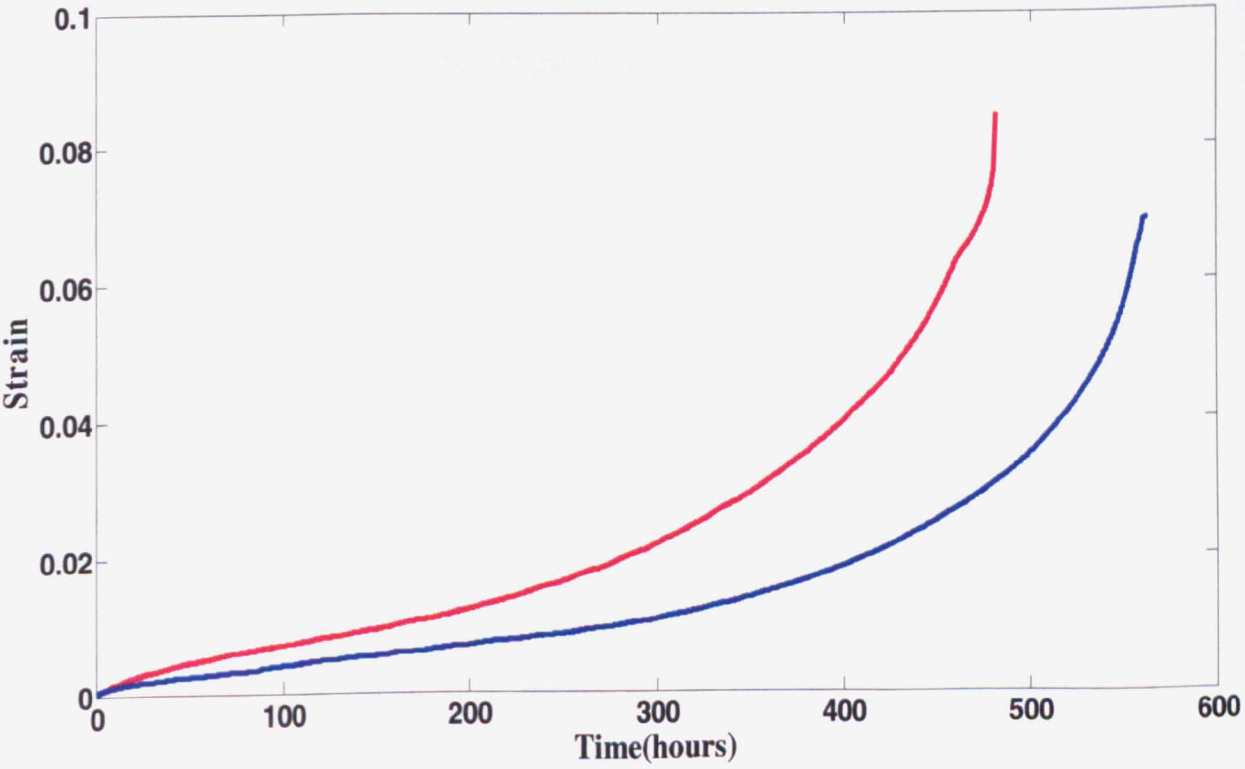

Fig. 4.6 Creep rupture tests conducted at 650°C 180MPa

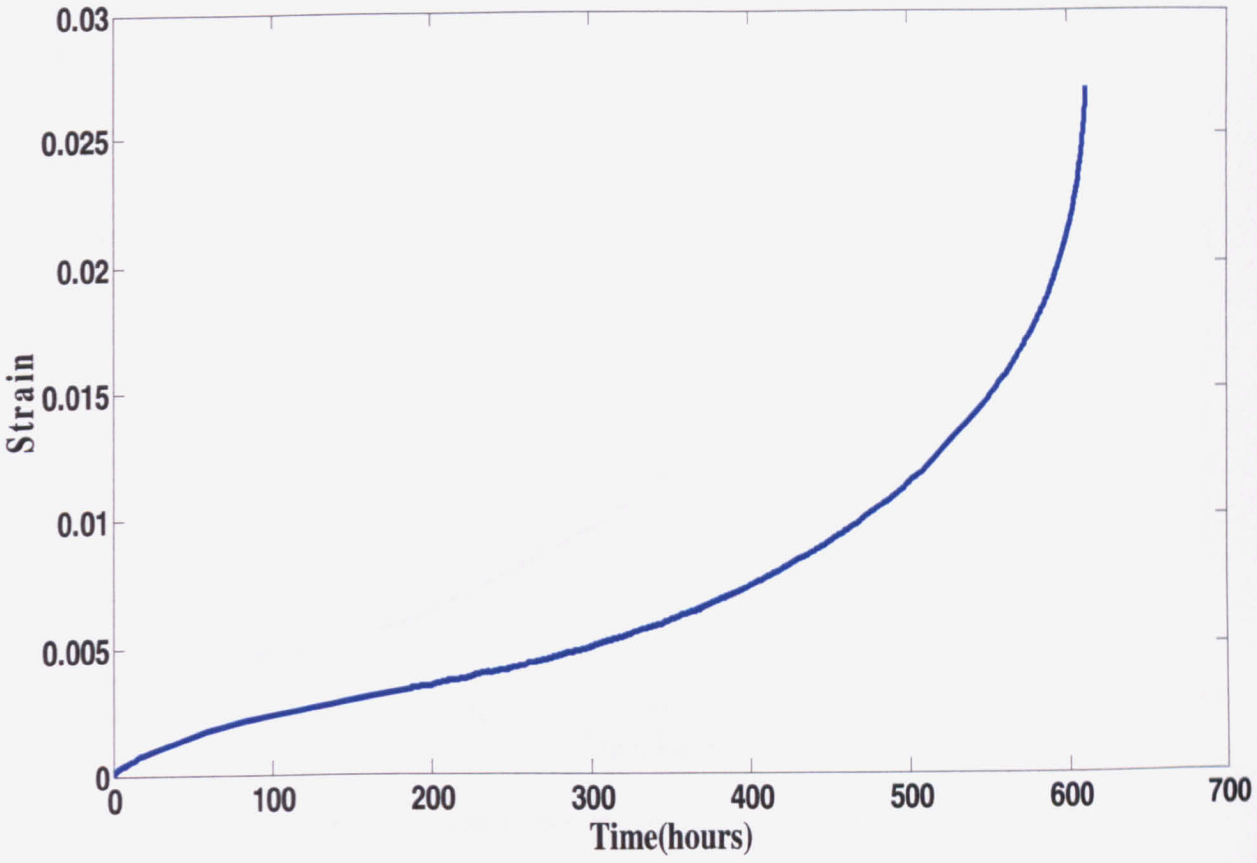

Fig. 4.7 Creep rupture test conducted at 650°C 200MPa

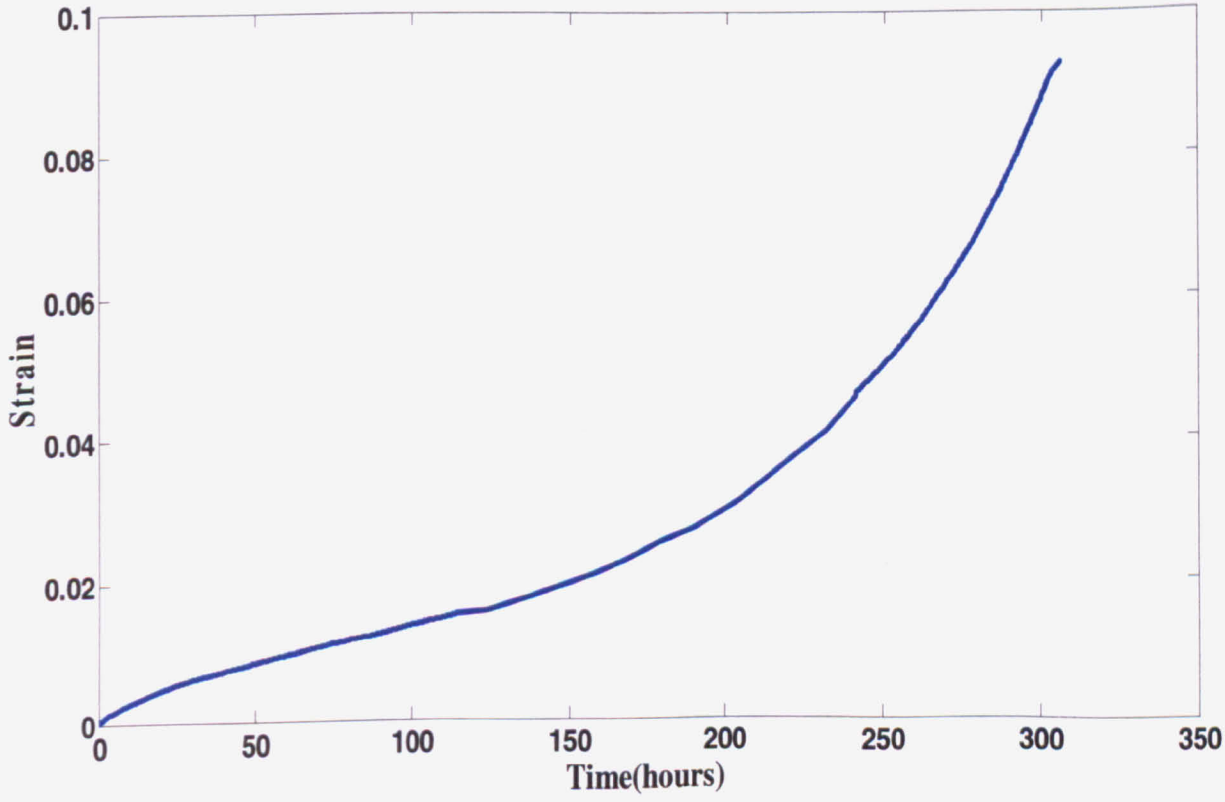

Fig. 4.8 Creep rupture test conducted at 650°C 220MPa

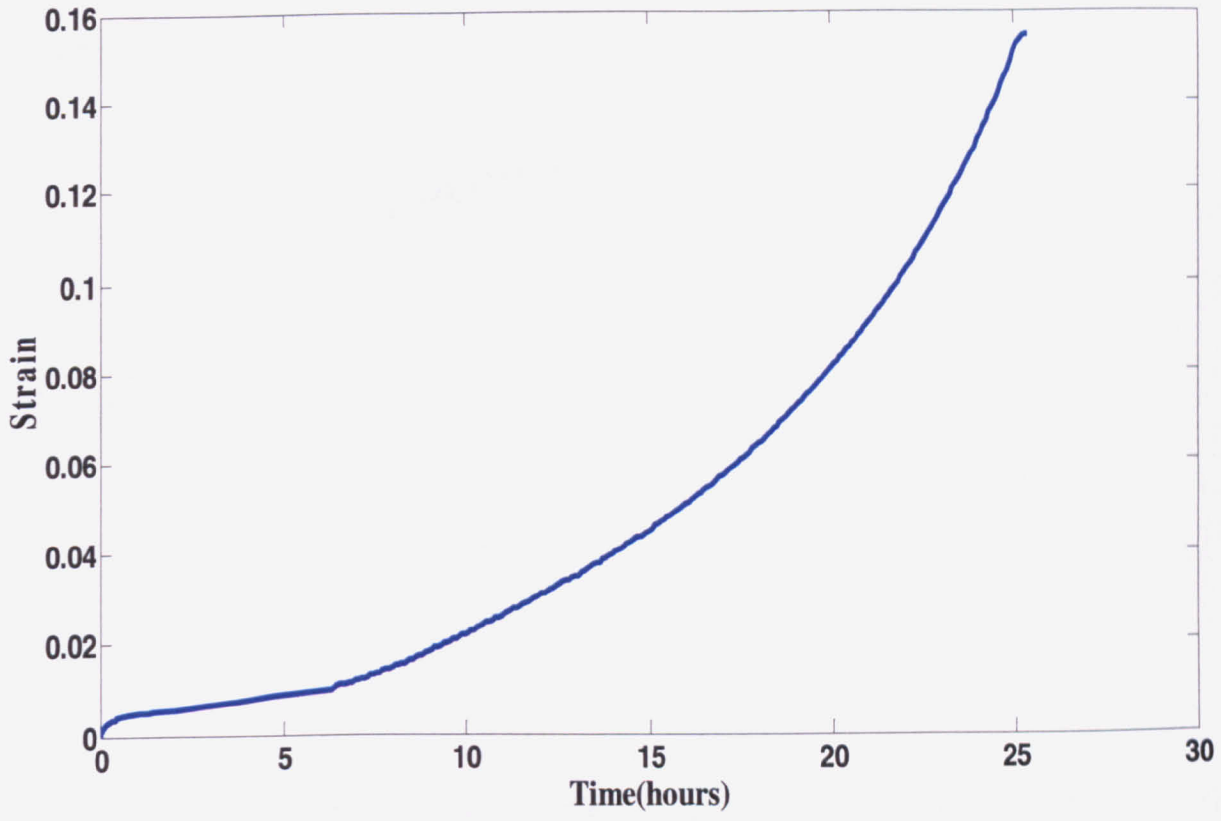

Fig. 4.9 Creep rupture test conducted at 650°C 250MPa

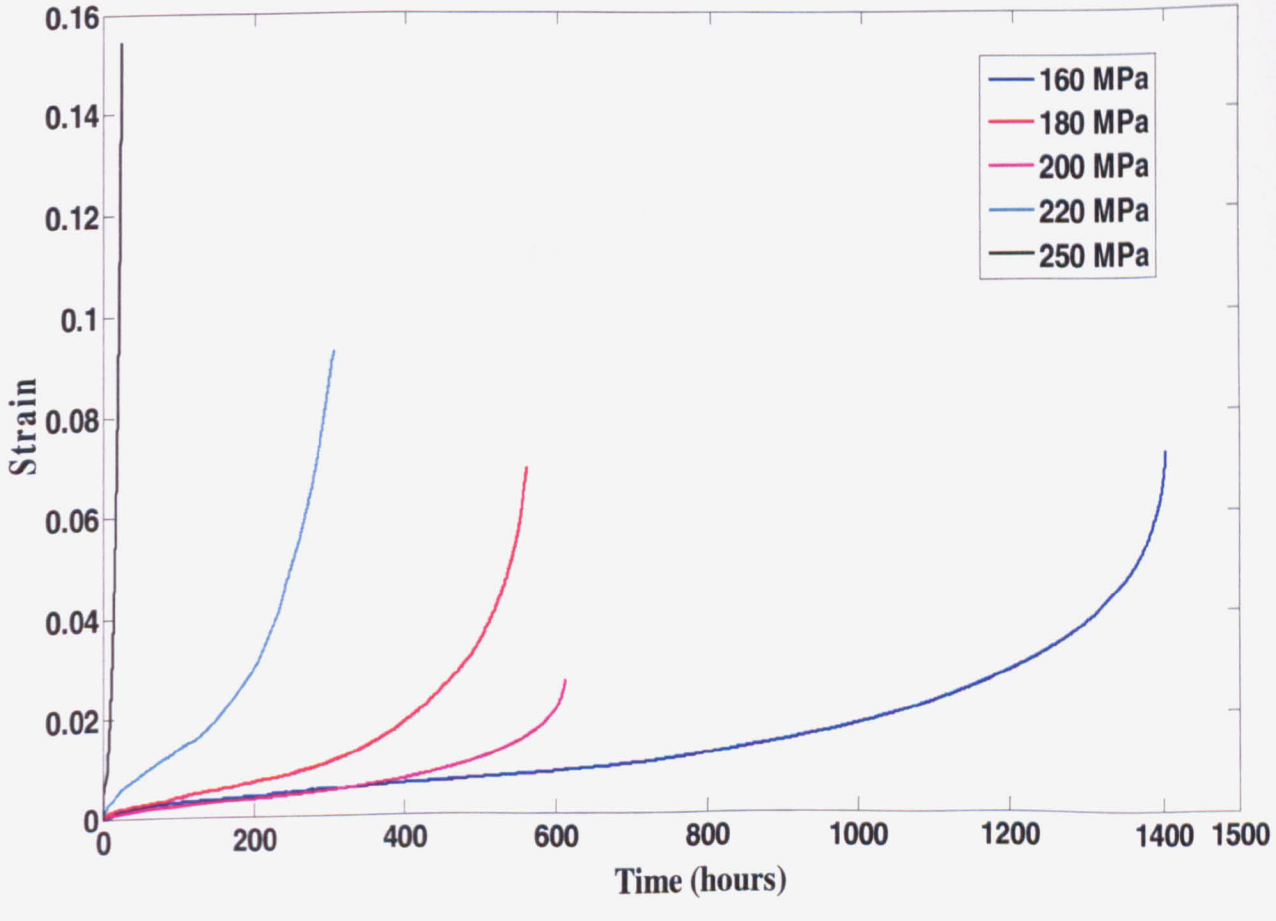

Fig. 4.10 Comparison of creep rupture tests at 650°C

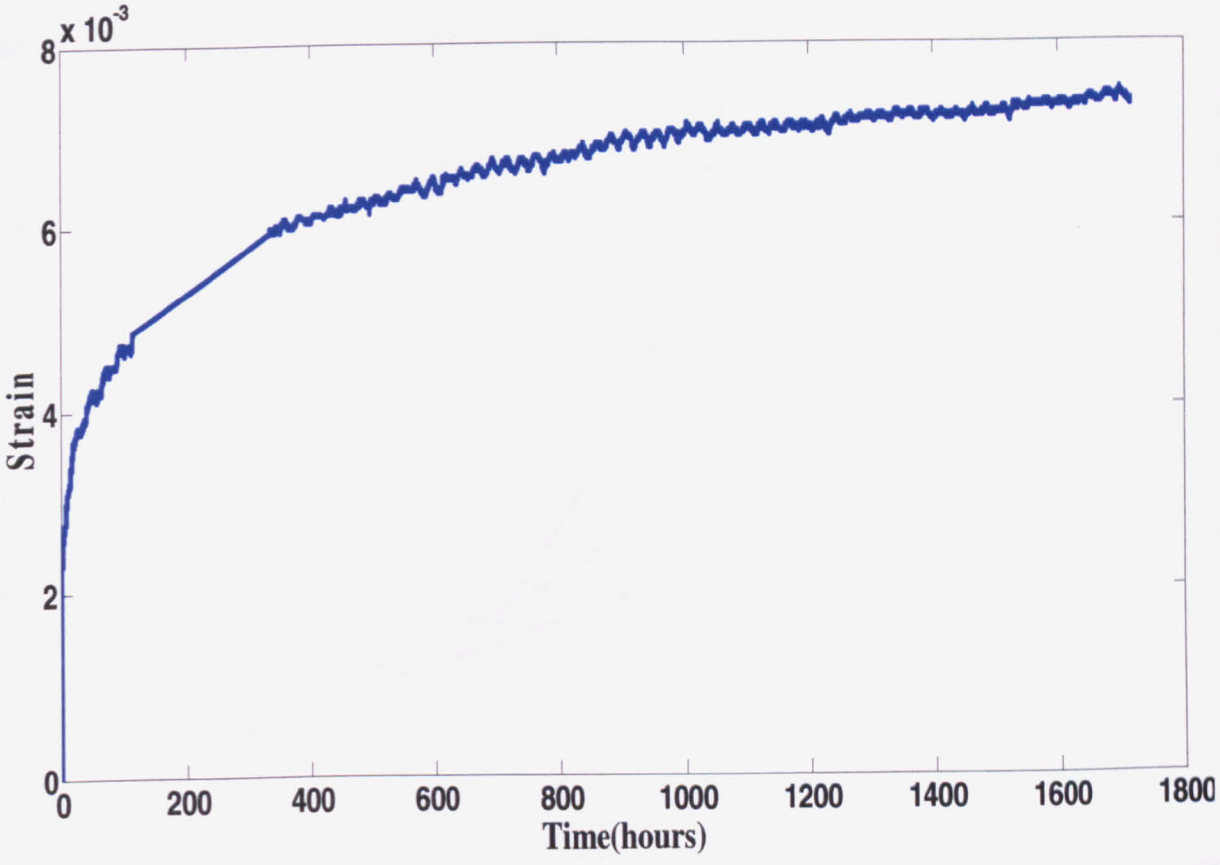

Fig. 4.11 Creep rupture test conducted at 600°C 230MPa. Test stopped after 1700 hours

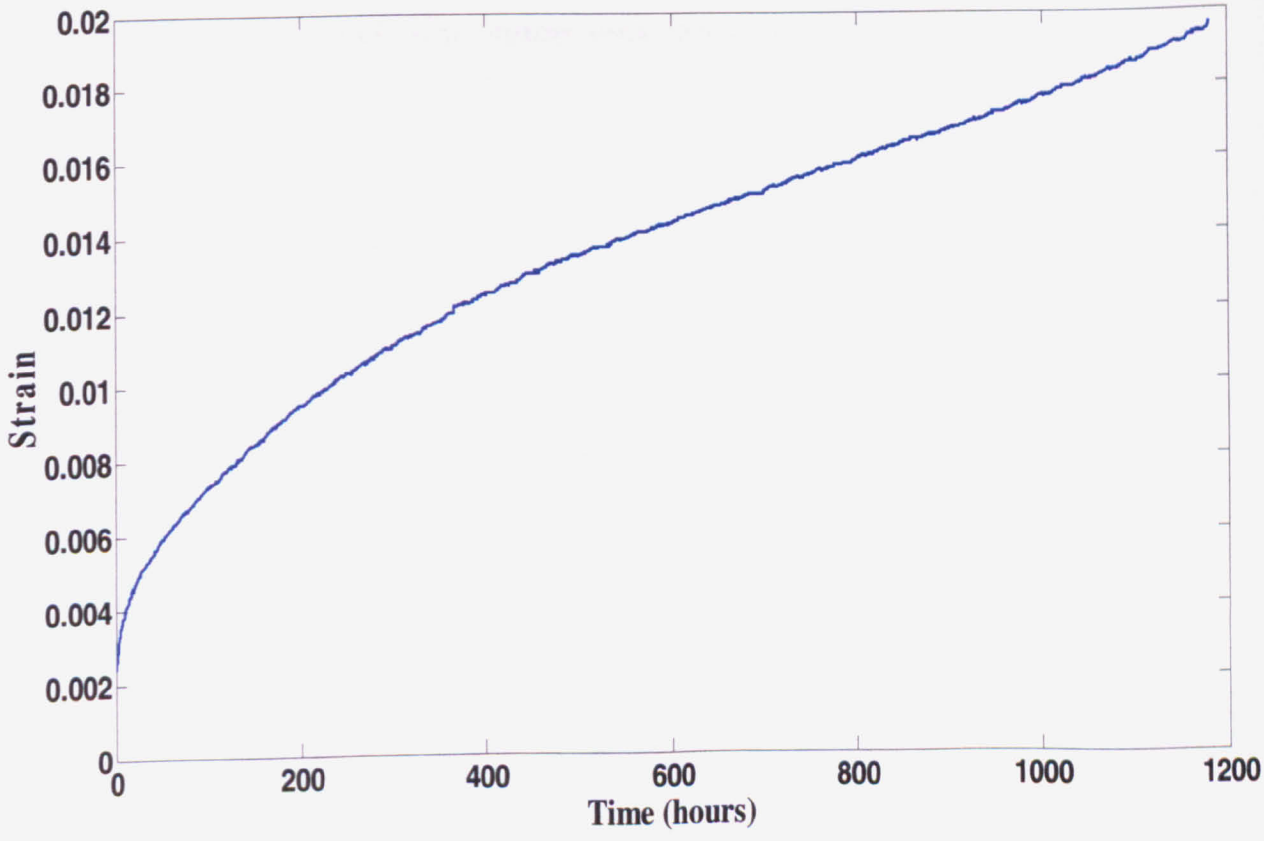

Fig. 4.12 Creep rupture test conducted at 600°C 250MPa. Test stopped after 1200 hours

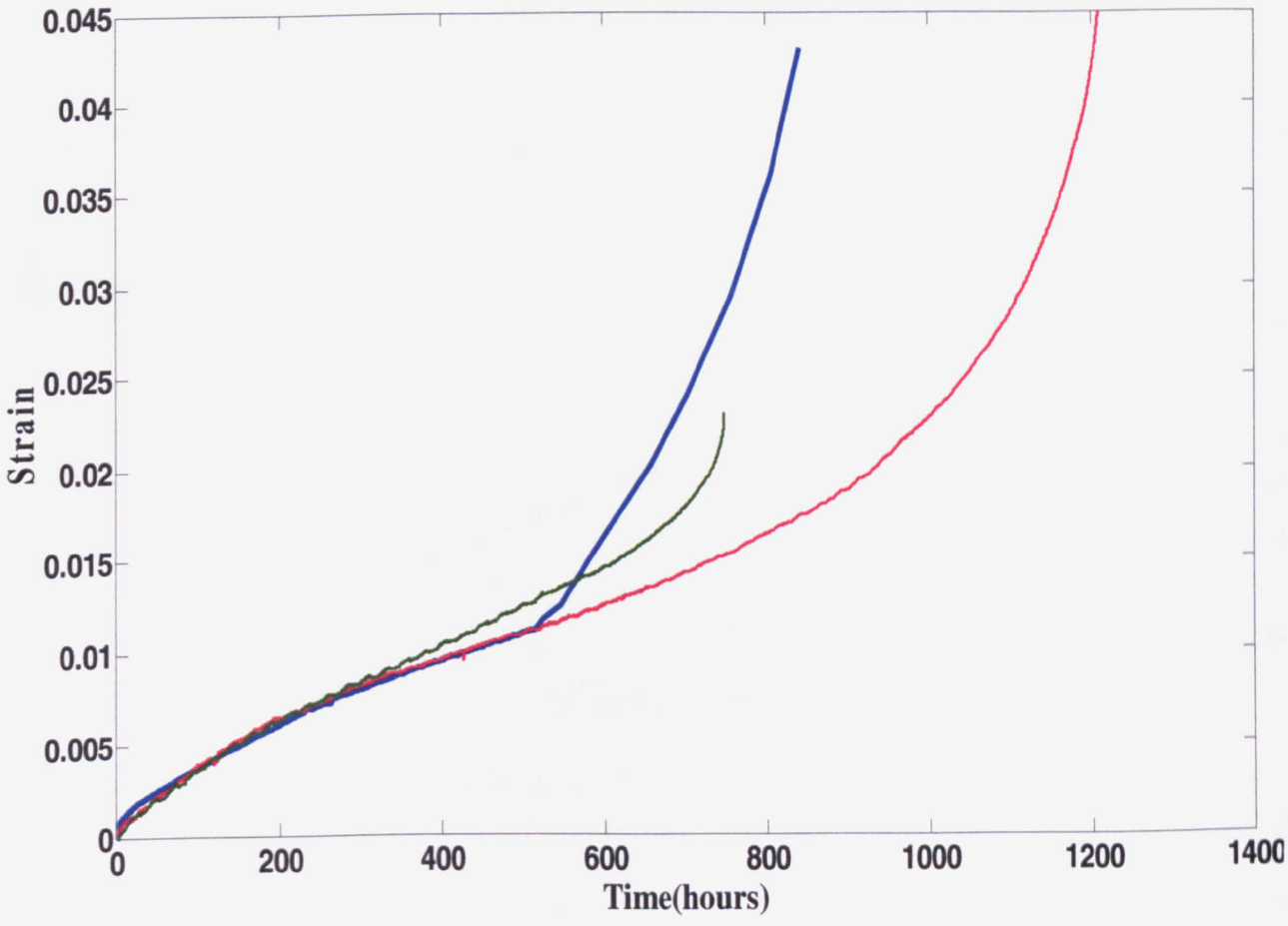

Fig. 4.13 Creep rupture tests conducted at 550°C 335MPa

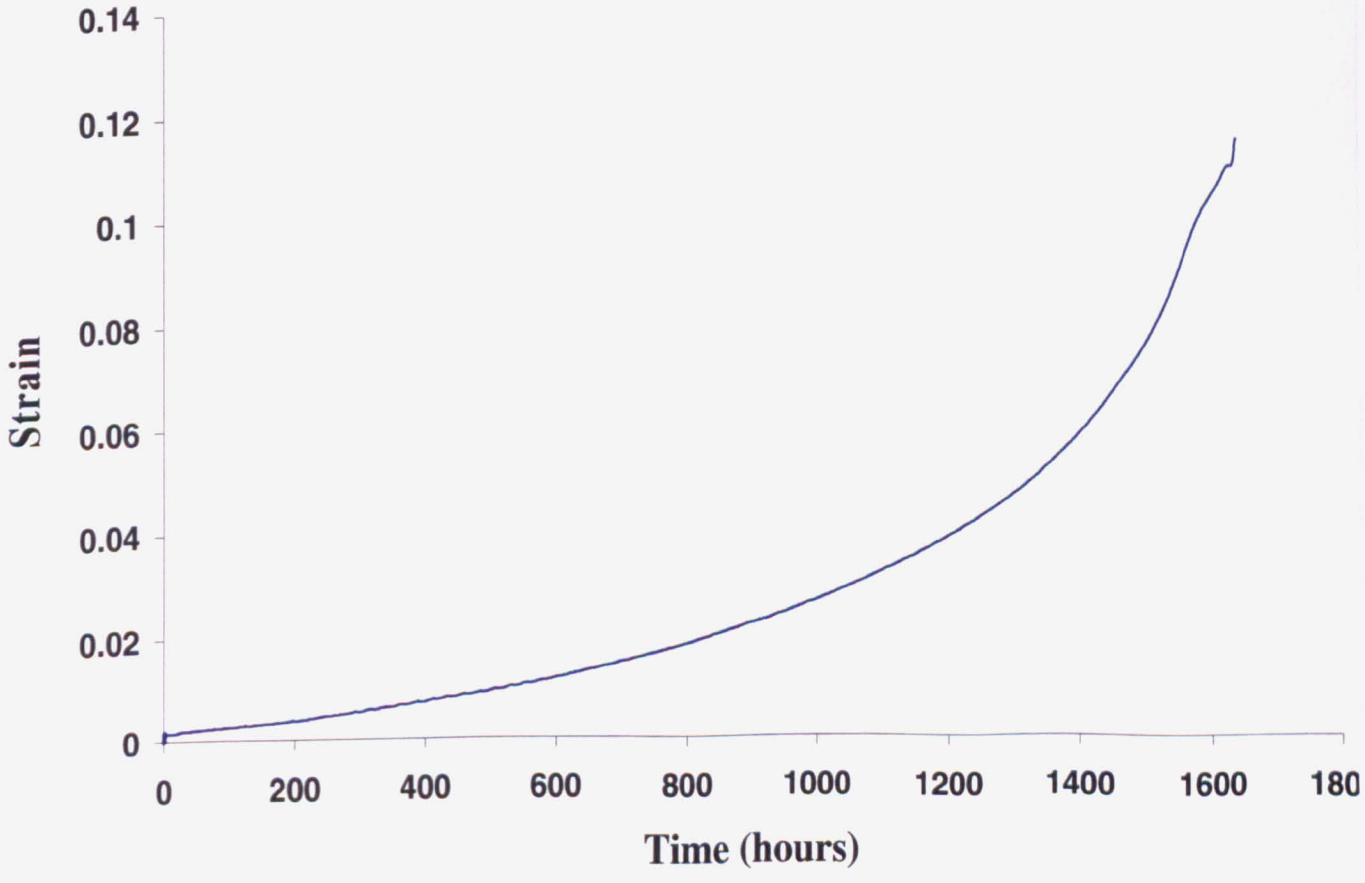

Fig. 4.14 Creep rupture test at 700°C 100MPa

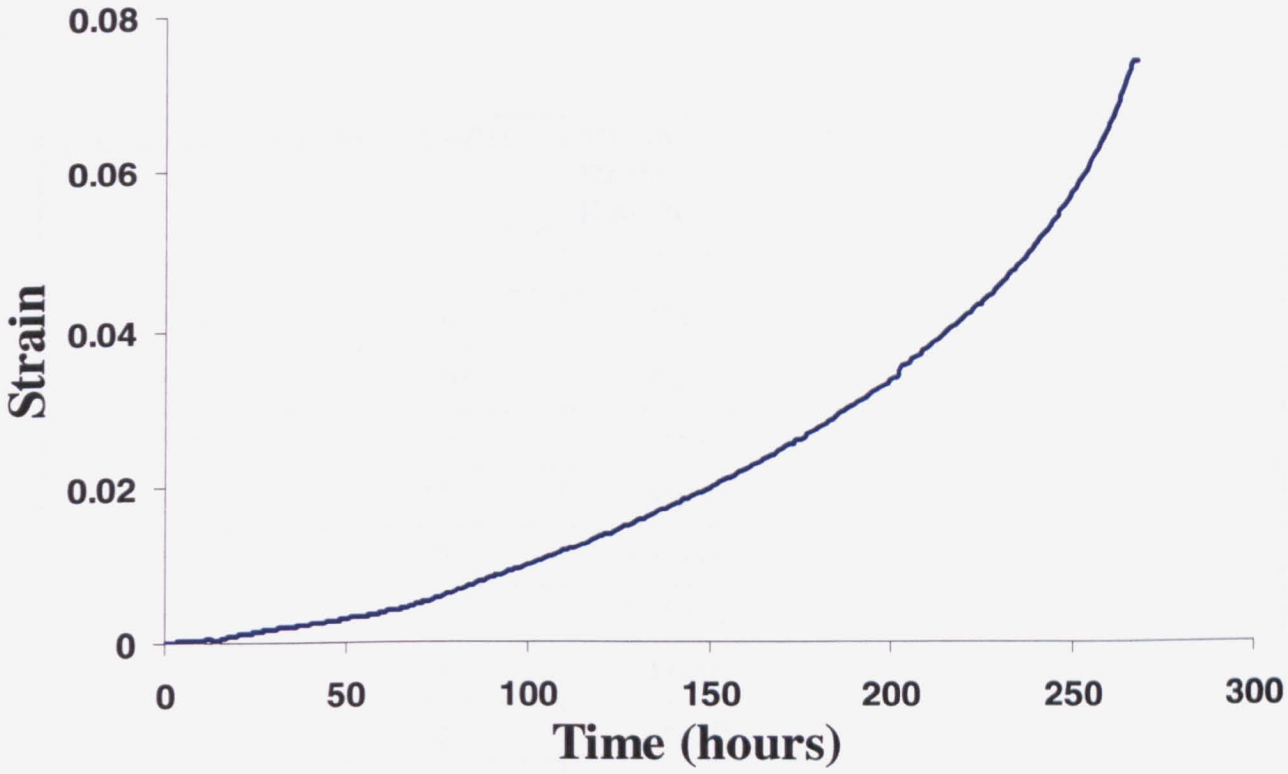

Fig. 4.15 Creep rupture test conducted at 750°C 100MPa

Temperature(°C)	Stress(MPa)	Minimum Strain Rate(/h)	Time to Failure(h)	Rupture Strain (%)
650	160	1.19×10^{-5}	1398	7.183
650	180	3.25×10^{-5}	560	6.95
650	180	4.96×10^{-5}	481	8.8
650	200	1.23×10^{-5}	611	2.68
650	220	1.62×10^{-4}	303	9.1
650	250	9.01×10^{-4}	26	15.43
550	335	1.71×10^{-5}	842	4.7
550	335	1.43×10^{-5}	1220	5.5
550	335	2.08×10^{-5}	747	2.3
600	230	5.02×10^{-7}	-	-
600	250	8.29×10^{-6}	-	-
700	100	1.81×10^{-5}	1637	11.5
700	150	1.08×10^{-4}	151	16.7
700	200	2.93×10^{-3}	50	21
750	100	1.52×10^{-4}	260	14.2
750	150	4.10×10^{-3}	68	17.3
750	200	1.23×10^{-2}	36	23.1
800	100	2.01×10^{-3}	105	12.4
800	150	1.22×10^{-2}	40	19.4
800	200	2.05×10^{-1}	24	28.2

Table 4.5 Summary of creep rupture data

Creep data can also be represented in other ways. Common ways include plotting time to rupture against stress for each particular temperature. This is shown in Fig. 4.16. A change in the gradient in any particular data can mean a change in creep deformation mechanisms. Rupture strain values do not differ greatly amongst the data (Fig. 4.17). Fig. 4.18 shows the strain rate against the applied stress for each temperature.

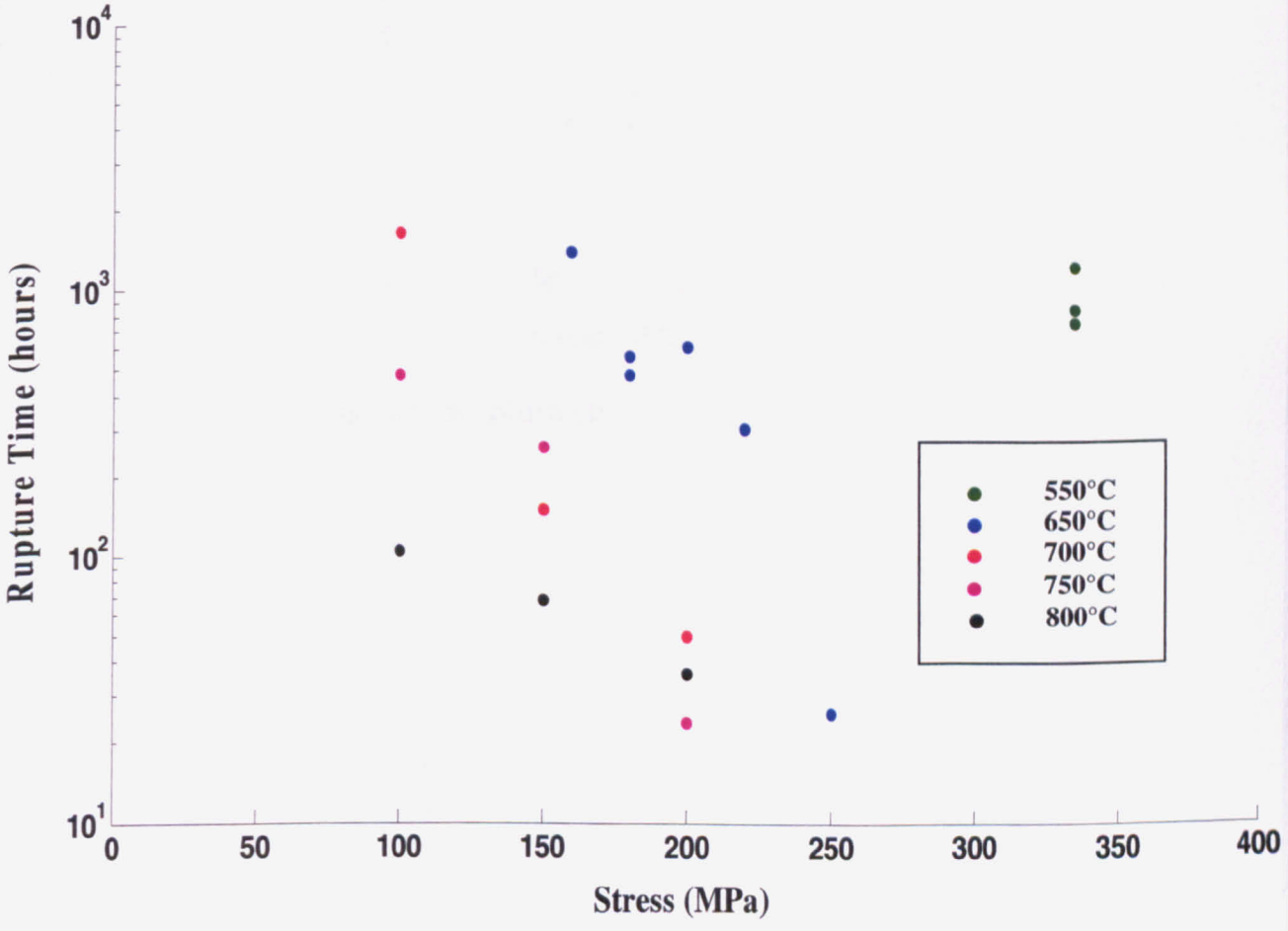

Fig. 4.16 Rupture time vs. applied stress

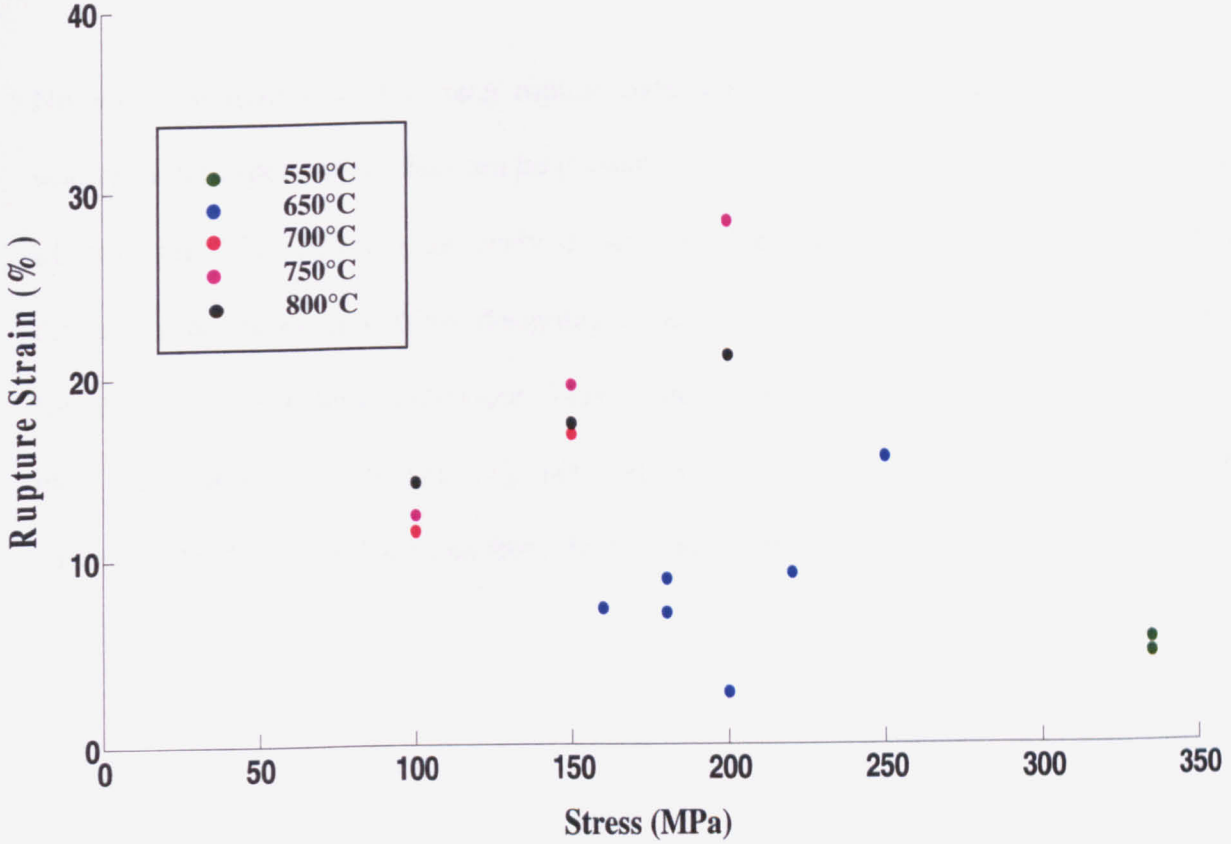

Fig. 4.17 Rupture strain vs. applied stress

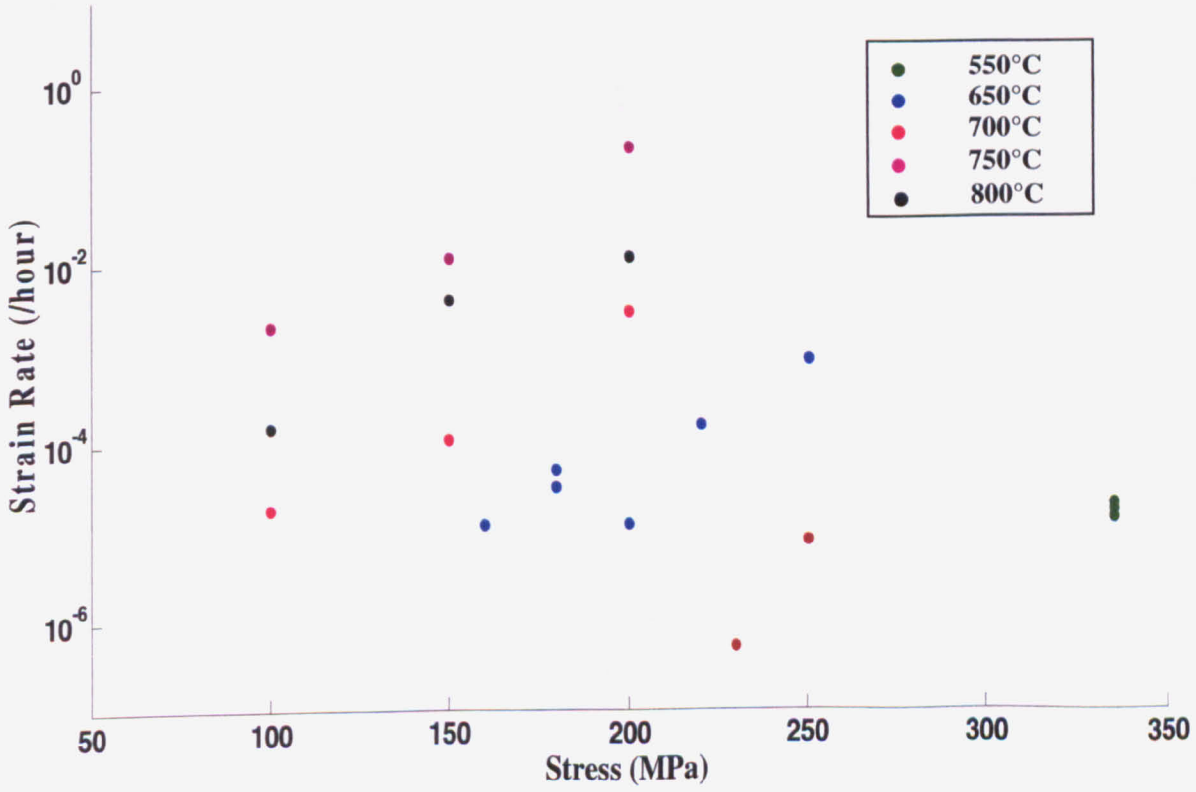

Fig. 4.18 Minimum strain rate vs. Applied stress

4.4.3 Comparison of Data Obtained with data from External Sources

Numerous sources exist for creep rupture data. However for the same material, a large scatter in the experimental data can be present. Scatter can also exist within the same stock of material. The different as-received bars obtained might themselves have slightly different creep properties. When designing a component, a safety factor is given to account for the scatter in material behaviour. This section compares some of the data obtained to data from other sources [6], [7], [8], [9]. Fig. 4.19 shows the comparison of the experimental data with databases from the National Institute of Material Science, Japan.

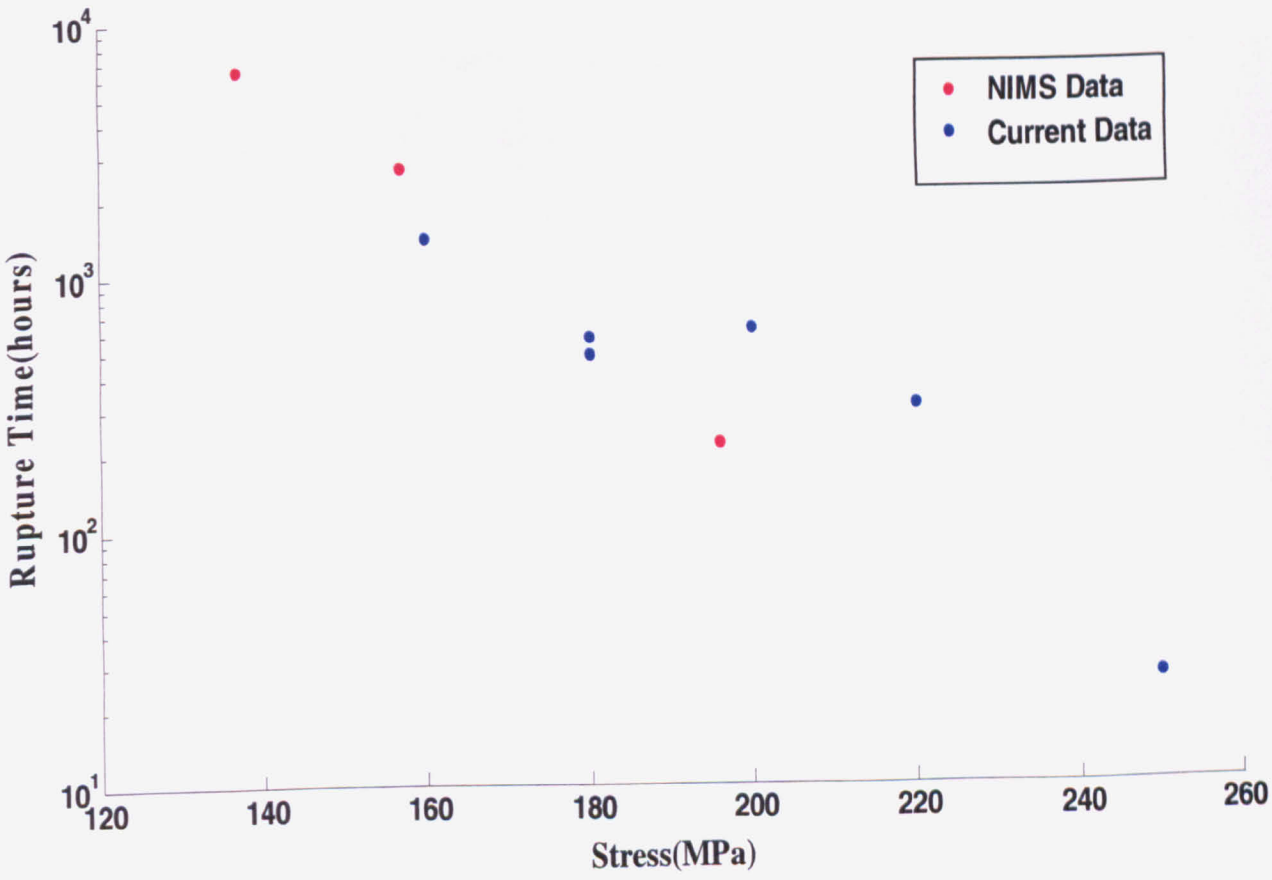

Fig. 4.19 Comparison of rupture times with external data at 650°C

The data obtained in these tests match relatively well with data from other sources.

4.5 Conclusions

- Material characterisation of as received AISI 316H steel was conducted.
- Grain size calculations have shown that the average grain size is around 60 microns.
- Tensile testing of the material was conducted. Room temperature yield strength (0.2%) was 220MPa. Elevated tensile tests concluded yield strength at 550°C is 120MPa and 110MPa at 650°C.
- Creep rupture tests were performed at 550°C, 600°C and 650°C. Referring to the creep deformation maps, it can be reasonably concluded that same creep deformation mechanisms are prevalent in most tests.
- Comparison with data from external sources showed that the data generated in these experiments showed good agreements.

References

[1] ASTM A240 / A240M - 09a Standard Specification for Chromium and Chromium-Nickel Stainless Steel Plate, Sheet, and Strip for Pressure Vessels and for General Applications.

[2] F. Nabarro and F.de Villiers, *Physics of Creep and Creep-resistant Alloys*, Taylor & Francis, 1995.

[3] H.Frost and M.Ashby, *Deformation-Mechanism Maps: The Plasticity and Creep of Metals and Ceramics*, Pergamon Press, 1982.

[4] Gittus, *Creep, Viscoelasticity, and creep fracture in solids*, 1984. Applied Science Publishers.

[5] ASTM E112 - 96(2004) e2 Standard Test Methods for Determining Average Grain Size.

[6] NIMS Data Sheets (6B) on the Elevated Temperature Properties of 18Cr-12Ni-Mo Stainless Steel for Boiler and Heat Exchanger Seamless Tubes (SUS 316 HTB).

[7] NIMS Data Sheets on the Elevated Properties of 18Cr-12Ni-Mo Stainless Steel for Reactor Vessels (SUS316HP).

[8] NIMS Data Sheets on the Elevated Properties of 18Cr-12Ni-Mo Stainless Steel Bars for General Application (SUS 316-B).

[9] ECCC Creep Data Sheets 2005.

CHAPTER 5: LOAD-ON/LOAD-OFF TESTING

The major part of this study involves understanding the behaviour of structural materials under simulated operating conditions. Materials used in the construction of nuclear power plants see fluctuations in operating loads and temperature changes. If the material exhibits damage, it may have to be repaired using welding procedures, which can result in structural changes. All these factors can influence the behaviour of the material. The design codes used in power plants are generally based on data obtained by standard laboratory procedures. Some of the maintenance and assessment procedures are also based on such data. In some cases, material behaviour may be different to standard results. This generates the need to conduct tests which are better replicate in-service conditions.

5.1 Load Changes in Power Plants

Power plants are subject to load/temperature variations during their lifetime. The stress on a particular component will vary depending on the capacity of the power plant. It is extremely rare for a power plant to be run at its designed capacity throughout its lifetime. Nuclear power stations need to be shut down for long durations (>100 hours) for regular maintenance and also for refuelling depending on the design of the reactor. Sometimes, plants are operated at capacities much lower than their designed capacity in order to extend the life of the plant. All these factors will have an effect on the overall conditions a material experiences in-service. Since creep is very sensitive to temperature and stress, small and sudden changes in these can cause large fluctuations in the creep behaviour.

During a shut down, a material will effectively cycle between its designed load and zero (or a very low load). Temperature can also change from the operating range (>400°C) to room temperature. For a material experiencing creep, this would mean a change in the

creep mechanism. Referring to the creep deformation maps (sections 2.7 and 4.2.3), the dominant creep mechanism will change from power-law creep to diffusion creep when the material is unloaded. When reloaded back again, power law creep becomes the major mechanism. When the stress on the material is removed completely or partially, other mechanisms significantly influence the material characteristics. A phenomenon called anelasticity seems to greatly influence the material properties. Mechanical properties like creep life and ductility can show large deviations from uniaxial creep testing due to the unloading.

5.2 Introduction to Anelasticity

5.2.1 Definition and Calculation of Anelastic oStrain

Anelasticity can be defined as the time-dependent recovery of plastic s1train after unloading during a creep test. A strain curve for a creep test where the stress was unloaded is shown in Fig. 5.1. As shown in the figure, the stress was unloaded from an initial value σ to zero.

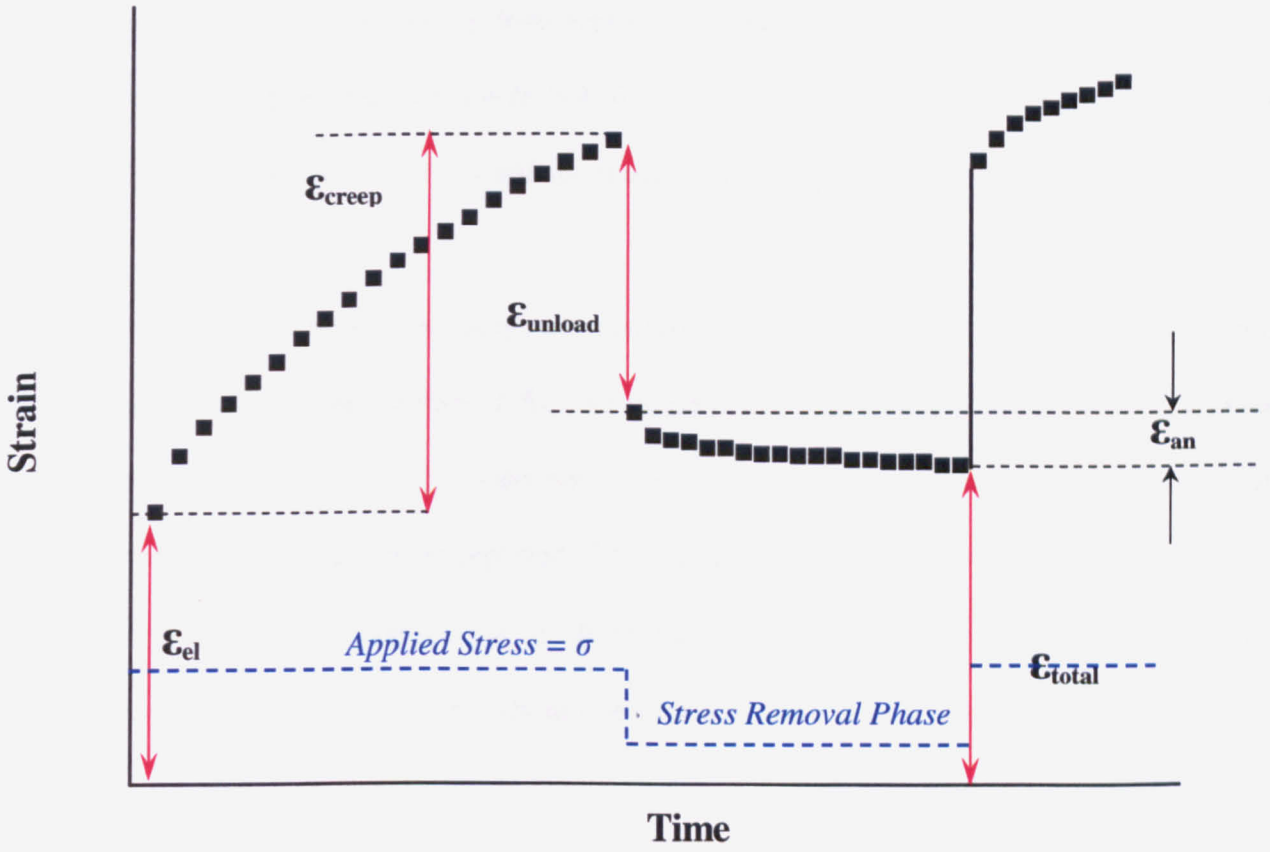

Fig. 5.1 Definition of anelasticity. The blue dotted lines represent the stress profile. Upon application of a stress, the sample starts to creep. When unloaded, some of the accumulated creep strain is recovered

When the load is initially applied during a creep test, there is an instantaneous elastic strain ε_{el}. The creep strain (ε_{creep}), which is a plastic strain, then starts to accumulate. When the specimen is unloaded, an instantaneous elastic strain can be observed (ε_{unload}). Following this, there is a recovery of plastic creep strain (net decrease in accumulated creep strain). This recovery is termed anelasticity (represented by ε_{an}). and results in a reduction of the total strain accumulated.

5.2.2 Load Drop Experiments on Metallic Materials

A number of studies involving load removals during creep have been carried out. These studies also propose mechanisms responsible for anelasticity. This section presents some of the work relevant to this project and the mechanisms proposed.

Time-dependent strain recovery of materials following stress reduction has been investigated by several authors [1-8]. The studies have been carried out on different classes of metals and non-metals [9]. Depending on the material under study, different levels of recoverable strain have been reported. The recoverable strain can reach values as high as 2–8 times the elastic contraction in aluminium [13], whereas they are equivalent to the elastic strain in copper, and only about one fourth of the elastic strain in lead [10].

Studies which have looked at material behaviour following stress reductions have proposed possible reasons for this occurrence. Dislocation behaviour will affect the deformation greatly. Interactions of dislocations with precipitates and other entities like grain boundaries and dislocation tangles will cause changes in the internal (intergranular) stress state. These changes will influence the effective backstress within the material which causes anelasticity. Theories have been proposed regarding the behaviour of dislocations and the evolution of the internal stress state in tests involving load reductions. Some of the important ones have been described in this section.

Gielbling and Nix [10, 11] have conducted several studies which involved stress reduction during creep of pure metals. The tests were conducted on pure aluminium, lead and copper. The aluminium samples were tested between 300°C and 400°C. Recovered strains were about 2-5 times the elastic strain. Copper was tested between 400°C and 600°C and recovered strains were almost equal to the elastic strain. For pure aluminium, the

recoverable anelastic strain increases with creep strain during primary creep. They have concluded that during primary creep, the dislocation substructure of most homogenous metals changes from a uniform distribution to a heterogeneous distribution. Development of heterogeneous dislocation substructures produces an inhomogeneous stress which can lead to anelasticity.

Pahutová and Čadek [7] conducted some experiments involving stress changes on α-zirconium. They observed anelastic strains equal to three times the elastic strains. The cause for forward creep after stress reduction is based on a creep model proposed by Mitra and Mclean [17]. The model is based on a three-dimensional dislocation network. The links of this network are of a subcritical length and bow under action of a stress. When the stress is removed, they unbow due to the dislocation line tension. This line tension can also bow the links in the opposite direction and contribute to backward strain. However, such a mechanism would require an incubation period. This has not been seen in most of the stress drop experiments. They also mention that anelasticity may consist of two mechanisms with sub-boundary 'dissolution' and migration connected with applied stress changes.

Mills [12] has also found anelastic behaviour in aluminium with 5.5%Mg. The tests were carried out at 300°C and 400°C with stresses ranging from 11.5MPa to 47.5MPa. The stresses were not unloaded completely. He mentions that dislocation flow is affected by an 'effective' stress which is the resultant arising from the applied and the internal stress. Structural inhomogeneities like dislocation networks and subgrains [18, 19] give rise to an inhomogeneous stress distribution [20]. If the observed negative straining were due to the action of an internal stress, this would mean the features responsible for this behaviour will have to undergo a reordering.

Lupinc and Gabrielli [8] have performed stress drop experiments on IN597 which is a Ni-Cr alloy. Tests were conducted at temperatures between 700°C-800°C. An initial stress of 200MPa was applied and specimens were unloaded to 5MPa. They found that immediately after unloading, a very fast anelastic contraction (about 10% of the total contraction) occurs and the rest of the anelastic contractions occur over a much longer time scale. They [11] have also proposed anelasticity may consist of two mechanisms. Their TEM observations showed no observations of subgrain boundaries. Dislocations were also seen to be bowed in equilibrium with the local stress. The dislocation-particle interactions were mainly dislocation climb or Orowan looping. They have proposed a model based on two deformation mechanisms- matrix glide and jog generation. Bueno [13] has also done stress drop experiments on RR-58 aluminium alloy where the specimens were unloaded completely. The tests were carried out at 180°C with stresses ranging from 120-230MPa. He has also reported strains recovered are equivalent to about twice the elastic strain. His argument is based on the work done by Lupinc and explains that there may only be one mechanism for anelasticity but this may consist of two stages. The first is an initial stage where the pinned dislocation unbows quickly as soon as the specimen is unloaded. This rate would depend on the precipitation distribution within the material. The second stage is a slower process where the material tries to reach an equilibrium state. The length of the dislocations will affect such mechanisms. Dislocation link lengths will vary greatly within a material and the link lengths will depend on precipitate density and distribution. Lupinc also suggests that if the ratio of link length to radius of curvature when it is bent is less than 0.3, this will causes a faster contraction. Theoretical dislocation line tension models can explain such contractions. Features such as grain boundaries and dislocation interactions have generally been neglected in the explanations given for anelasticity. These features will inherently affect the internal stress state, thus causing changes in the recovered strain. Gibbons et al. [23, 24] have conducted stress drop experiments on Ni and

Ni-Cr alloys. Their experiments involved pre-straining to develop a substructure and then testing at a lower stress where forward creep is negligible. They have concluded that the backflow mechanism involves viscous bowing and unbowing aided by unzipping of network modes.

Morris [14], [16] has conducted several tests involving unloading of creep specimens on AISI 316 steel. Tests were done at a temperature of 625°C with stresses varying from 200-290MPa. He has also observed that recoverable strain was greater during primary creep and attributes this to the increased number of mobile dislocations. He explains that the effective stress present during dislocation bowing is in the range of 0.75-1.25 σ (σ being the applied external stress). This result confirms that dislocation bowing is controlled by a stress close to the applied stress. He also states that the magnitude of frictional stress (backstress) is small compared to applied stresses. Tests were also done on pre-crept materials where the stress dependence of the creep rate of pre-crept materials was analysed. For all tests, he observed the apparent internal stress is lower for applied stresses below the original pre-creep stress. He further comments that the main impact due to the carbides present will be with regards to the network spacing. The frictional stress contribution from the carbides is small.

In the study conducted, he has used trapezoidal waveforms as shown in Fig. 5.2. Tests were conducted at a temperature of 625°C. When this is compared to results presented in this chapter, there are similarities in the trends observed. Reduction is strain rate due to the unloading is seen along with some extension in the creep life. A summary of the results from his work is presented in Table 5.1. However, where the work presented in this study differs from reported work is the extended load/unload time. The time a material spends on load is more representative of loading conditions seen in power plants. Tests have also

shown that in some cycles it takes about 4-5 hours for the material to reach secondary creep after being reloaded. Thus it is necessary to give it sufficient time so that secondary creep is fully reached before unloading. The application of extended loading time also means that creep strain accumulation is higher when it is unloaded compared to results reported in [14, 16]. This may explain some of the variations observed.

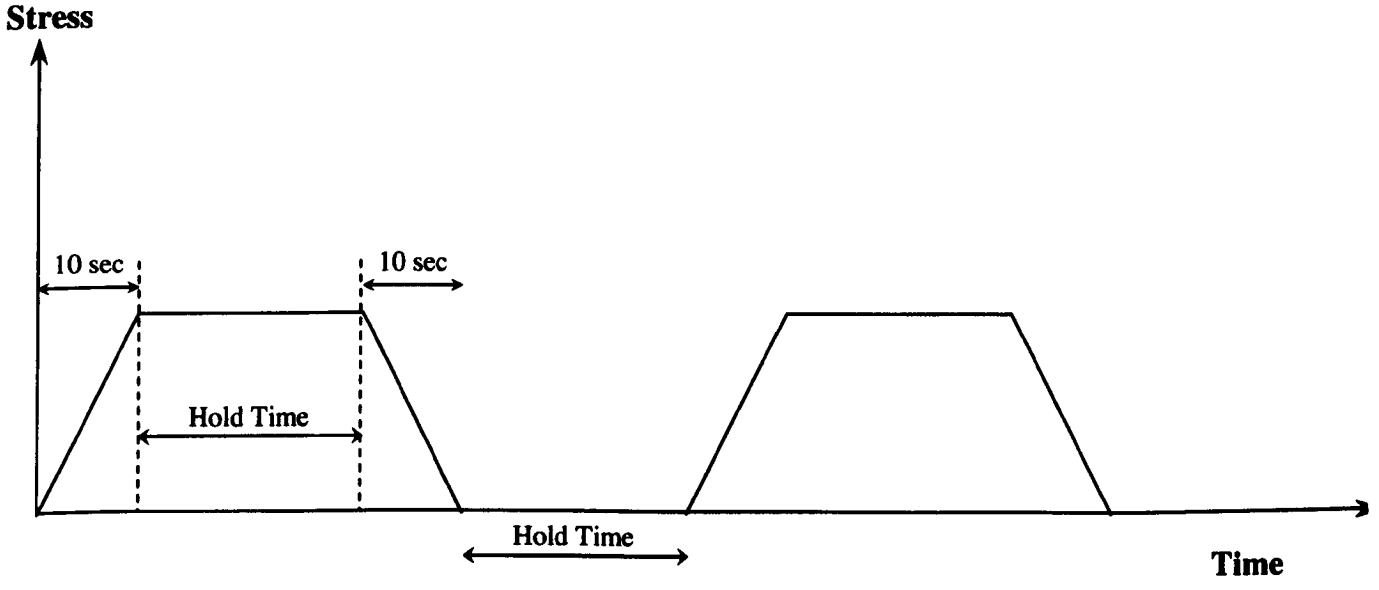

Fig. 5.2 Stress profile used in [14, 16]

Hold Period	Stress(MPa)	Creep Rate (/hour)	Anelastic Creep Rate (/sec)	Time on Load (hours)	Ductility	No. of Cycles
Creep Rupture	290	1.02×10^{-2}	-	17	0.55	-
Creep Rupture	250	2.3×10^{-3}	-	70	0.60	-
Creep Rupture	230	9.1×10^{-4}	-	150	0.60	-
Creep Rupture	200	2.5×10^{-4}	-	750	0.70	-
30 sec	290	9.0×10^{-03}	3×10^{-7}	24	0.65	2900
6 hours	250	3.60×10^{-03}	8×10^{-7}	65	0.80	11
1 hour	250	4.32×10^{-03}	7×10^{-7}	47	0.7	47
6 min	250	4.32×10^{-03}	1.5×10^{-7}	55	0.7	550
30 sec	250	9.36×10^{-04}	3×10^{-8}	150	0.7	18000
5 sec	250	7.20×10^{-04}	-	200	0.7	144000
6 min	230	9.36×10^{-04}	4×10^{-9}	200	0.65	2000
30 sec	230	2.16×10^{-04}	6×10^{-9}	700	0.7	84000
168 h	200	2.34×10^{-04}	6×10^{-8}	830	0.7	5
24 h	200	2.34×10^{-04}	6×10^{-8}	850	0.7	35

Table 5.1 Summary of results from [14, 16]

Sawada et al. [21], [22] have performed stress drop experiments on martensitic steels and have also observed anelasticity. They reported results from tests conducted at 700°C. Loads applied were between 100-180MPa. Comparing anelastic behaviour of steels with different carbides in it, he concluded that anelasticity originates from the martensitic lath structure. The dislocation cell structure observed seems to be independent of the presence of a high dislocation density, precipitates or solute atoms.

The remainder of this chapter presents some of the experimental results obtained from tests which involved unloading/ reloading during creep tests. Mechanisms responsible for anelasticity were investigated using electron microscopy and neutron diffraction techniques. These are reported in later chapters.

5.3 Description of Test Programme

As mentioned previously, one of the main aims of the study was to characterise material behaviour during in-service creep conditions. The formation of the test programme for this purpose involved:

- Selection of appropriate test conditions (stress and temperature) that would enable the material to experience creep mechanisms similar to that in practical situations. In most industrial situations, material creep behaviour can be classified under power-law creep.
- Test conditions which would enable the study to be finished in a reasonable duration of time.
- Appropriate load and unload periods.

From the information obtained from tensile testing and also other project partners, two sets of conditions were chosen: 650°C with a stress of 180MPa and 550°C with a stress of 335MPa. For these conditions, appropriate load and unload times had to be chosen. The specimens were loaded for a minimum of 48 hours before unloading to ensure they reached a steady state before reloading back. The unloading periods chosen were 48 hours, 4 hours and 5 seconds. Most of the testing was done using either a 48 hour unload or a 5 second unload.

Unloading can involve removal of stress and/or temperature. Tests were conducted with both these situations. It was important to understand the role of stress on material behaviour. Stress removal would influence the dislocation motion significantly. The influence of temperature removal could then be added. Table 5.3 presents the entire test matrix.

Shut downs in power plants occur infrequently. The material can hence see varying amounts of creep damage before an unload occurs. Two time periods were chosen (48 hours and 170 hours) for the on-load period to account for the varying creep damage that can occur. The stress profiles used for the tests have been shown below.

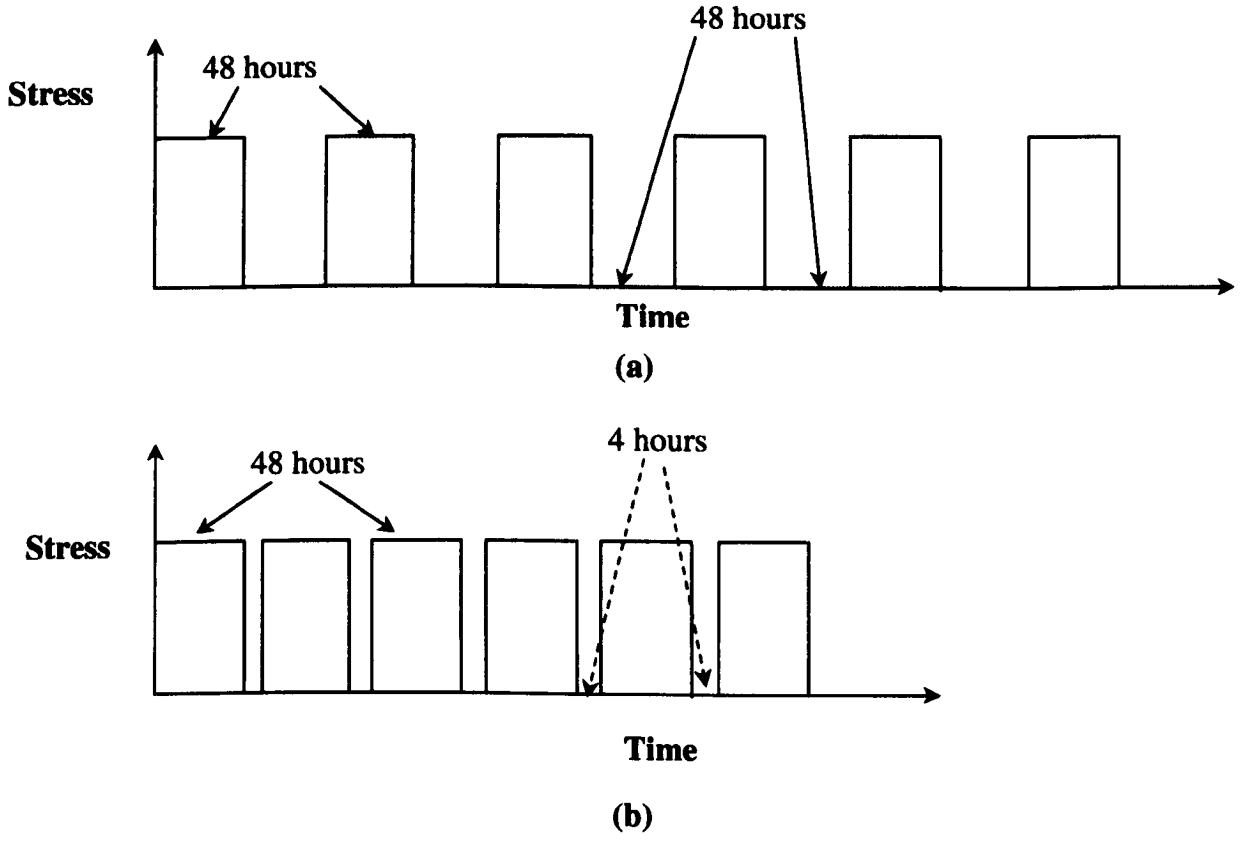

Fig. 5.3 Examples of stress profiles used (a) Load for 48 hours and unload for 48 hours (b) Load for 48 hours and unload for 4 hours

5.4 Experimental Results

This section presents strain curves which were obtained when the loads were removed and reapplied during a creep test. Before applying a load, the temperature was allowed to stabilise to within ±3°C of the test temperature. An initial load of 100 N was applied on the lever arm after which the lever arm was allowed to stabilise using the limit switches. The remaining load was applied after this procedure. Recording of strain was done at intervals of 1 minute for the first 6 hours and then once every 10 minutes. Before unloading, the sampling rate was again changed to 1 minute and changed to 10 minutes

Test Identifier	Test Temperature(°C)	Applied Stress (MPa)	On Load Time (hours)	Off Load Time	Temperature Removal	Stress Removal
1(a)	650	180	48	48 hours	No	Yes
1(b)	650	180	48	4 hours	No	Yes
1(c)	650	180	48	5 seconds	No	Yes
1(d)	650	180	48	48 hours	Yes	Yes
2(a)	650	180	170	48 hours	No	Yes
2(b)	650	180	170	5 seconds	No	Yes
2(c)	650	180	170	48 hours	Yes	Yes
3(a)	550	335	48	48 hours	No	Yes
3(b)	550	335	48	4 hours	No	Yes
3(c)	550	335	48	5 seconds	No	Yes
4(a)	550	335	170	48 hours	No	Yes
4(b)	550	335	170	5 seconds	No	Yes
4(c)	550	335	170	48	Yes	Yes

Table 5.2 List of test conditions

after 1 hour of unload. However, in tests which involved removal of load for 5 seconds, strain was recorded every second for 1 minute during the unload/reload procedure.

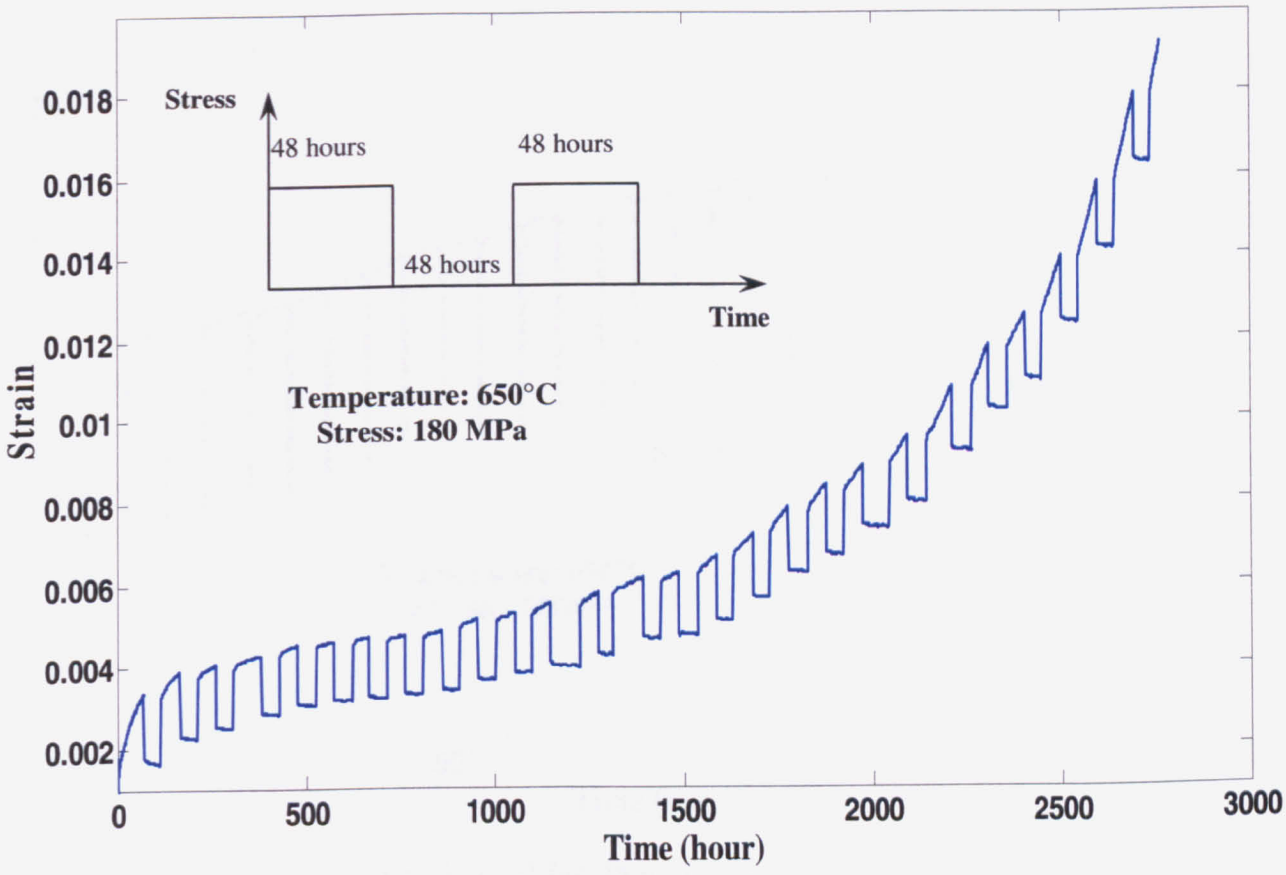

Fig. 5.4 Sample was loaded for 48 hours and unloaded for 48 hours

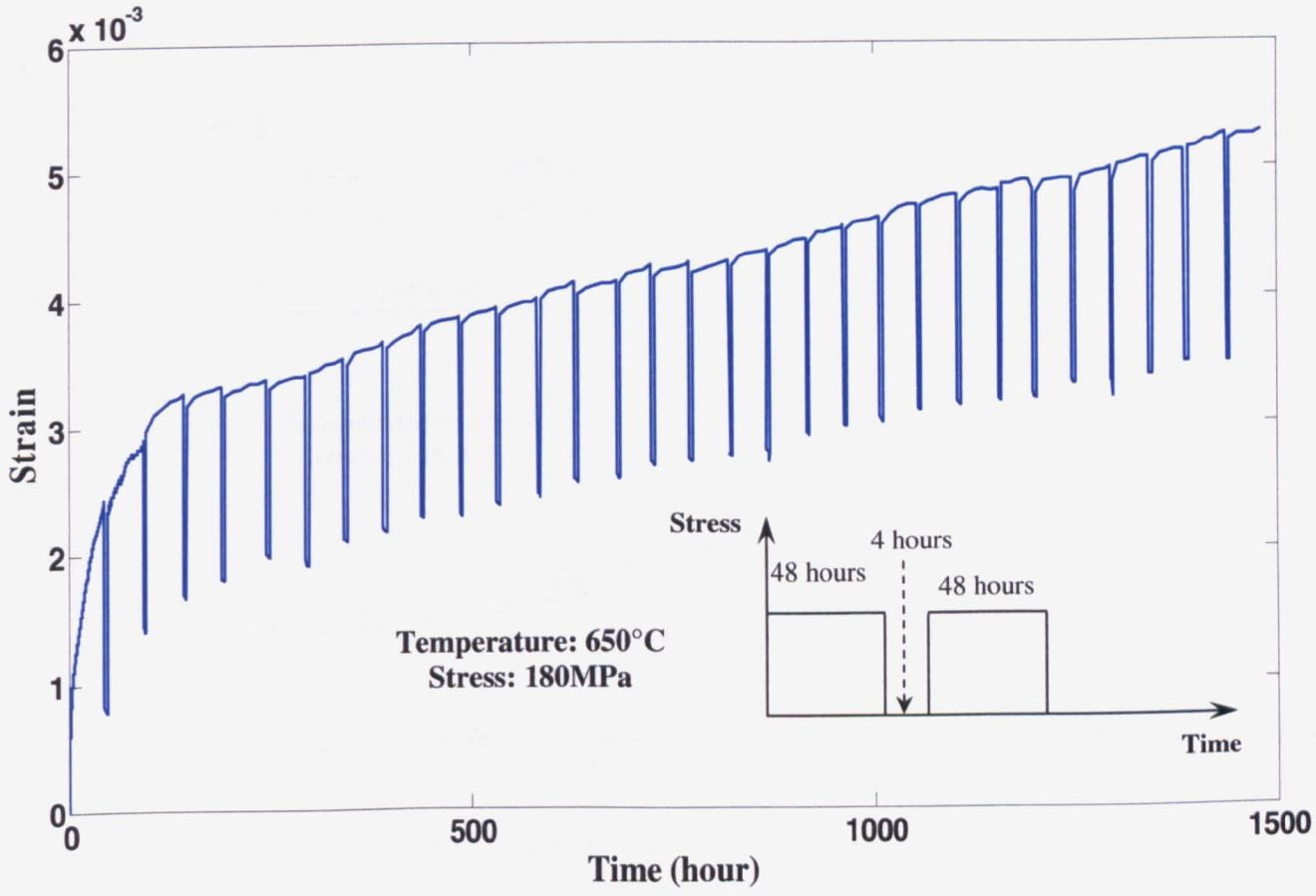

Fig. 5.5 Sample was loaded for 48 hours and unloaded for 4 hours. Test stopped after 30 unload cycles

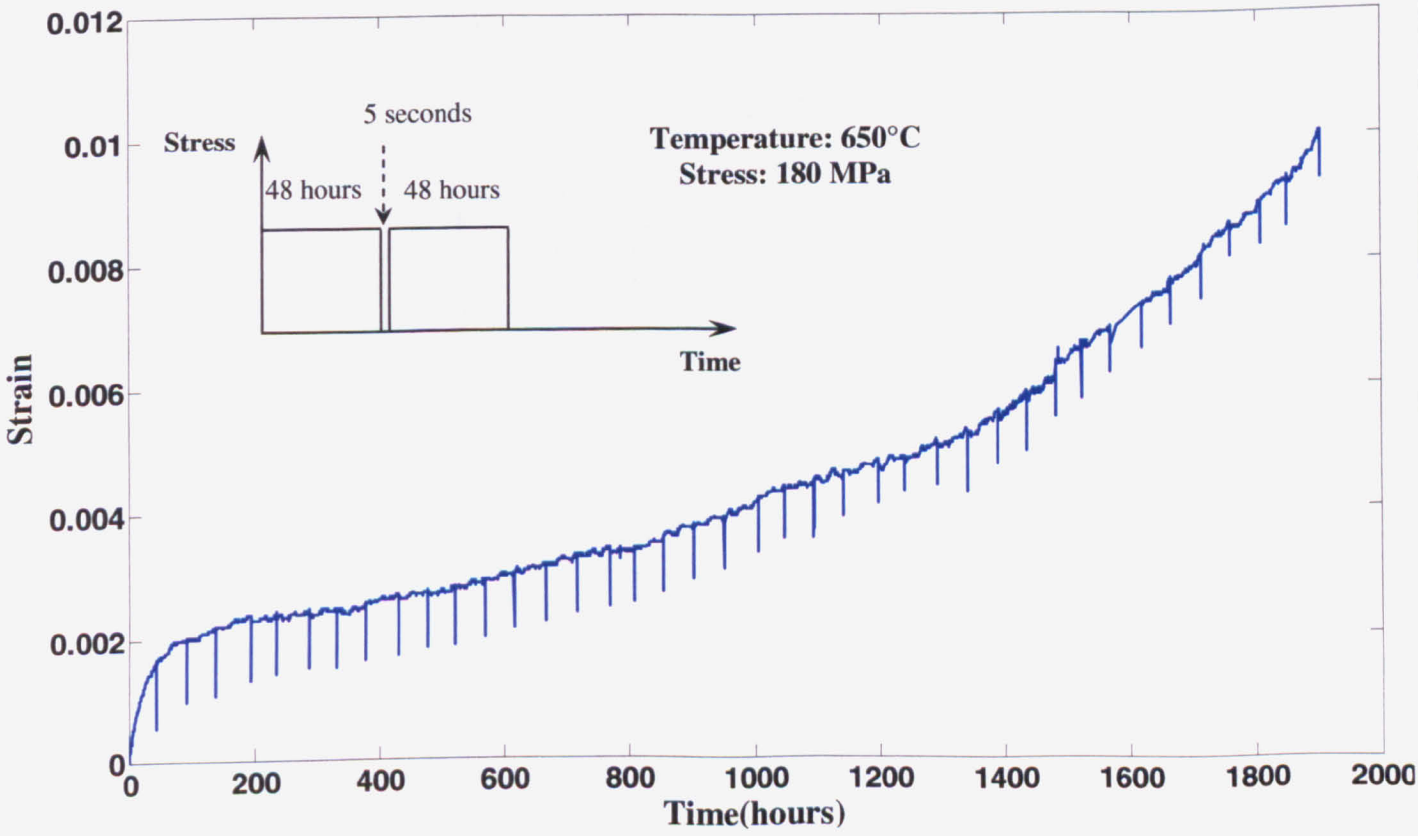

Fig. 5.6 Sample was loaded for 48 hours and unloaded for 5 seconds

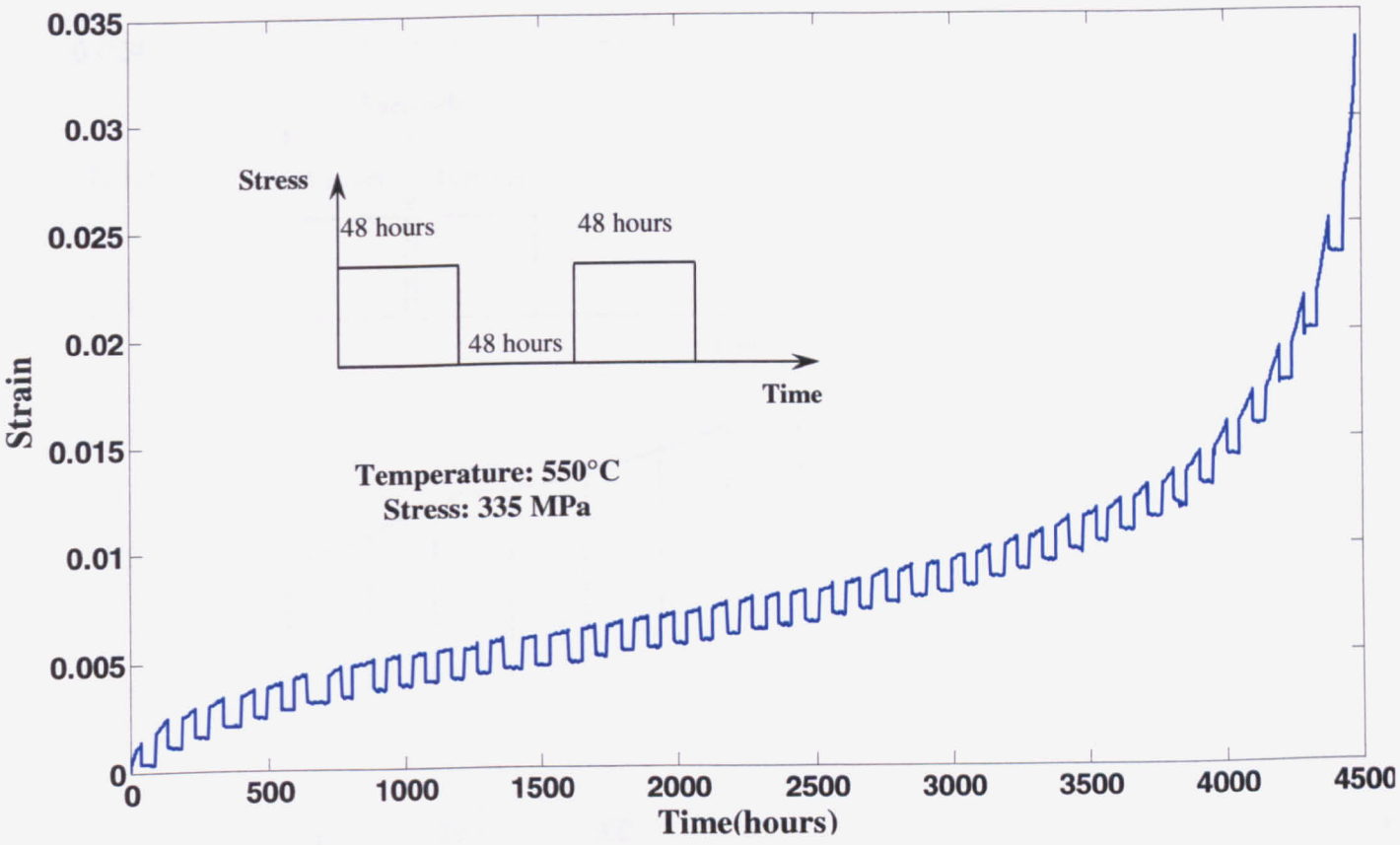

Fig. 5.7 Sample was loaded for 48 hours and unloaded for 48 hours.

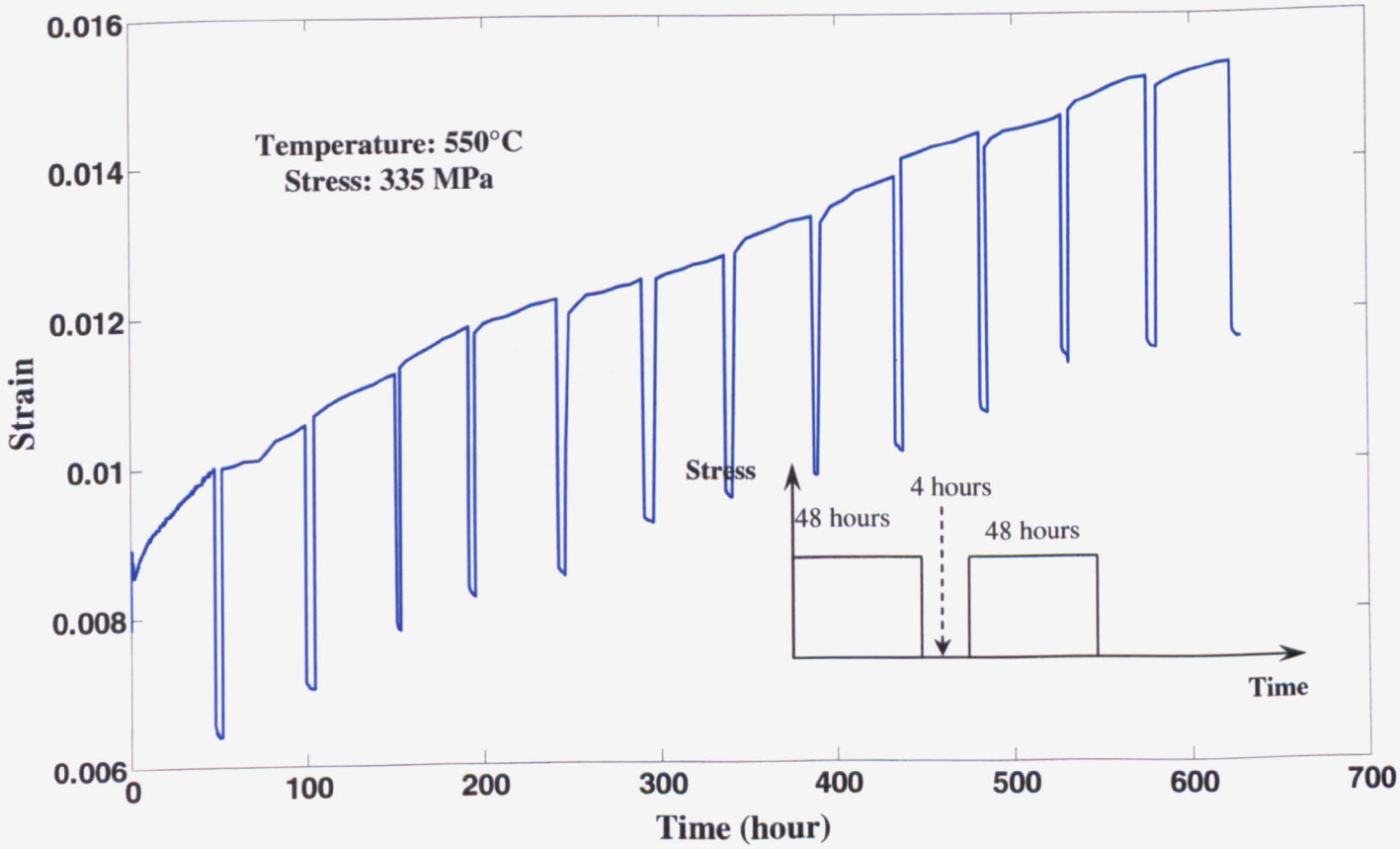

Fig. 5.8 Sample was loaded for 48 hours and unloaded for 4 hours. Test stopped after 12 unload cycles

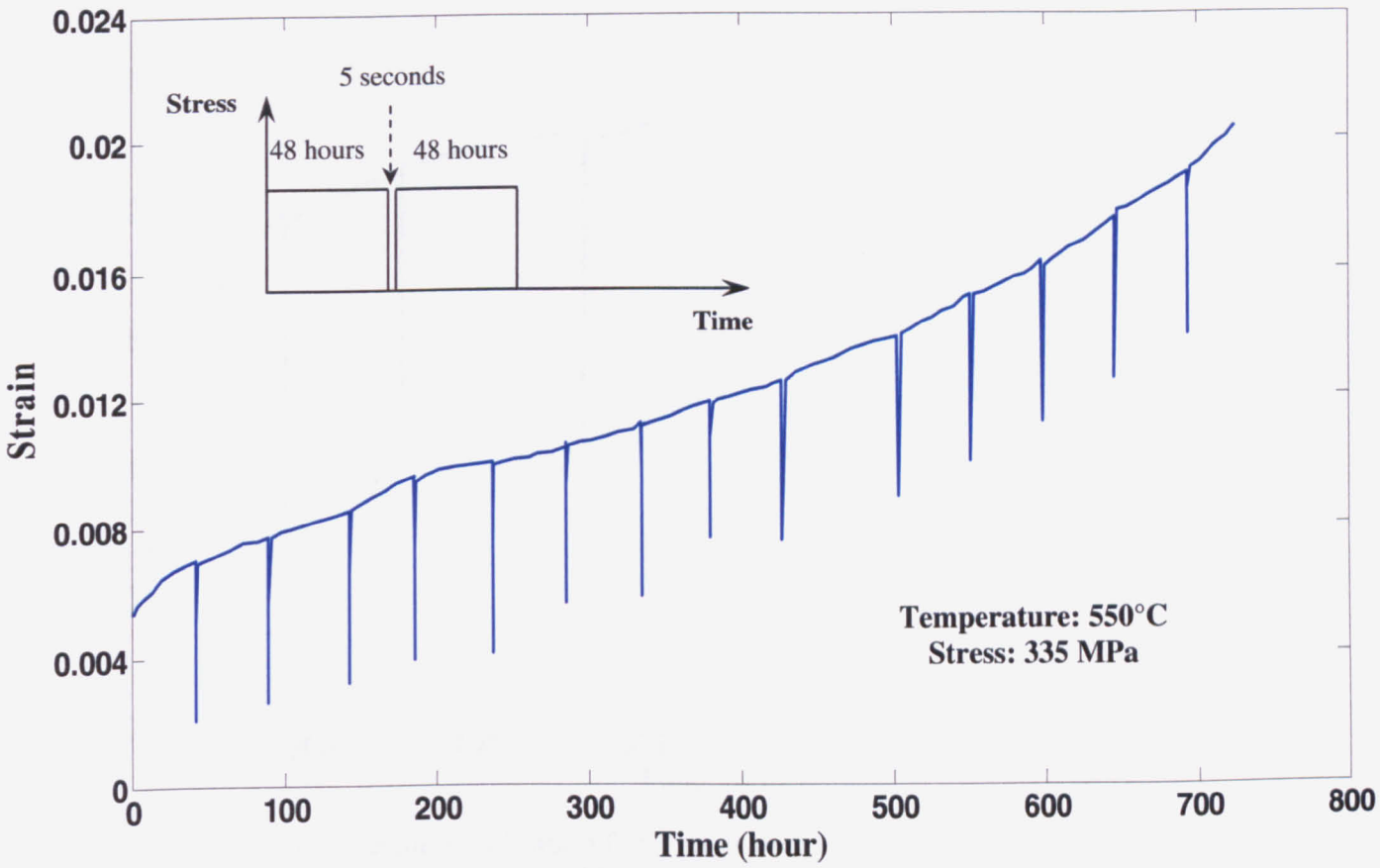

Fig. 5.9 Sample was loaded for 48 hours and unloaded for 5 seconds.

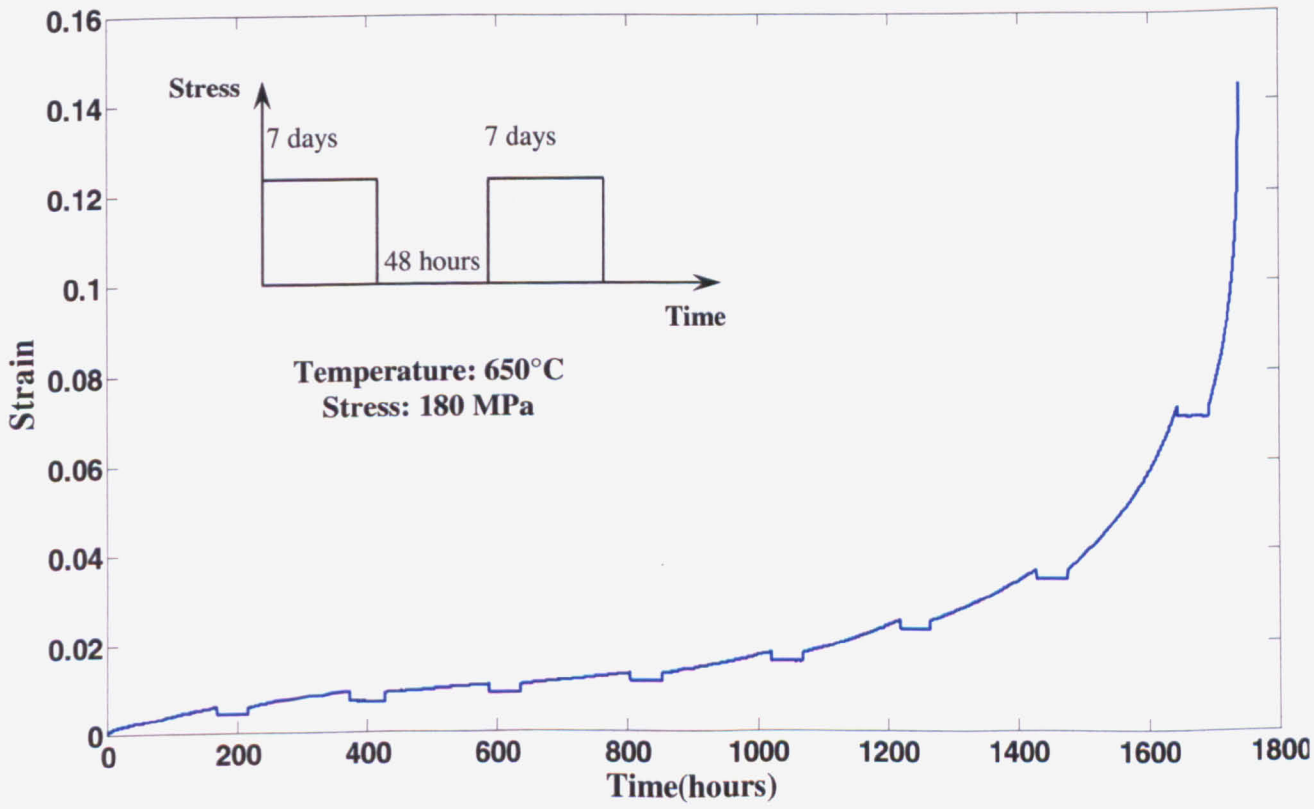

Fig. 5.10 Sample was loaded for 7 days and unloaded for 48 hours.

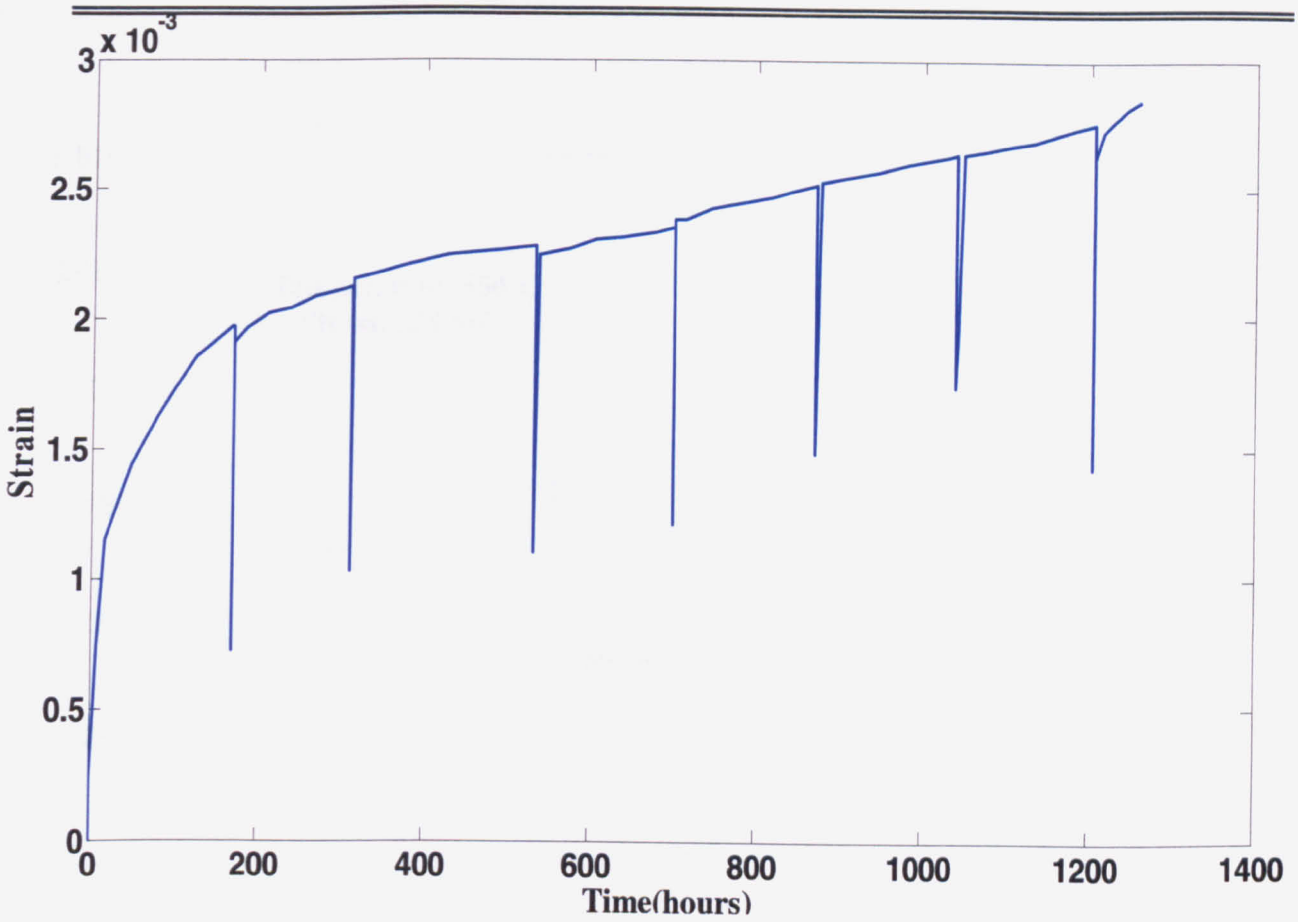

Fig. 5.11 Sample was loaded for 7 days and unloaded for 5 seconds. Test was stopped after 1200 hours due to temperature instability

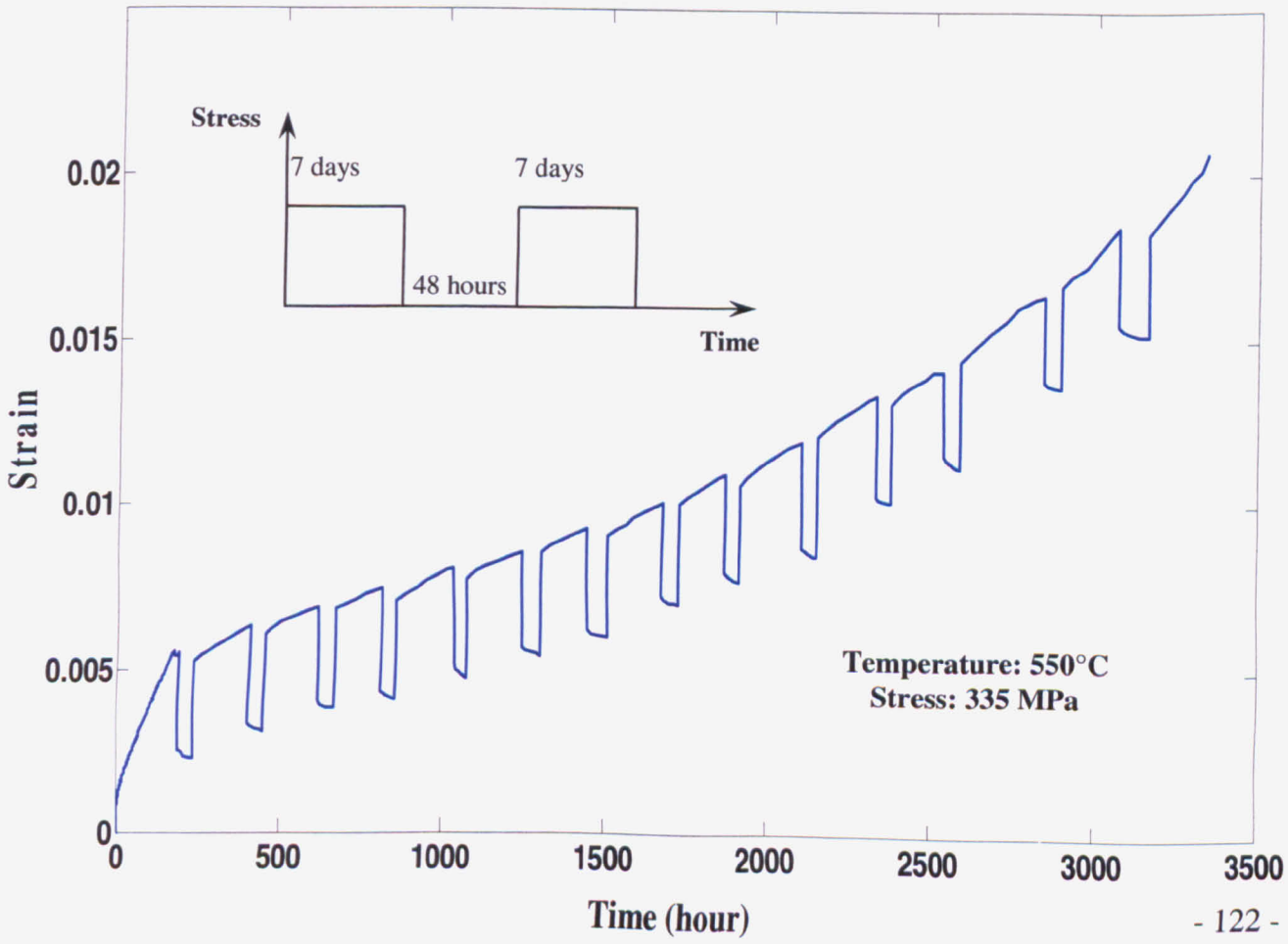

Fig. 5.12 Sample was loaded for 7 days and unloaded for 48 hours

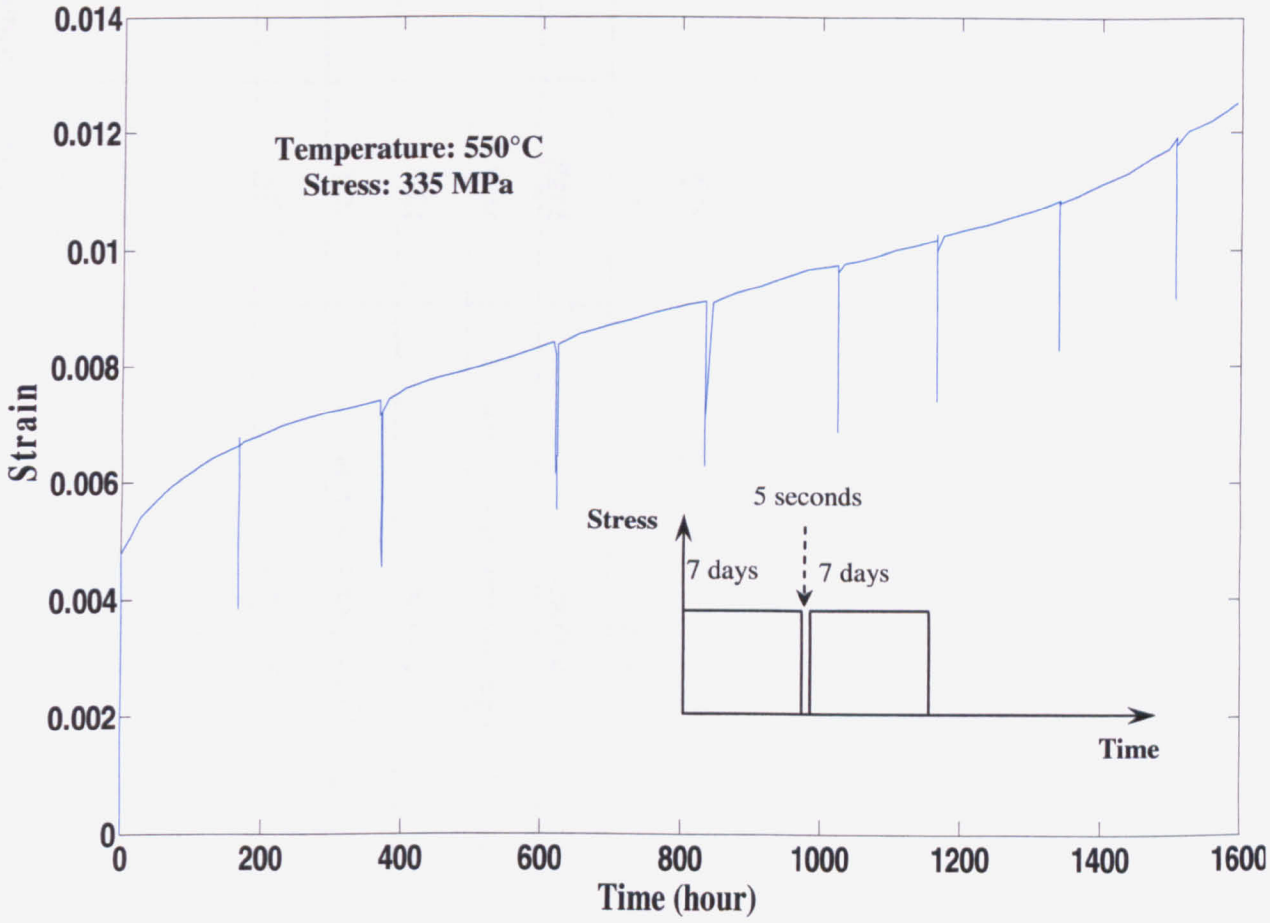

Fig. 5.13 Sample was loaded for 7 days and unloaded for 5 seconds

Test Identifier	Number of Load/Unload Cycles	Test Duration(hours)	Status	Rupture Time(hours)	Rupture Strain (%)
1(a)	27	2764	Ruptured	1410	2.20
1(b)	30	1500	Test Stopped after 30 cycles	N.A	N.A
1(c)	40	2051	Ruptured	2045.2	1.25
1(d)	35	3500	Test Stopped after 35 cycles	N.A	N.A
2(a)	8	1738	Ruptured	1027	7.7
2(b)	7	1260	Test stopped due to temperature instability	N.A	N.A
2(c)	15	3326	Ruptured	2788	5.52
3(a)	45	4485	Ruptured	2221	3.31
3(b)	13	635	Stopped after 13 cycles	N.A	N.A
3(c)	15	740	Ruptured	737.3	1.45
4(a)	14	3330	Stopped after 14 cycles	3405	2.10
4(b)	8	1617	Ruptured	1620	1.23
4(c)	14	3120	Stopped after 14 cycles	N.A	N.A

Table 5.3 Summary of load-on/load off testing

It is evident the material behaviour is different to the standard creep rupture testing presented in section 4.4.2. A few observations were made from the data obtained.

- Initially upon loading, the sample undergoes creep deformation.
- Upon unloading/reloading, an instantaneous elastic strain reduction/increase occurs.
- During the unload period, a plastic strain recovery (anelasticity) can be observed. This phenomenon has been seen in all the tests which involved unloading. Examples are shown in Fig. 5.14.
- In some tests following reloading, there was a small amount of primary creep behaviour. This was mostly observed if the unload occurred during primary creep. Test results shown in Fig. 5.4 and 5.7 shows some evidence of primary creep behaviour after reloading.

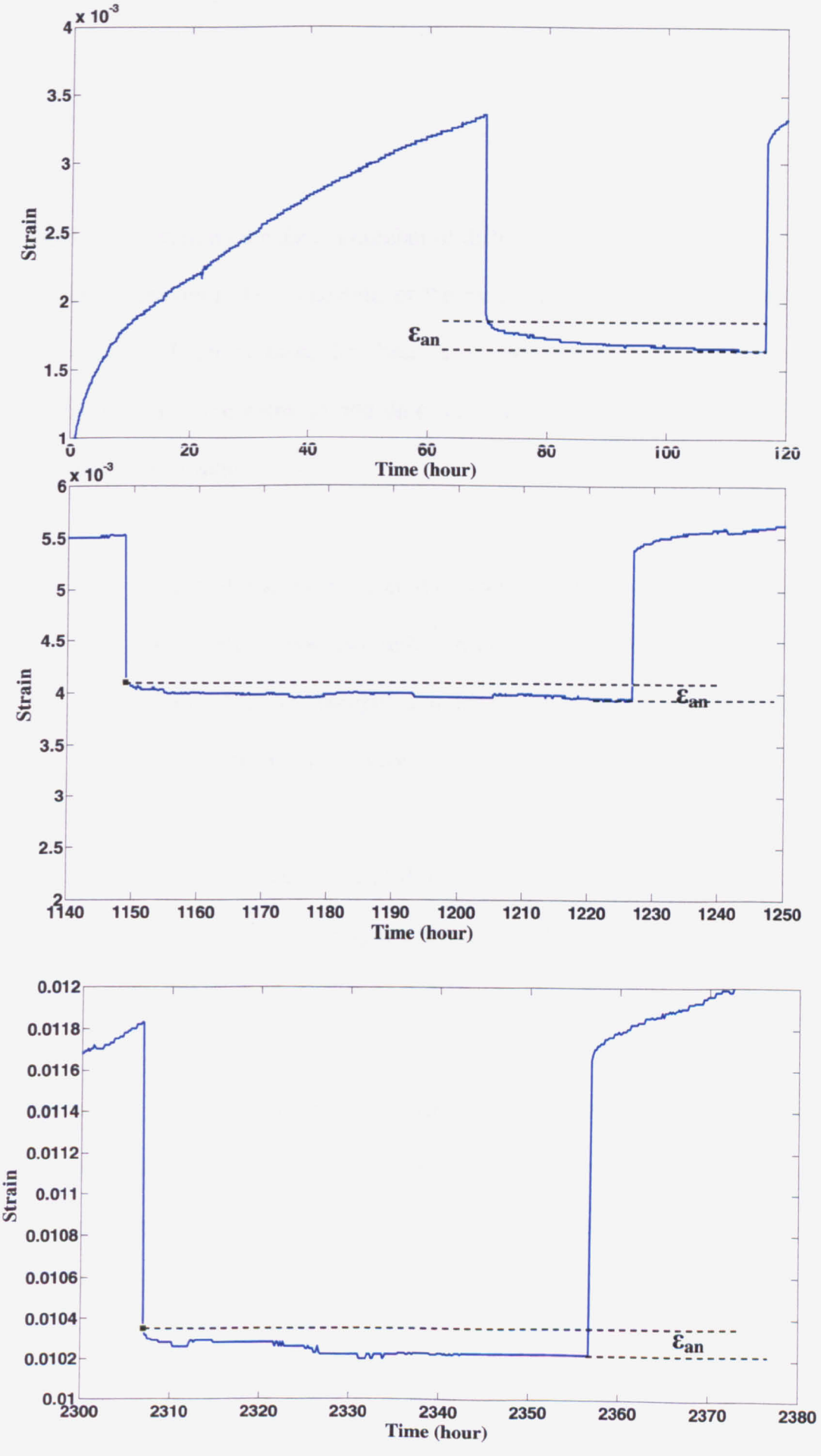

Fig. 5.14 Examples of creep strain recovery during the unload. Fig. 5.4 gives the complete strain curve of the experiment

Further to obtaining the data, a number of different analyses can be done to understand the material behaviour. The behaviour of the material involves both the loading part and the unload part. Each of these has been analysed separately. From the loading part, the following data were gathered and they were compared with the results obtained from the standard creep rupture tests:

- The total sum of the time the material spent under load was computed. Strain rates, rupture time and rupture strain were calculated from these curves.
- Strain rates were computed at different intervals. This enables finding the onset of the different creep stages.

From the unload part of curves, the following data were calculated:

- Variations in the magnitude of anelastic strain with number of load/unload cycles.

Anelasticity may be caused by more than one mechanism. It is also possible that different mechanisms may initiate at different times during the unload. It was also important to understand the effect of accumulated creep strain on anelastic behaviour as well as the role of temperature.

5.5 Calculation of Load Times

For all the load-up/load down tests conducted, it was necessary to calculate the response of the material when it was under load. Fig. 5.15 shows the method of calculating this.

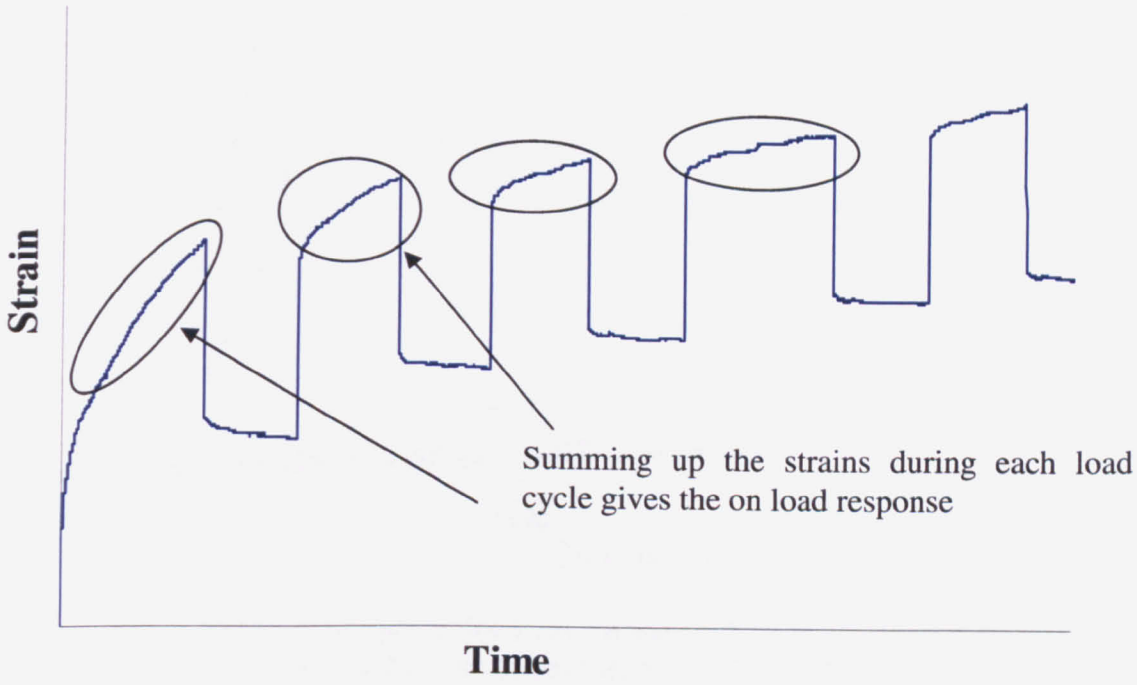

Fig. 5.15 Calculating on-load curves

Such calculations were done for all the tests. Fig. 5.16-5.19 shows the curves for the test matrix presented in Table 5.3. Uniaxial steady load curves have also been plotted for comparison.

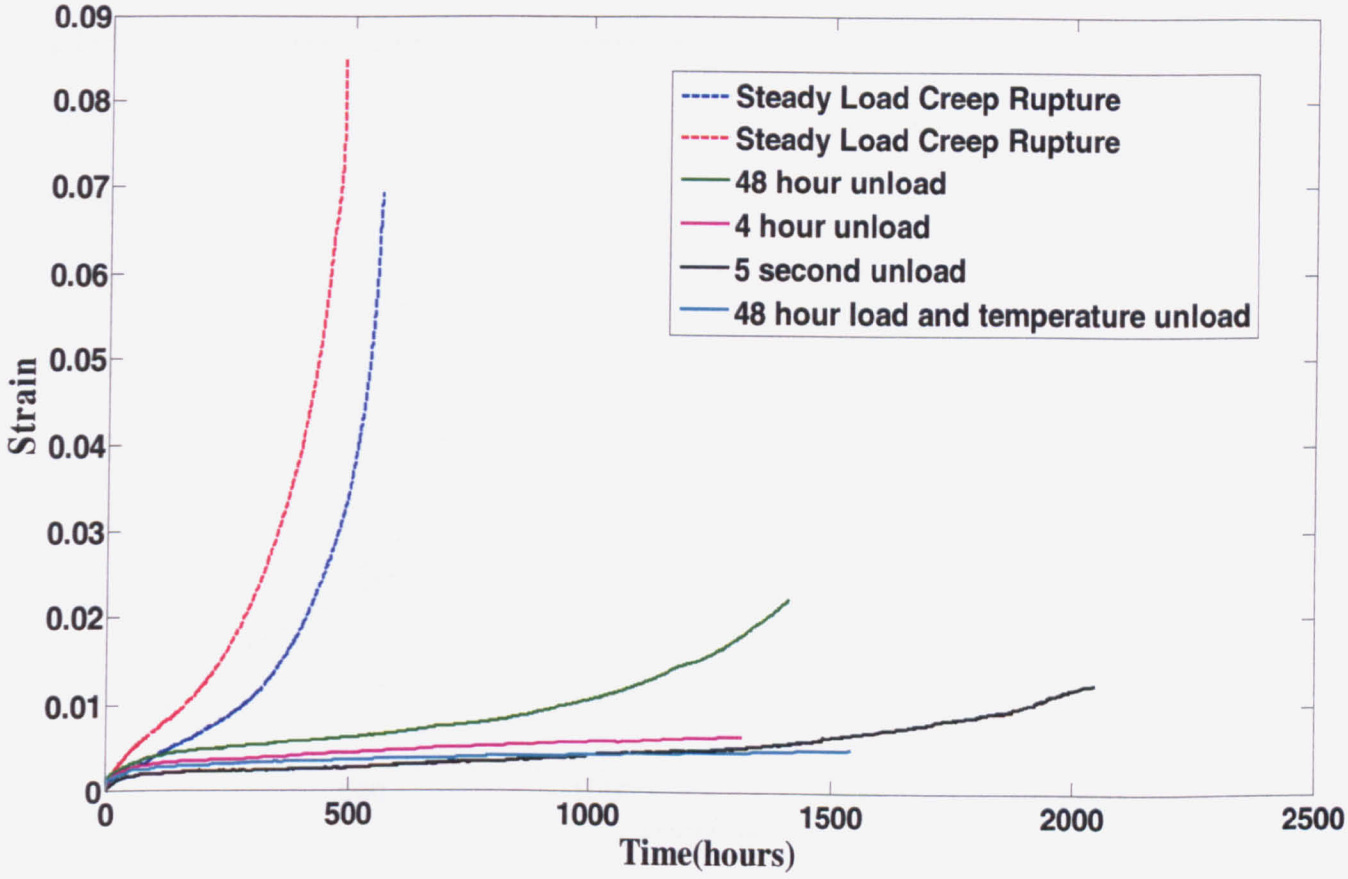

Fig. 5.16 On-load curves for load-on/load-off tests conducted at 650°C. Loads were applied on the sample for 48 hours before unloading

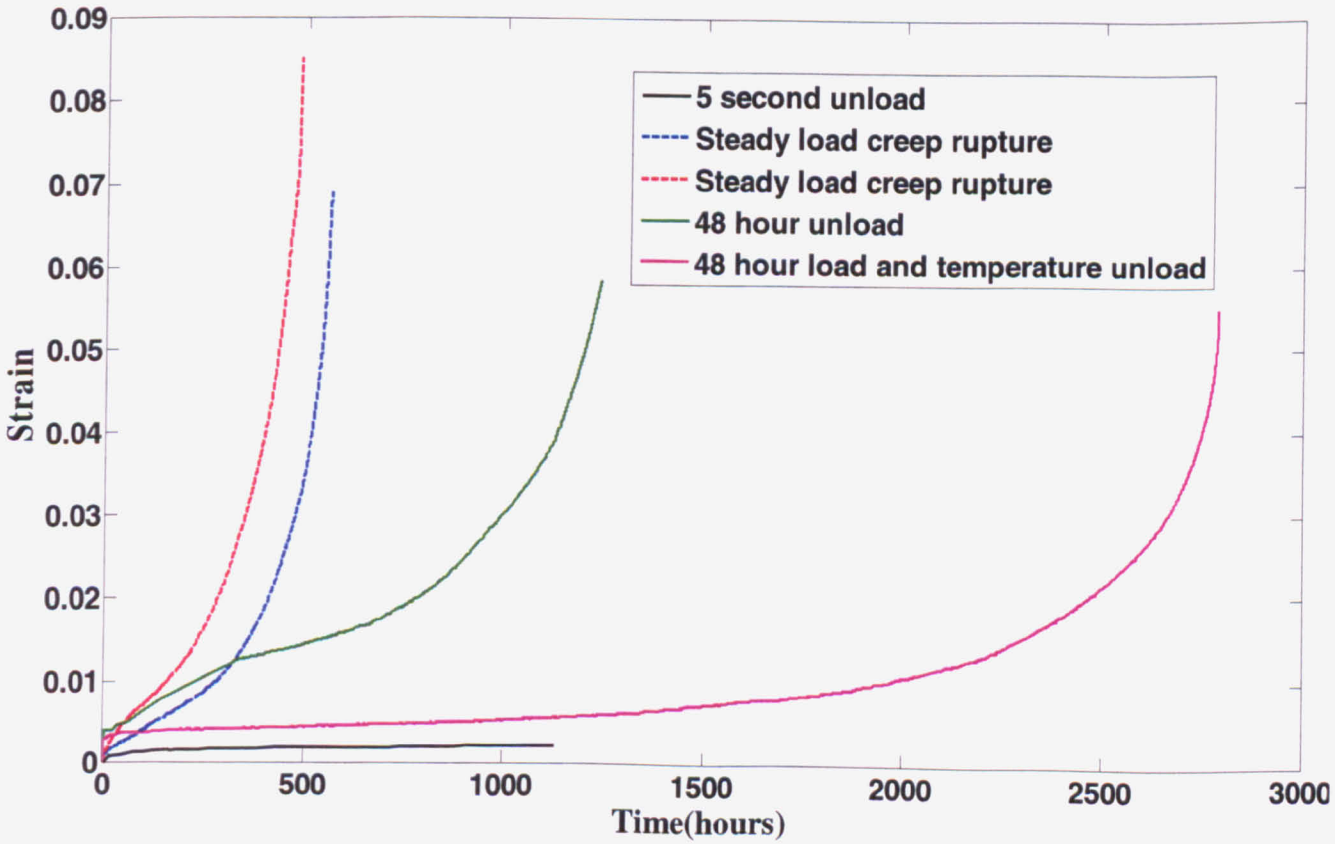

Fig. 5.17 On-load curves for load-on/load-off tests conducted at 650°C. Loads were applied on the sample for 170 hours before unloading

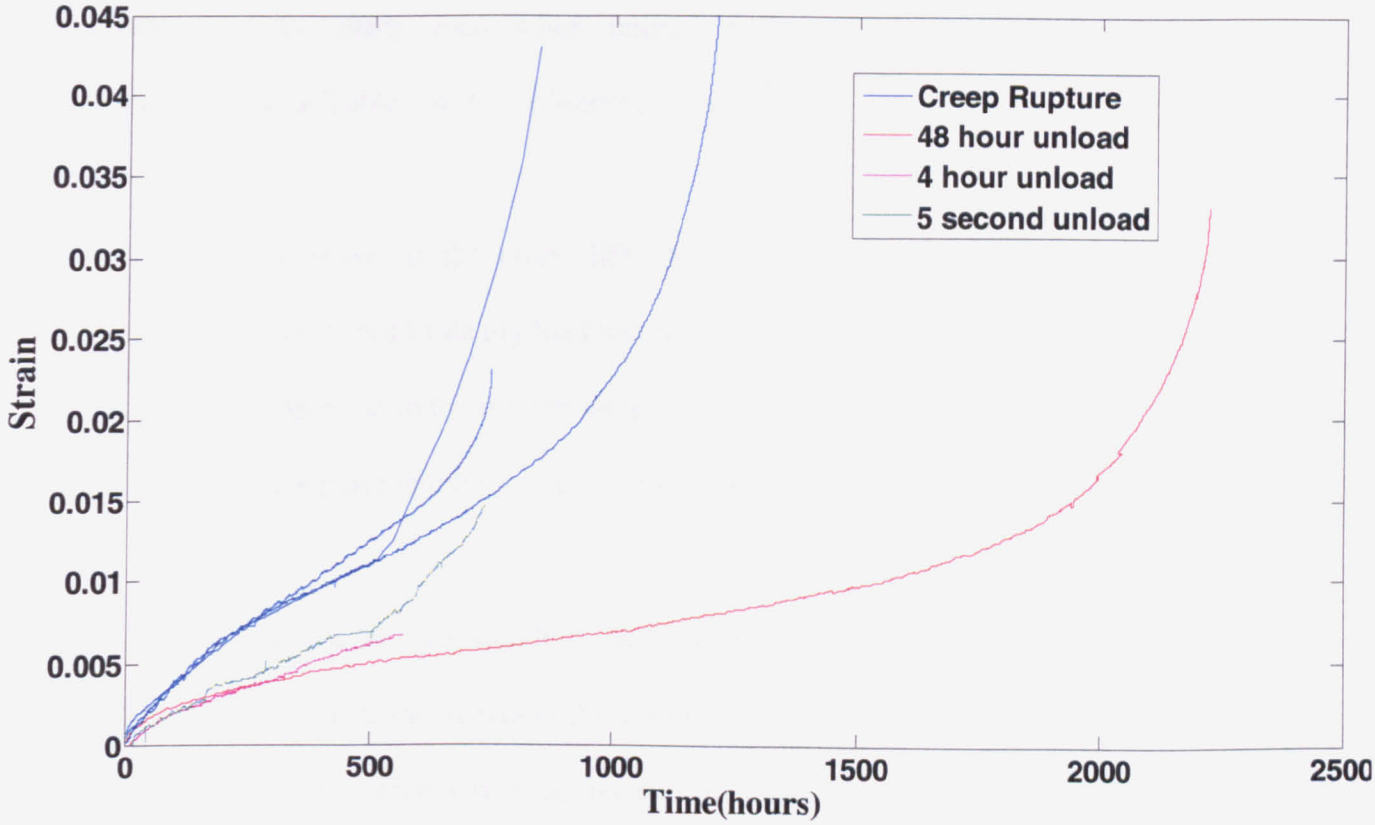

Fig. 5.18 On-load curves for load-on/load-off tests conducted at 550°C. Loads were applied on the sample for 48 hours before unloading

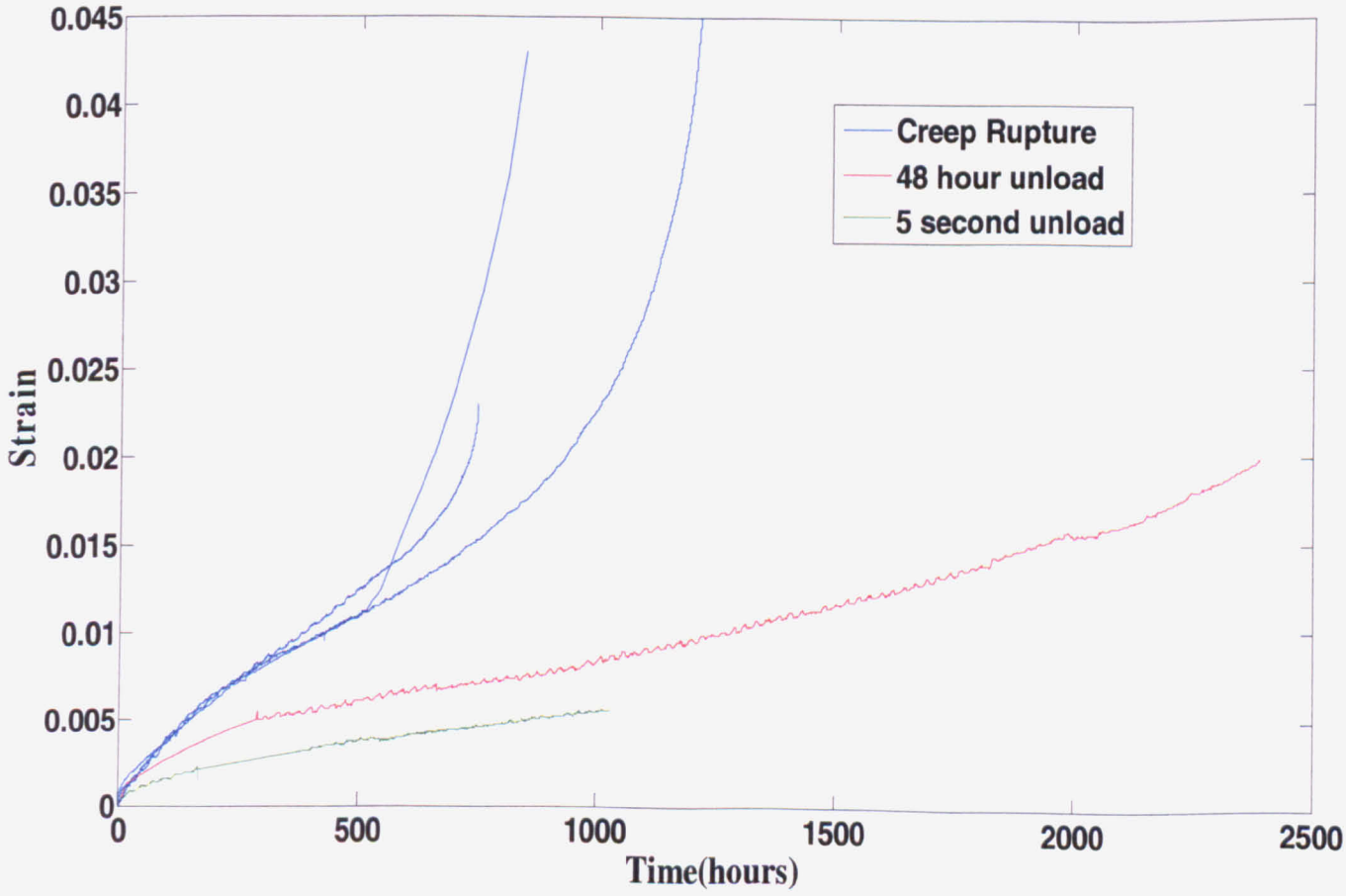

Fig. 5.19 On-load curves for load-on/load-off tests conducted at 550°C. Loads were applied on the sample for 170 hours before unloading

As seen in the graphs, the material response during load has changed significantly compared to steady load when unload cycles are introduced. Results have been summarised in Table 5.4. Key observations were:

- Increase of the creep life. An increase of 2-3 times has been seen when compared to steady load results.
- Decrease in the rupture ductility by about 50%.
- Decrease in the minimum strain rate by a factor of ten.

In order to assist in understanding the prevalent mechanisms, further analysis was done. These involved looking at where the different stages of creep initiate, the amount of time each test took to reach a particular strain or the strain after a set number of hours.

Test Identifier	Rupture Time(hours)	Rupture Strain (%)	Minimum Creep Rate(/hour)
1(a)	1410	2.2	5.08e-6
1(b)	NA	N.A.	3.02e-6
1(c)	2045	1.25	2.71e-6
1(d)	NA	N.A.	1.35e-6
2(a)	1027	7.72	1.96e-5
2(b)	N.A	N.A.	6.68e-7
2(c)	2788	5.51	1.83e-6
3(a)	2221	0.033	3.68e-6
3(b)	NA	N.A.	9.97e-6
3(c)	737	1.4	1.41e-5
4(a)	NA	N.A.	5.57e-6
4(b)	1560	1.2	3.98e-6
4(c)	N.A	N.A.	3.17e-6

Table 5.4 Summary of on-load curves

5.5.1 Change in Strain Rate with Time

Changes in the strain rate can be observed during the different stages of creep. This section presents the evolution of strain rates in the load-on/load-off tests. The on-load curves shown in the previous section is used for this purpose. These calculations would enable finding out the amount of time the material spent in each stage of creep. By comparing this to the creep rupture data, any changes can be observed.

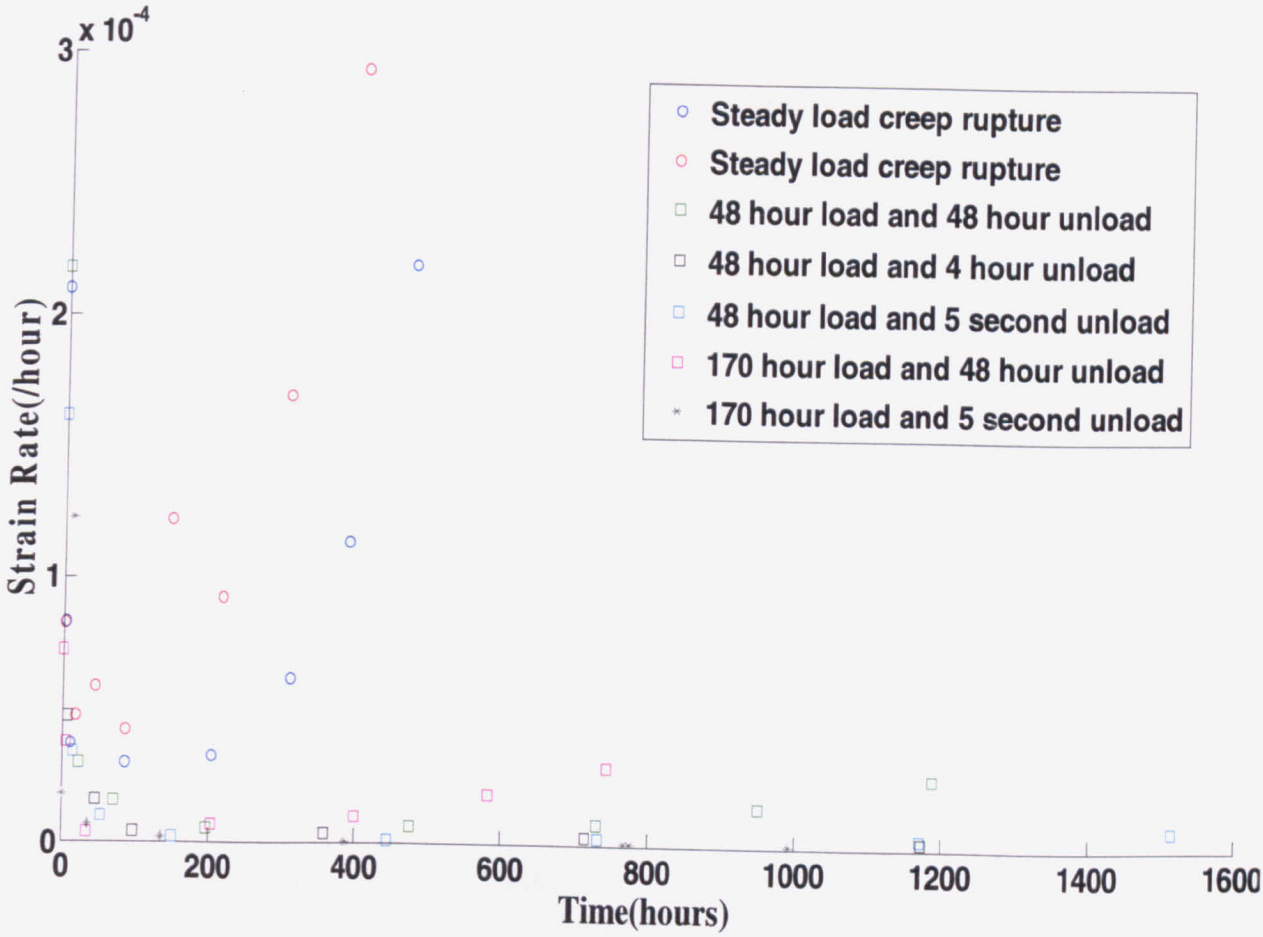

Fig. 5.20 Comparison of strain rates calculated from the 'on-load' curves at 650°C

Fig. 5.20 and 5.21 shows the change in strain rate which has been calculated from the 'on-load' curves. When compared to the 'on-load' curves, it can be seen that the behaviour of the secondary and the tertiary stages have been altered due to the unloading. The material spends a longer time in the secondary stage and also the acceleration in the tertiary stage is not as great of those of the creep rupture tests due to the loss in ductility. The amount of time spent in each stage was calculated as was the strain fraction.

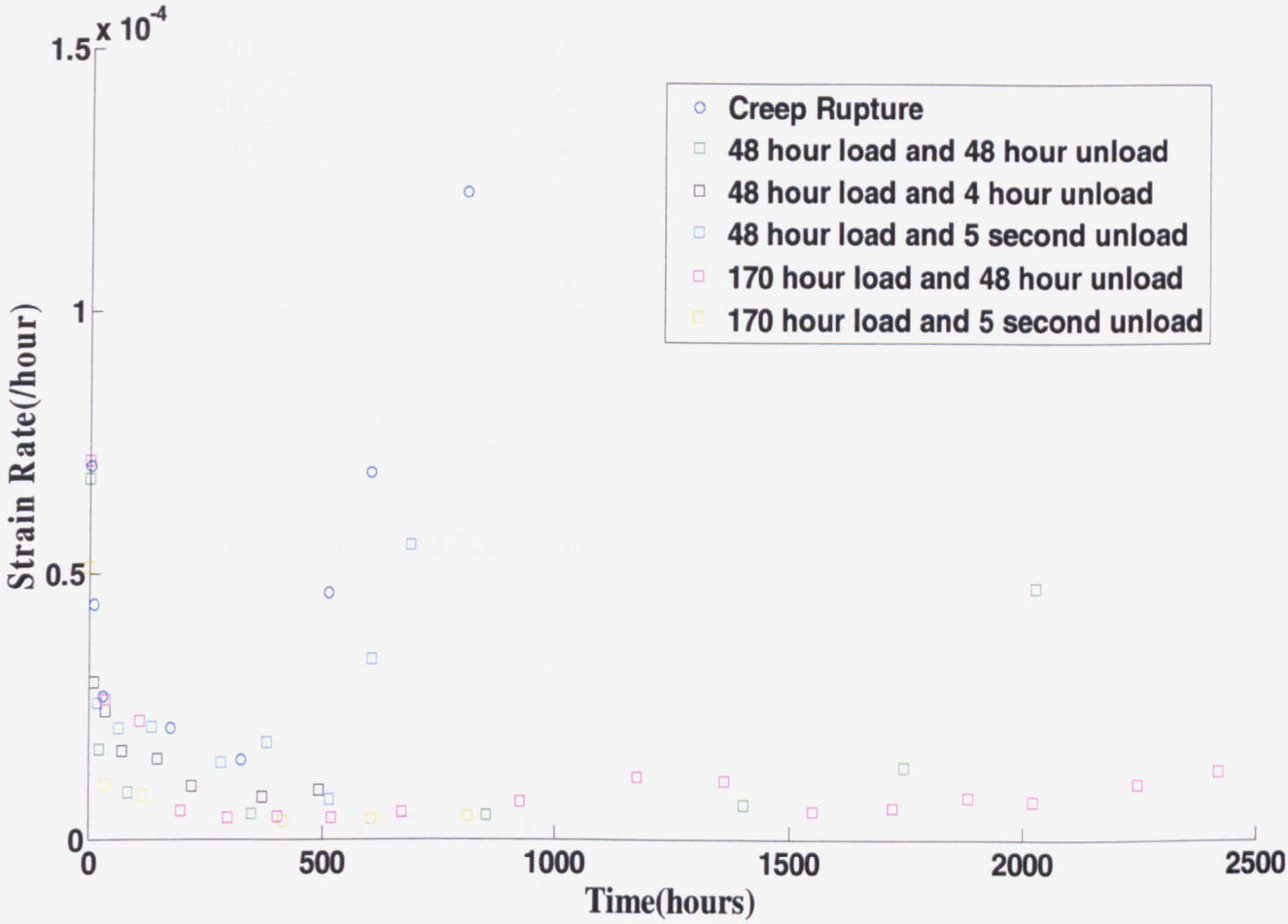

Fig. 5.21 Comparison of strain rates calculated from the 'load on' curves at 550°C

Fig. 5.20 and 5.21 shows that there is variation regarding the initiation points of the different creep stages when compared to steady load creep rupture tests. To verify this, one can use time and strain fractions to compute the ratio of time and/or strain the material is spending in each stage of creep. The different stages were computed based on their strain rates. Secondary creep is assumed to start when the strain rate of primary creep decreases by more than a third. Similarly, tertiary creep starts when the strain rate of secondary creep increases by three times. t_p, t_s, t_t represent the time period the material spends in primary, secondary and tertiary creep respectively. ε_p, ε_s, ε_r are the strains accumulated in each stage of creep. t_r, ε_r are the rupture time and failure strain.

Test Identifier	t_p/t_r (%)	t_s/t_r (%)	t_t/t_r (%)	$\varepsilon_p/\varepsilon_r$ (%)	$\varepsilon_s/\varepsilon_r$ (%)	$\varepsilon_t/\varepsilon_r$ (%)
Creep Rupture	6.8	44	48	3.8	15	81
Creep Rupture-2	2.9	60	36	2	18	80
1a	6	53	40	17	21	61
1b	7.3	92	-	47	52	-
1c	5.9	54	39	16.7	22	60
1d	7.8	92	-	55	44	-
2a	10.8	47	42	5.3	8.2	86
2b	8.7	91	-	56	43	-
2c	2.6	55	41	6.3	7.6	86

Table 5.5 Time and life fractions spent in each stage for all 650°C tests

Some differences can be observed when compared to the steady-load creep rupture tests. In some of the tests, the material is seen to be spending more time in the primary stage. The strain fraction during primary creep in the load-on/load-off tests is also high. The strain fraction during secondary creep is also increased in some cases. One possible reason for this could be each time the specimen is reloaded, there is a small amount of primary creep. The hardening mechanisms may be more dominant upon reloading in some tests which may explain the reoccurrence of primary creep.

5.6 Changes to Primary and Tertiary Creep Behaviour

The data from the load-on/load-off tests show significant deviations from steady-load creep rupture behaviour. The primary, secondary and tertiary behaviour of the load-on/load-off tests can be looked at separately, and comparing this to creep rupture behaviour will help in understanding some of the underlying reasons for the material response during such conditions. Fig. 5.22 shows comparison of creep rupture behaviour and the load-on/load off behaviour during the primary stage of the load-on/load off test 1(a).

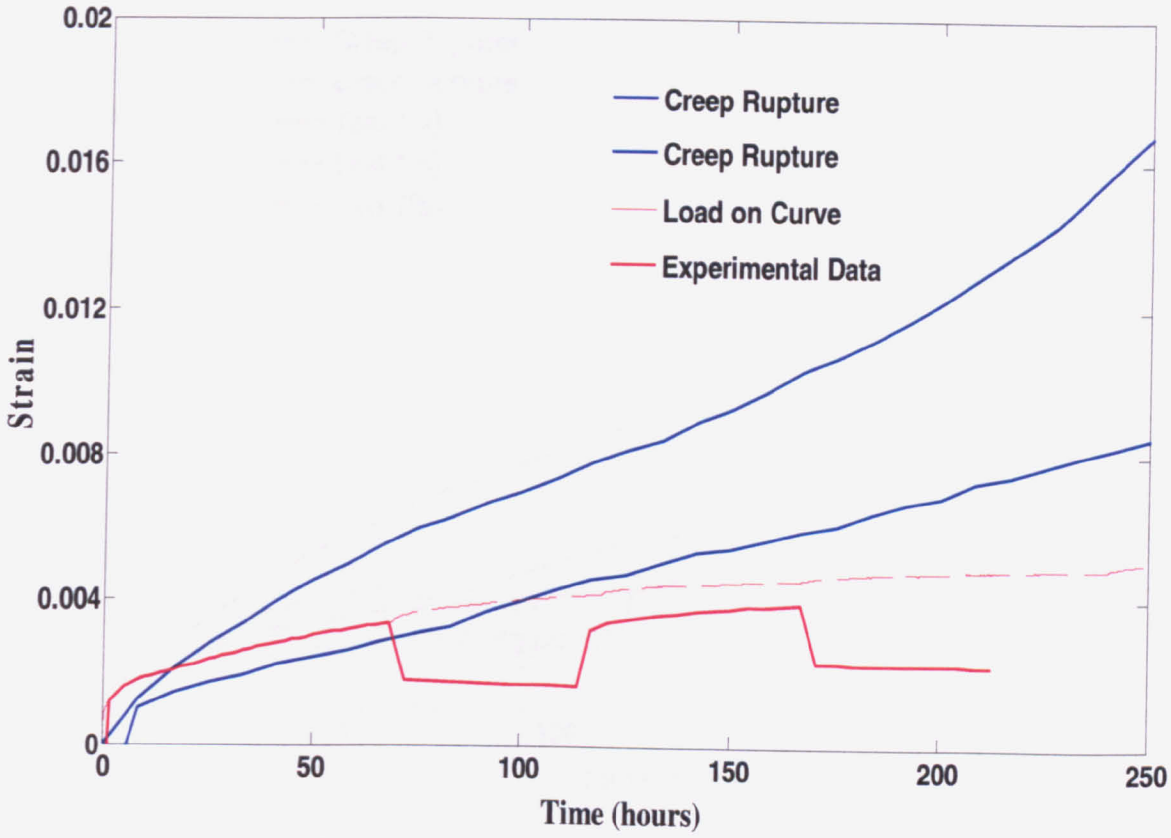

Fig. 5.22 Comparison of primary creep behaviour of the load-on/load-off test with creep rupture data

The material response is similar to the creep rupture curve until the first unload. Upon reloading, the material shows a reduced secondary creep rate. The anelasticity seems to introduce a higher level of backstress within the material which is resulting in the material displaying a reduced creep rate. The development of this backstress can be due to dislocation structures changing during the unload. Dislocation structures will affect the long-range internal stresses within the material. In conventional creep behaviour, dislocation generation and subsequent strain hardening occurs during primary creep. It is possible that similar mechanisms are acting during the unload. Similar graphs can also be drawn using the data obtained in Test 1(b) and Test 1(c) (Fig. 5.23).

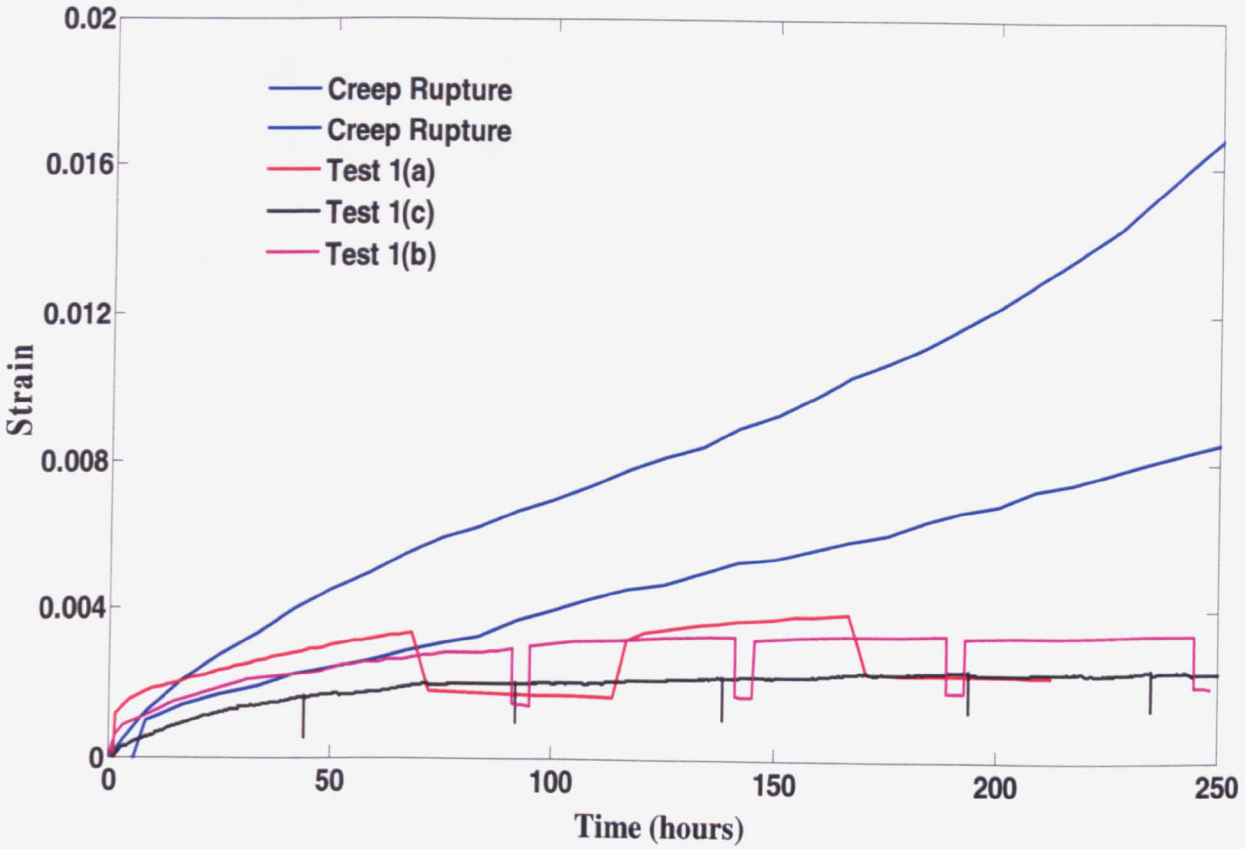

Fig. 5.23 Behaviour of the Test 1(b) and Test 1(c) during the initial cycles

As in the previous figure, a reduction in the secondary creep rates can be observed. An interesting observation in this figure is the reduction of the creep rate in test 1(c) (unloaded for 5 seconds) is much greater than the others. The mechanisms responsible for secondary creep consist of both hardening and recovery types. The reduction in creep strain when unloaded means that the hardening mechanisms are dominant during the initial stages of the unload. When the specimen is unloaded for a longer time (i.e. 4 hours or 48 hours), recovery mechanisms will start playing more prominent roles. Based on this hypothesis, the sample unloaded for 5 seconds will have no or very little recovery mechanisms acting which would mean dislocation hardening would be greater which can explain the lower creep rate.

The change in strain rates during a creep test can also be used to obtain information about the creep mechanisms. Fig. 5.24 shows the strain rates for the first three cycles in test 1(a). During this time, the material would have progressed from primary to secondary creep.

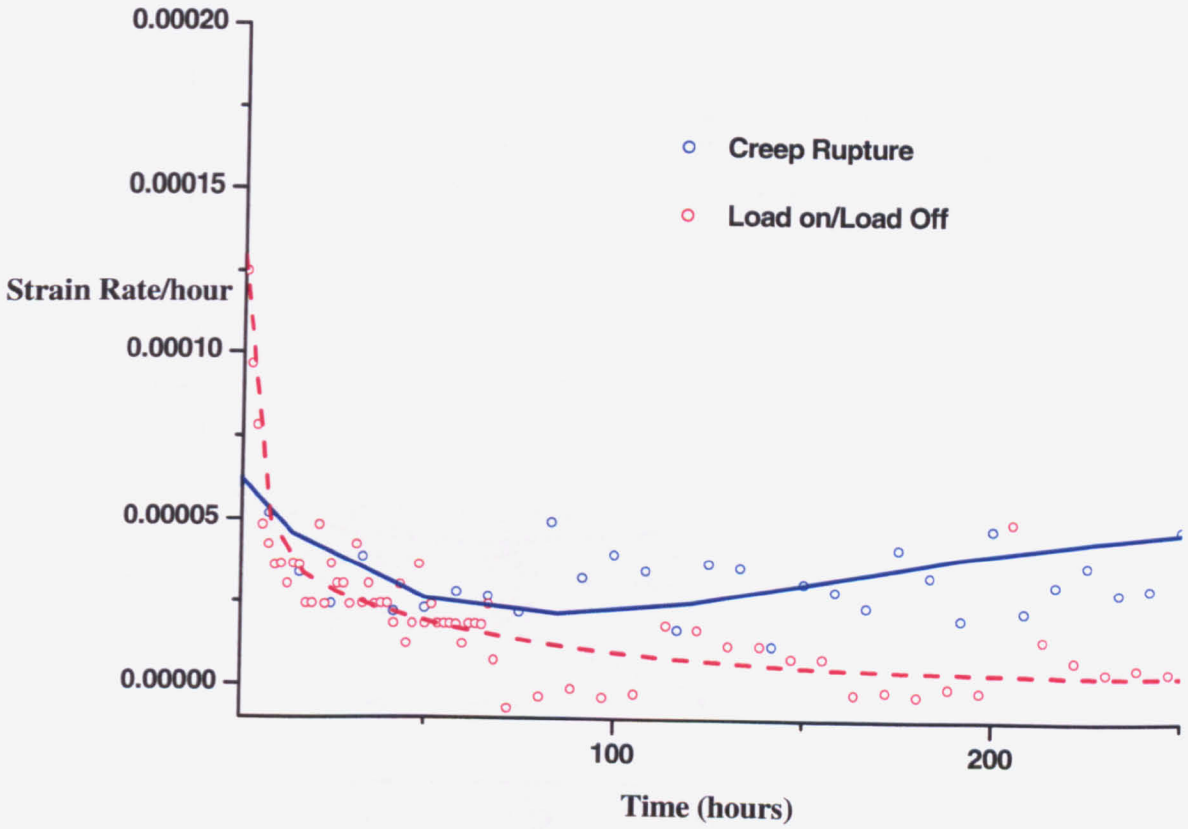

Fig. 5.24 Strain rate evolution during the first three cycles of Test 1(a). The dashed blue line represents the strain rate seen in the steady-load creep rupture test at the same conditions (650°C 180MPa)

The primary creep behaviour of the material follows the trend of the creep rupture curve. The first unload occurs at the end of the primary stage. Upon reloading, the strain-rate achieved thereafter is much smaller than the creep rupture data. As mentioned before, secondary creep consists of both hardening and recovery mechanisms. It seems plausible that anelasticity influences the material mechanisms and the hardening mechanisms become more dominant which might explain the reduction in strain rates. Later chapters describe how plastic strain changes affect the anisotropy in the material causing intergranular strains. The reduction in the strain rate due to anelasticity can be attributed to

load redistributions occurring within the various crystal planes. A similar behaviour can also be seen in the tests where the specimens were unloaded for shorter times (Fig. 5.25).

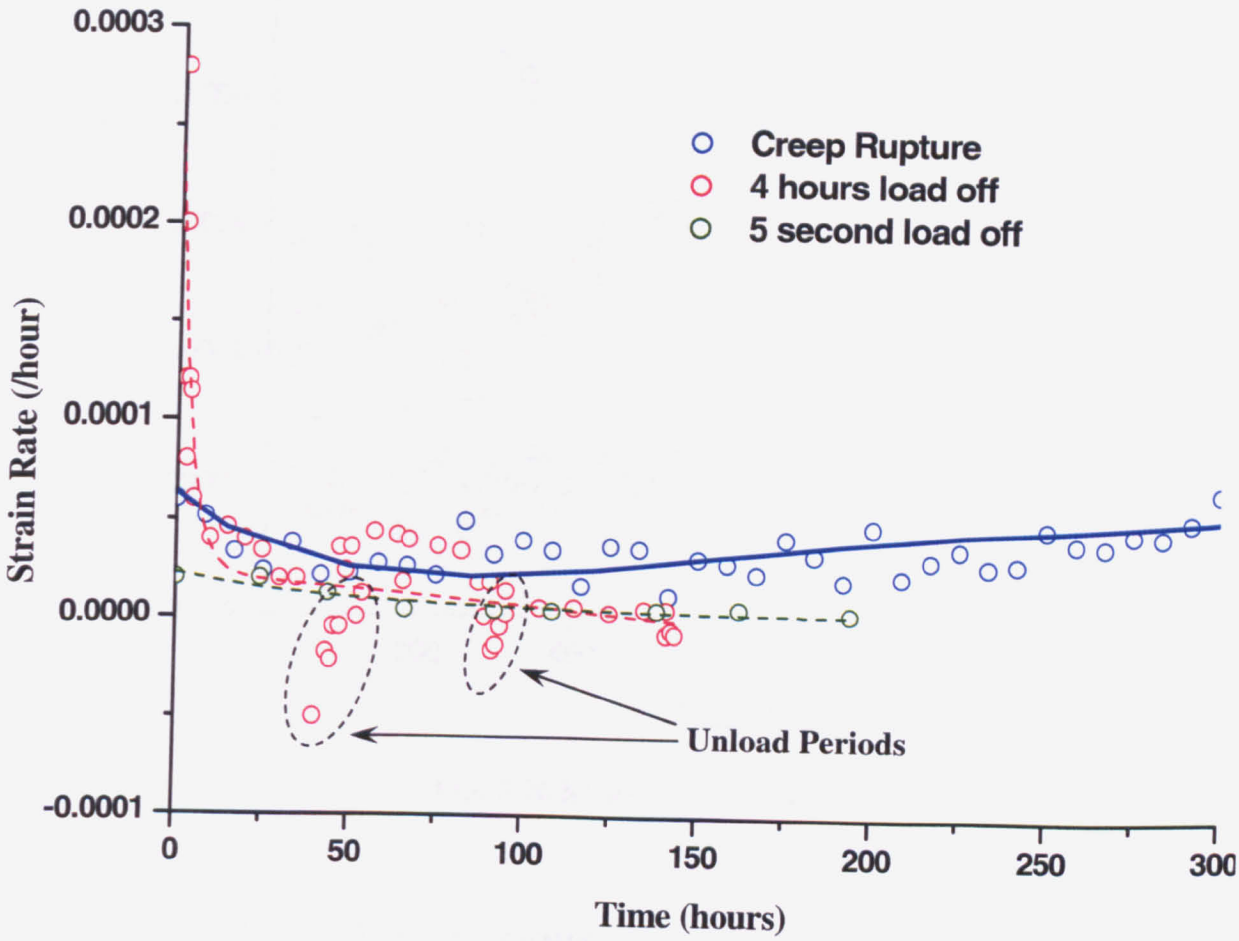

Fig. 5.25 Strain rate evolution during the first three cycles of Test 1(b) and 1(c). The blue line represents the strain rate seen in the creep rupture at the same conditions (650°C 180MPa)

As the creep strain increase, the material reaches tertiary creep. The propagation of intergranular cracks causes larger creep cracks to develop which leads to failure. Fig. 5.26 shows the strain rate behaviour during the tertiary stage. The major difference between the creep rupture data and load-on/load off tests is that the amount of strain a material spends in tertiary stage seems to be much less. Further chapters suggest reasons to explain this behaviour.

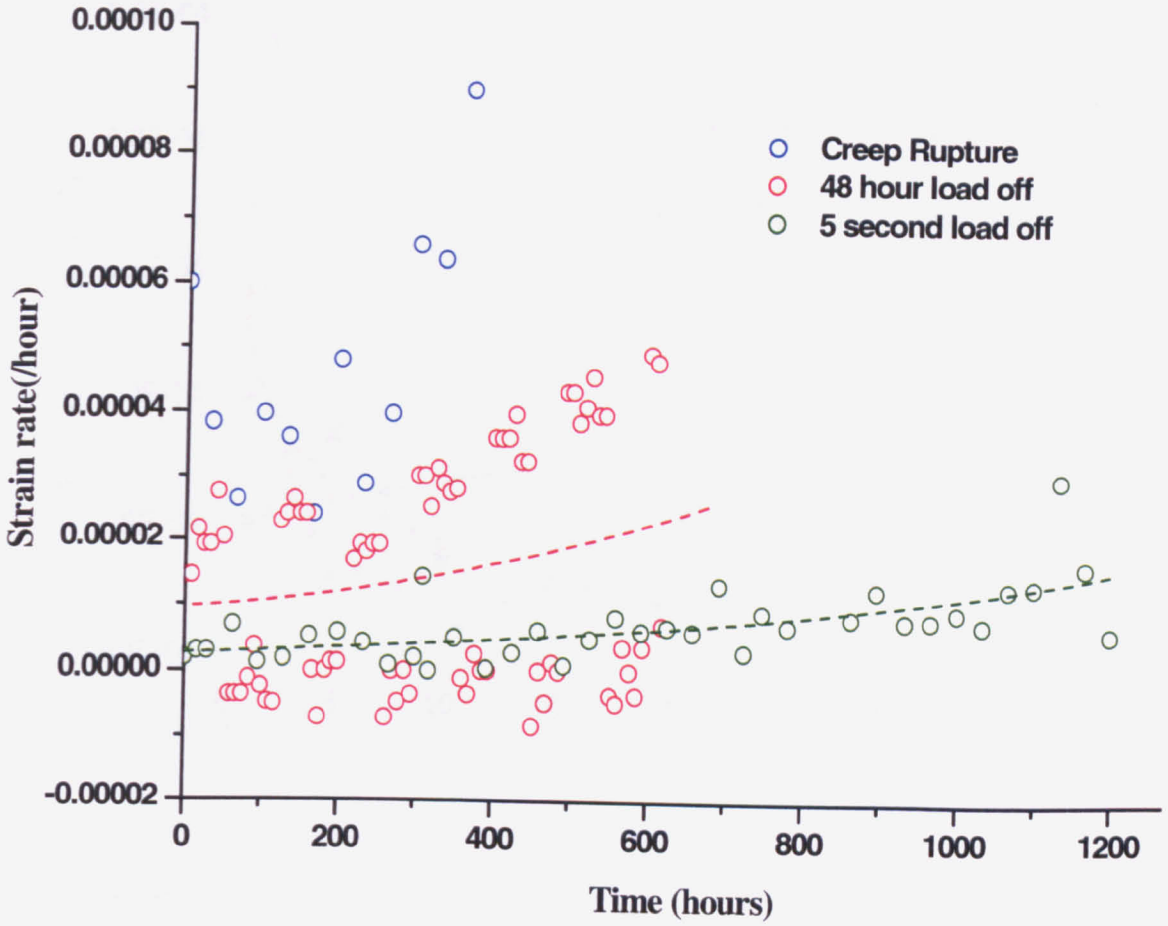

Fig. 5.26 Strain rate during tertiary creep

5.7 Anelasticity Calculations

This section deals with the analysis of the unload part of the strain curves. The variation in the anelastic strains as the number of load/unload cycles increased was calculated. The influence of creep strain on anelastic behaviour was also analysed.

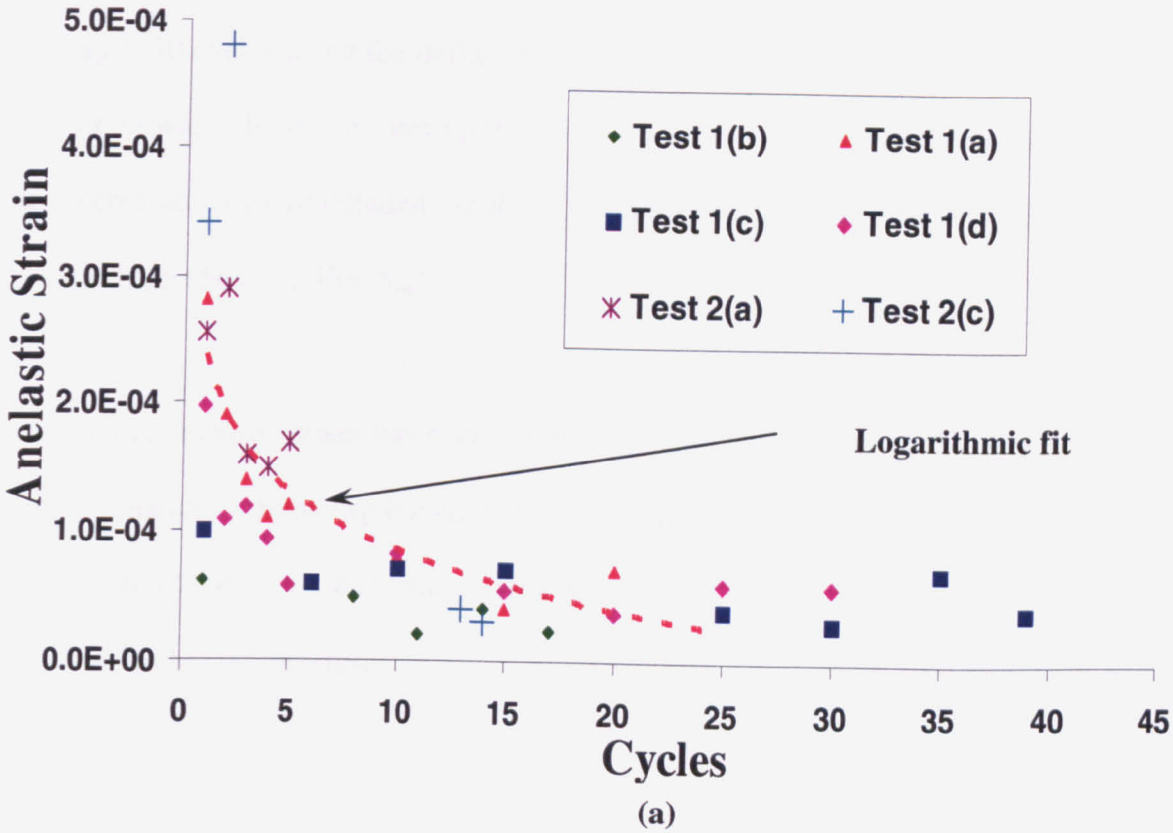

(a)

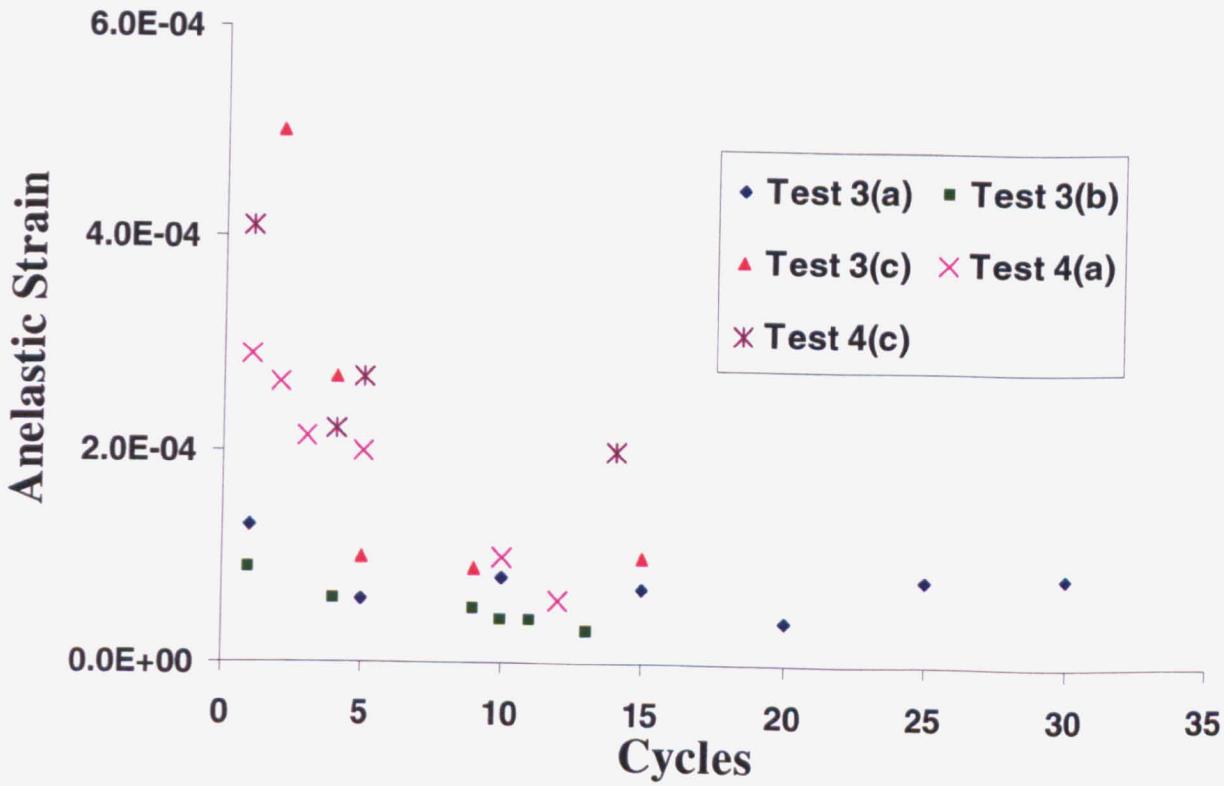

(b)

Fig. 5.27 Saturation of recovered strain as number of cycles increased (a) 650°C (b) 550°C

Initially, the magnitude of anelastic strain was calculated for the initial first five cycles and then at every 5-10 cycles using the definition of anelastic strain described in section 5.2.1. Anelastic strain was at its highest during the initial cycles and then saturated as the number of cycles increased. A more detailed graph which compares different unload cycles in the same test has been shown in Fig. 5.28.

The saturation of anelastic strain has been observed at both temperatures. This saturation is exponential in nature. Comparing the anelastic strains at 550°C and 650°C (Fig. 5.26), one can see the magnitude of the anelastic strains are similar, but the saturation of the strain takes longer at higher temperatures.

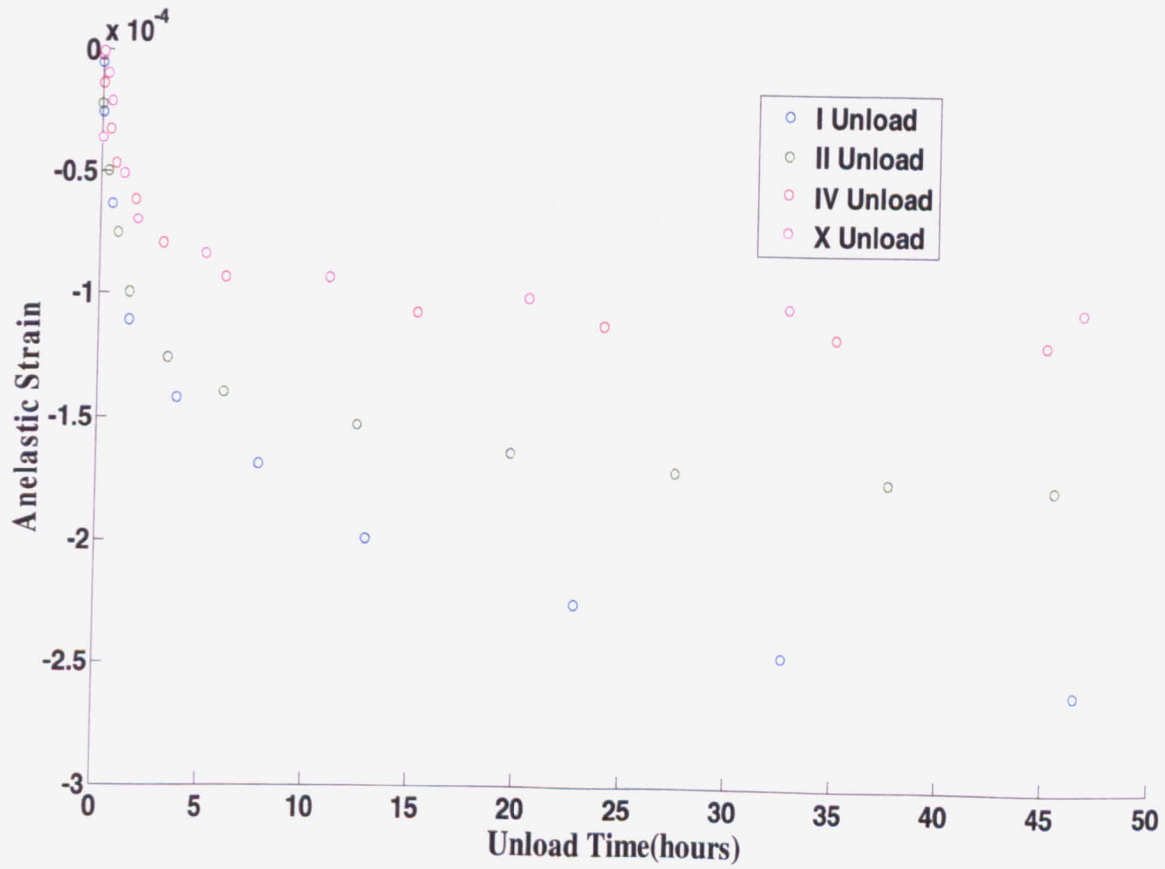

Fig. 5.28 Variation of unload behaviour as number of cycles increase for Test 1(a)

5.8 Influence of Creep Strain on Anelastic Behaviour

Power plant shut downs can occur randomly during a material's lifetime. This requires understanding the effect of the accumulated creep strain on anelastic behaviour. For example, comparing Fig. 5.10 and Fig. 5.4, the point on the strain curve where the first unload occurs is different. The amount of creep strain accumulated before the first unload is much greater in Fig. 5.10.

The anelastic behaviour during the first unload in tests 1(a) and test 2(a) were compared (Fig. 5.29 (a)).

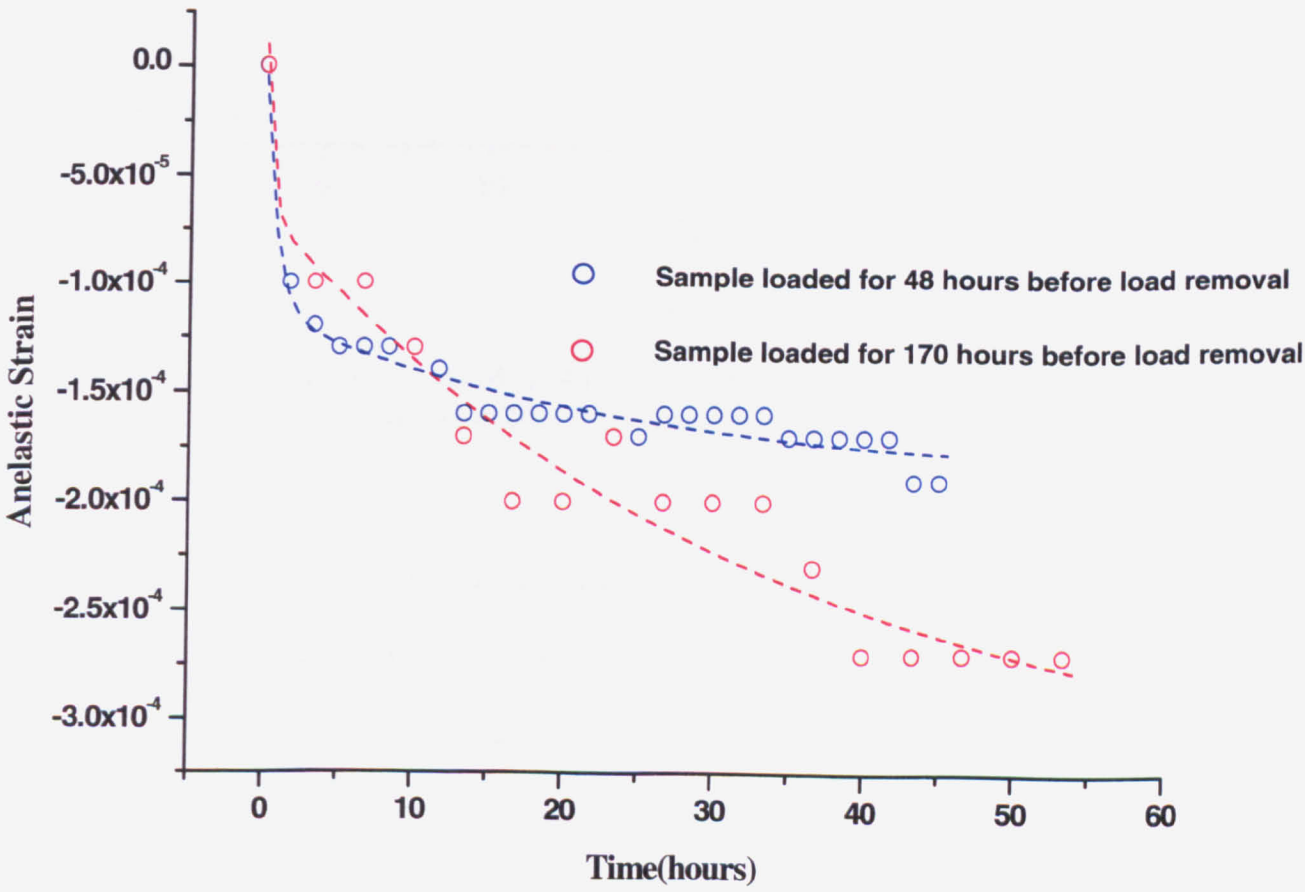

(a)

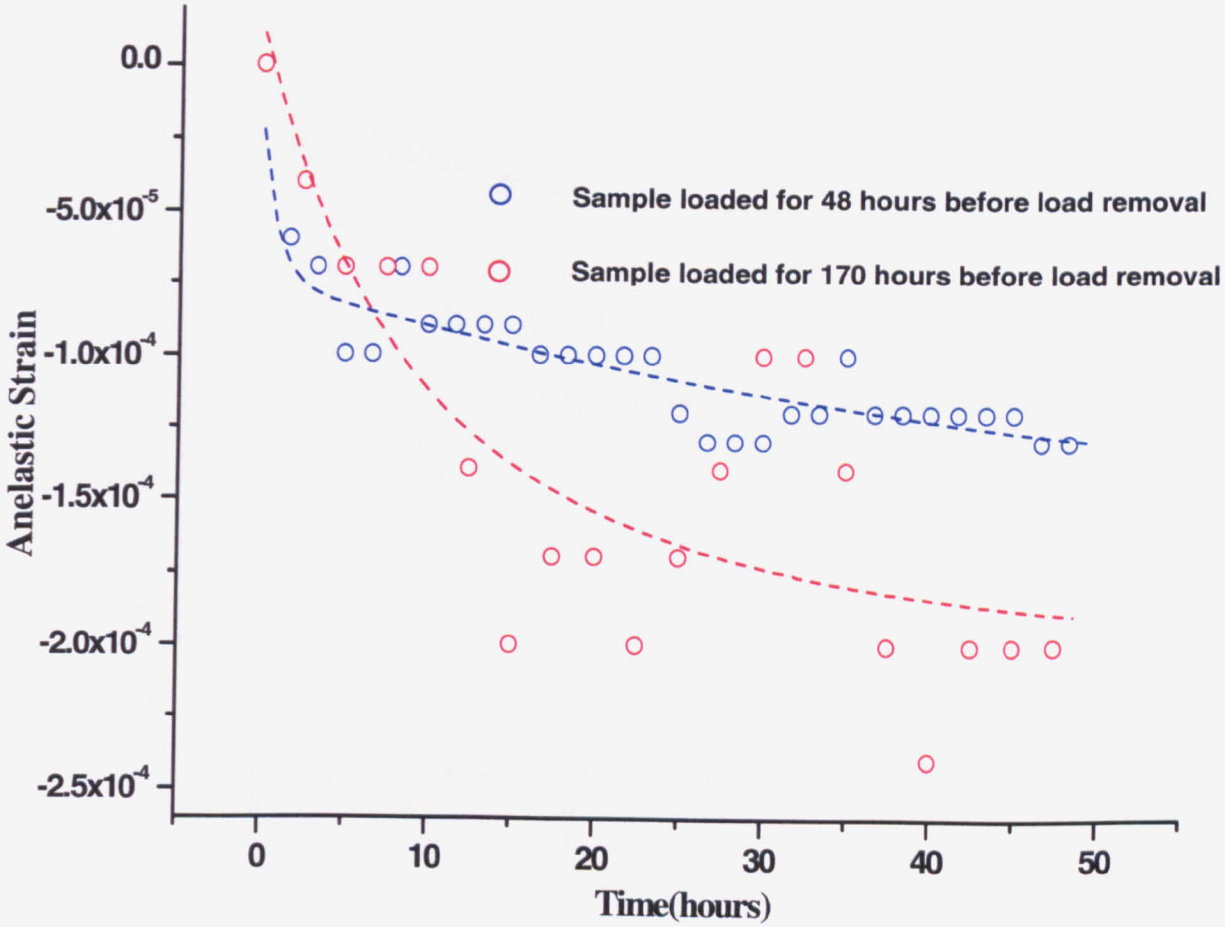

(b)

Fig. 5.29 Comparisons of (a) First unload (b) Fifth unload between Test 1(a) and Test 2(a). Test conditions 650°C 180MPa

The above figure shows comparisons of the first and fifth unloads of tests 1(a) and 2(a). Considering Fig. 5.29 (a), the magnitude of the recovered strain is higher in test 2(a) which indicates if the material is first unloaded longer into its life; a higher greater strain recovery may occur. Similar calculations were also done on tests conducted at 550°C (Fig. 5.30). These results again showed the importance of accumulated creep strain.

Dislocation hardening is one of the main mechanisms responsible for primary creep. The density of mobile dislocations is less in primary creep compared to secondary as they start

forming subgrains. If a material is unloaded during primary creep, the amount of recovered strain would be less than a specimen which was unloaded during secondary creep.

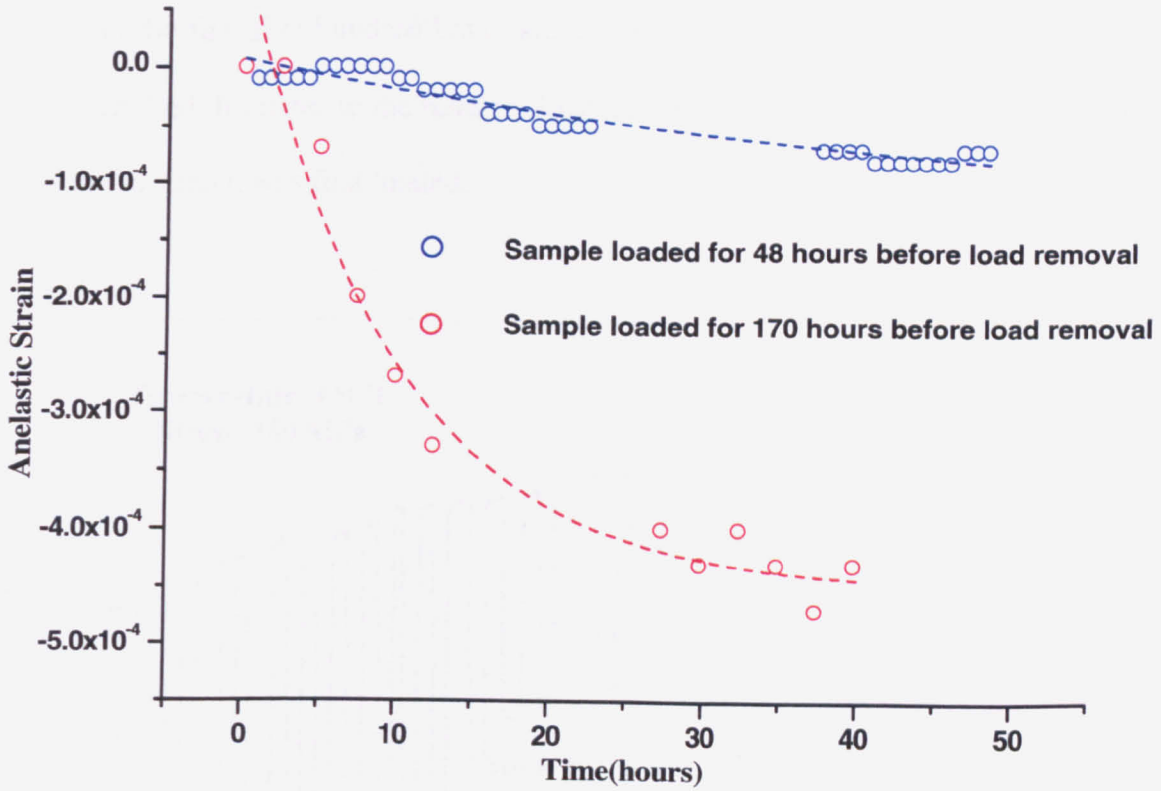

(b)

Fig. 5.30 Comparisons of (a) First unload (b) Fifth unload between Test 3(a) and Test 4(a). Test conditions 550°C 335MPa.

5.9 Removal of both Stress and Temperature

Shut downs in power plants involve removal of both stress and temperature. Understanding the mechanism of anelasticity therefore shall involve both stress and thermal effects. The results presented in the previous section can explain the effect of stress on anelasticity. Tests were also done where both load and temperature removal was done. These tests will help in understanding the role of temperature during the unload process.

Fig. 5.31 shows the strain curve for Test 1(d) where the specimen was loaded for 48 hours and then both stress and temperature were removed for 48 hours. Fig. 5.32 shows the strain data superimposed on the stress and temperature profiles. Some of the strain values, especially in the first five hundred hours are negative. This does not mean a compressive strain was applied. It relates to the relative displacements in the transducer when compared to when the specimen was first loaded.

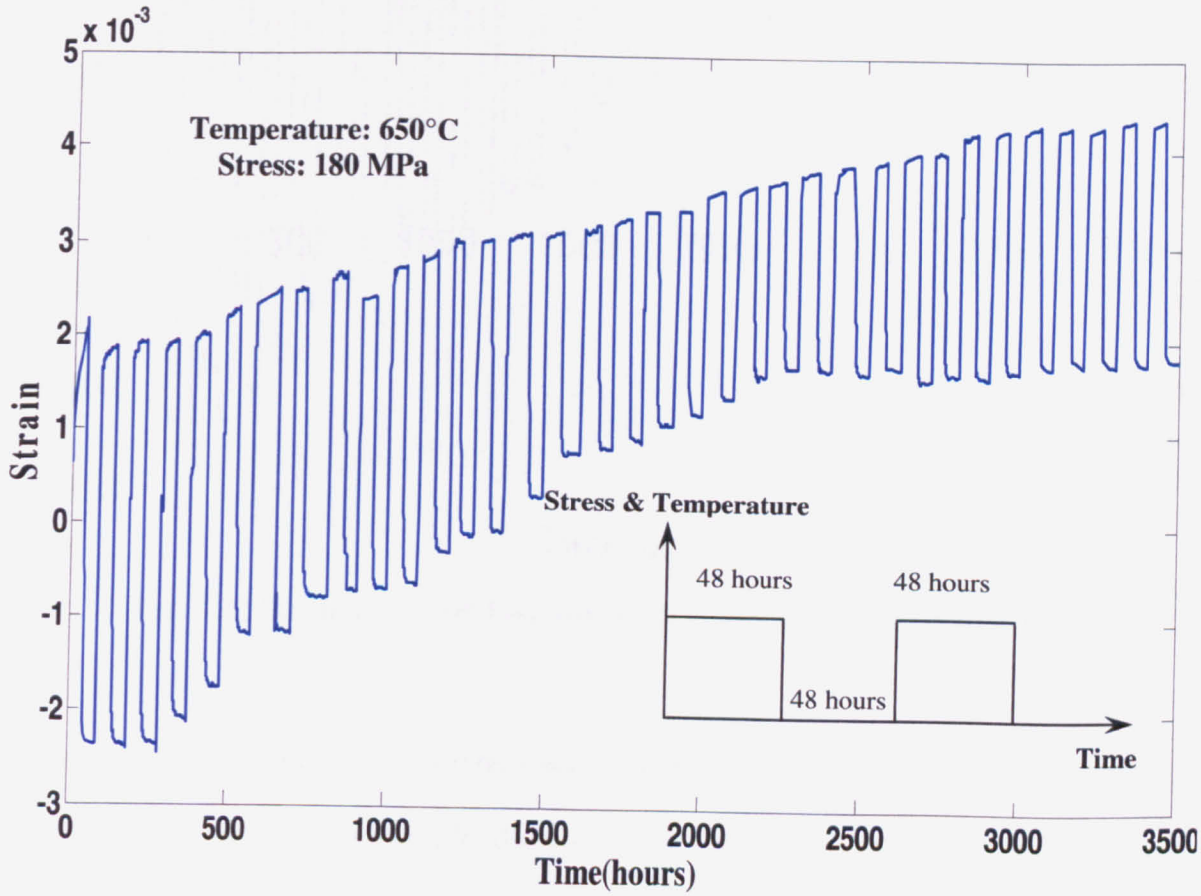

Fig. 5.31 Strain curve of Test 1(d)

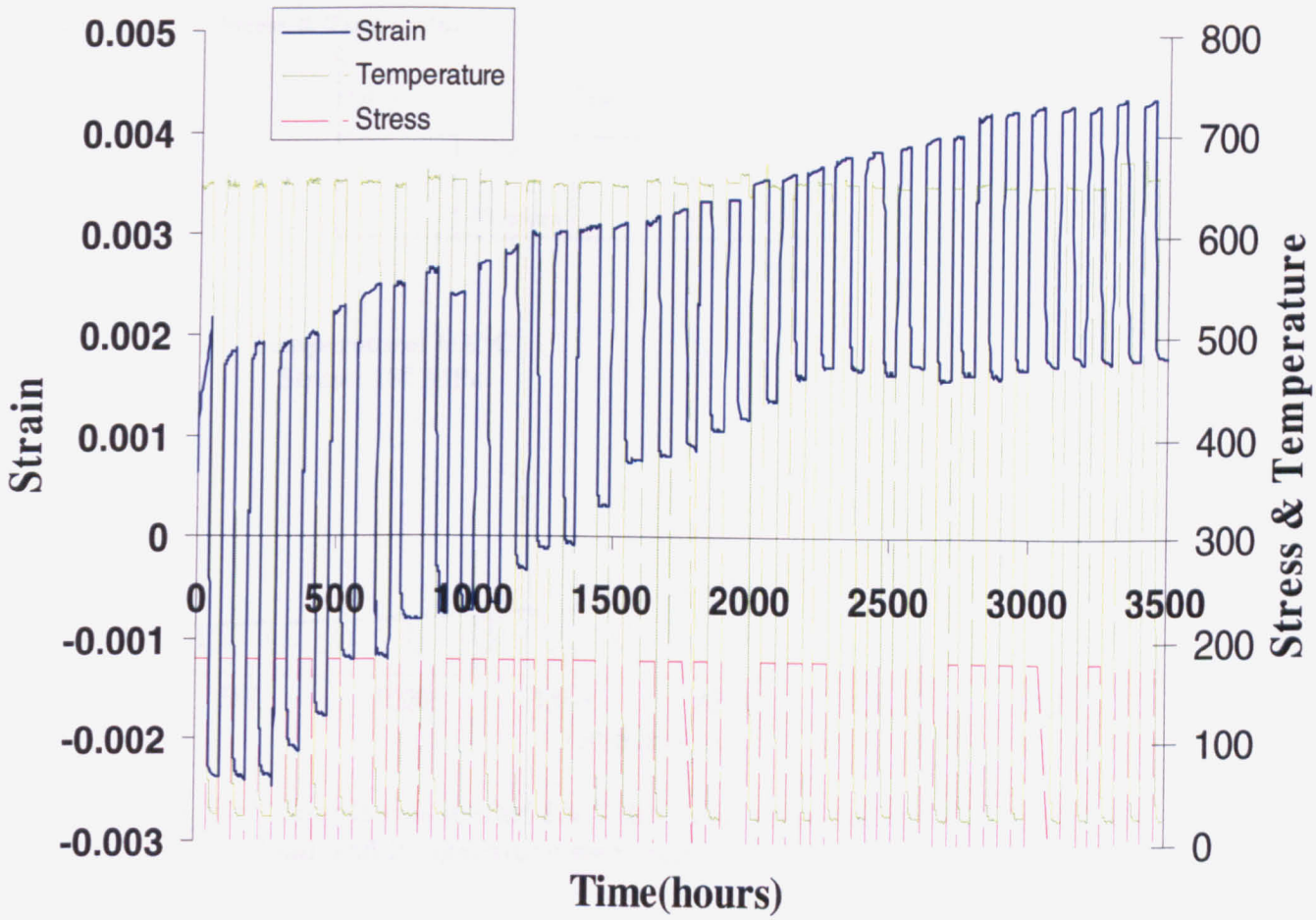

Fig. 5.32 Strain curve of Test 1(d) with stress and temperature profiles

Tests with other operating conditions were also done. Fig. 5.33 shows the strain curve for test 2(c) where the specimen was loaded for 7 days before removal of load and temperature for 48 hours.

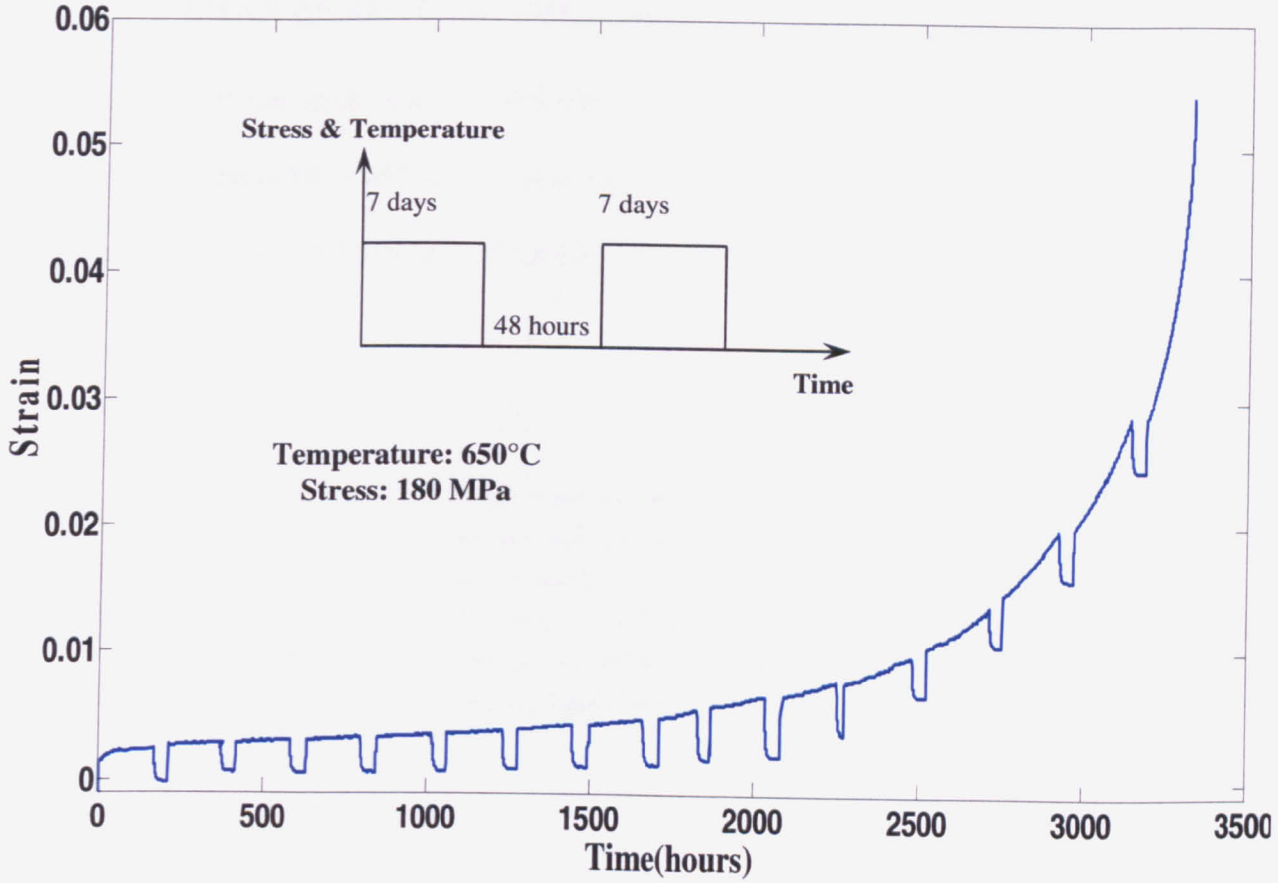

Fig. 5.33 Sample was loaded for 7 days and unloaded for 48 hours. Both load and temperature were removed during the unload

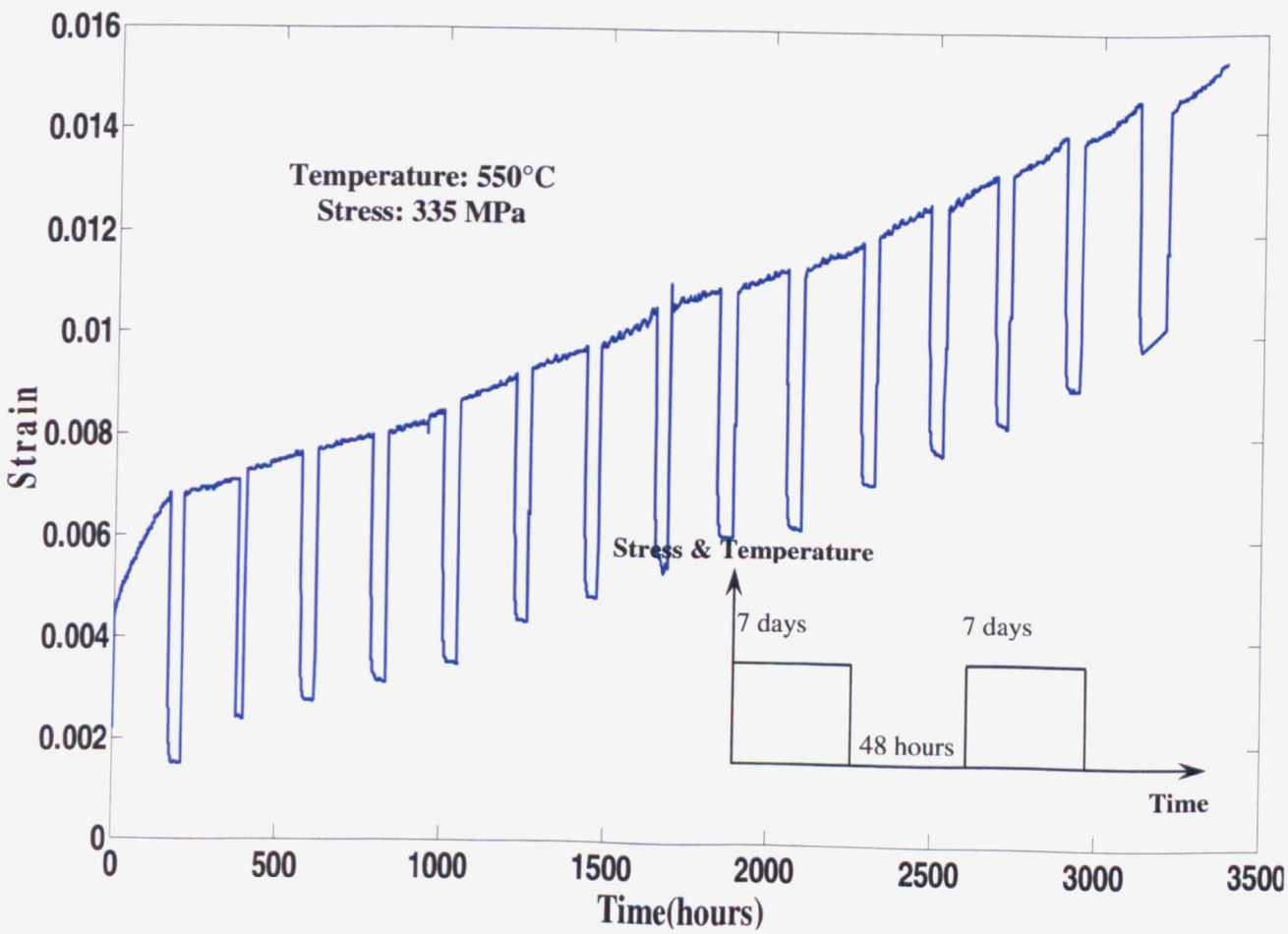

Fig. 5.34 Sample was loaded for 7 days and unloaded for 48 hours. Both load and temperature were removed during the unload

5.9.1 Effect on On-Load Behaviour

As seen in the strain curves, removal of temperature alters the behaviour of the material when compared to conditions where only stress was removed. The effect of the unloading on the load-only behaviour is shown in Figs. 5.35, 5.36.

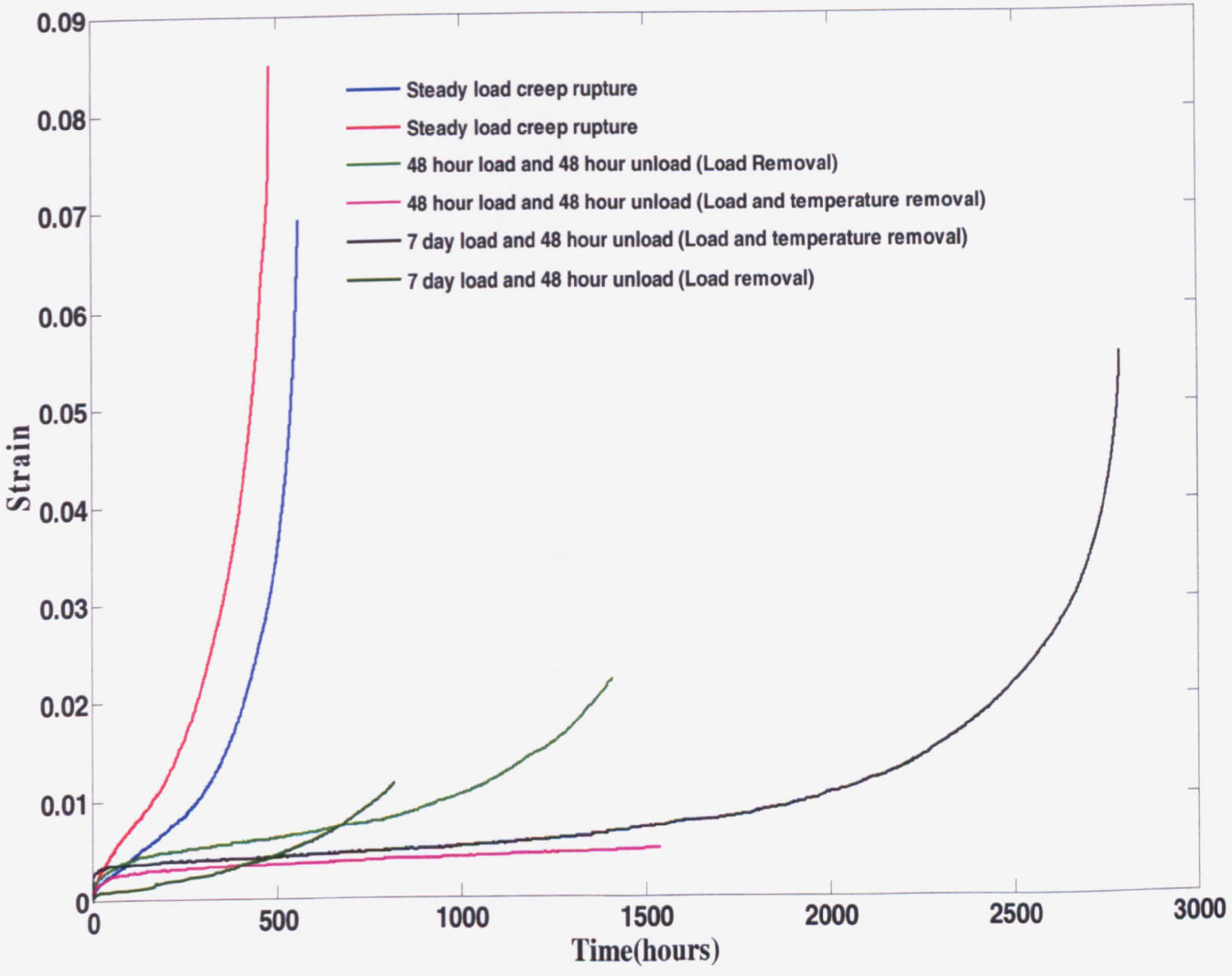

Fig. 5.35 Effect of temperature removal on rupture life (650°C tests)

One of the main observations from these tests was the further decrease in strain rate when compared to tests where only the load was removed. Tests conducted at a temperature of 650°C showed a decrease of more than 50% in strain rate in some cases. Tests conducted at 550°C (Fig. 5.36) showed a lesser decrease in strain rate. These data may imply that the mechanism responsible for anelasticity has a thermal dependence.

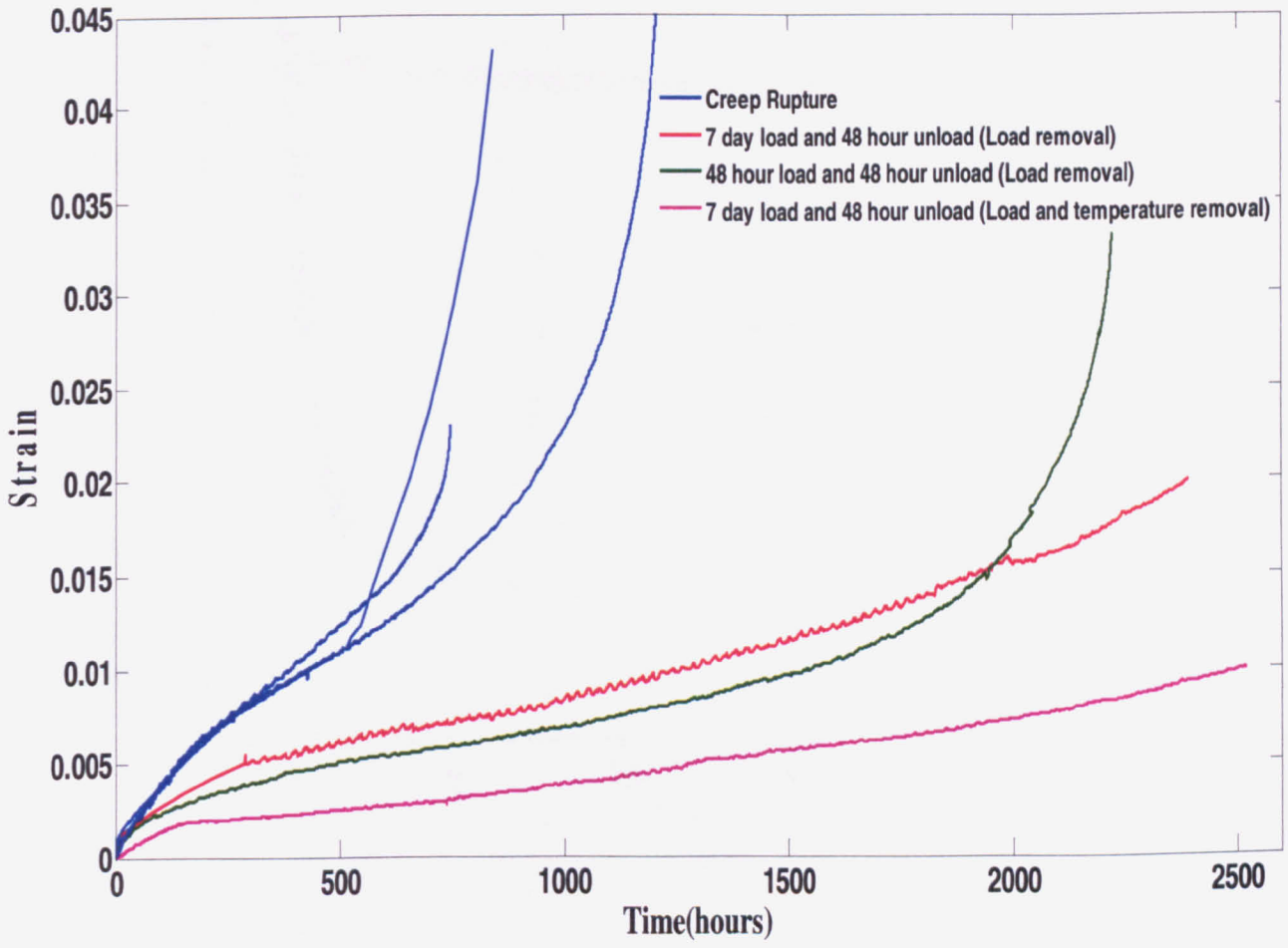

Fig. 5.36 Effect of temperature removal on rupture life (550°C Tests)

5.9.2 Effect on Unload Behaviour

Mechanisms responsible for creep have a strong thermal influence. By comparing the material behaviour during the unload period of a test where only the stress was removed to a test where both stress and temperature was removed, the effect of temperature can be assessed.

To compute the 'normalised' strain, the thermal strain due to removal of temperature and the instantaneous elastic strain due to unloading were removed. All the remaining strain is assumed to be the anelastic strain.

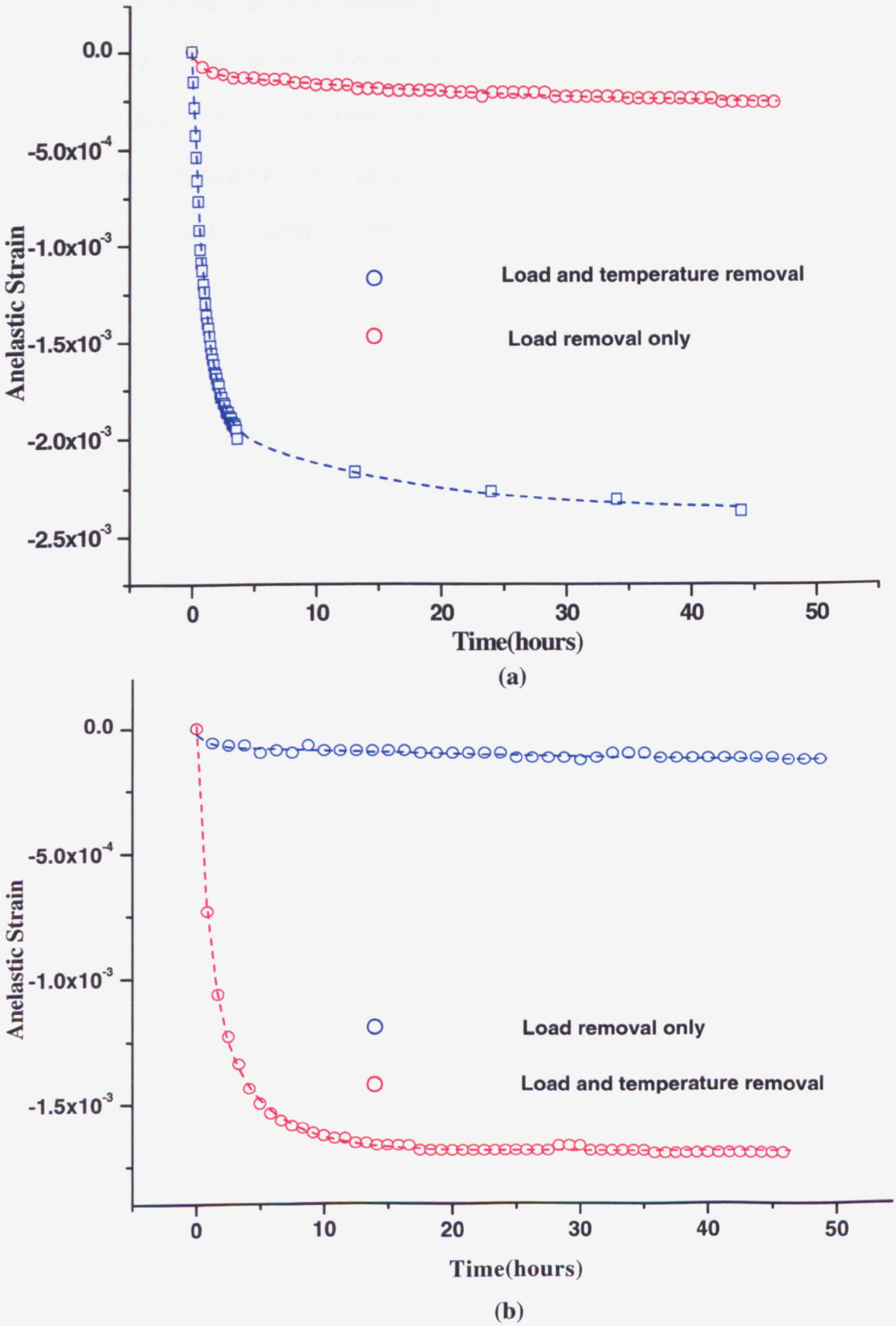

Fig. 5.37 Comparisons showing effect of temperature removal (a) First unload (b) Fifth unload between Test 1(a) and Test 1(d). Test conditions were 650°C 180MPa

Fig. 5.37 shows the difference in the unload behaviour of the first cycle between the test 1(a) where only the load was removed and test 1(d) where both stress and temperature were removed. It can be seen that in test 1(d), the amount of recovered strain is much greater. Similar observations were noted in other tests as well. Fig. 5.38 shows the comparison in the first cycle behaviour between test 2(a) and test 2(c). This behaviour was also observed at tests performed at 550°C as well (Fig. 5.39).

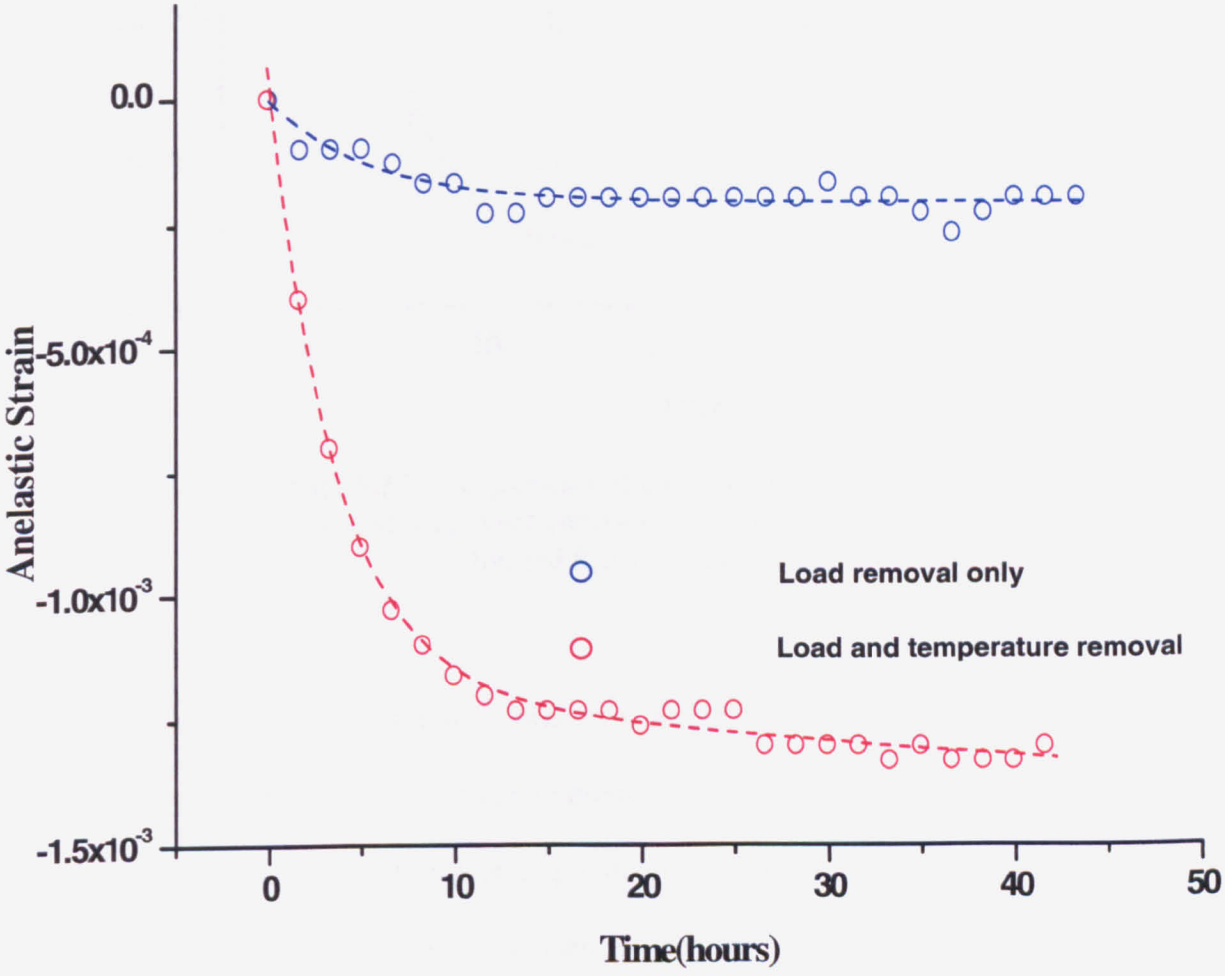

Fig. 5.38 Comparison of first cycle unload behaviour in test 2(a) and test 2(c). Test conditions were 650°C 180MPa. Sample was loaded for 170 hours before unloading

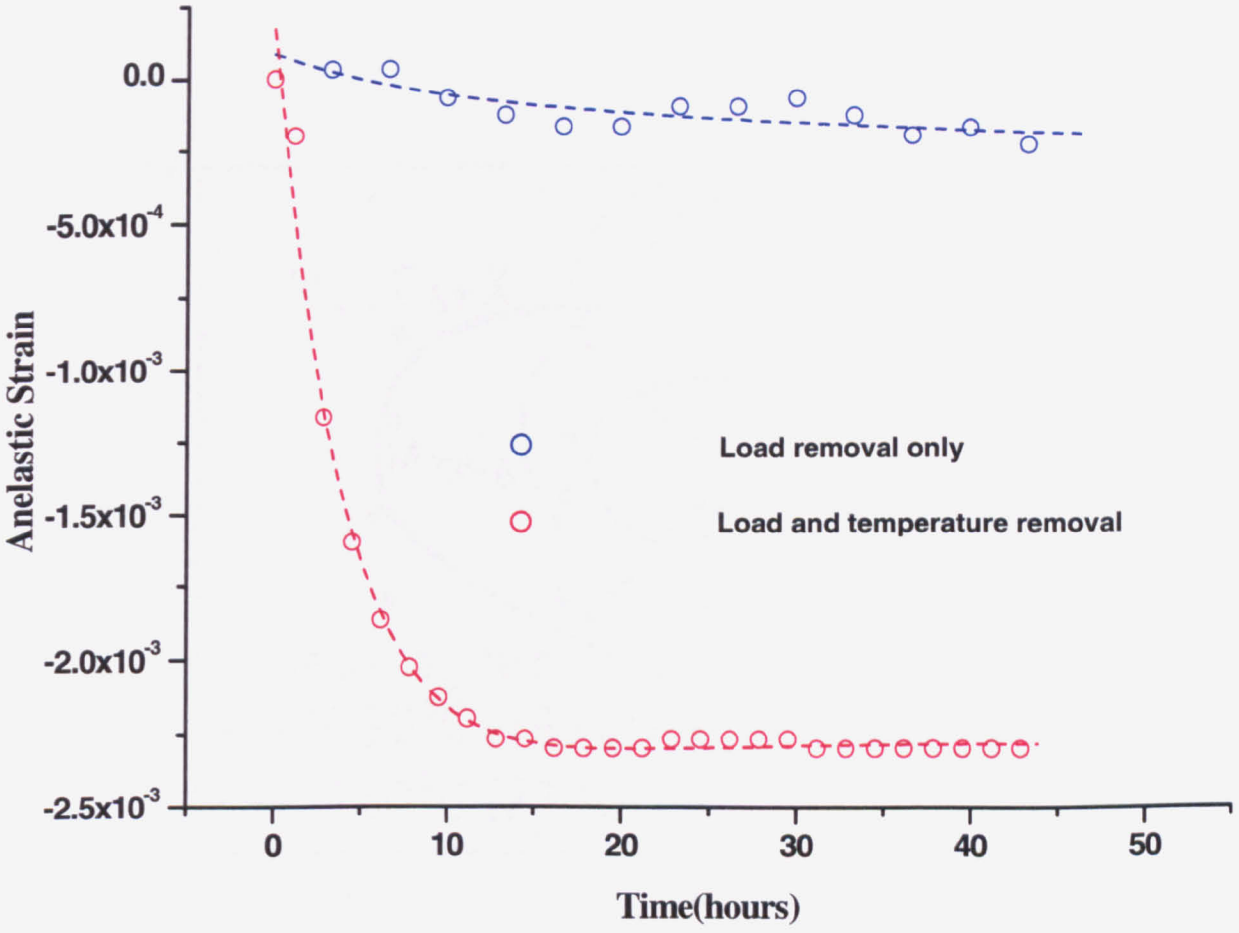

Fig. 5.39 Comparison of first cycle unload behaviour in test 4(a) and test 4(c). Test conditions were 550°C 335MPa. Samples were loaded for 170 hours before unloading

The mechanisms of precipitation formation would be one of the mechanisms which would be greatly affected by temperature removal. There are a number of metastable precipitate structures which form before forming a stable precipitate phase. To form a stable carbide, precipitation kinetics follow a sequence such that a greater kinetic stability can be achieved. Fig. 5.40 shows a time-temperature-transformation diagram for an annealed 316 steel. It is evident from the figure that depending on the temperature and the rate of cooling, the kinetics of the precipitate formation will vary. As a result, the overall carbide density will be different which will affect the strengthtening and the Orowan bending mechanisms. These, in turn will affect the amount of recovered plastic strain.

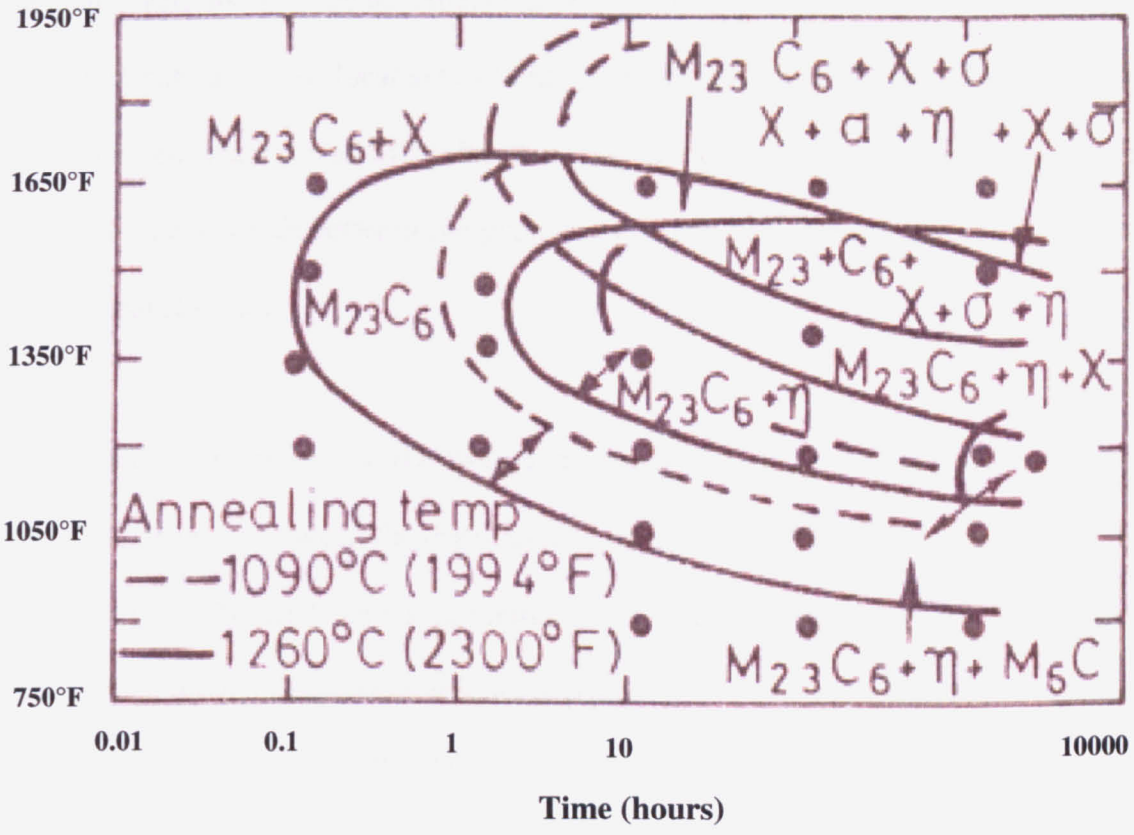

Fig. 5.40 TTT precipitation diagrams for 316 annealed steel [25]

5.10 Stress-Dip Testing

Material microstructures can exhibit a stress which acts in an opposite sense to the applied external stress. Generally, this backstress is considered to be an athermal stress [20] and is considered as a long range internal stress acting within the material.

The movement of the dislocation in the glide plane will influence the equilibrium stress state between the dislocation and its surroundings. This in turn will cause changes to the internal stress state of the material. When mobile dislocations encounter immobile dislocation networks, a local straining process will result. This interaction can also lead to development of a back stress. Sawada [21, 22] and Gibbons [23] have also described this

backstress as a directional component of hardening and is associated with the local straining process inducing longer-range interactions with mobile dislocations. At an intragranular level, dislocations accumulating at grain boundaries and obstacles will cause pile-ups which can affect the local stress fields. Between different regions of the material, changes in the deformation rate will exist. If a grain deforms at a strain rate different to its neighbours, the stress fields between the grains will be affected. This mechanism again can generate internal stresses.

Precipitate-dislocation interaction (Orowan bending) will also cause the local stress fields to change. The distance between the carbides will directly influence the line tension on the dislocation (Fig. 2.13). Dislocation generation will also occur through the Frank-Reed mechanism when the bending radius reaches a critical point. The change in the dislocation densities can result in changes to the dislocation substructures.

The application of the external stress would thus result in a net 'effective' stress acting on the material. At a local scale, this effective stress would be local stress required to move a dislocation. One method to estimate the value of the backstress is to conduct a creep test where the load applied on the material is decreased to the estimated value of the backstress for a fixed duration and then increased back to the original value. Neutron diffraction results (chapter 7) have shown that the stress in the {111} and the {220} plane is in the order of 50-60 MPa acting in the compressive direction. To verify if the internal stress was around this value, a test was done where a load of 180MPa was applied on the sample at 650°C for 48 hours after which the load was reduced to 45MPa for 48 hours. The sample was then reloaded back to 180MPa. Four such cycles were conducted. The assumption here is if the the applied stress during the stress reduction is equal to the backstress, then

the strain (either creep or anelastic) during this period will be nearly zero as the applied external stress will balance the internal backstress.

One of the drawbacks of this method will be the changing internal stress state. The internal stress state within the material will change with the number of the load/unload cycles. Thus the applied external stress during the stress reduction will not be equal to the internal backstress. Fig. 5.41 shows the result of the test.

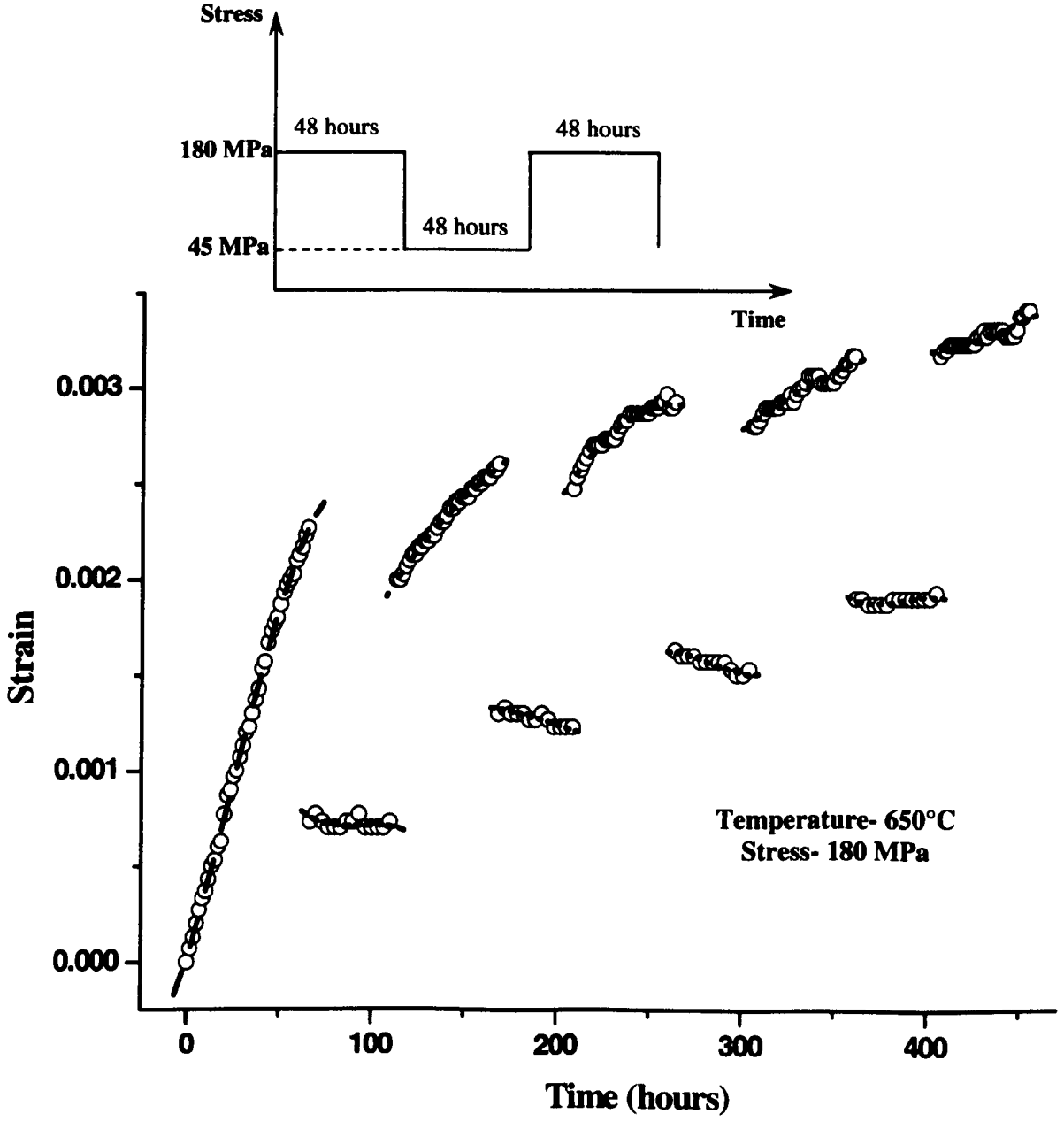

Fig. 5.41 Strain data for stress-dip testing

During the first load reduction, the amount of anelastic strain accumulated is almost zero. As the load/unload cycles increase, there is a change in the material behaviour. The second and third load reduction results in some anelasticity being observed. The effect of the changing internal stress state is clearly visible in this cycle. In the fourth load reduction, there is no anelasticity observed, but there is an increase in the creep strain. As an estimate, it can concluded that the effective backstress for these conditions is around 45-55 MPa.

Another method to estimate the backstress is to conduct a creep test with an applied stress equal to the backstress. Theoretically, the resultant secondary strain rate should be close to the observed strain rate during anelasticity.

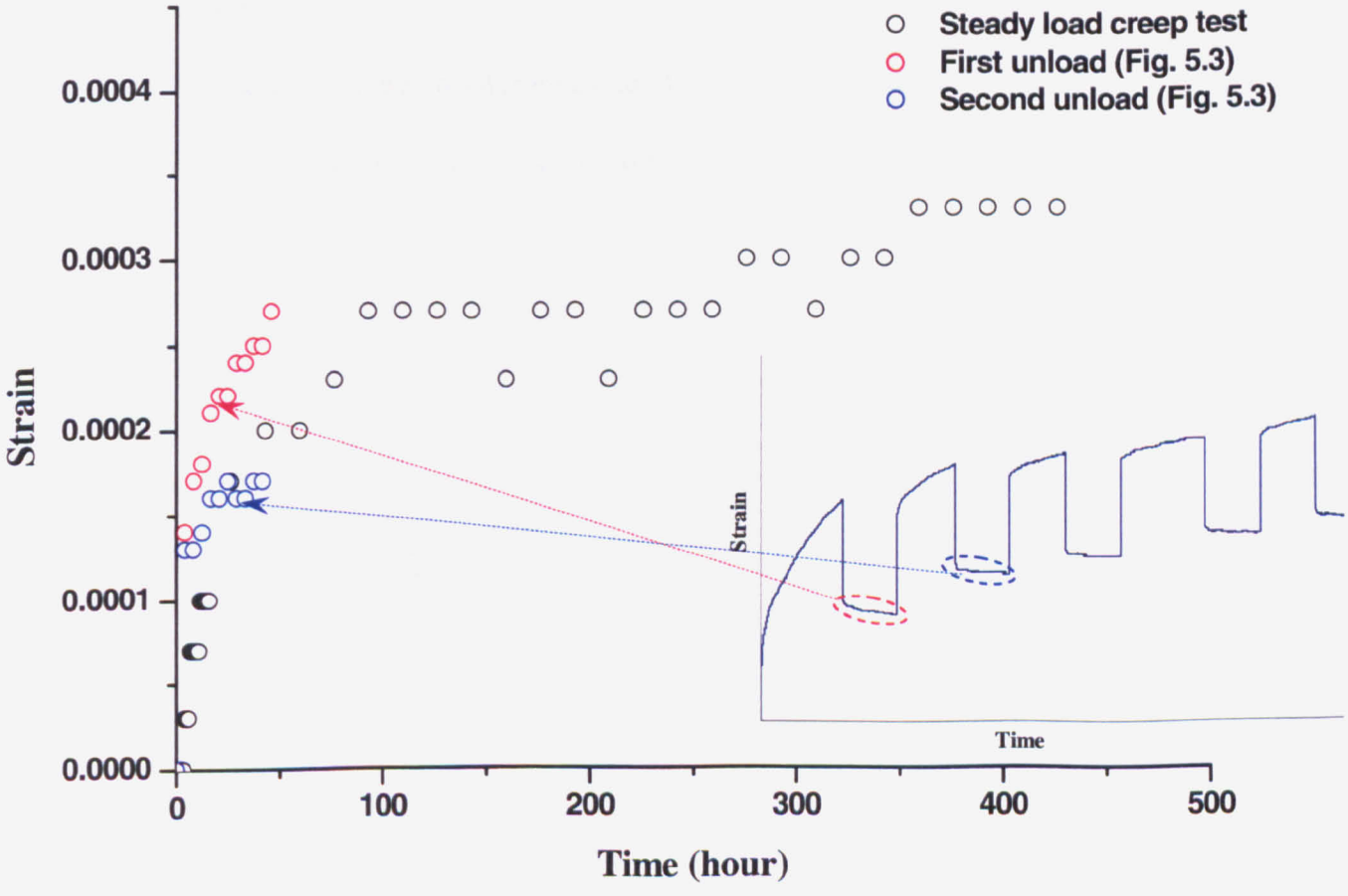

Fig. 5.42 Comparison of creep rupture test (650°C 50MPa) with first and second unload cycles in Fig. 5.4

Fig. 5.42 shows the comparison between the creep rupture test and the unload data for the first and the second cycles in Fig. 5.4. The strain behaviour seen seems to match reasonably with the creep rupture at 50MPa.

5.11 Conclusions

- Tests which involved removal of load/temperature during creep have been carried out.
- All tests showed plastic strain recovery during the unload. This recovery has been called anelasticity.
- Computing load on response shows significant deviations to monotonic creep rupture testing. Increased rupture times and decreased rupture strains have been observed.
- Anelasticity seems to saturate as number of unload/load cycles increase.
- Removal of temperature with stress shows an increase in the anelastic strain.

References

[1] A.E. Johnson, *The creep recovery of a 0.17% carbon steel*, Proc. Inst. Mech. Eng. 145 (1941), pp. 210–220.

[2] J.D. Lubahn, *The Role of Anelasticity in Creep, Tension and Relaxation Behavior*, Trans. ASM 45 (1953), pp. 787–838.

[3] A.E. Johnson, J. Henderson and B. Kanh, Acta. Metal. 63 (1963), pp. 173–177.

[4] J.D. Snedden, Nat. Eng. Laboratory NEL Report No. 533, 1972.

[5] P.W. Davies, G. Nelmes, K.R. Williams and B. Wilshire, *Stress changes experiments during high temperature creep*, Metal Sci. J. 7 (1973), pp. 87–92.

[6] G.J. Lloyd and R.J. McElroy, *A model for the quantitative interpretation of high-temperature stress relaxation phenomena: The effect of anelasticity*, Philos. Mag. 32 (1975) (1), pp. 231–244.

[7] M. Pahutova, J. Cadek and P. Rys, *Some stress change experiments on creep in α zirconium*,Mater. Sci. Eng. 39 (1979), pp. 169–174

[8] V.Lupinc, F.Gabrielli, *Effect of grain size, particle size and γ' volume fraction on strain relaxation in Ni---Cr base alloys*, Mater. Sci Eng, 37(1979) 143-149

[9] A. Kuršumović, B. Cantor, *Anelastic crossover and creep recovery spectrain Fe 40Ni40B20 metallic glass*, Scripta Mater. Vol. 34, Issue 11, June 1996, pp 1655-1660

[10] J.C. Gibeling, W.D. Nix, *Observations of anelastic backflow following stress reductions during creep of pure metals*, Acta. Metall. 29 (1981), pp. 1769–1784

[11] J.C. Gibeling, W.D. Nix, Acta. Metall. 28 (1980), pp. 1743.

[12] M.J.Mills, J.C. Gibeling, W.D. Nix, *Measurement of anelastic creep strains in Al-5.5 at.% Mg using a new technique: Implications for the mechanism of class I creep*, Acta. Metall. Vol. 34 No.5 (1986), pp. 915-925.

[13] L.O.Bueno, R.L.Bell, *Anelastic creep behaviour of RR-58 aluminum alloy at 180 °C: Phenomenological aspects and analysis based on the unbowing of dislocation segments*, Mater. Sci. Eng. A 410-411(2005) 72-78.

[14] D.G.Morris, *Anelasticity and creep transients in an austenitic steel*, Mat. Sci. J. 13 (1978), pp. 1849-1854

[15] D.G.Morris, *Creep in type 316 stainless steel*, Acta. Metall. 26 (1978), pp. 1143-1151.

[16] D.G.Morris, D.R.Harries, The *cyclic creep behaviour of Type 316 stainless steel*, Mat. Sci. J. 13, 1978, pp. 985-996.

[17] S.K.Mitra, D.Mclean, Proc. Roy. Soc. London, Sect. A, 295(1966) 288.

[18] Hasegawa. T, Ikeuchi. Y, Karashima S., *Internal Stress and Dislocation Structure during Sigmoidal Transient Creep of a Copper-16 at.-% Aluminium Alloy*, Metal. Sci. Jour.6 (1972), pp.78

[19] H. Yoshinaga, K.Toma, Trans. Japan Insti. Metals. 17, 559, (976)

[20] W.D. Nix, B. Ilschner, *Mechanisms controlling creep of single phase metals and alloys*, Proc. ICSMA 5, Vol.3, p.1503, Pergamon Press, Oxford (1980).

[21] K.Sawada, K. Kimura, F.Abe, *Mechanical response of 9%Cr heat-resistant martensitic steels to abrupt stress loading at high temperature*, Mater. Sci. Eng. A358 (2003) 52-58.

[22] K.Sawada, K. Kimura, F.Abe. *Deformation behavior of high Cr ferritic steels upon abrupt stress loading*, Mater. Sci. Eng. A387-389 (2004) 683-686.

[23] T.B.Gibbons, V.Lupinc, D.Mclean., *Effect of grain size, particle size and γ' volume fraction on strain relaxation in Ni-Cr base alloys*, Mater. Sci. Eng. 9 (1975), 437.

[24] T.B.Gibbons, B.E.Hopkins, Met. Sci. Jour. 5(1971) 233.

[25] B.Weiss, R.Stickler, *Phase instabilities during high temperature exposure of 316 austenitic stainless steel*, Met. Trans. Vol. 3 (1972), pp.851.

CHAPTER 6: MECHANISMS FOR ANELASTICITY

The previous chapter highlights the importance of conducting tests which are relevant to power plant loading cycles. Anelasticity is seen to play a major role in influencing the material behaviour. A decrease in rupture strain and increase in creep life was observed. In order to explain these trends, it is important to understand the microstructural changes occurring within the material particularly during the unload phase. Previous studies of anelasticity [1] have observed reordering of dislocation substructures during anelasticity. This chapter presents results obtained from electron microscopy. Changes in the deformation mode (from conventional creep to anelasticity or vice versa) may result in changes to dislocation/precipitate densities which will affect the material behaviour. This objective of this part of the study was to characterise the changes in dislocation substructure occurring during plastic recovery.

6.1 INTRODUCTION

Identifying mechanisms which give rise to 'reverse' creep during stress reductions is fundamental for prediction methods used in assessing material behaviour. Generally, such behaviours have been explained using dislocation studies. Lloyd and McElroy [2] have suggested all creep transients may be described by a superposition of anelasticity and forward creep and also mention anelasticity is due to unbowing of the pinned dislocations. In order for anelastic strain to occur, there must be an inhomogeneous distribution of stresses within the material. Also, there must be a viscous process by which external force is removed [3].

Both dislocation-particle interactions and grain boundaries control creep rate and in a way also control the mechanisms of anelastic recovery. Steady state creep and the slow-stage

strain relaxation may be controlled by recovery which is enhanced in the vicinity of grain boundaries which can act as vacancy sources and sinks [12]. There can be effects of dislocation densities on the material behaviour. It has been observed that during steady state creep, if the grain size is less, increased dislocation numbers are seen [12]. This might contribute to the influence of grain size on the relaxed strain. Also, dislocation densities increase with plastic strains which could explain the influence of plastic deformation on anelastic strain.

Reviewing the past work done on anelasticity, it is evident that both internal stresses and dislocation interactions play a role. Interactions of dislocations with precipitates and other entities is one of the main mechanisms of creep as explained in chapter 2. The number, size and distribution of precipitates and dislocations will influence the overall behaviour of the material. Internal stresses if any can cause mismatches in the crystal lattice which can be measured through diffraction. For these reasons, two main techniques were employed to understand the material mechanisms during anelasticity. TEM examination was used to understand precipitate/dislocation numbers and neutron diffraction was used to study the internal stresses. This chapter presents the observations obtained from TEM microscopy.

6.2 TEM Examination

6.2.1 Equipment Details

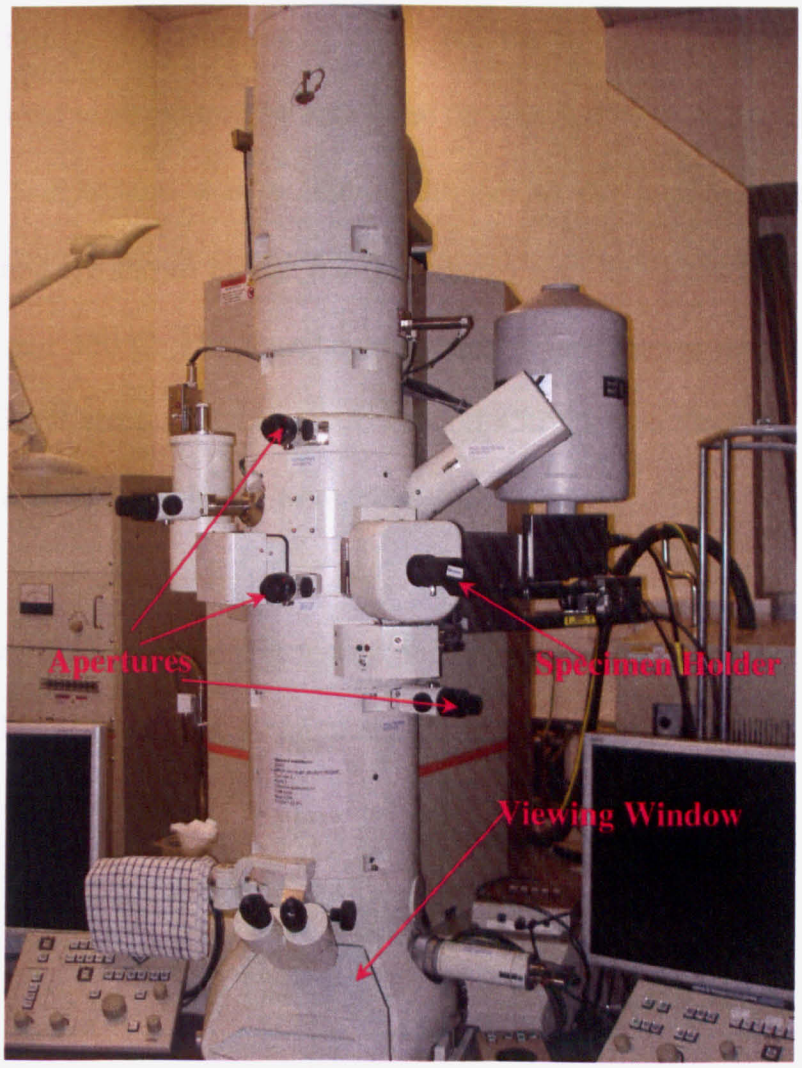

Fig. 6.1 JEM 2100 microscope

The microscope used in this project was a JEM 2100 manufactured by JEOL. The accelerating voltage was 200keV. The emitter was a lanthanum hexaboride crystal. The microscope had a magnification range of 1500-1200000X and a point resolution of 0.25nm.

6.2.2 Specimen Preparation

Specimens which represented different periods of unloading were generated. This was done by stopping the specimens at different times during the unload. The specimens were first taken through one load/unload cycle and the test was stopped during the second unload. The tests were stopped by lifting the furnace and then cooling the specimens in air using fans. Temperature was monitored throughout the process. Some of the cooling curves obtained are shown in Fig. 6.2. Specimens were extracted from tests conducted at both 650°C and 550°C. The time taken by the temperature to reduce to a value below which significant creep does not occur (around 450°C) was about 2-3 minutes. For each condition at least two specimens were prepared.

Fig. 6.3 shows the approximate stoppage points on the strain curve. For 650°C, specimens were stopped after 5 seconds, 30 minutes, 1 hour, 4 hours, 12 hours, 36 hours and 48 hours into the unload.

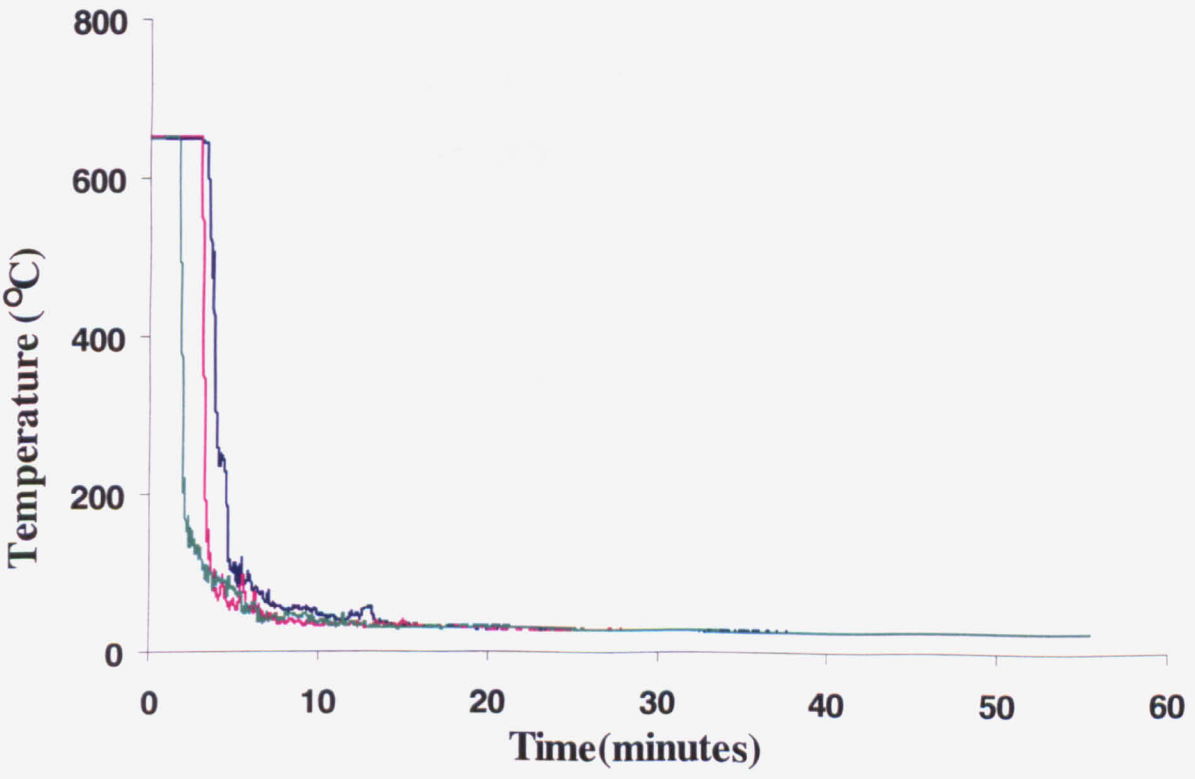

Fig. 6.2 Cooling curves obtained during specimen extraction

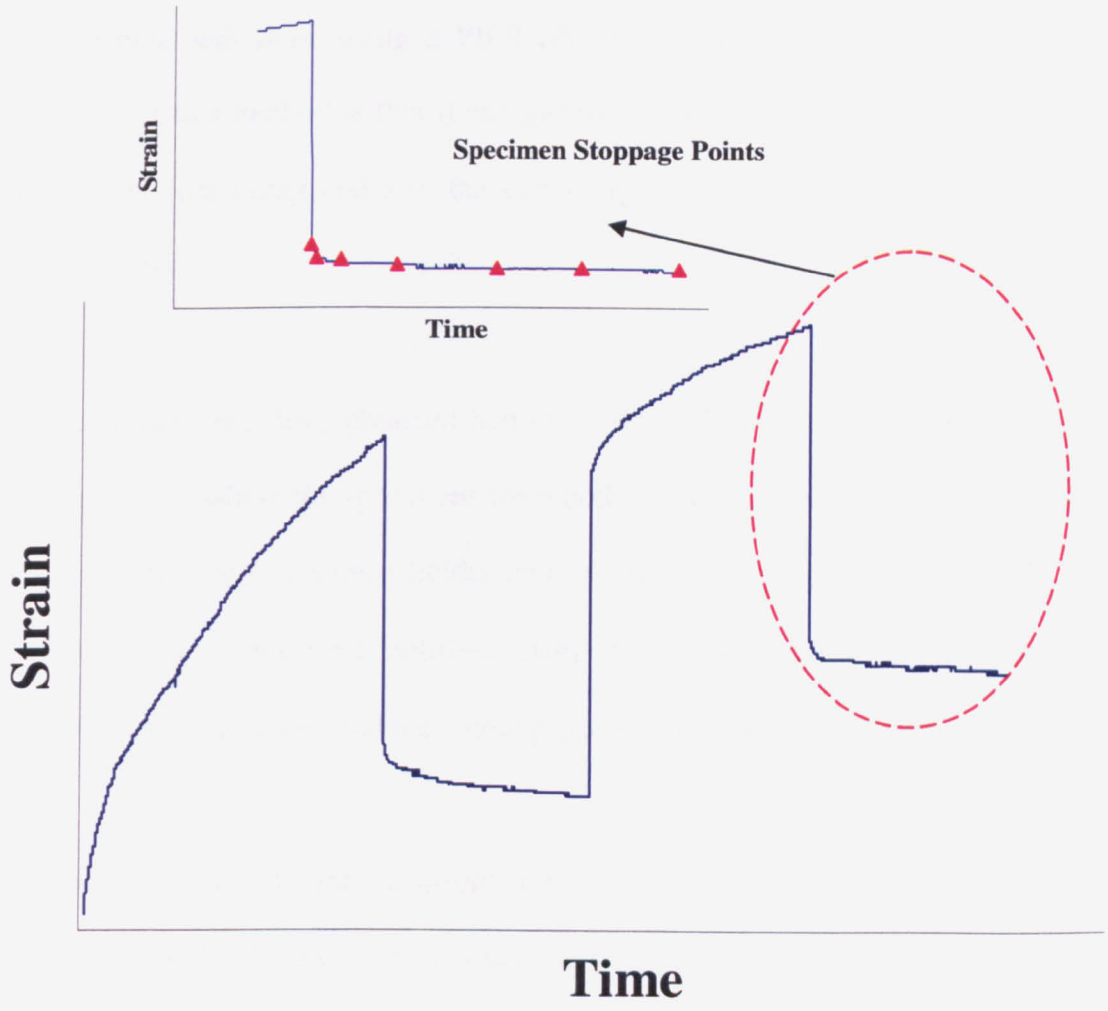

Fig. 6.3 TEM specimen extraction

TEM specimen preparation consists of a number of steps depending on the type of preparation method used. Two different methods were used: ion polishing and electropolishing.

Initially, thin discs with thickness of 250-350 microns were cut from the samples using Electric Discharge Machining (EDM). These samples were 6 mm in diameter (gauge diameter). Smaller discs (3 mm diameter) were then manufactured using these. Care was taken not to plastically deform the specimens during this process. Techniques to achieve minimal alteration to the material during the preparation stage have been briefly described in [14] and [17].

Ion Polishing

Ion Polishing was done using a PIPS (Precision Ion Polishing System) machine. The advantage of this method is that it can generate a thin area fairly reliably but the method can be time consuming and also the surface quality of the specimens generated may be relatively poor.

The 3 mm diameter discs obtained had to be thinned down to about 50-60 microns. This was done by polishing the specimens from both sides. Initially the specimens were stuck to a specially designed specimen holder and ground using 40 grit, 15 grit and 5 grit paper. Finally the specimens were polished using one micron diamond polishing liquid. The specimen was then turned and the whole process repeated for the other side.

The next step was to mount the specimen inside the ion polisher. The specimen was placed in a dual-clamp holder and placed in the chamber. A photograph of the system is shown in Fig. 6.4. The whole chamber was set in vacuum. The specimen holder was rotated inside the chamber. Two ion guns were present in the system. The angles of these guns could be adjusted so that the beams are incident on the specimen at different angles. The intensity of these beams could also be changed. An automated system monitored the formation of thin areas and stopped the machining if a hole was detected.

Initially the beams were kept at an angle of 8°. An initial voltage of 5 keV was used in the guns. As the sensitivity in the monitoring system increased due to the creation of thin areas, the gun voltage and the angle of incidence were decreased. After the hole was created, the specimen was machined at 4 keV and a gun angle of 4° for 15-20 minutes.

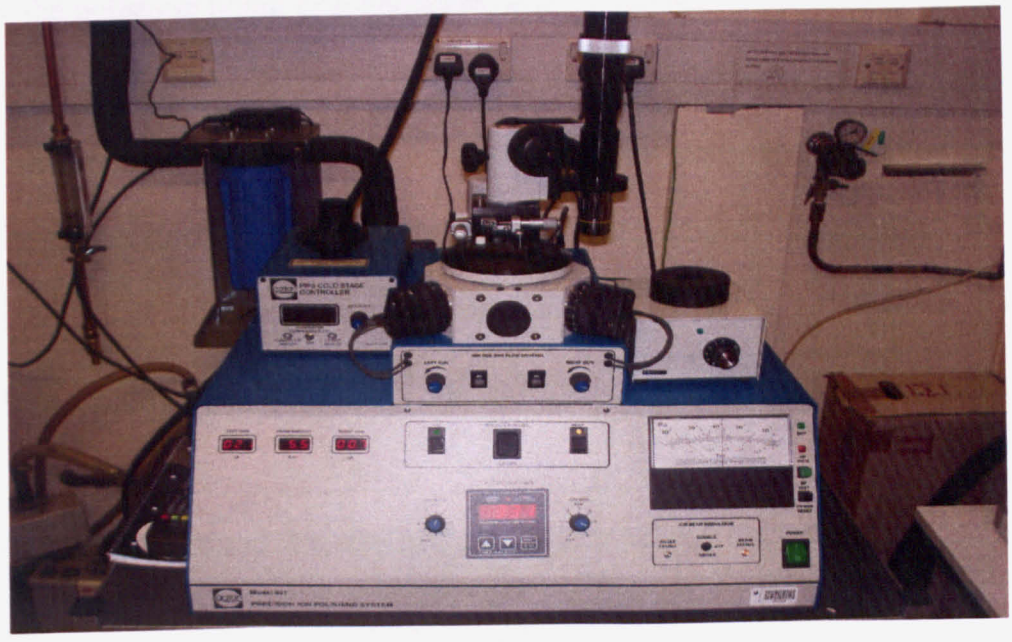

(a)

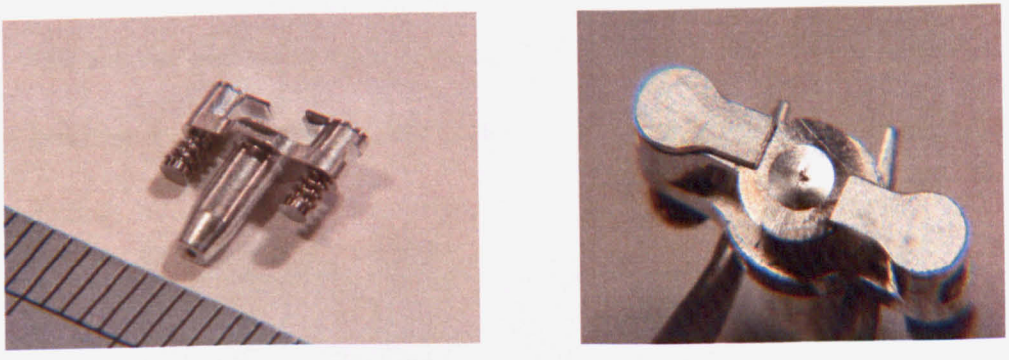

(b)

Fig. 6.4 (a) PIPS System (b) Dual clamp specimen holder

Electropolishing Technique

This is an alternative method to produce TEM samples. The technique is much quicker than the ion polishing method but sometimes can produce inconsistent results if the polishing conditions are not maintained carefully. The technique initially consisted of polishing the specimen to about 100-120 microns as described in the previous section. The second step was to place the specimen in a holder which would keep it in place during the electro-polishing. The interior of the holder had a base plate made of platinum.

Initially the polishing liquid (5% perchloric acid in methanol) was poured into the system and was cooled to a temperature of -60°C using a unipump which circulated liquid nitrogen around the system. Once the system reached the desired operating temperature, the specimen holder was placed in the system and the polishing was started. The voltage during the whole polishing process was kept at 20V. A photo-detector assisted in terminating the process when the hole was created.

Once the hole was created, the specimen was cleaned using a three step cleaning process. Initially, the specimen and specimen holder assembly was cleaned using laboratory grade methanol. The cleaning was done by dipping the system into the liquid and removing it quickly. The second and third steps consisted of removing the specimen from the holder and then holding it using forceps. This assembly was then dipped and removed from lab-grade methanol.

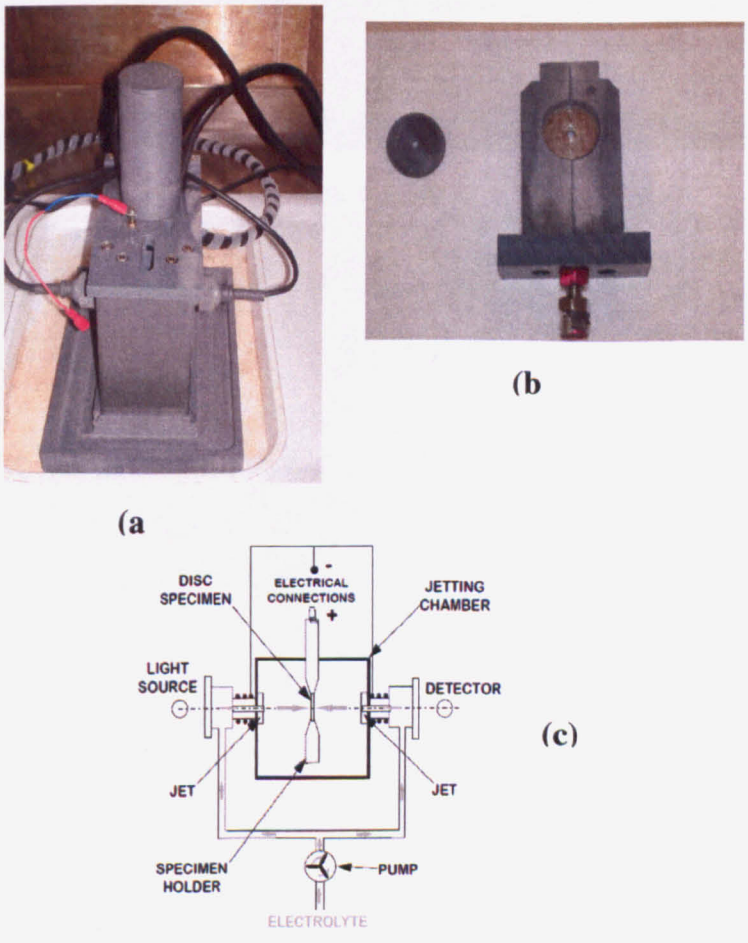

Fig. 6.5 (a) Electropolisher system (b) Specimen holder (c) Schematic of electropolshing system

6.3 Microstructural Observations

This section presents some of the TEM observations. Only a sample of the photographs has been presented for each condition.

As Received Condition- Fig. 6.6

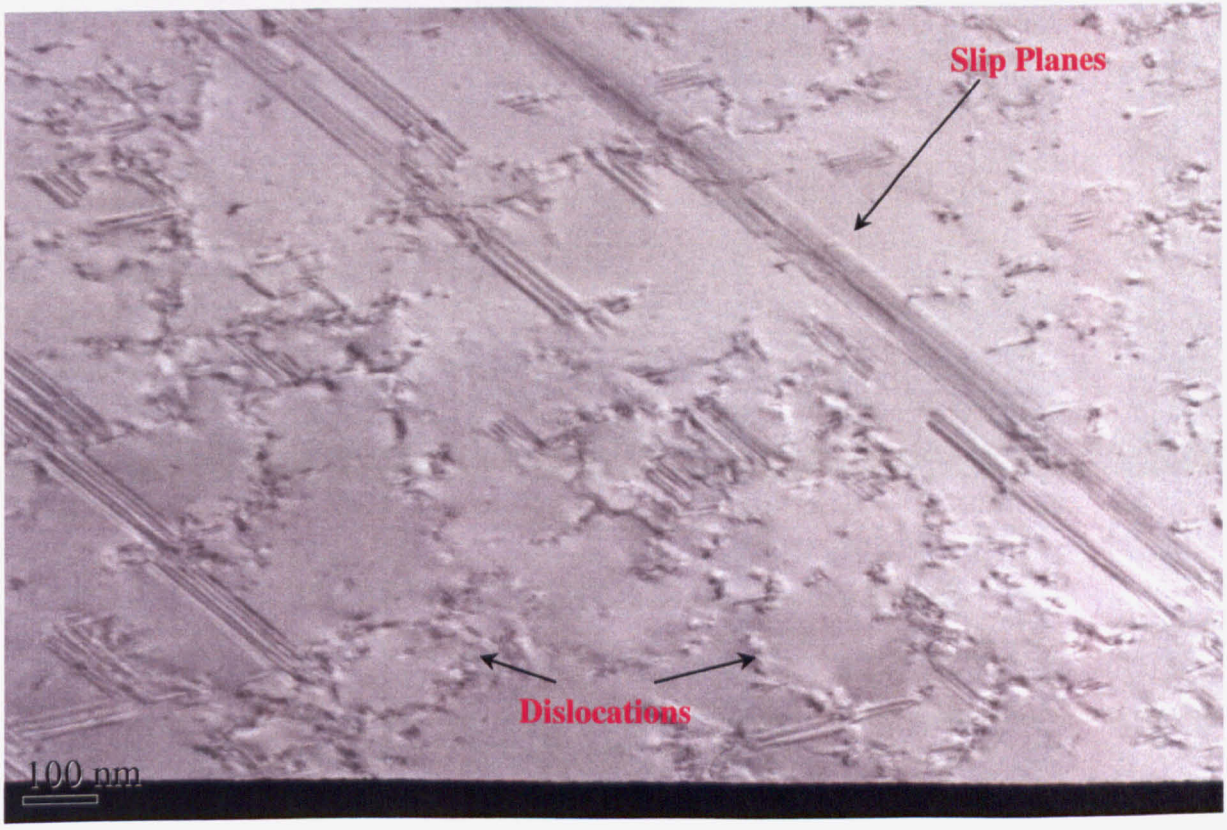

Fig. 6.6 (a)

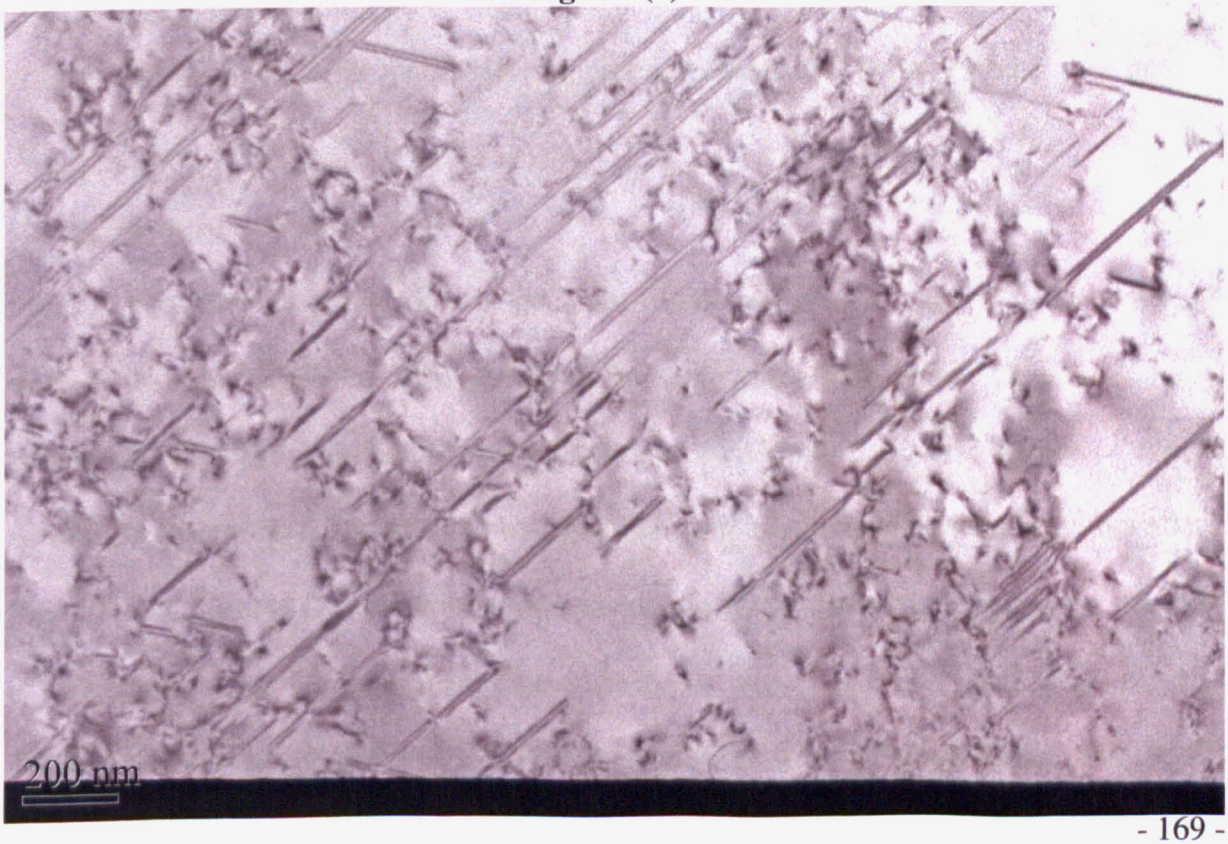

Fig. 6.6 (b)

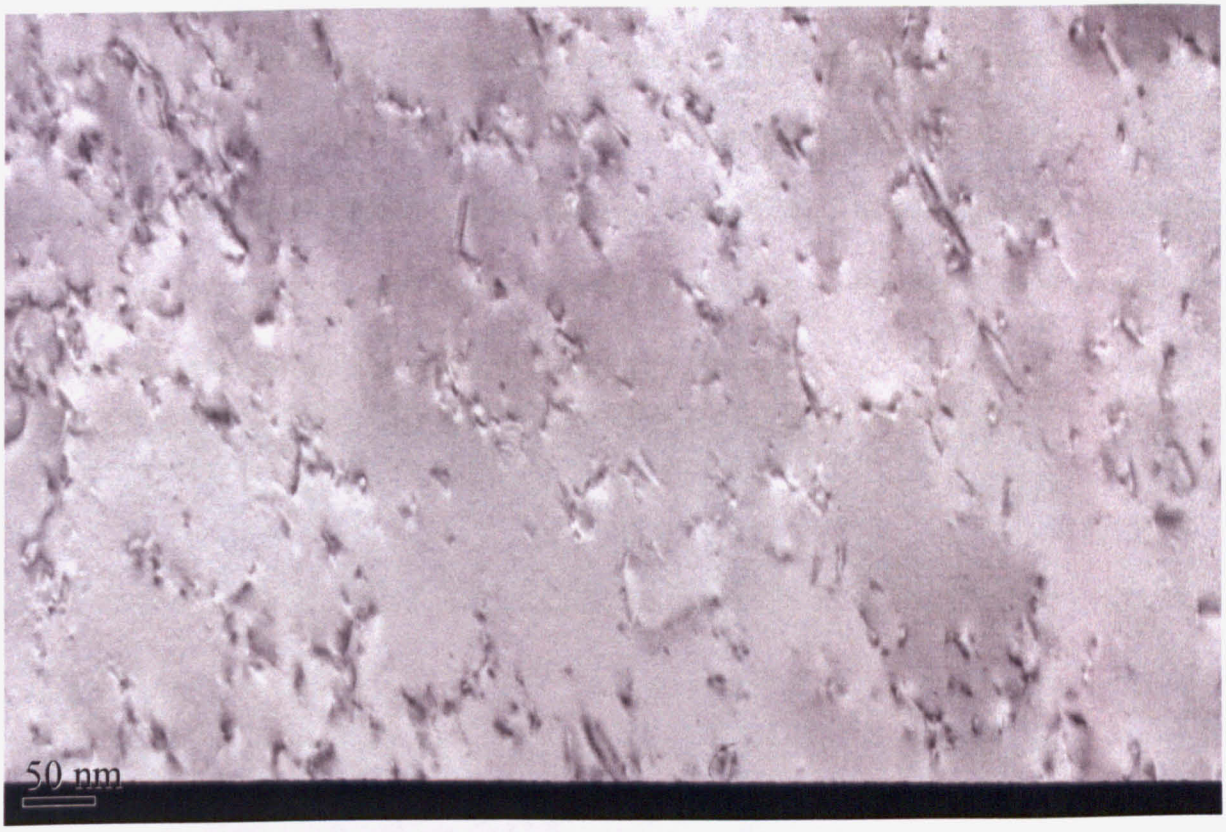

Fig. 6.6 (c)

Fig. 6.6 (a), (b), (c) As-received microstructures

The as-received material shows the presence of slip planes. Some dislocations can also be seen. The initial dislocation density was estimated to be about $10^8/m^2$. Figures 6.6(a), (b), (c) are photographs of the as-received material from different bars. The observed deformations are due to the manufacturing processes associated with producing the bars.

Creep Rupture Specimen- Fig. 6.7

Fig. 6.7 shows images from a creep specimen which was taken to rupture. Test conditions were 650°C and 200MPa. The specimen ruptured after 600 hours. Carbides tend to precipitate along the grain boundaries initially and then along slip planes and other entities within the grain. Fig. 6.7(a) shows two $M_{23}C_6$ precipitates situated along a grain boundary. Fig. 6.7(b) shows the Orowan bending mechanism with the material. As seen, a dislocation is being pinned between two precipitates. Fig. 6.7(c) shows extensive dislocation pinning. There is also some evidence of dislocation tangles. A stack of dislocations along a slip

plane can also be observed. Fig. 6.7(d) is a good example showing interactions between dislocations. A dislocation of about 500nm is pinned by two precipitates. Smaller dislocations (less than 100nm) can be seen to interact with it. As explained in section 2.11.1, this interaction(s) will depend on the orientation of the stress field around the dislocation. Other dislocation interactions can also be seen.

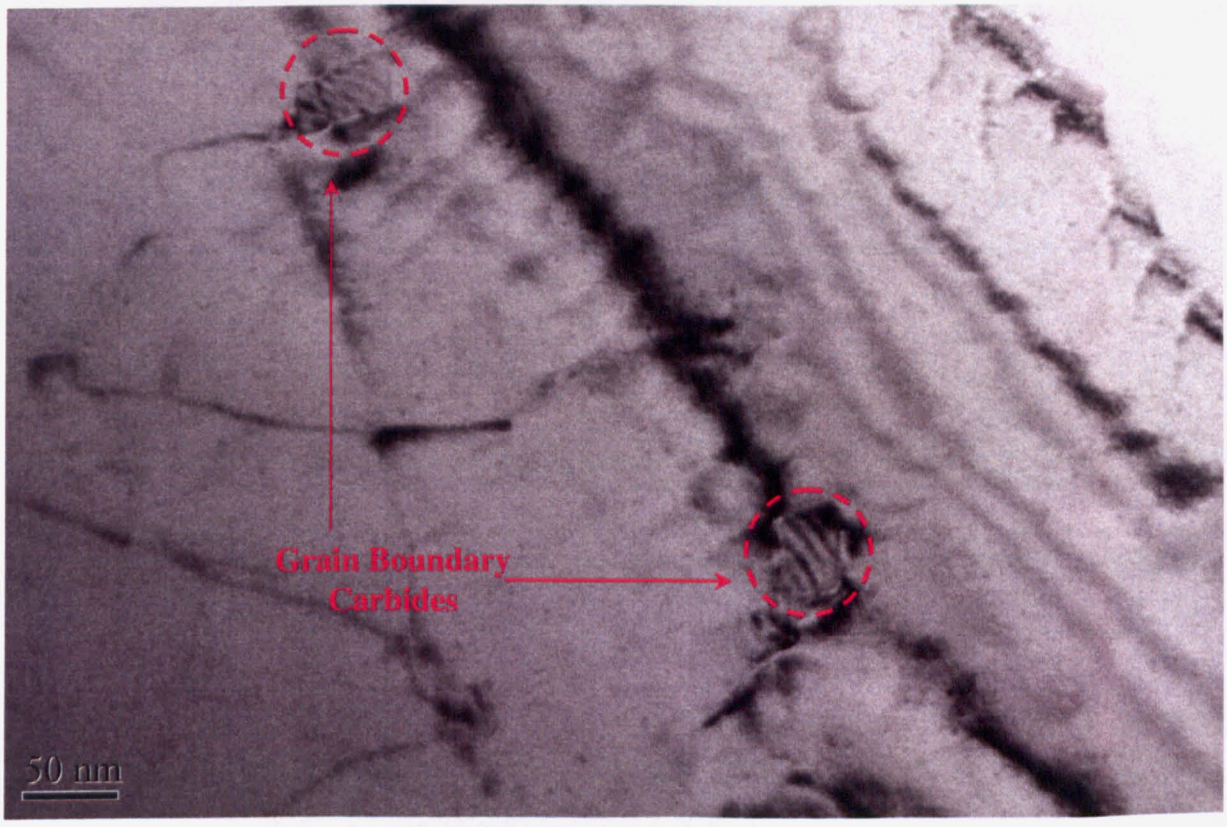

Fig. 6.7(a) Showing grain boundary precipitates. Specimen is a creep rupture specimen with test conditions 650°C and 200MPa

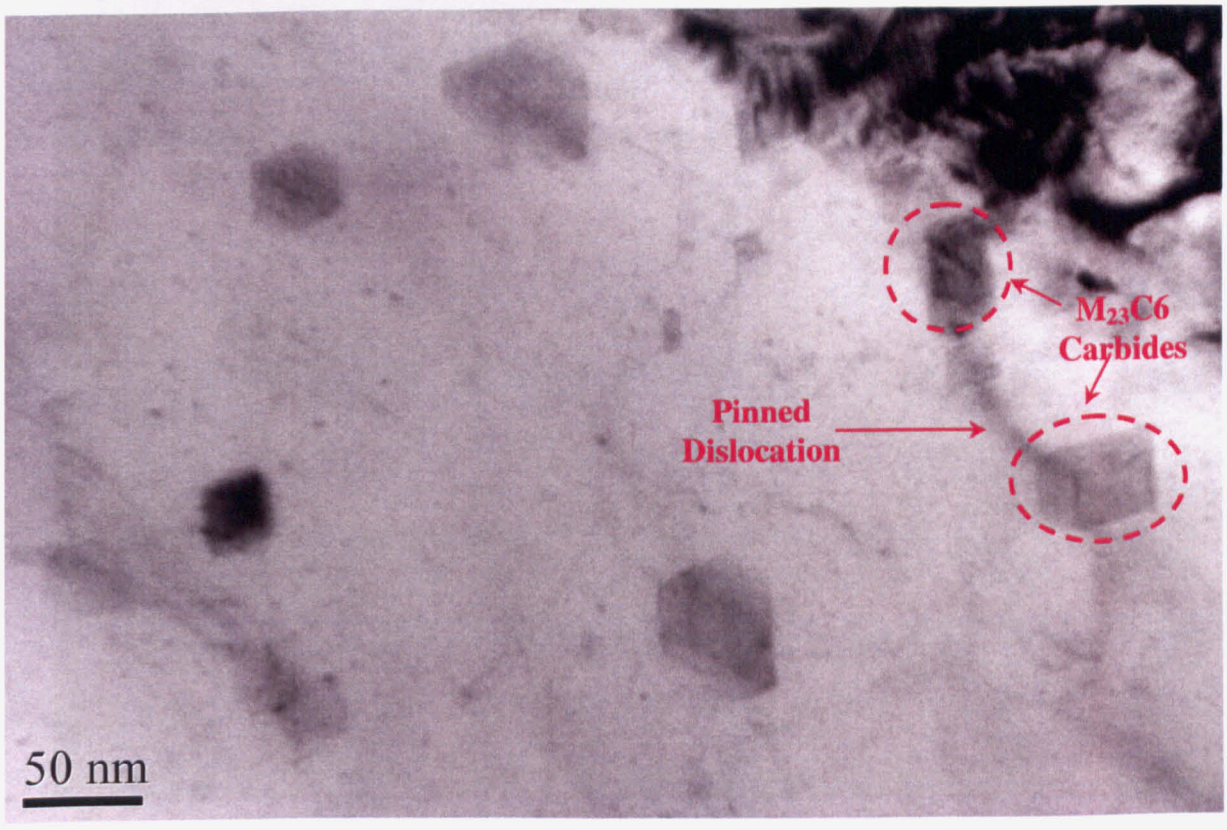

Fig. 6.7(b) Orowan bending observed in a creep rupture specimen (650°C 200MPa)

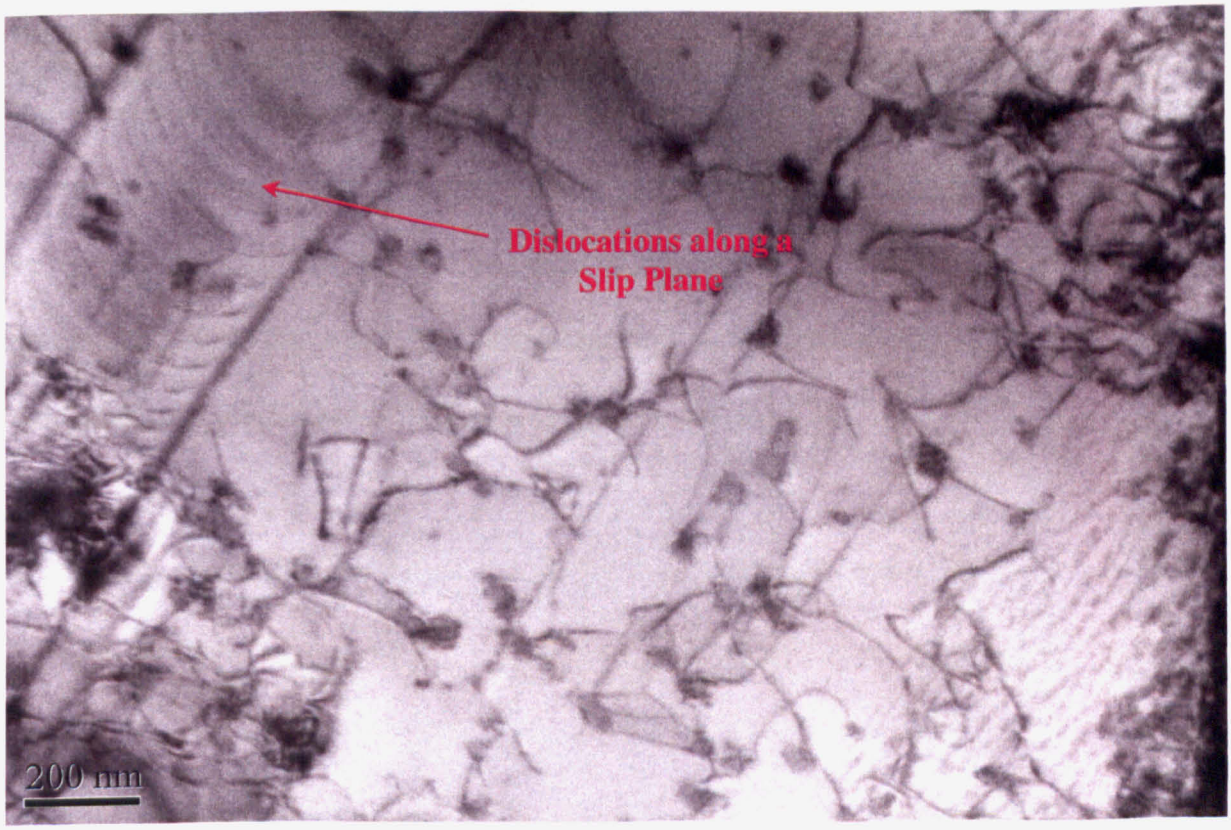

Fig. 6.7(c)Interactions between dislocations and precipitates. A stack of dislocations along a slip plane can also be seen

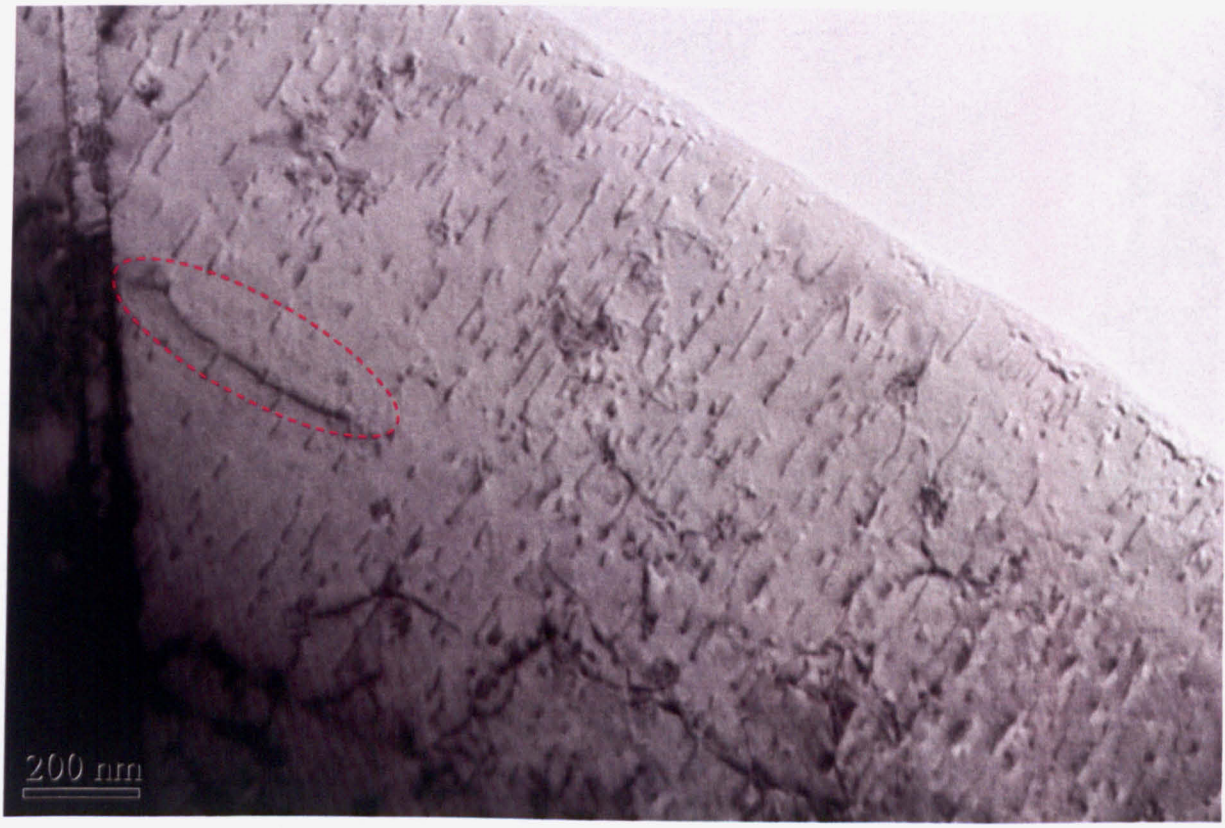

Fig. 6.7(d) Interactions between different dislocations

Specimen Stopped Immediately after Unloading (Test Conditions 650°C 180MPa) - Fig. 6.8

The specimen was tilted and dislocations along several 'g' vectors were observed. Interactions of dislocations with precipitates can be observed. There is some evidence of decrease in dislocation networks compared to specimens which were stopped further into the unload period (Fig. 6.12). The microstructural state of this specimen can be compared with specimens unloaded for 5 seconds (Figs. 5.6, 5.9 and 5.11).

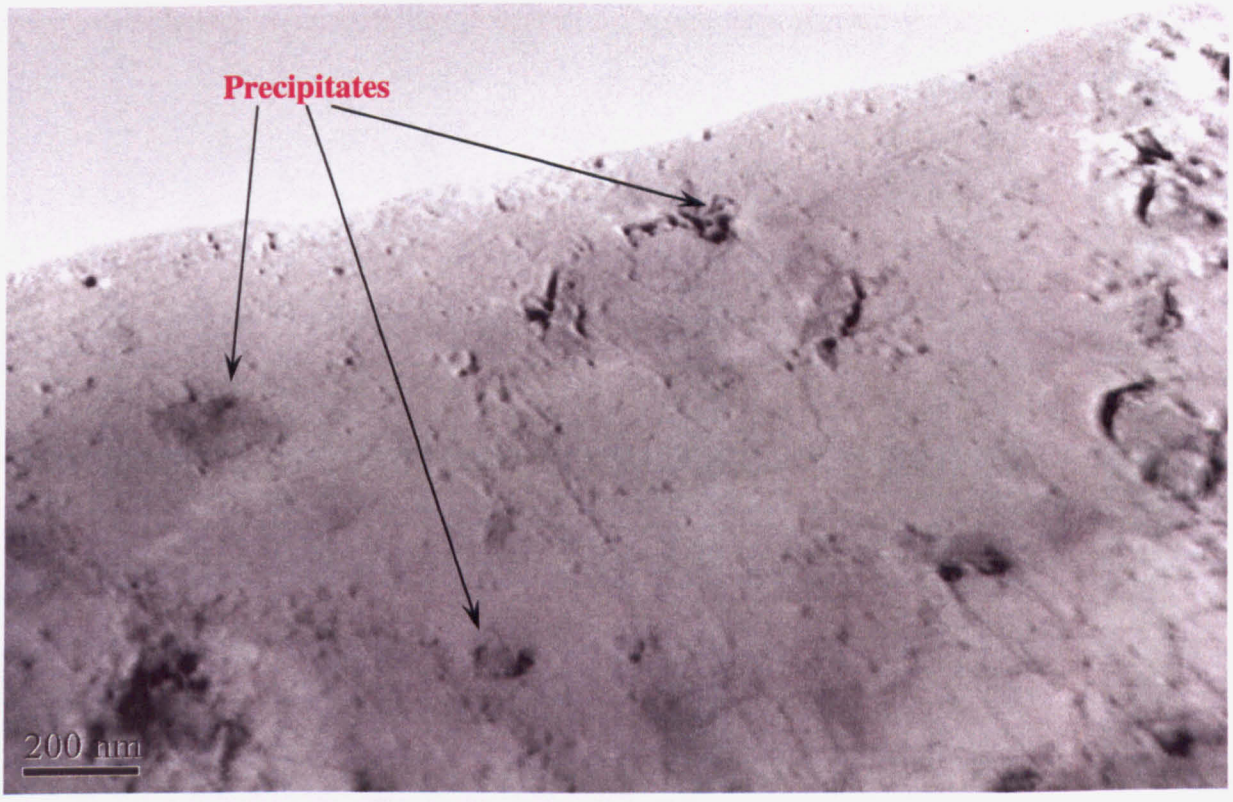

Fig. 6.8 Specimen stopped immediately after unloading. There is strong evidence of reduced number of dislocation networks

Specimen stopped 30 minutes after unloading (Test Conditions 650°C 180MPa) – Fig. 6.9

Looking at the strain curve obtained when the specimen was unloaded, this specimen represents the highest anelastic strain rate. There is greater evidence of dislocations interacting among themselves as seen in Fig. 6.9 (a). Along with grain boundaries, slip planes are preferential carbide precipitation sites. In such regions a higher probability of dislocations interacting with carbides will exist. One such region is shown in Fig. 6.9(b).

In order to calculate carbide densities, the specimen was tilted so as to remove the dislocations from the picture. Fig. 6.9 (c, d) shows the result of tilting the specimen so that only precipitates are visible. Certain areas within the specimen also show some evidence of precipitate coarsening.

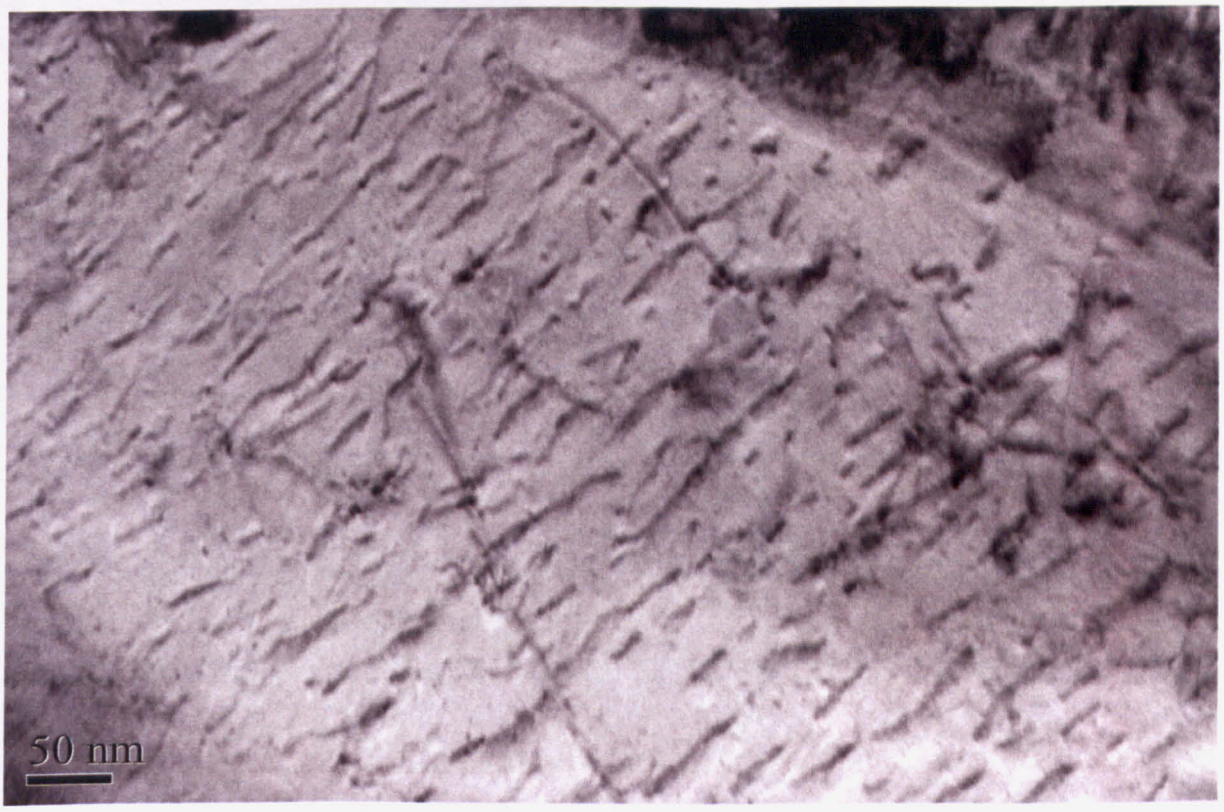

Fig. 6.9 (a) Interactions of dislocations with other dislocations. Specimen was stopped 30 minutes after unloading

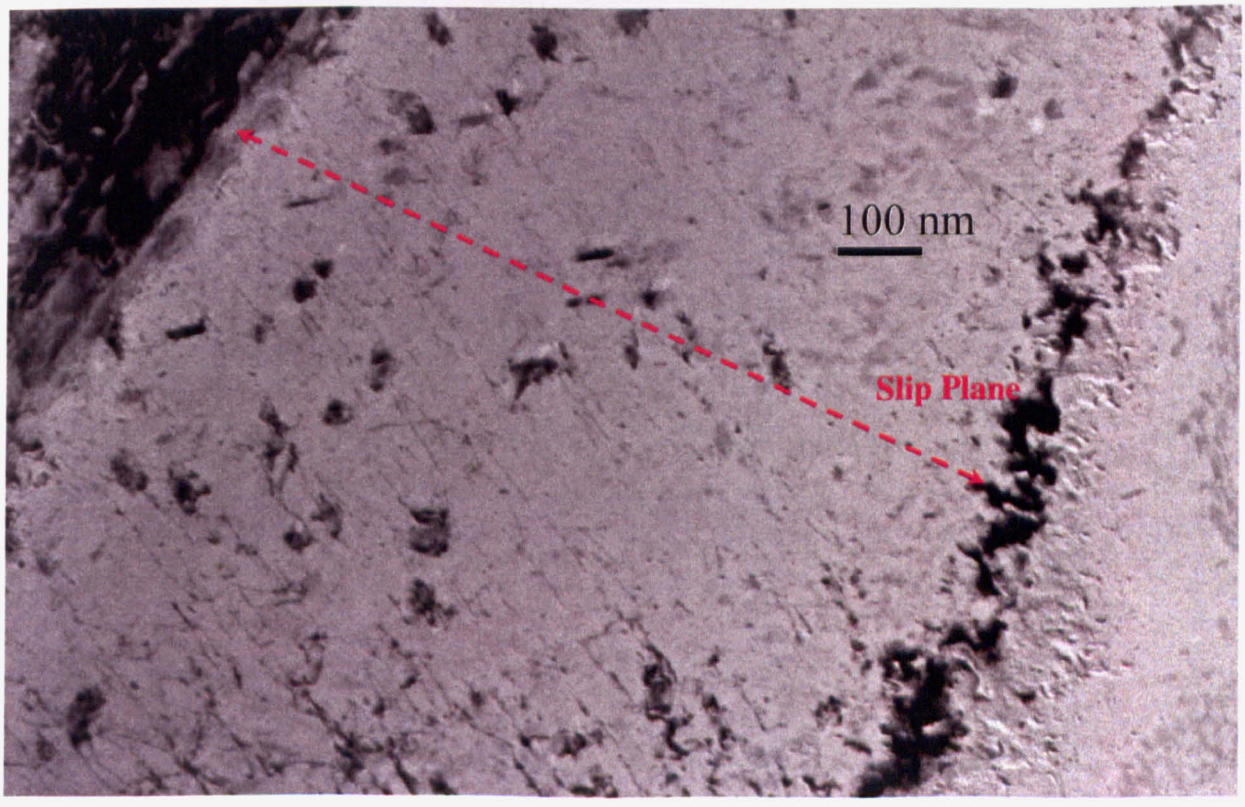

Fig. 6.9(b) Precipitates along a slip plane. Specimen was stopped 30 minutes after unloading (Test conditions 650°C 180MPa)

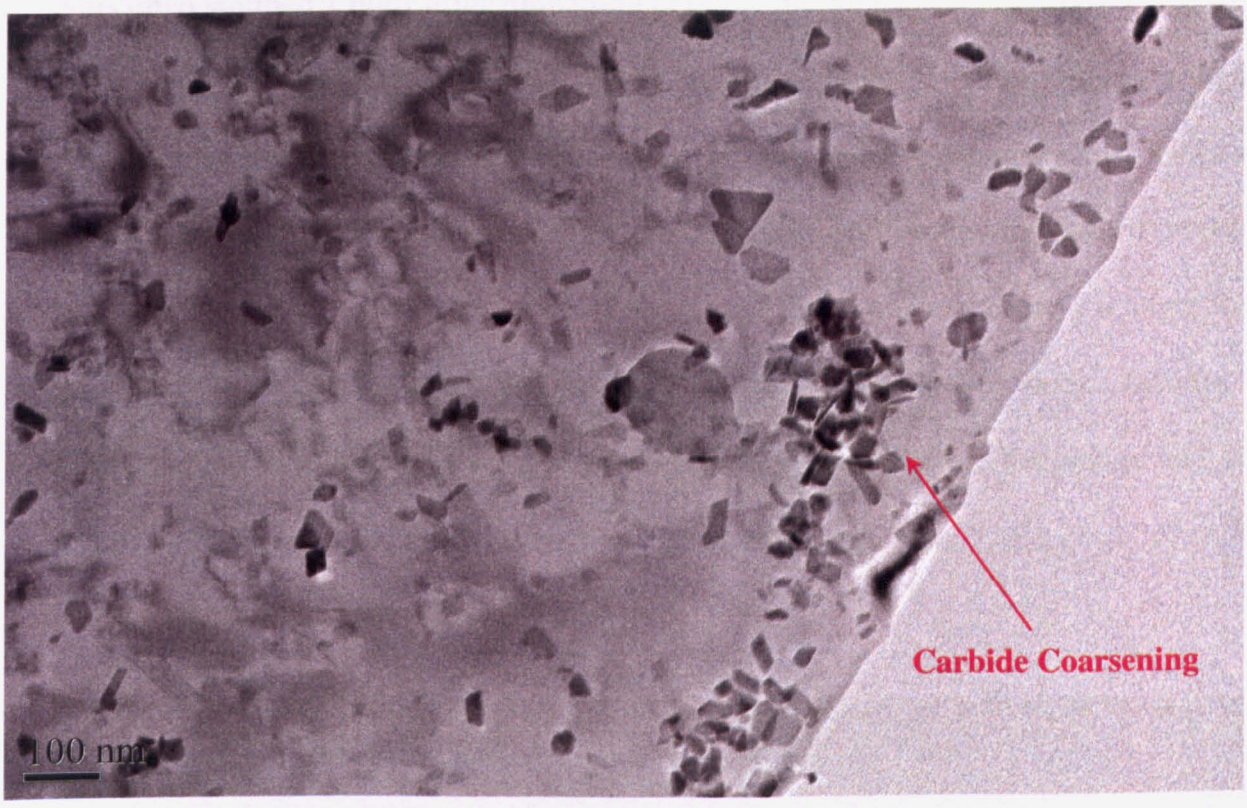

Fig. 6.9(c) Estimating carbide densities. Specimen was tilted so that dislocations were invisible. Carbide coarsening can also be observed. Carbide sizes ranged from 20 microns to 100 microns. Specimen was stopped 30 Minutes after unloading.

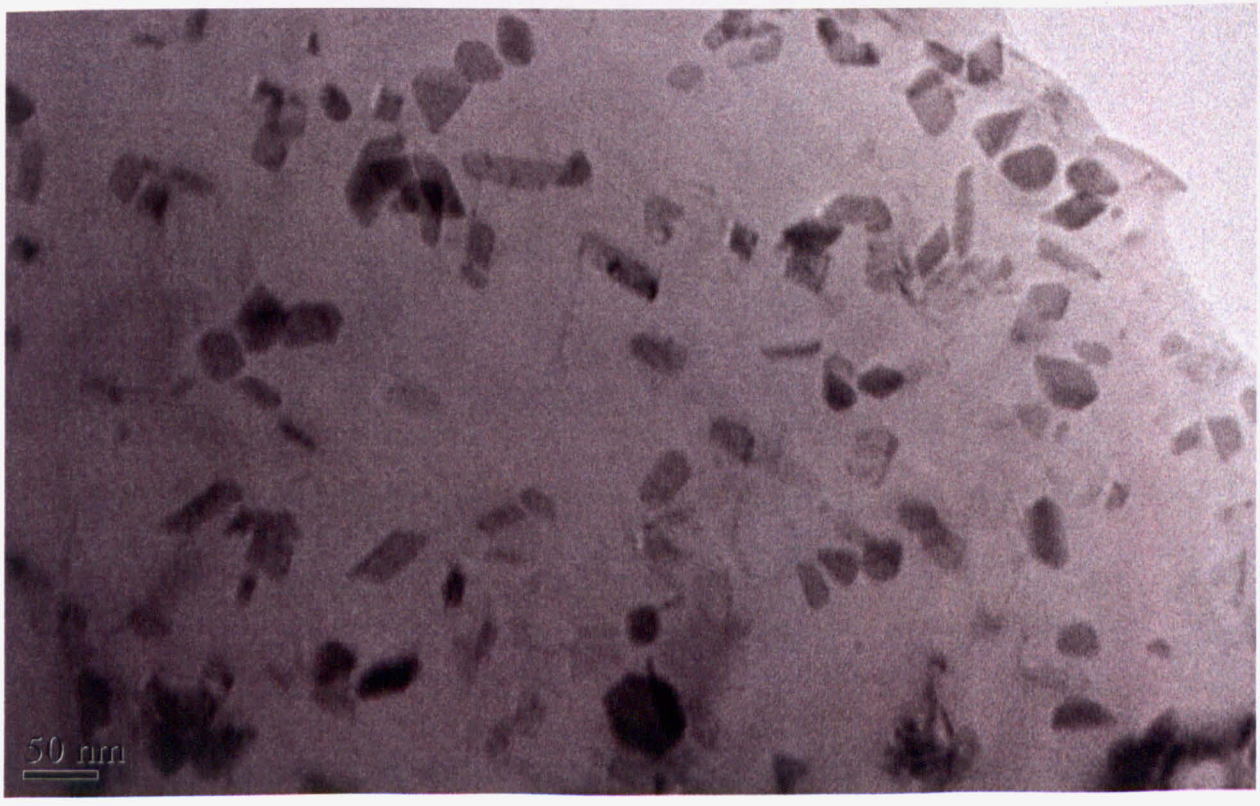

Fig. 6.9(d) Carbides structures inside the specimen. Specimen was stopped 30 Minutes after unloading. (Test conditions 650°C 180MPa)

Specimen stopped 1 hour after unloading (Test Conditions 650°C 180MPa) - Fig. 6.10

Looking at the anelastic strain curve (Fig. 5.14), this specimen corresponds to a higher anelastic strain than the specimen used in the previous set of photographs. At this point, one can expect changes in the dislocation substructures as dislocation motion will result in some annihilation. Fig. 6.10(a) shows dislocation-precipitate interactions in a larger field of view. Observation of the other areas within the sample showed lesser densities of dislocations within tangles. It may be that dislocations can untangle themselves and as a result, an increased number of interactions with carbides are seen. Fig. 6.10 (b, c) shows carbide structures and their distributions.

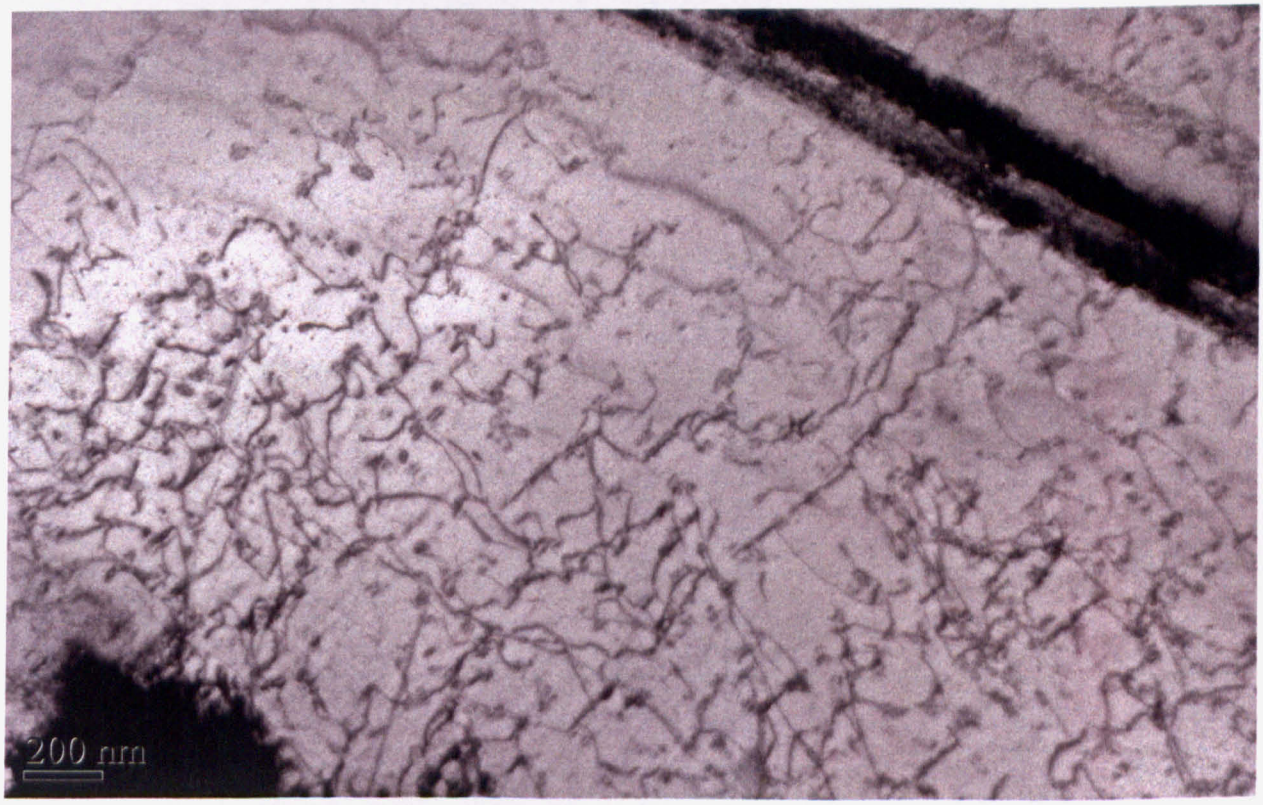

Fig. 6.10(a) Precipitate-carbide interactions seen in a Specimen 1 hour after unloading (Test conditions 650°C 180MPa)

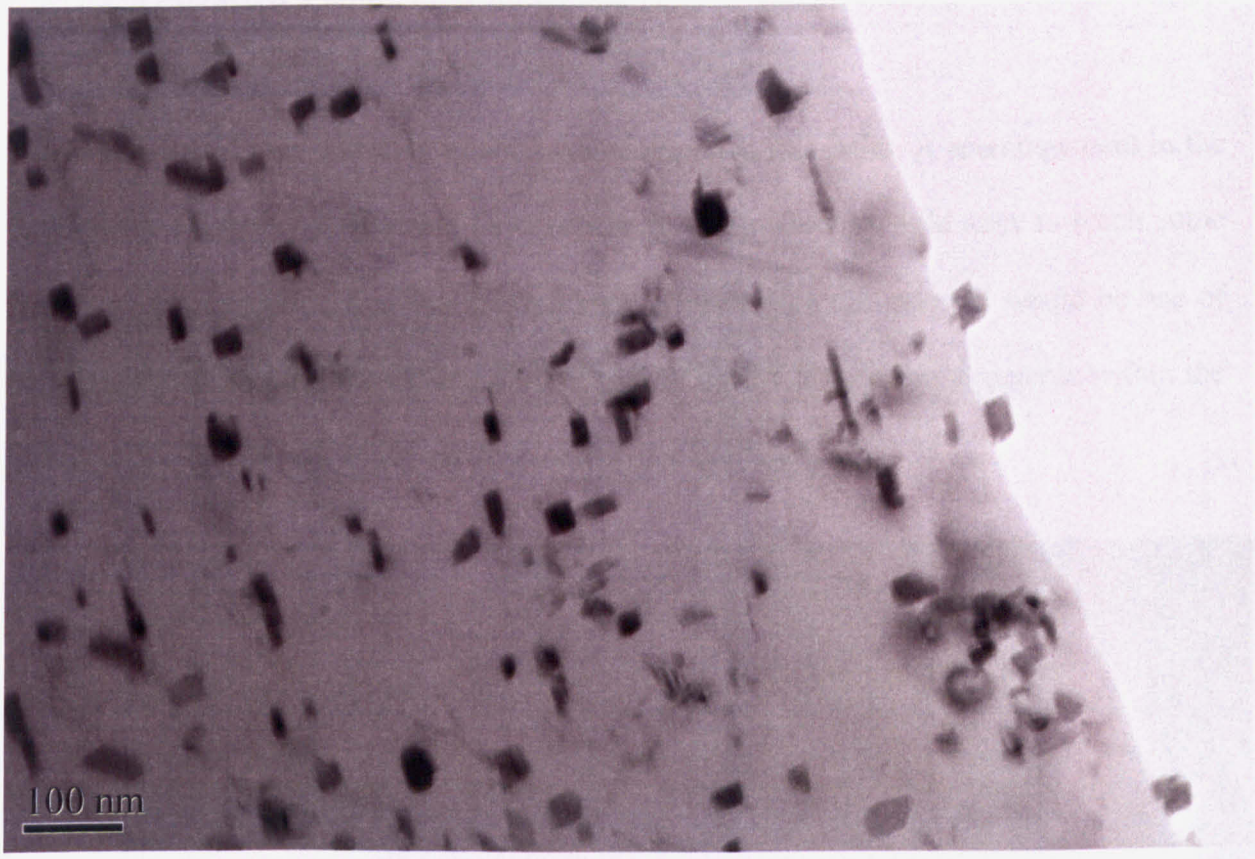

Fig. 6.10(b)

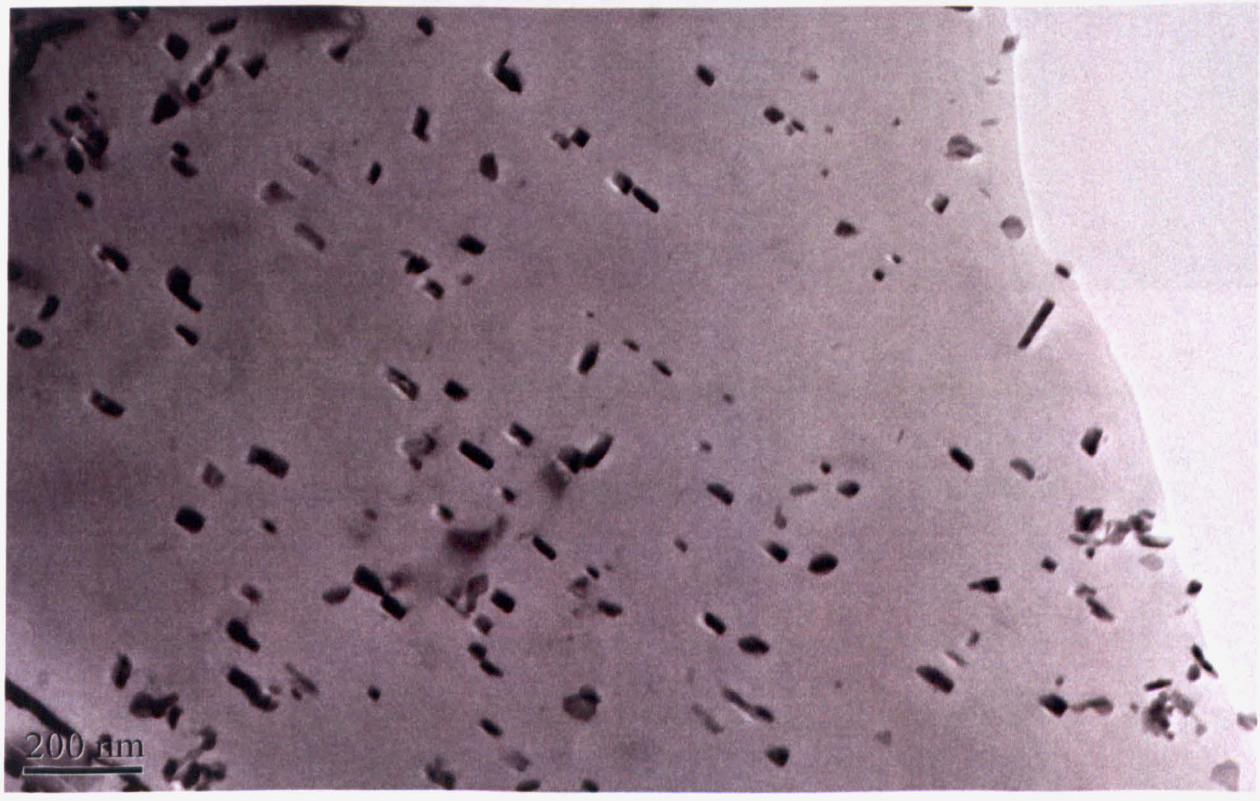

Fig. 6.10 (b) and Fig. 6.10(c) Distribution of carbides within the material. Specimen was stopped 1 hour after unloading (Test conditions 650°C 180MPa)

Specimen extracted 4 hours after unloading (Test Conditions 650°C 180MPa) - Fig. 6.11

Anelastic strain in the material would have saturated at this point. A rearrangement in the dislocation structures would also have occurred. The material would start to reach some sort of an equilibrium state. The internal back stress within the material would be one of the main driving forces for deformation. Fig. 6.11 shows dislocation structures within the material. Most dislocations interactions seem to be with carbides.

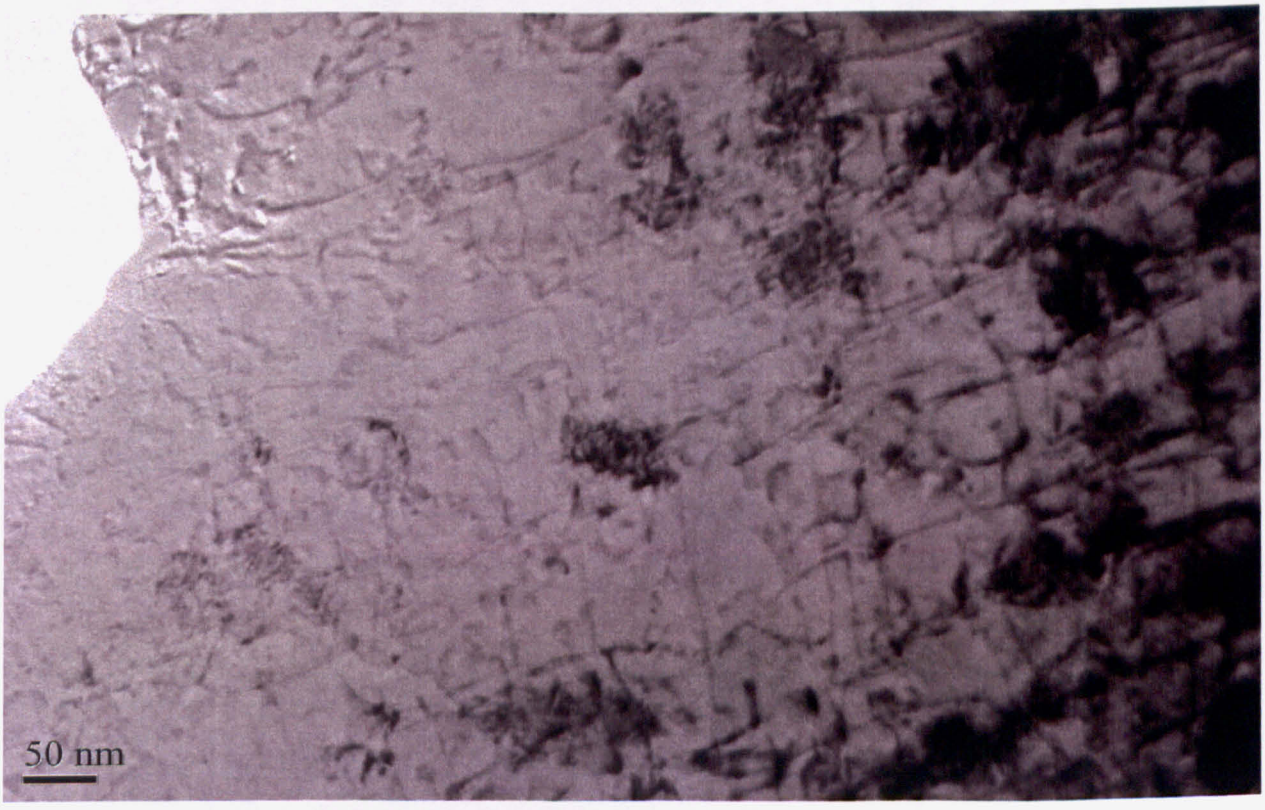

Fig. 6.11 Dislocation networks start to form around 4 hours after unloading

Specimen stopped 12 hours after unloading (Test Conditions 650°C 180MPa) – Fig. 6.12

The anelastic strain in the material would be saturated by this time. One of the main observations in this specimen was the emergence of dislocation tangles and networks. Fig. 6.12 (a) shows dislocations interactions with carbides. The observed dislocations seem to form a network. Fig. 6.12 (b) again shows evidence of dislocation tangling. Strain curves

obtained from the load-on/load-off testing suggest that anelastic strain saturates around 4-5 hours after unloading. However, microscopic examination shows that the dislocation substructure takes a longer time to reorder.

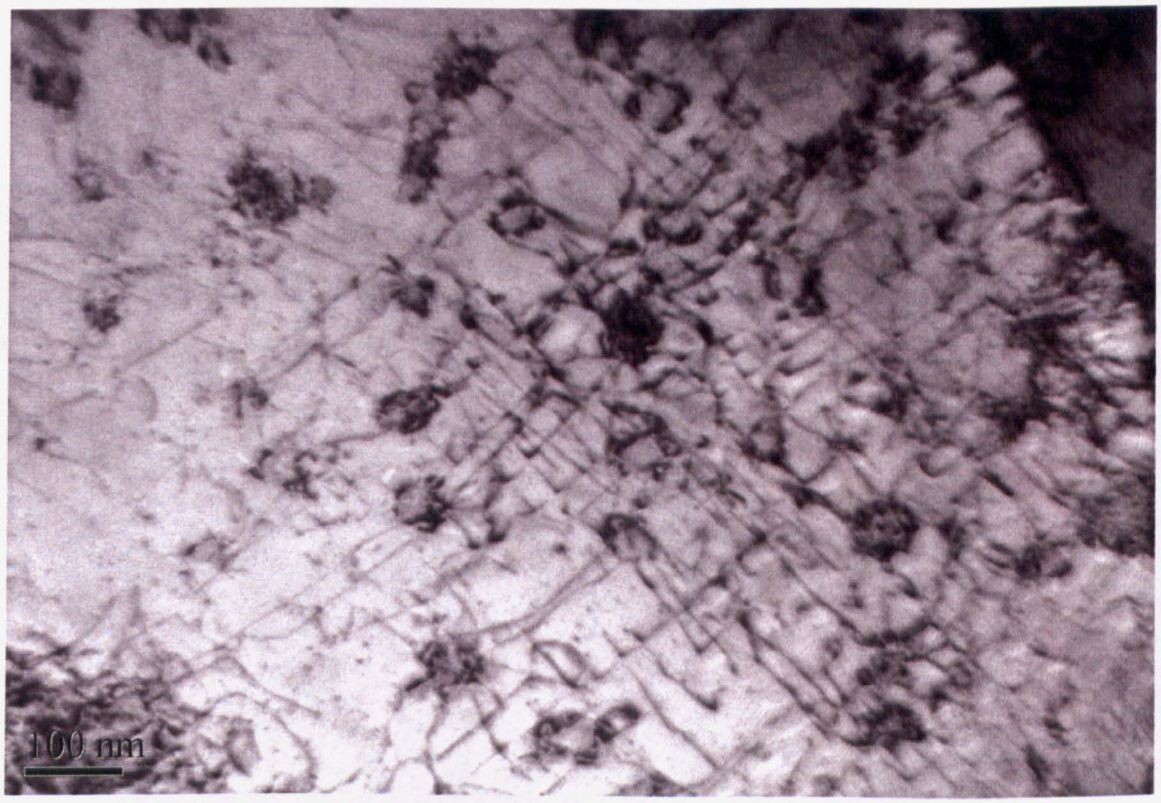

(a)

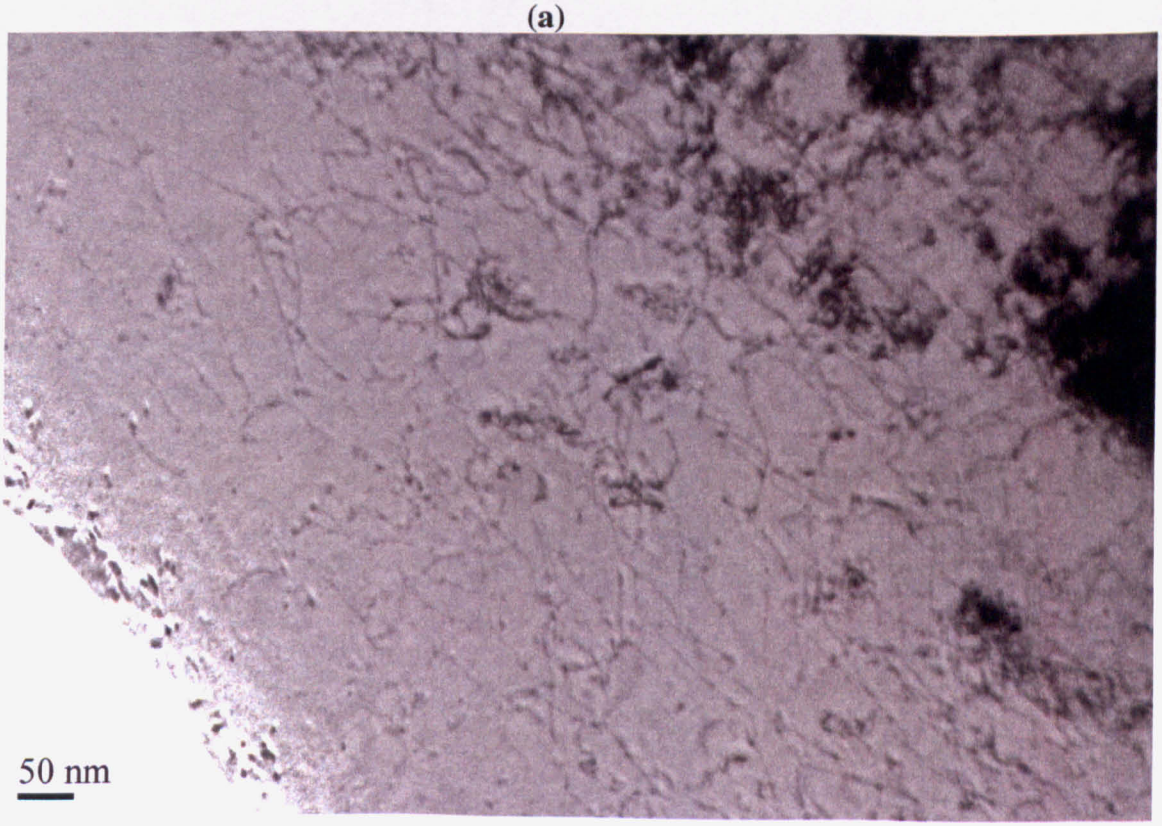

(b)

Fig. 6.12 (a) and Fig.6.12 (b) Dislocation structures seen in a specimen 12 hours after unloading. (Test conditions 650°C 180MPa). A network mode of dislocations can be observed

Specimen was stopped 24 and 48 hours after unloading (Test Conditions 650°C 180MPa) - Fig. 6.13 and Fig. 6.14

These samples would correspond to a saturated anelastic strain state. Dislocation interactions will lead to a change in the internal stress state. Hence, at a grain level, dislocation interactions and pileups will lead to a change in the backstress.

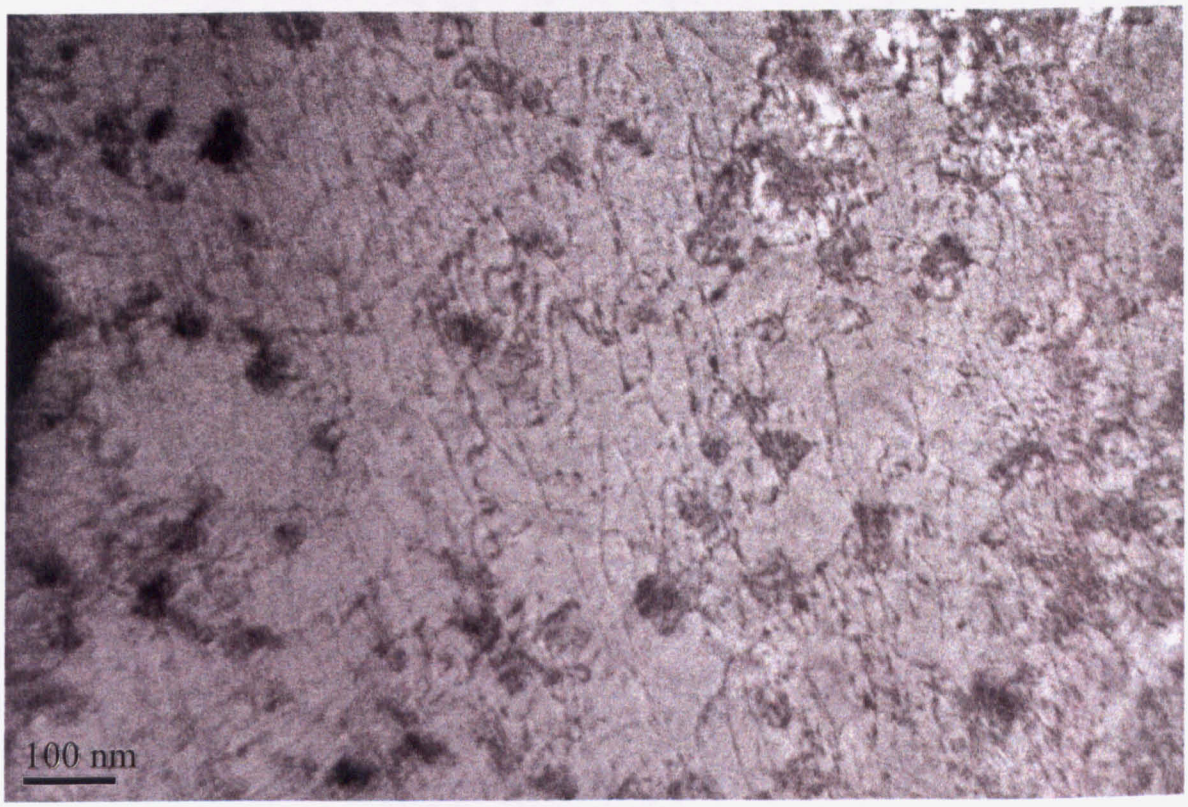

Fig. 6.13 Specimen stopped 24 hours after unloading. Dislocation-carbide interactions can still be observed in some areas. (Test Conditions 650°C 180MPa)

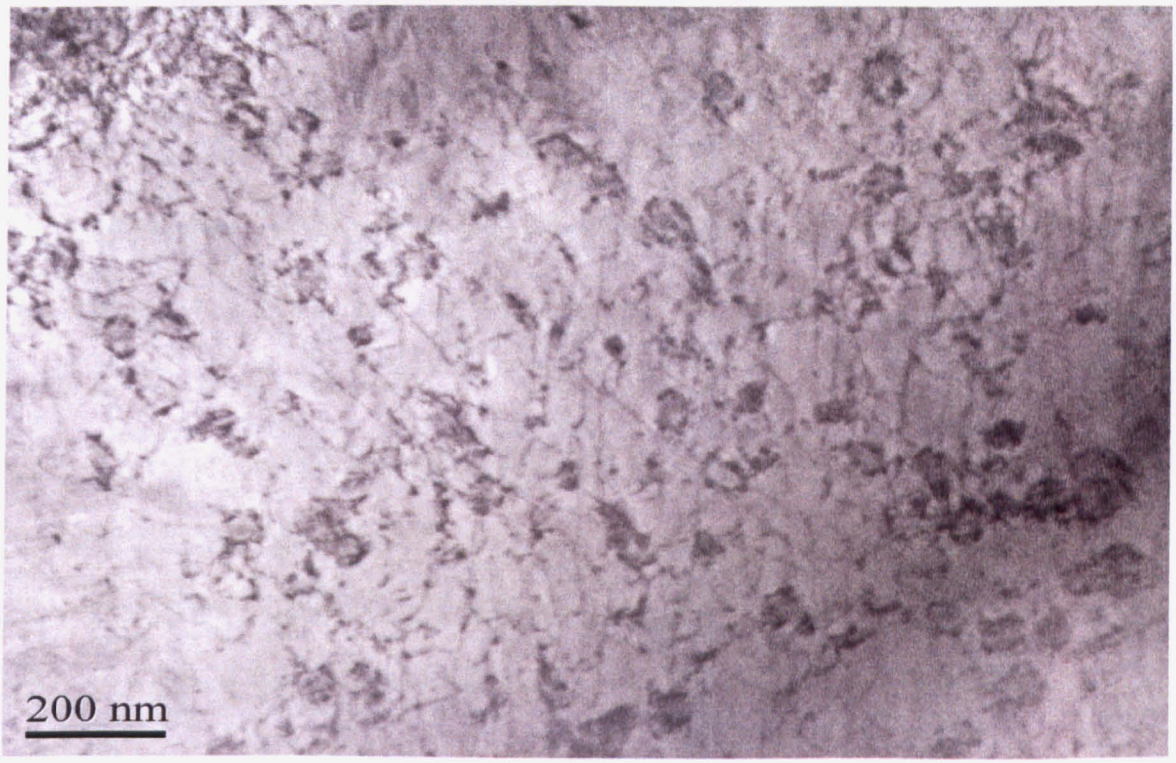

Fig. 6.14(a)

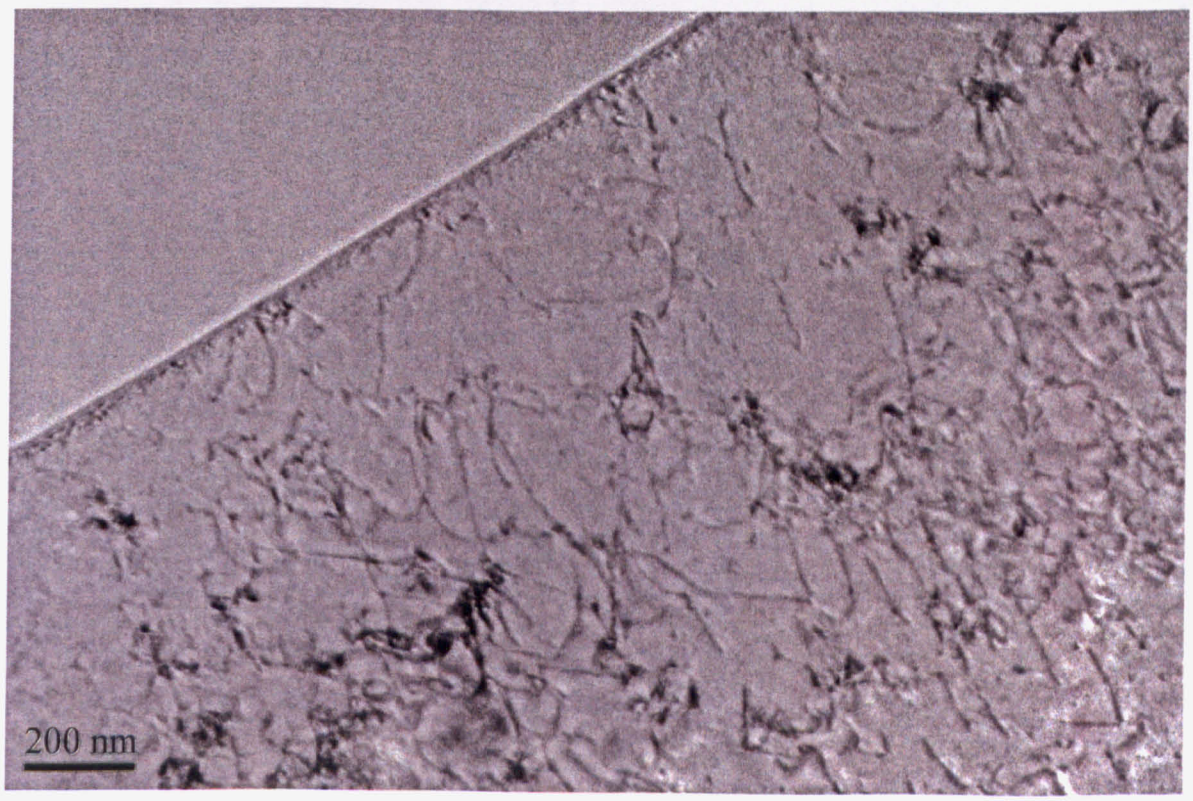

Fig 6.14(b)

Fig. 6.14 (a) and (b) Dislocation-carbide interactions observed in a specimen 48 hours after unloading. (Test Conditions 650°C 180MPa)

Specimen extracted immediately after unloading (Test Conditions 550°C 335MPa) – Fig. 6.15

If behaviour of dislocations is responsible for backstress driving anelasticity, temperature will influence these mechanisms. Observing specimens which were obtained from tests conducted at 550°C there were some differences. One of the key differences in observing the specimens obtained at 550°C and 650°C was the observation of dislocation tangles. Figures 6.15 (a) and (b) show extensive areas where dislocations are in tangles. Generally, this occurs when the dislocation motion is in the same plane as that of the obstacle. In this case, it is possible that dislocation glide is the major mechanism for dislocation motion. Due to the lower temperature, the dislocations have lower energies and thus cannot execute a climb motion.

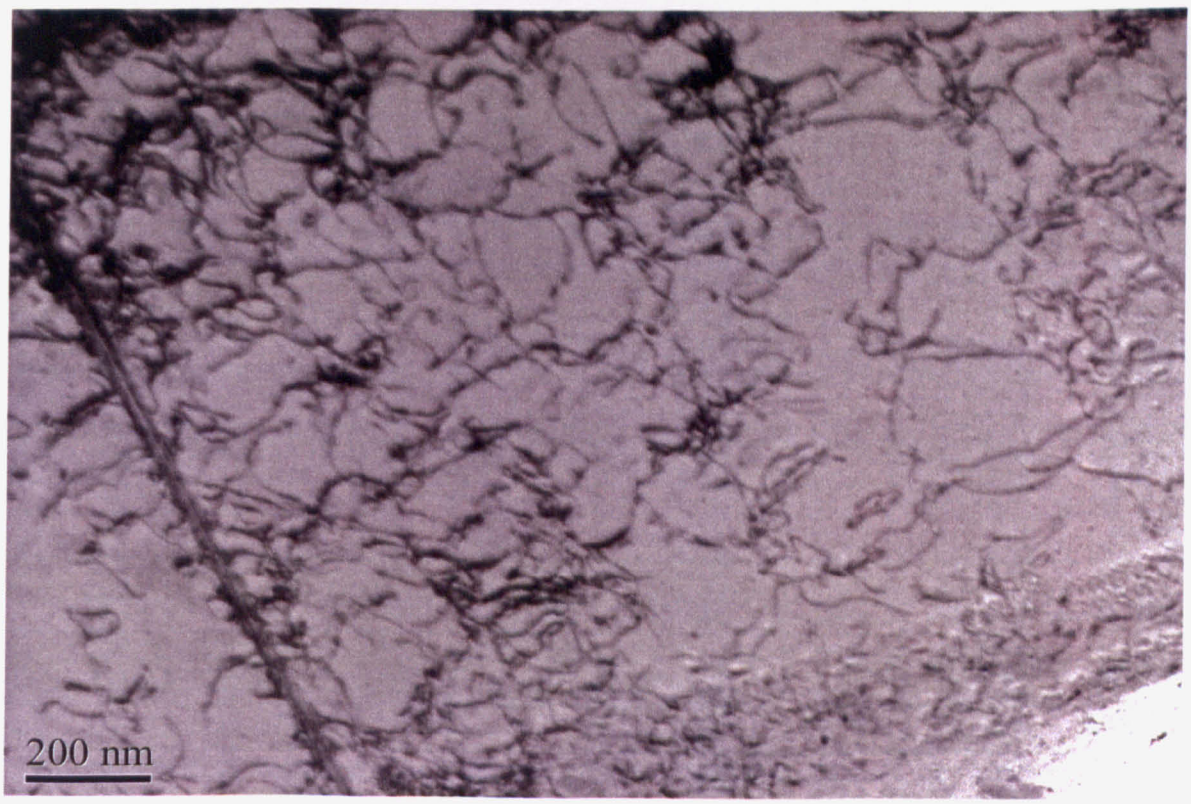

Fig.6.15(a)

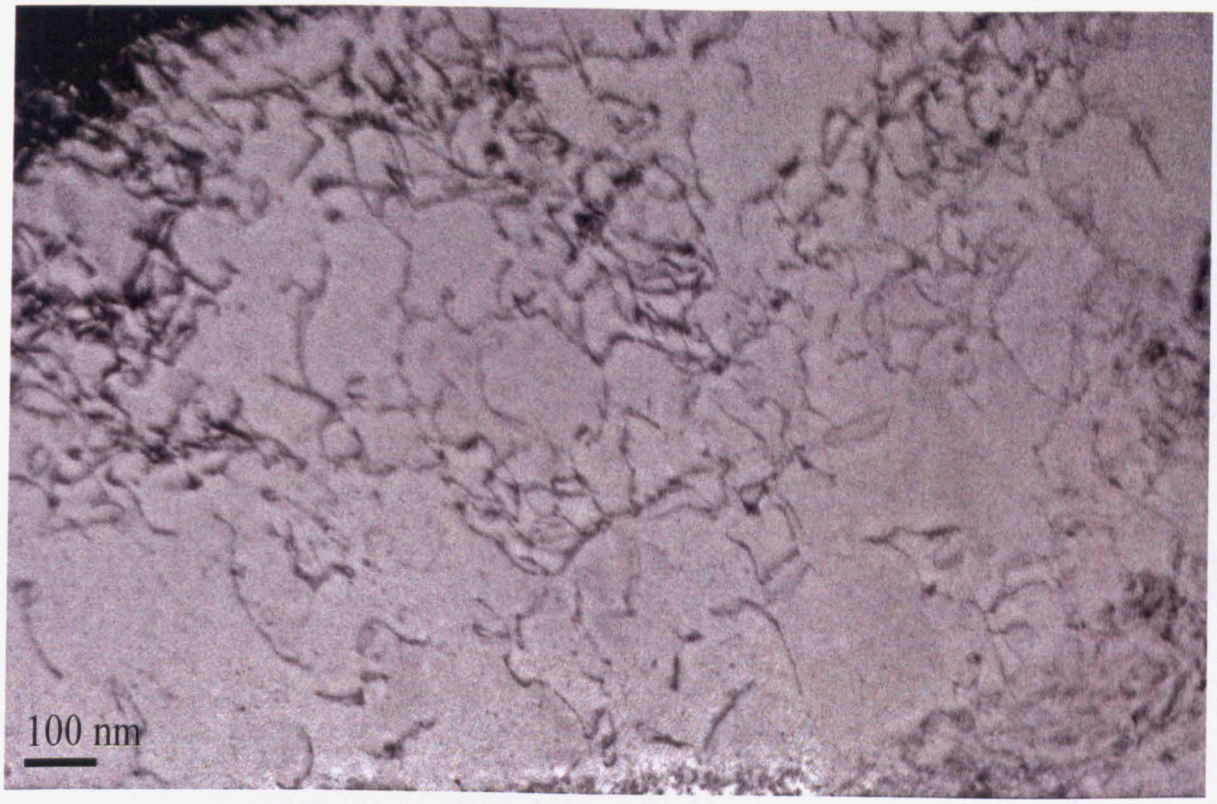

Fig. 6.15 (b)

Fig. 6.15 (a), (b) Dislocation tangles observed in a specimen immediately after unloading. Test conditions were 550°C and 335MPa.

Specimen stopped 24 hours after unloading (Test Conditions 550°C 335MPa) – Fig.6.16

Dislocation networks and tangles can still be observed. Compared to Fig. 6.15, a lesser number of dislocations are involved in tangles. In case of this specimen which was 'frozen' 24 hours after unloading, the dislocations would have had the time to untangle themselves owing to the prevalent temperature (550°C). A similar behaviour was observed in specimens prepared from tests conducted at 650°C after 4 hours of unloading. This signifies the importance of temperature. A higher temperature would mean the energy available for dislocations will be higher which would mean easier motion. Diffusion rates will be higher at 650°C when compared to 550°C and this enables dislocations to execute

the 'climb' motion more readily, thus overcoming obstacles. At 550°C, the time needed to overcome the energy barrier will be greater.

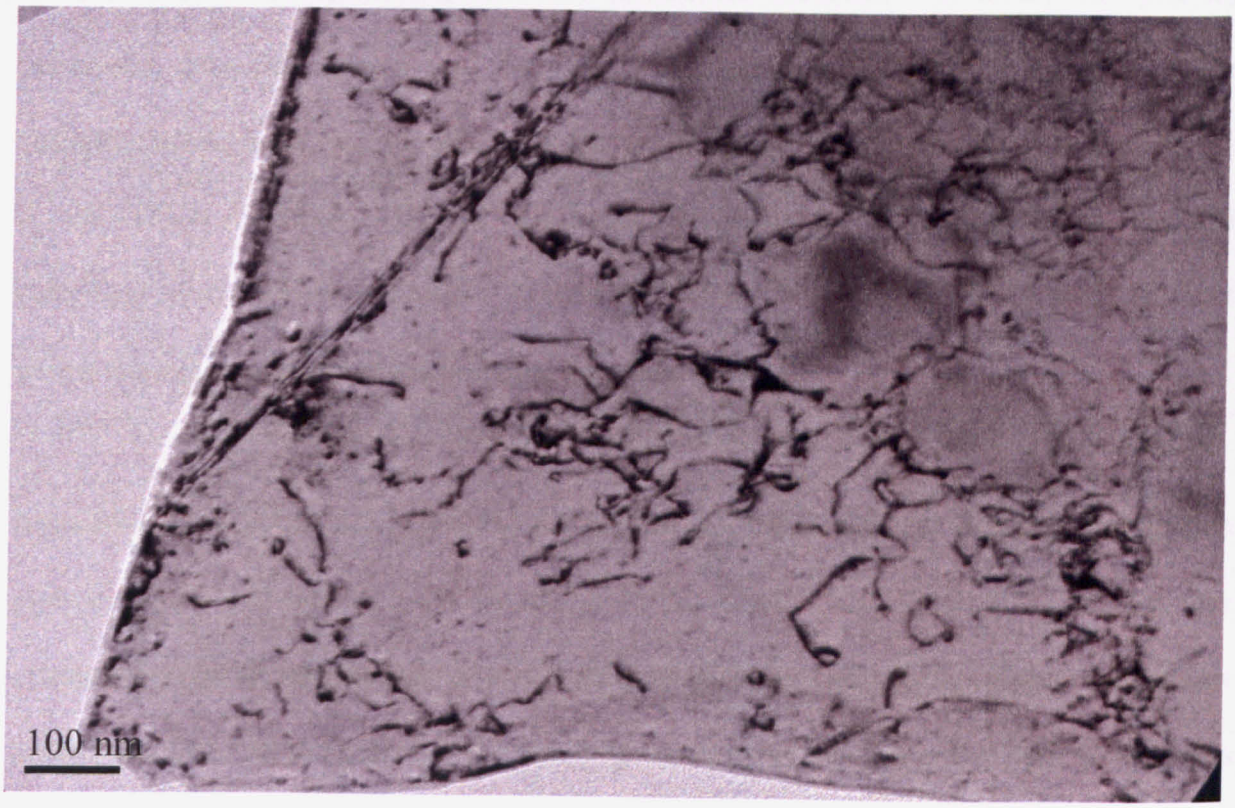

Fig. 6.16(a)

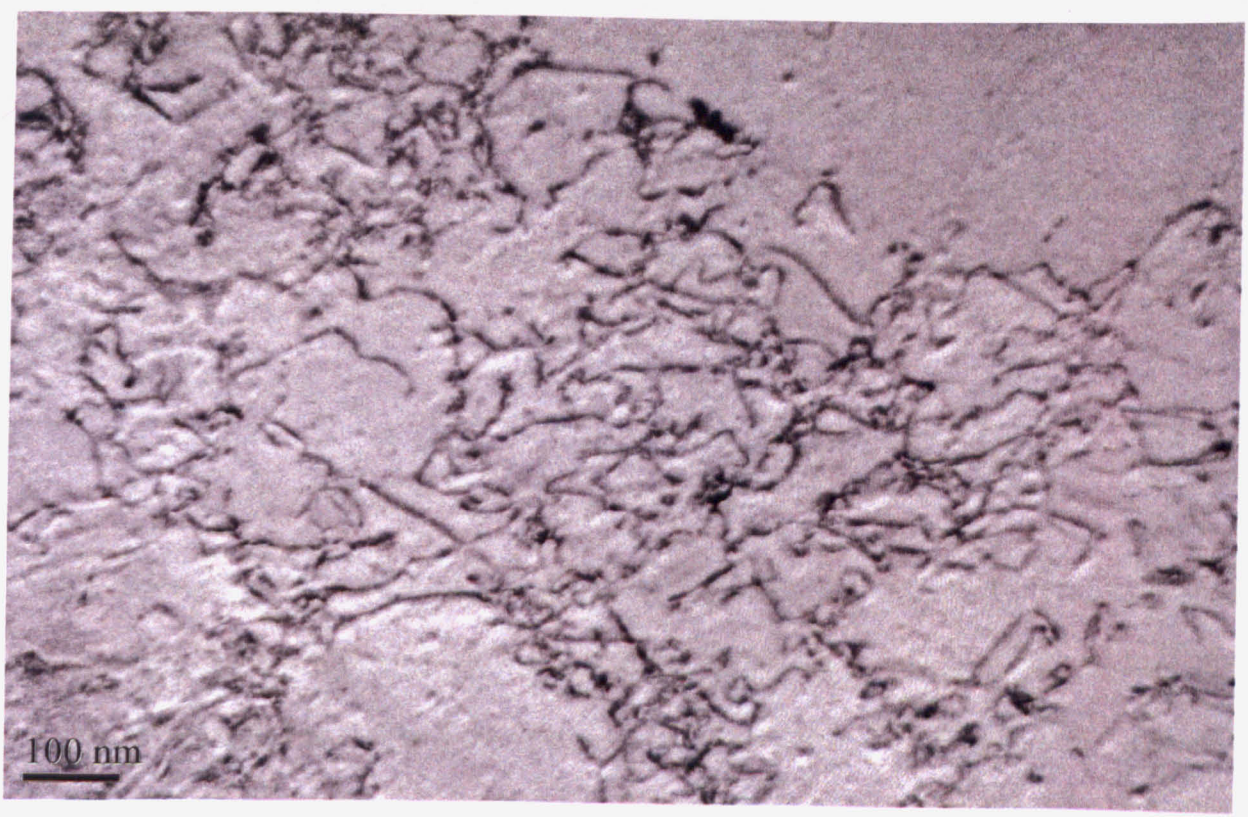

Fig. 6.16(b)

Fig. 6.16(a), (b) Dislocation tangles start to disappear. Due to the lower prevalent temperature, mechanisms like dislocation climb and dislocation annihilation can take more time to occur. Specimen was stopped 24 hours after unloading. Test conditions were 550°C and 335MPa.

6.4 Dislocation Densities

As discussed in the preceding sections, dislocation densities will affect the material behaviour. Any deformation will also result in altering the dislocation densities. Since austenitic steels have an f.c.c. structure, the preferred slip system would be of type {111} in the <110> direction. One of the potential drawbacks of understanding material behaviour from dislocation densities is the role of immobile dislocations. Only dislocations which can move will affect the deformation characteristics.

Immobile dislocations are generally formed at the intersection of different dislocation regions. These will require a greater energy to move and can cause strain hardening. One example would be intersection of screw dislocation lines. When this occurs, the product dislocation line lies in neither of the slip planes and becomes 'sessile'. These dislocations can also act as obstacles, inhibiting further dislocation motion. Observing and counting such dislocations using a TEM is almost impossible as they can lie on any given slip plane. For this reason when dislocation densities are considered, this aspect will have to be accounted for. In either case dislocation numbers will indicate whether dislocation substructures are changing or not. The dislocation link length will be proportional to the carbide spacing. Link lengths will influence the bending radius thus affecting the line tension.

6.4.1 Calculation of dislocation densities

While estimating the carbide and dislocation densities, it is necessary that the values obtained are representative of the bulk of the material. The number of dislocations and precipitates counted should be large enough to account for statistical errors. The counting should also be done in a number of areas so that the final density value obtained is an

average of the whole sample. This section describes how the counting was carried in this project.

For each point on the unload curve, two or three TEM specimens were prepared. Once the specimens were placed for observation in TEM, the first step was to indentify the areas which were thin enough for the beam to pass through. In all specimens at least three such areas were identified. Dislocations can be orientated in different crystallographic orientations. To account for this, the specimen was tilted through a range of 80°. If dislocations were seen, the tilting was stopped and the image was saved. Despite being time consuming, the probability of sampling dislocations in most orientations will be high.

Within each image, lines were drawn randomly across the specimen. The number of dislocation intersections was then counted which was used to calculate the dislocation density. For each area, a minimum of 1000 dislocations were counted. Appendix II shows details of the calculations for each area.

For each area, dislocations were imaged using various g-vectors to ensure all dislocations were accounted for. A test line of length L was drawn which intersected a certain number of dislocations. Dislocation density (ρ_d) was then calculated using [13], [14]:

$$\rho_d = \frac{2N_d}{LS} \qquad 6.1$$

where N_d is the number of dislocations intersecting the test line of length L. S is the foil thickness. An example showing how the calculations were done is shown in Fig. 6.17. The dislocation densities for the various specimens are shown in Fig 6.18.

The true dislocation length can be calculated from the projected length using [15]:

$$l = \frac{(LS)^{1/2}}{2} \qquad 6.2$$

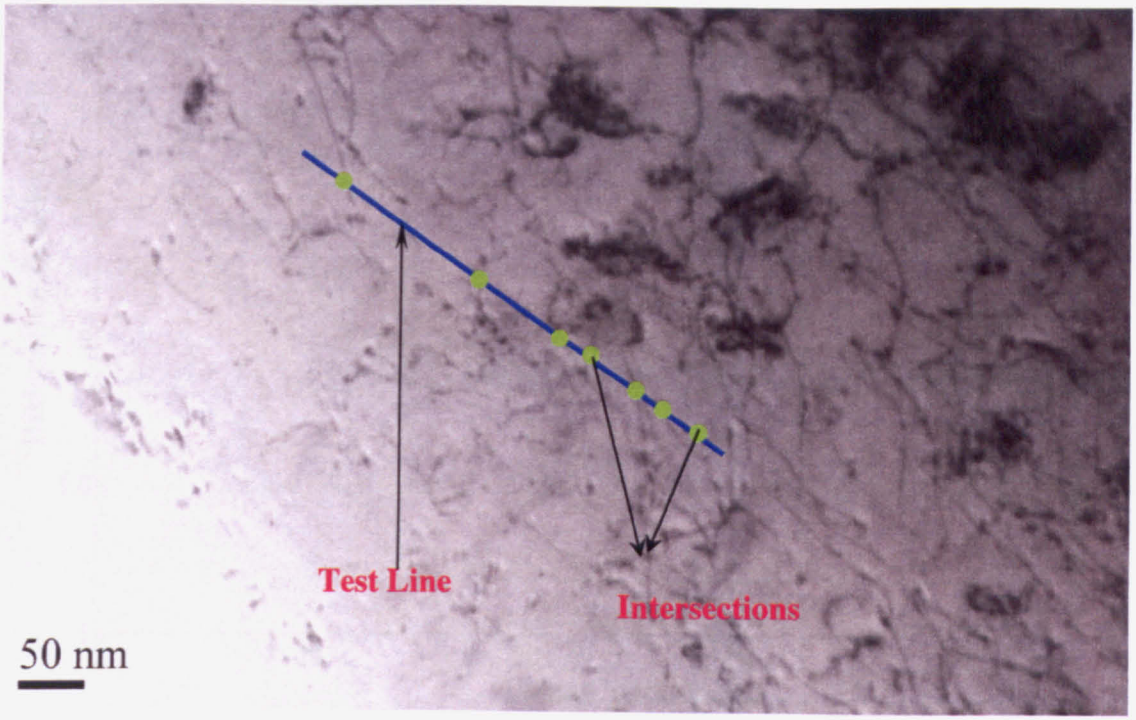

Fig. 6.17 Calculating dislocation densities

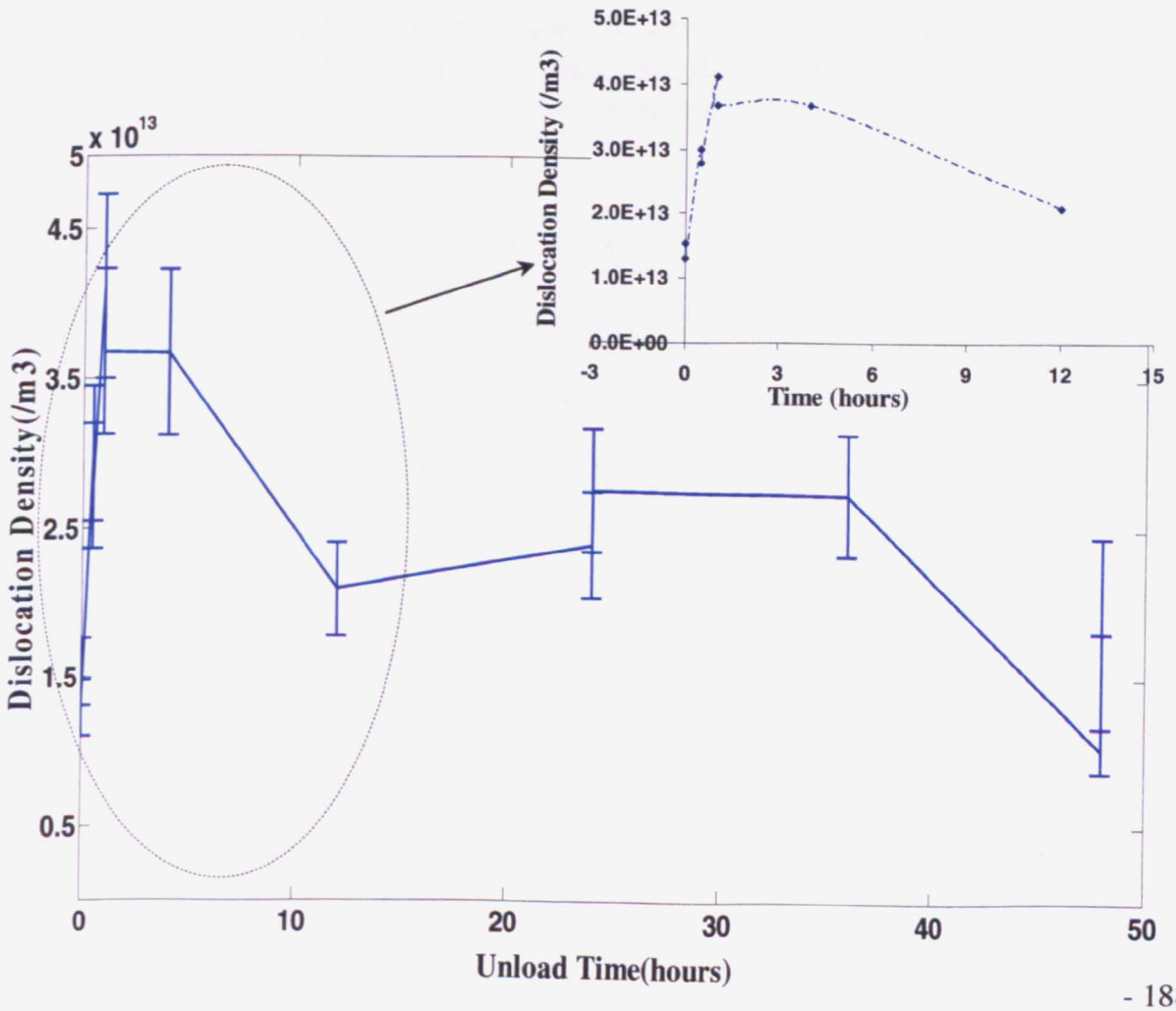

Fig. 6.18(a)

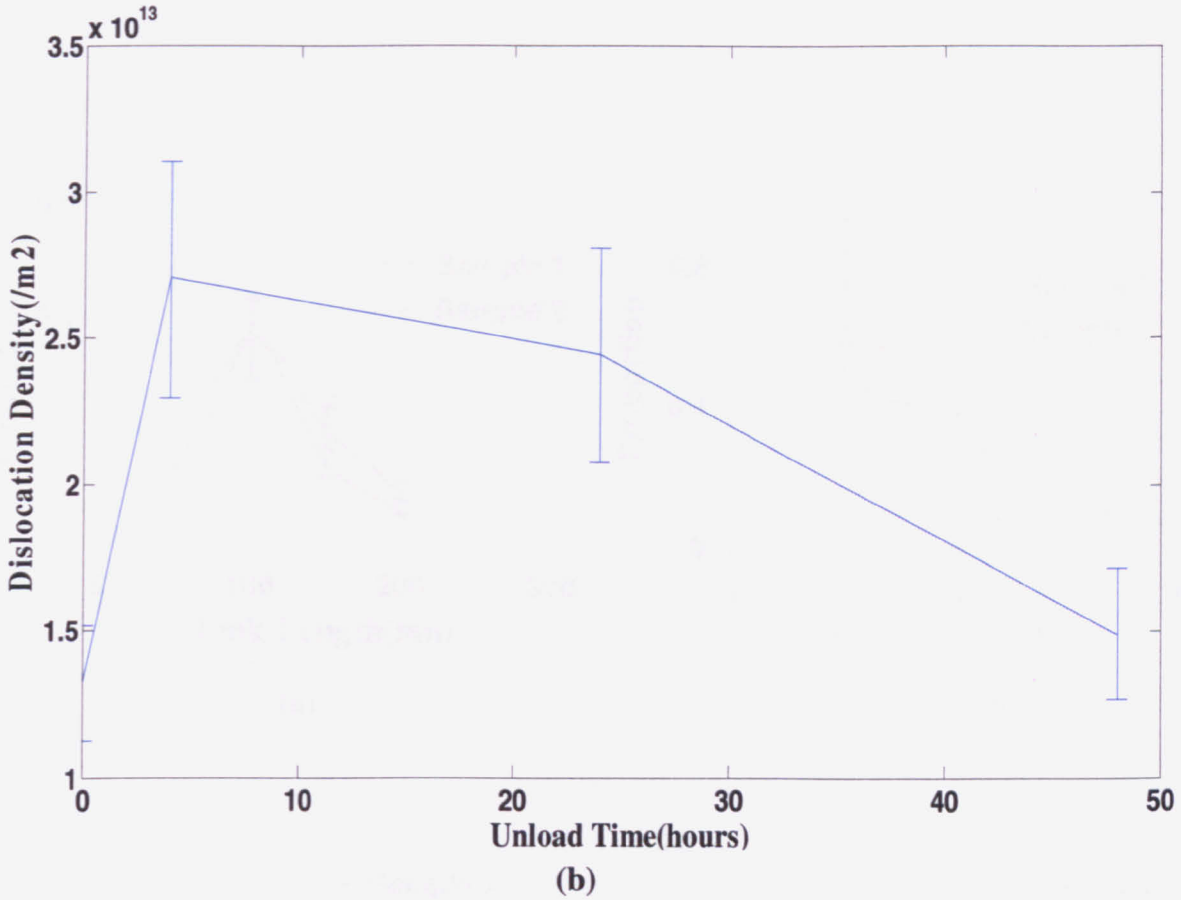

Fig. 6.18 Variation in dislocation density during the unload period (a) 650°C (b) 550°C. Inset in (a) shows detailed numbers during the initial stages of unload

From Equation 6.2, the distributions of dislocation lengths can also be computed. This was done by measuring the projected length of the dislocations and converting them to the actual length. The proportion of dislocations within a given length range was then calculated. The results for some of the different unload times have been shown in Fig. 6.19.

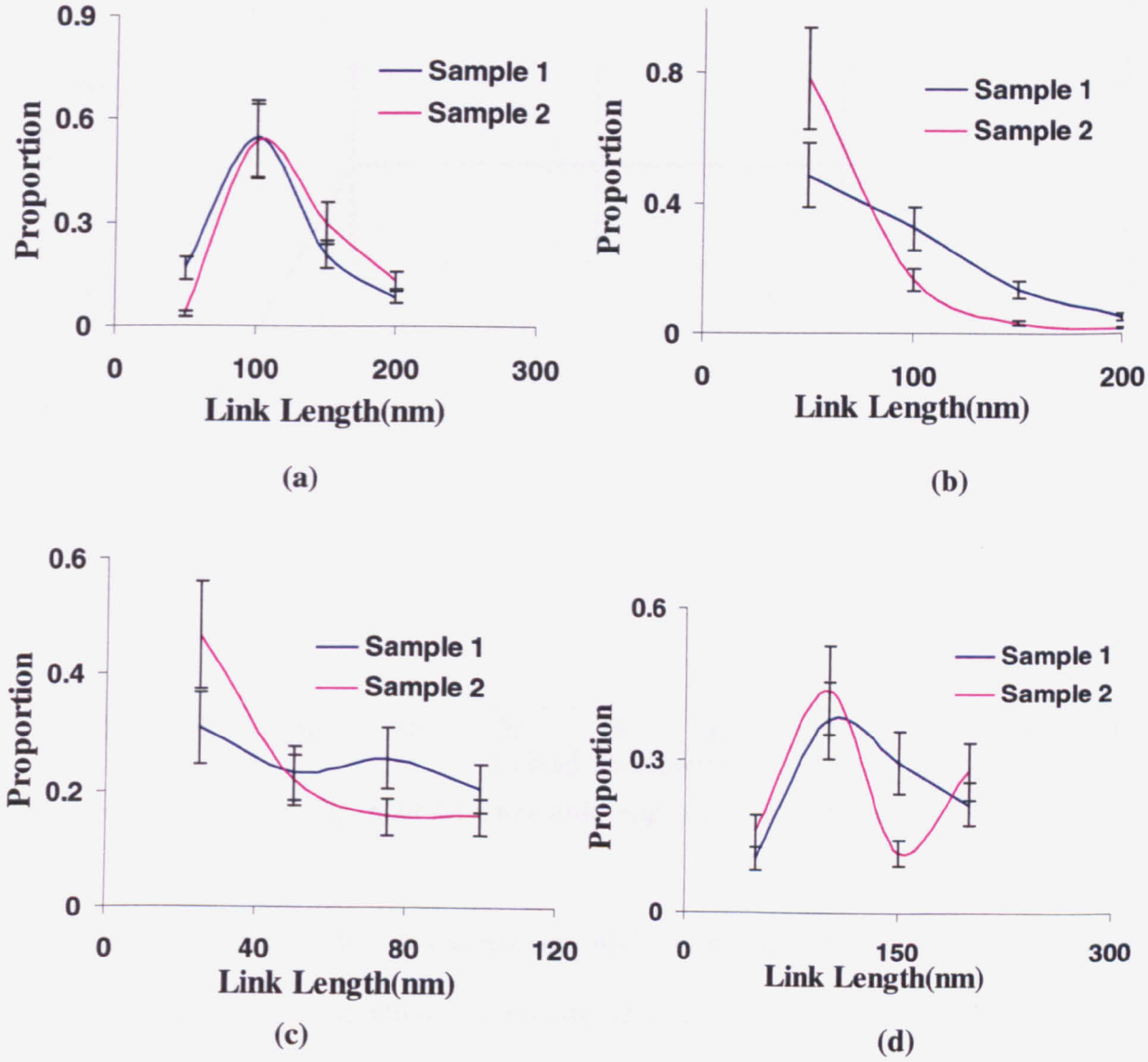

Fig. 6.19 Dislocation link length distribution Through the unload period at 650°C(a) start of unload (b) 30 minutes into unload (c) 1 hour into unload (d) 48 hours into unload

From these calculations, the average dislocation length was computed.

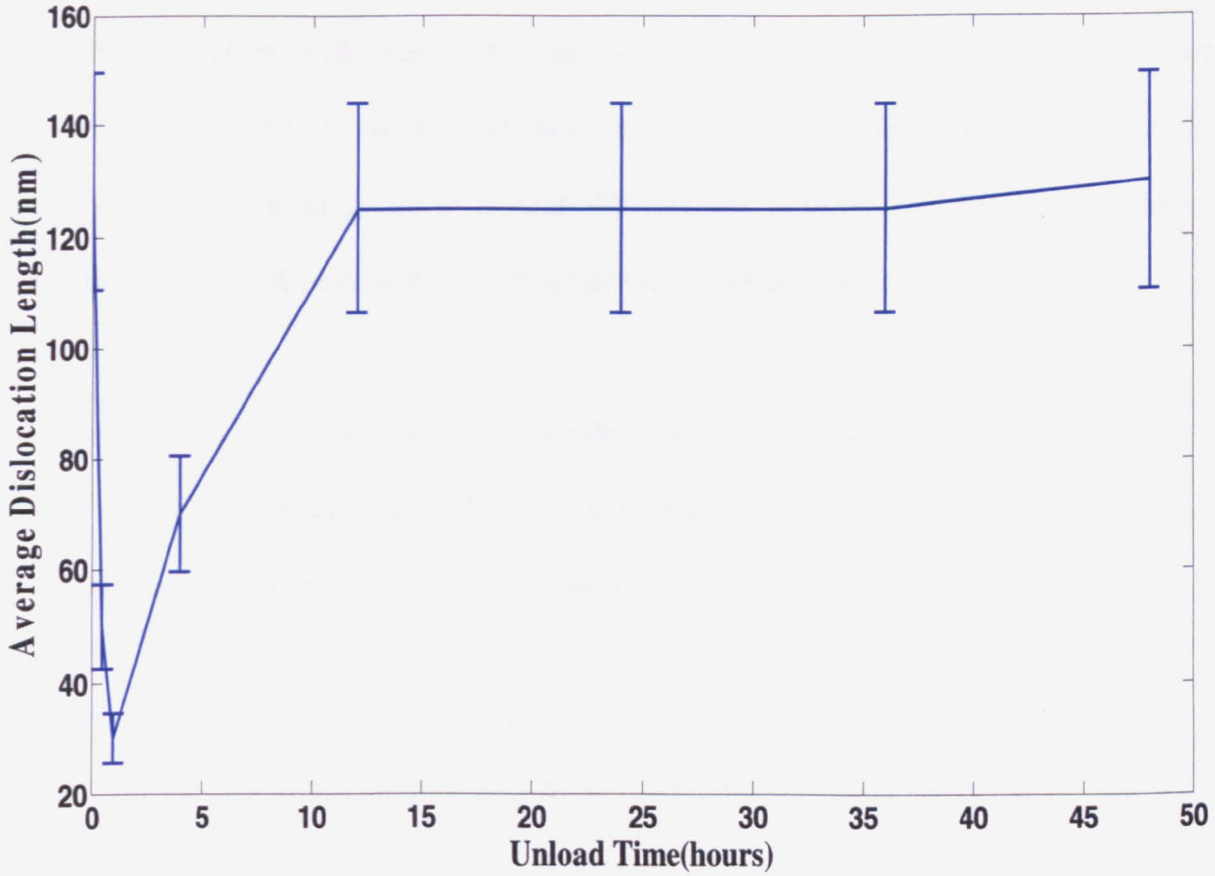

Fig. 6.20 Average link length vs. Unload time

Fig. 6.20 shows the change in the average dislocation link length through the unload period. Changes in the dislocation substructures lead to dislocations untangling themselves. As the carbide density also increases (described in section 6.5), this can result in a decreased spacing of carbides. Dislocations thus will have a bigger probability of interacting with carbides.

6.5 Calculation of Precipitate Densities

Precipitate densities will influence the amount of dislocations being formed. They will also affect the precipitate strengthening mechanisms. A greater number of precipitates will

assist in pinning more dislocations but conversely will not allow dislocations to grow to bigger lengths.

As in the calculation of dislocation densities, it was necessary that the number of carbides and the areas sampled account for statistical variations. Three or four areas were chosen in each specimen and a minimum of around 500 carbides were counted for each specimen. Appendix III shows the detailed breakdown of the calculation of each area.

Precipitate densities are calculated in a similar manner to dislocation densities. Initially a known area is chosen and then the number of precipitates within that area is counted. Precipitate density can then be calculated using [13], [14]

$$\rho_c = \frac{N_c}{SA} \qquad 6.3$$

where ρ_c is the precipitate density and N_c is the number of particles found in area A of thickness S.

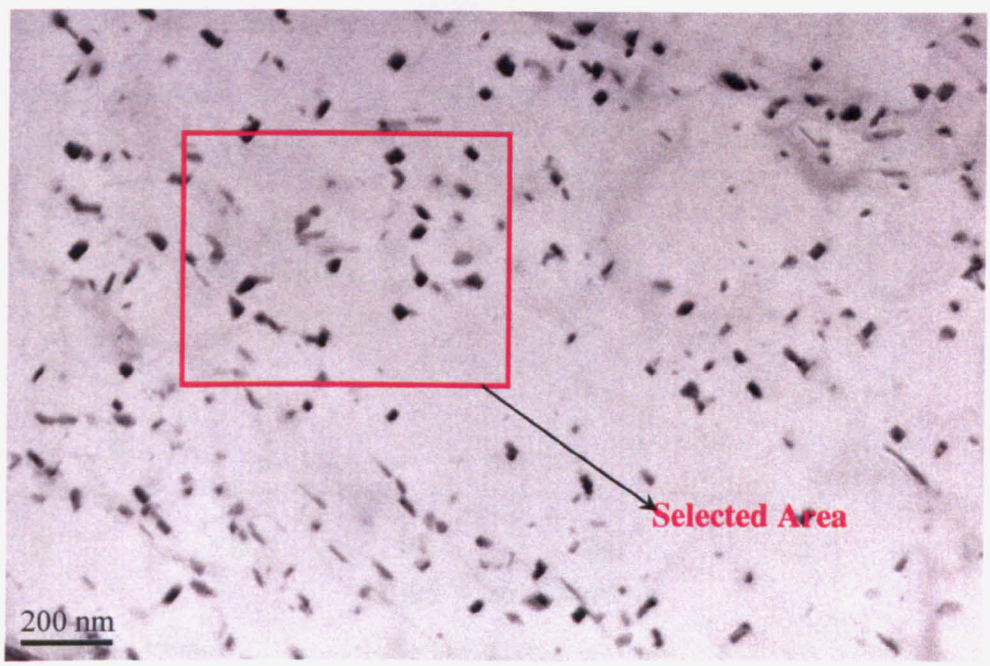

Fig. 6.21 Calculating precipitate densities

Using the above procedure, carbide densities were calculated for all the specimens. At least four areas were used to calculate the densities in each specimen. Three sets of calculations were performed. Results are shown in Fig. 6.22.

As seen in Fig. 6.22, precipitate numbers change during the unload period. During the initial stages of the unload, there seems to be an increase in the precipitate numbers. This value seems to reach a saturation point and then reverts back to its initial value at the start of the unload. The trend has been observed using both preparation methods and thus cannot be an artefact of the preparation technique. Pipe diffusion is a probable method which can be used to explain this. Section 9.2 presents further explanation.

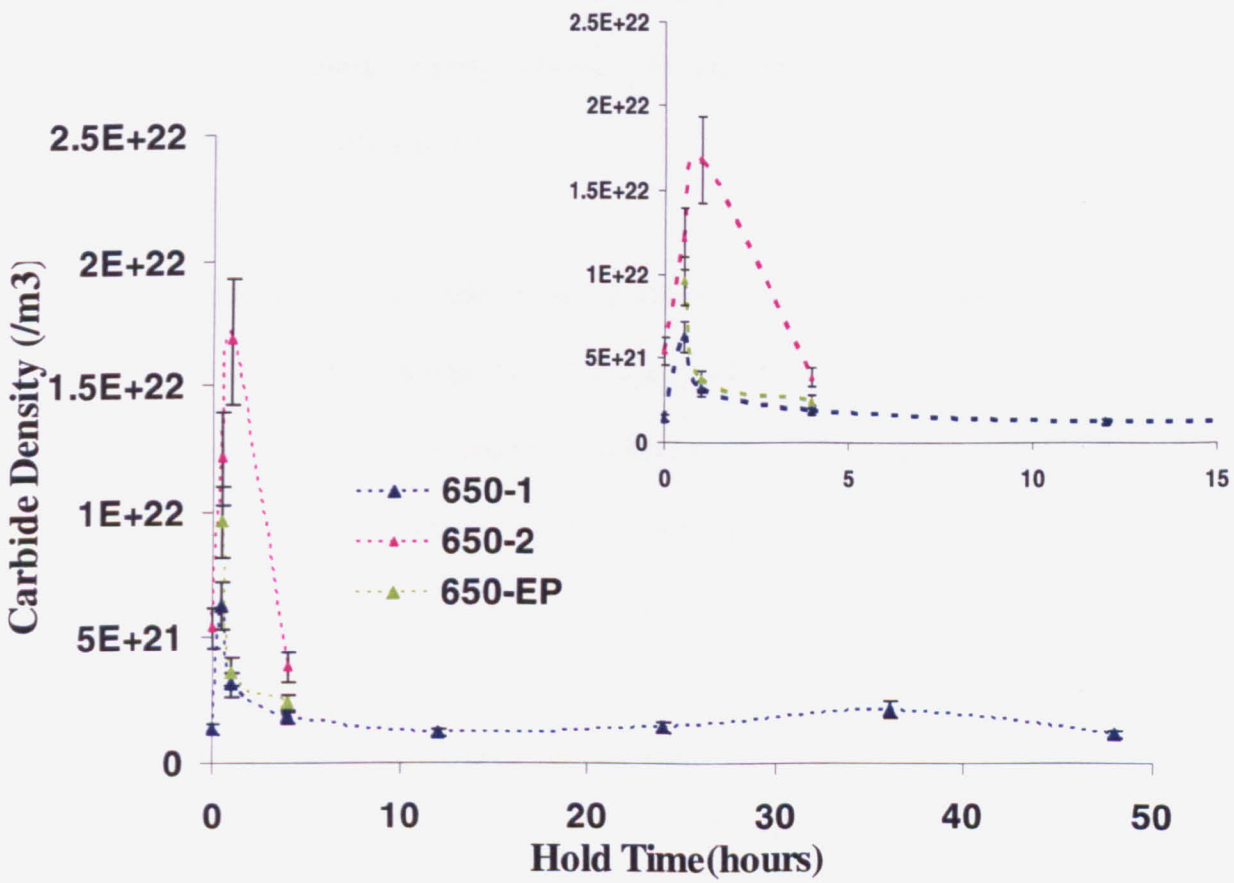

Fig. 6.22 Precipitate densities during the unload. Inset shows the details during the initial stages. Series 650-1 and 650-2 are two sets where the specimen was prepared using the ion-polisher. 650-EP represents calculations on specimens made using electropolishing

6.6 Conclusions and Discussions

A number of conclusions were derived from the body of work.

- Electron microscopy was conducted to examine the behaviour of dislocation substructures during anelasticity. Studies were conducted using TEM specimens prepared from samples stopped at different stages of anelastic/creep deformation. TEM samples were prepared using ion polishing and electropolishing techniques.

- Observations of these specimens have concluded that the dislocation substructure changes during anelastic deformation. When the initial stages (<60 minutes) of the unload are considered, there is an increase in dislocation densities. Following this, dislocation densities decrease and reach a steady value at around 12 hours after unload. As anelastic strain increase, the dislocation also form networks suggesting a more stable substructure.

- Calculations of precipitate densities were also performed. They suggest an increase in carbide number during the initial stages of the unload (<60 minutes). The carbide numbers then decrease and reach values comparable to the start of the unload. One possible reason for this to occur is a mechanism called 'pipe diffusion'. This has been discussed in chapter 9.

- When samples which were obtained after testing at different temperatures (550°C and 650°C) were compared, significant differences can be observed. At 650°C, the dislocations have greater mobility and can execute the climb motion more readily, thus a lesser number of dislocation tangles were observed. However, in samples

obtained after testing at 550°C, a greater number of dislocation tangles were observed.

- Chemical changes in precipitates were not seen. This was concluded after conducting EDS (Energy Dispersive Spectroscopy) measurements. Further details of this technique and some results have been presented in Appendix.

References

[1] J.C. Gibeling, W.D. Nix, *Observations of anelastic backflow following stress reductions during creep of pure metals*, Acta. Metall. 29 (1981), pp. 1769–1784

J.C.Gieibling, W.D. Nix, Acta Metal. Vol. 29 (1981), pp 1769-1784.

[2] P.W. Davies, G. Nelmes, K.R. Williams and B. Wilshire, *Stress changes experiments during high temperature creep*, Metal Sci. J. 7 (1973), pp. 87–92.

P.W.Davies, G.Nelmes, K.R.Williams, B.Wilshire. Metal. Sci. J. 7(1973), pp.87.

[3] G.J. Lloyd and R.J. McElroy, *A model for the quantitative interpretation of high-temperature stress relaxation phenomena: The effect of anelasticity*, Philos. Mag. 32 (1975) (1), pp. 231–244.

[4] C.M.Zener, *Elasticity and Anelasticity of Metals*, Uni. of Chicago press. (1948).

[5] T.B.Gibbons, V.Lupinc, D.Mclean., *Effect of grain size, particle size and γ' volume fraction on strain relaxation in Ni-Cr base alloys*, Mater. Sci. Eng. 9 (1975), 437.

[6] V.Lupinc, F.Gabrielli, *Effect of grain size, particle size and γ' volume fraction on strain relaxation in Ni---Cr base alloys*, Mater. Sci Eng, 37(1979) 143-149

[7] K.Sawada, K. Kimura, F.Abe, *Mechanical response of 9%Cr heat-resistant martensitic steels to abrupt stress loading at high temperature*, Mater. Sci. Eng. A358 (2003) 52-58.

[8] K.Sawada, K. Kimura, F.Abe. *Deformation behavior of high Cr ferritic steels upon abrupt stress loading*, Mater. Sci. Eng. A387-389 (2004) 683-686.

[9] M. Pahutova, J. Cadek and P. Rys, *Some stress change experiments on creep in α zirconium*,Mater. Sci. Eng. 39 (1979), pp. 169–174

[10] S.K.Mitra, D.Mclean, Proc. Roy. Soc. London, Sect. A, 295(1966),pp. 288.

[11] V.Lupinc, F.Gabrielli, *Effect of Grain Size, Particle Size and Gamma Prime Volume Fraction on Strain Relaxation in Ni-Cr Base Alloys*, Mater. Sci. Eng, 37(1979), pp.143-149

[12] T.B.Gibbons, B.E.Hopkins, Met. Sci. Jour. 5(1971), pp.233.

[13] P.B.Hirsch, A.Howie, R.B.Nicholson, D.W.Poshley, M.J.Whelan, '*Electron Microscopy of Thin Crystals*', Butterworths, London (1965).

[14] D.G.Morris, *Creep in type 316 stainless steel*, Acta. Metall. 26 (1978), pp. 1143-1151.

[15] A.Oden, E.Lind, R.Lagneborg, Proc. Conf. Creep Strength in Steels and High Temperature Alloys, Sheffield (1972).

[16] J.M.Race, H.K. Bhadeshia, *Carbide Precipitation Sequences during the Carburisation of CrMo Steels*, Mater. Sci. Tech., Vol.8 (1992), pp.875.

[17] D.G.Morris and D.R.Harries, *Recovery of a creep-deformed Type 316 stainless steel*, Jour. of Mater. Sci., 14 (1979) 2625--2636

CHAPTER 7: ROLE OF RESIDUAL STRESSES IN ANELASTIC/CREEP DEFORMATION

The importance of understanding the internal stress state of materials was described in chapter 2. Changing the plastic strain state of the material will result in changes to the intergranular stresses. This chapter discusses results obtained from a load/unload creep test where the internal strains were measured in-situ using neutron diffraction.

7.1 In-situ Neutron Diffraction Experiments

Residual stresses can influence the strain response of a material greatly. Material properties like fatigue, creep resistance, fracture toughness and strength can be affected by internal stresses. Diffraction techniques can be used to measure the internal stresses. Measurements can be done either in-situ when the deformation is occurring or on pre-deformed samples. Measurements of pre-deformed samples can be a little ambiguous as temperature/stress removal can influence the residual stress state. The removal of the load for example, will change the dislocation substructure state, thus changing the internal stress state. Temperature removal will influence the precipitation behaviour which again can cause changes to the local stress fields. To understand the influence of changing plastic strain due to anelasticity on the internal strains, the lattice strains had to be measured continuously. For this reason, in-situ neutron diffraction experiments were conducted in this project.

Most in-situ experiments use a conventional hydraulic (or screw driven) loading frame. This is oriented according to the diffraction scattering geometry. Typically, the load frame is oriented in the diffractometer such that the scattering vector lies either on the axis

parallel to the loading direction or perpendicular to it, thus measuring the axial and/or the Poisson strains. The applied load is incremented and held at a constant macroscopic stress while the neutron data is gathered before increasing the stress. In-situ testing has the advantage of monitoring the deformation history of a single specimen.

Diffraction studies which involve measuring residual stresses when the specimen was being deformed have been carried out on many different materials. There has been little work with regards to creep in ferrous materials. Winand has conducted some studies on in-situ measurement during creep of composites [24, 25]. Fitzpatrick and Daymond [28] have carried out studies looking at the internal stress behaviour during cycling loading of Al-SiC metal matrix composite and have found misfit stresses which are tensile in the matrix and compressive in the reinforcement.

The bulk of the in-situ measurements in steels have involved tensile loading of the material. In-situ tensile studies have been carried out by Daymond [2] on 316 stainless steel. The tests involved tensile testing the material at room and elevated temperatures. The results show development of tensile residual stresses in the {200} and the {311} directions, whereas the {220} and the {111} planes developed compressive residual stresses. The tests thus show a strong influence of anisotropy both in the elastic and plastic regimes.

Lin Peng et al. [26] conducted in-situ tensile testing on AISI 304 steel. The study also investigated the influence of texture on the tensile properties of the crystallographic planes. The development of residual stress in the different planes is similar to those obtained by [2]. They have also concluded that the {200} plane sustained the largest intergranular strains while the {111} has the lowest intergranular strain. Also based on their TEM microscopy they conclude that until the material reaches a plastic strain of around 30%,

slip is the main deformation mode and past that, twinning starts influencing the deformation.

Pang et al. [27] conducted in-situ tensile loading on 309H steel. They have reported that the relative peak intensities for the different planes change as plastic strain increases. They have attributed this to grain reorientations. They have also concluded that as the number of load/unload cycles increase; a reduction in the internal stresses will be seen. This is due to incompatibilities being accommodated by slip rather than by generation of internal stresses. The hysteresis loops during the load/unload cycles may result in point defects forming obstacles for dislocation motion.

7.2 Elastic and Plastic (Creep) Anisotropies

A number of the studies mentioned in the previous discuss the contribution of crystal anisotropies towards the internal stress generation within material. Anisotropies can exist in both the elastic and the plastic region. Stainless steels are anisotropic both elastically and the plastically, where as aluminium is isotropic in the elastic region but anisotropic when deforming plastically. This section explains the causes for these anisotropies.

A crystalline material can be considered as an aggregate consisting of a number of crystals in various orientations. A simple way to explain is to consider the response of the grain families when subjected to plastic deformation. Fig. 7.1 is a stress-strain curve showing response of different grain families during tensile loading in an austenitic stainless steel sample (Experimental details have been provided in section 7.3). The sample was loaded to a stress of 180MPa in steps of 20MPa.

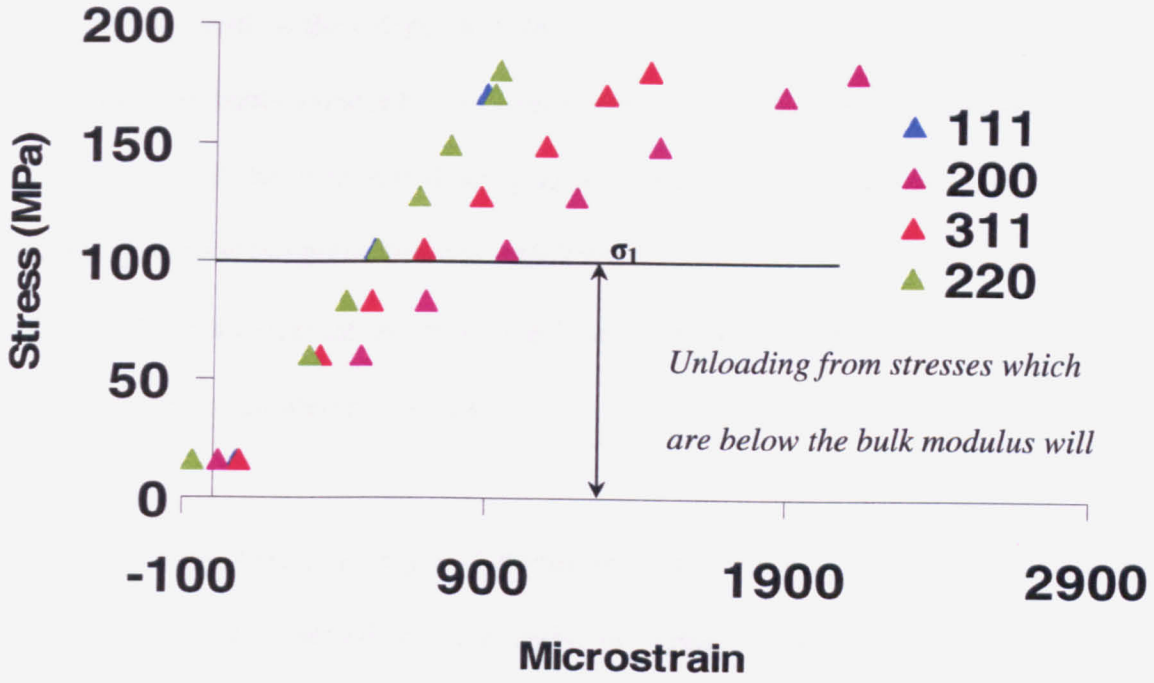

Fig. 7.1 Response of individual crystallographic grain families during tensile loading in austenitic stainless steel

The test was part of a loading sequence which was used to measure internal strain generation during creep deformation. Anisotropic behaviour of the individual crystal grain families can be observed both in the elastic regime and the plastic (or creep) regime. This type of behaviour has been observed in numerous studies (Examples include [2, 26, 27, 29]). Development of internal stresses during elastic loading occurs due to a number of factors: The anisotropic stiffness of a single crystal, the orientation of particular grain families to the loading direction and the constraint each grain places on its neighbours as it deforms. Clausen et al. [30] have stated that development of the intergranular microstresses is dependent elastic and plastic anisotropy inherent to the material. These properties determine the proportion of the applied load borne by grains in a given orientation and the order in which the different grain orientations yield.

The case of plastic deformation is considered next. Grain orientations will determine the load at which critically resolved shear stress required to initiate slip, which causes yielding

in families of grains orientated similarly. Determining the order in which each of these grain families yield is thus dependent on how each of these grains are oriented to the applied load (probably impossible to determine). At this point, a greater proportion of the applied load will be transferred to grains which have not yet yielded. This 'load partitioning' causes the grain families which were deforming elastically to yield. Once slip is initiated, further deformation can be easily accommodated plastically with little increase in the load being supported by the grain.

In austenitic steels, based on only on Schmid factor and the macroscopic applied stress, the 200 type grains are expected to yield early, but studies have shown the 220 and other orientations (Ex. 331) yield first [2]. These yielding grains then take up smaller increments in elastic strains than in the elastic regime. (moving towards compression relative to the elastic line). The 200 type grains then start bearing a larger share of the load and move into tension relative to their elastic response.

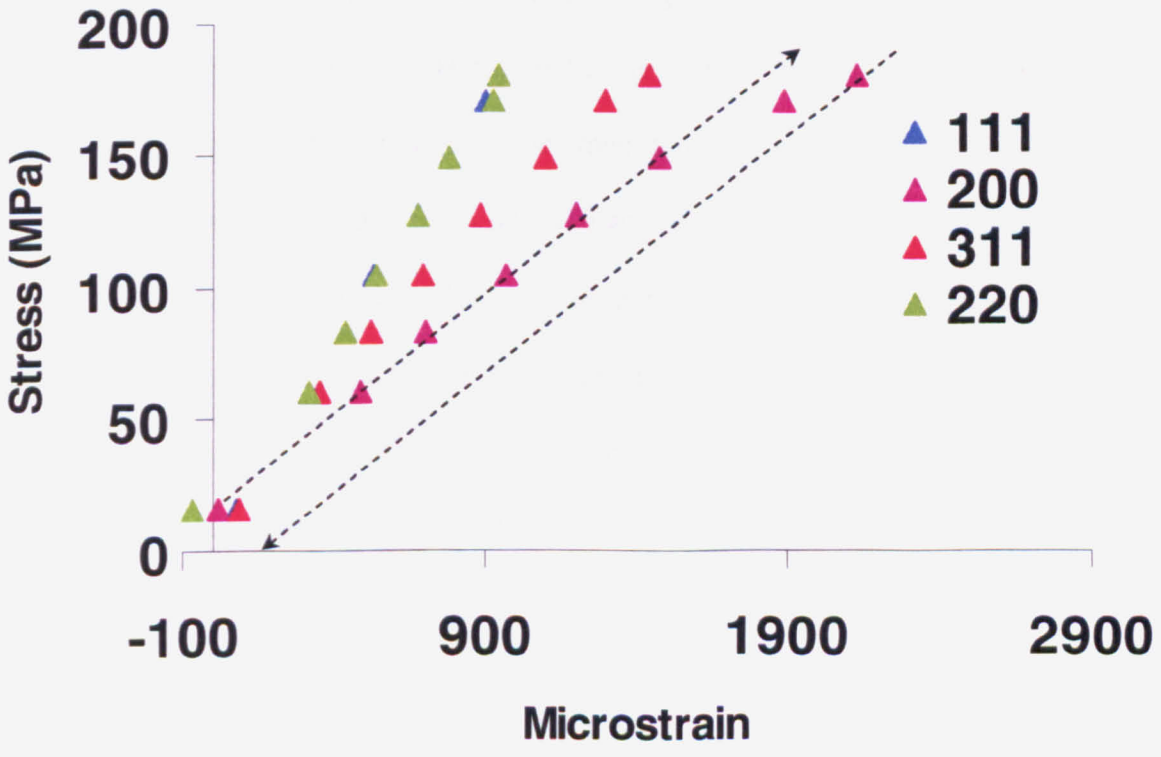

Fig. 7.2 Unloading after plastic deformation will result in development of inelastic strains in the grains. Arrows indicate the elastic response during loading and unloading

The above behaviour is clearly seen in the plastic regime of Fig. 7.2. At small plastic strains, microstrain accumulation is rapid as only a few grains are yielding. Further increase in the bulk plastic strain will not alter the elastic response of the grains by much as strain hardening and texture evolution mechanisms dominate the plastic strain response. If the behaviour of the {200} grain families are considered, unloading after the material has yielded will result in development of a net inelastic strain in grains of the 200 type. A similar approach can be used to understand intergranular strain accumulation in other crystallographic grain orientations.

An experiment was conducted to measure these anisotropies during creep deformation. The following section describes the experiment and the results obtained.

7.3 Experimental Details

The experiment was conducted using the ENGIN-X diffractometer based at ISIS, Rutherford Appleton Laboratory. The aim of the experiment was to investigate the internal strain behaviour of AISI Type 316H material during a uniaxial load/unload cycle creep test at 650°C using neutron diffraction. The specimen was initially loaded to 180MPa at 650°C for 24 hours and then unloaded for 6 hours. Two such cycles were conducted. The stress rig and the radiant furnace at ENGIN-X were used for this in-situ creep test. A test specimen with gauge diameter of 6 mm and a gauge length of 30 mm was used (similar to the specimens used in the creep testing). The specimen ends had M12 threads making them compatible with the stress rig at ENGIN-X. The bulk strain of the sample was measured using a high temperature strain gauge similar to the one described in section 3.3.2. Data obtained from the strain gauge has been referred to as macrostrain throughout this chapter. Temperature was monitored by using two thermocouples along the gauge length. The setup has been shown in Fig. 7.3.

Internal strains and stresses in the axial and radial directions were measured at mid-length of the test specimen gauge at regular intervals. During the initial stages of the test and also after each load/unload, neutron counts were taken for 5 minutes and then measurements were done for 10 minutes. A 3mm x 3mm x 3mm gauge volume was used. All data presented in this chapter are from the axial direction.

The experimental results would show how the distributions of strain and stress between lattice planes evolves during loading (primary and secondary creep), unloading and anelastic strain recovery.

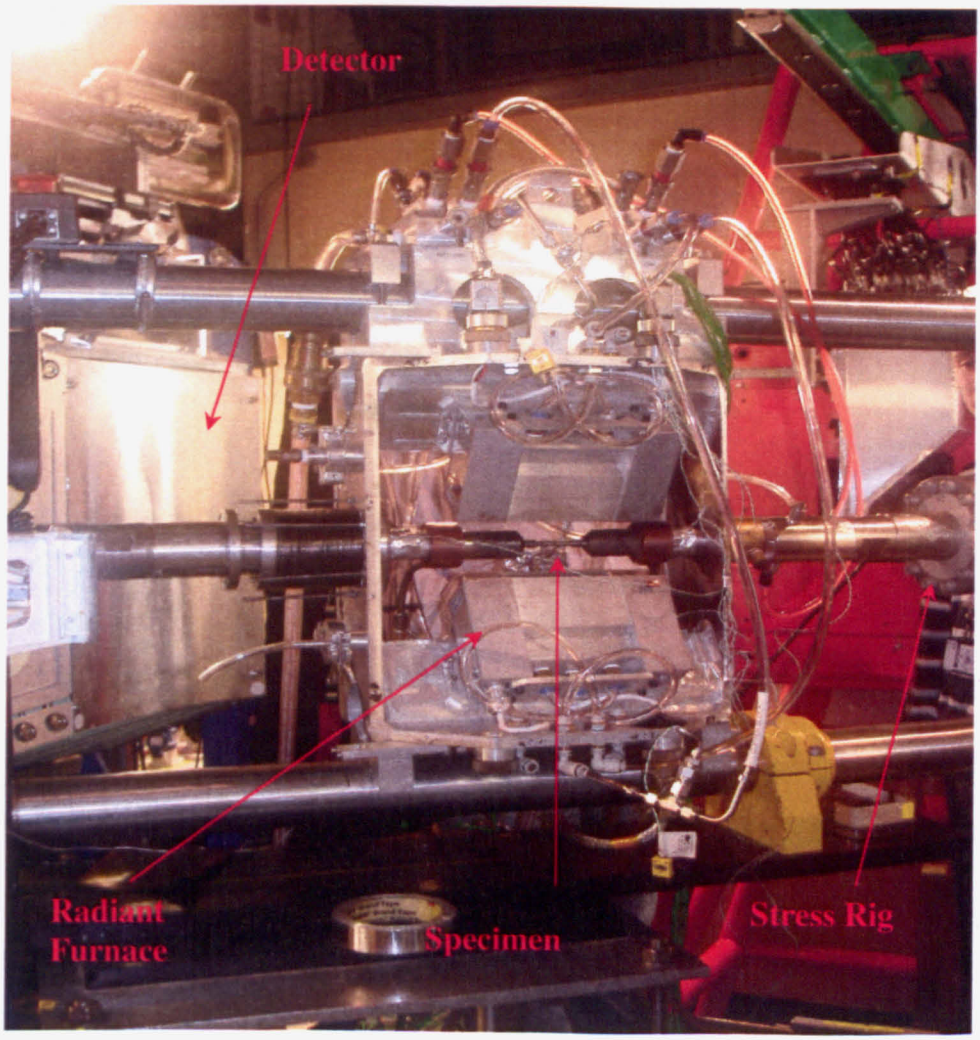

(a)

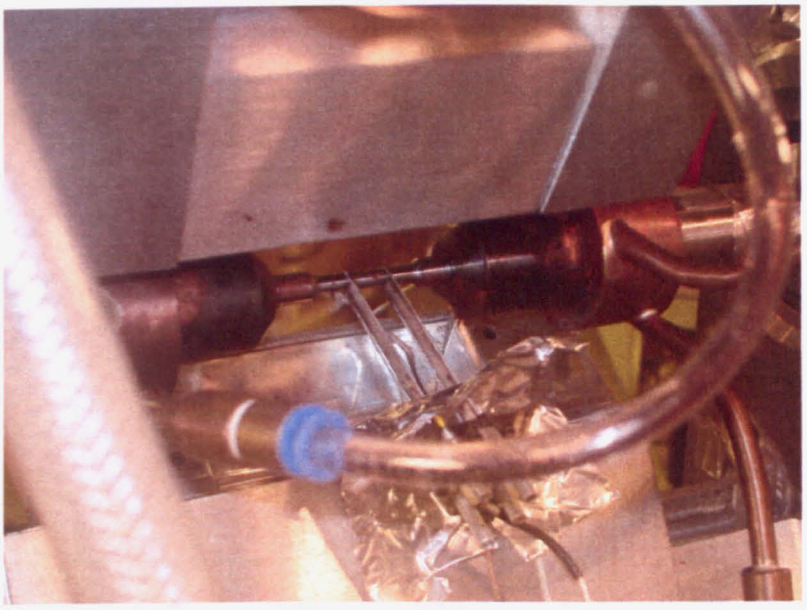

(b)

Fig. 7.3(a) Experimental setup for in-situ neutron diffraction experiment (b) Sample and strain Gauge

7.4 Results

The strain within the material can be calculated using

$$\varepsilon = \frac{d - d_o}{d_o} \qquad 7.1$$

Where d_o refers to the lattice spacing of an unstrained initial reference sample.

The first step was to check the variation of d-spacing with temperature. For this purpose, the specimen was heated to different temperatures and the d-spacing was measured. One measurement was also done at room temperature. Fig. 7.4 shows the variation of the strain with temperature. All results presented in this chapter are for the axial direction.

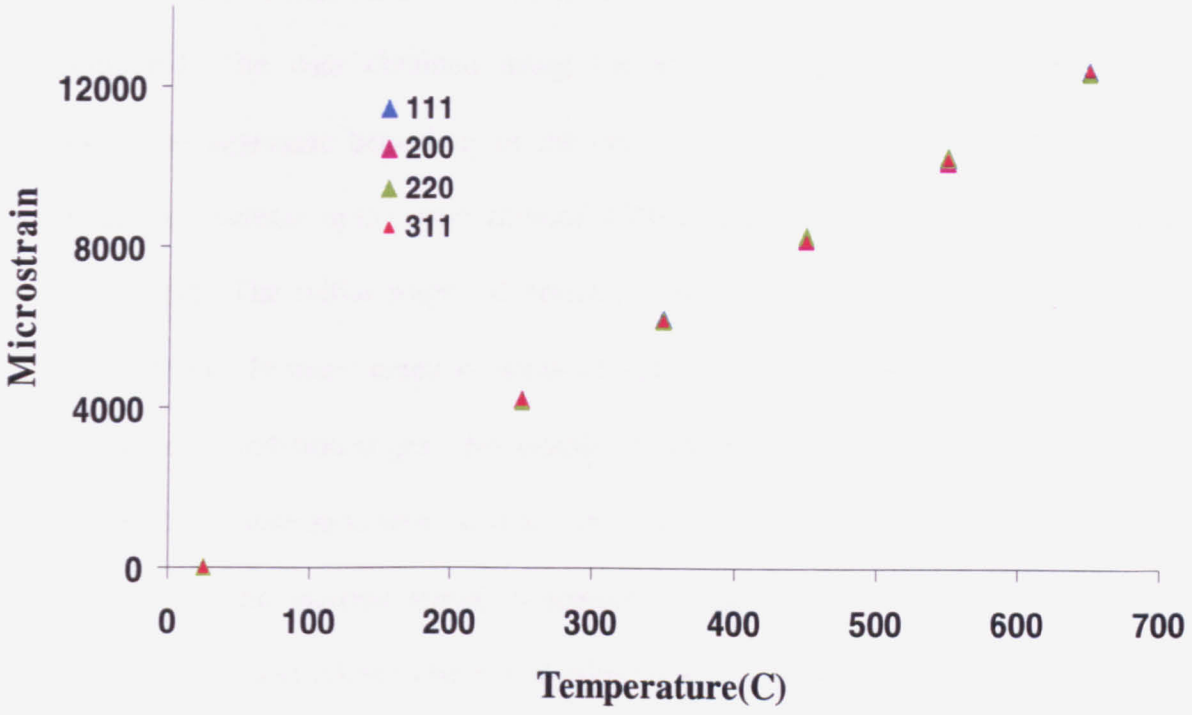

Fig. 7.4 Change in internal strain with temperature in the unloaded condition

The specimen was then loaded to 180MPa. The loading was done in steps of 20MPa and the d-spacing was measured in each step. The internal strain data was previously presented in Figures 7.1 and 7.2. A more detailed explanation of the results including reasons for elastic anisotropy was given in section 7.2. As the material starts creeping, it signifies the onset of yielding, which means plastic anisotropic behaviour will be observed.

7.4.1 Results of Load/Unload Test

d_0 was considered as the d-spacing value when the sample reached the desired temperature (650°C). Initially, sampling was done once every five minutes when the specimen was in primary creep. Once the secondary stage was reached, data was sampled for ten minutes. Also, during the unload phases; sampling was done for 5 minutes. Fig. 7.5 shows the overall response of all the planes. For estimating the multi-peak response a Reitveld refinement technique was used. Further details of the technique can be found in [17, 29].

There is significant difference when the behaviour of the individual crystallographic planes is compared. The data obtained using the Reitveld refinement should theoretically represent the aggregate behaviour of the crystal planes (Fig. 7.7). Initially, there is an instantaneous increase in the strain (around 1200 microstrain). Following this, the material starts to creep. The initial stages of primary creep show an increase in the microstrain (internal strain). Primary creep consists of hardening mechanisms which occur due to dislocation accumulation at grain boundaries, dislocation tangles, etc. These processes can cause the initial increase in internal strain observed. The onset of secondary creep results in a reduction of the internal strain. Secondary creep consists of recovery mechanisms (dislocation glide and climb) which will contribute to this reduction in the internal strain. When the material is unloaded, there is an instantaneous elastic drop. The value of the microstrain (Reitveld) at the end of this drop is close to zero. During the unload, anelasticity results in plastic strain (macro) recovery. A small decrease in the microstrain (about 70 microstrain) can also be observed during the unload. Upon reloading, the data

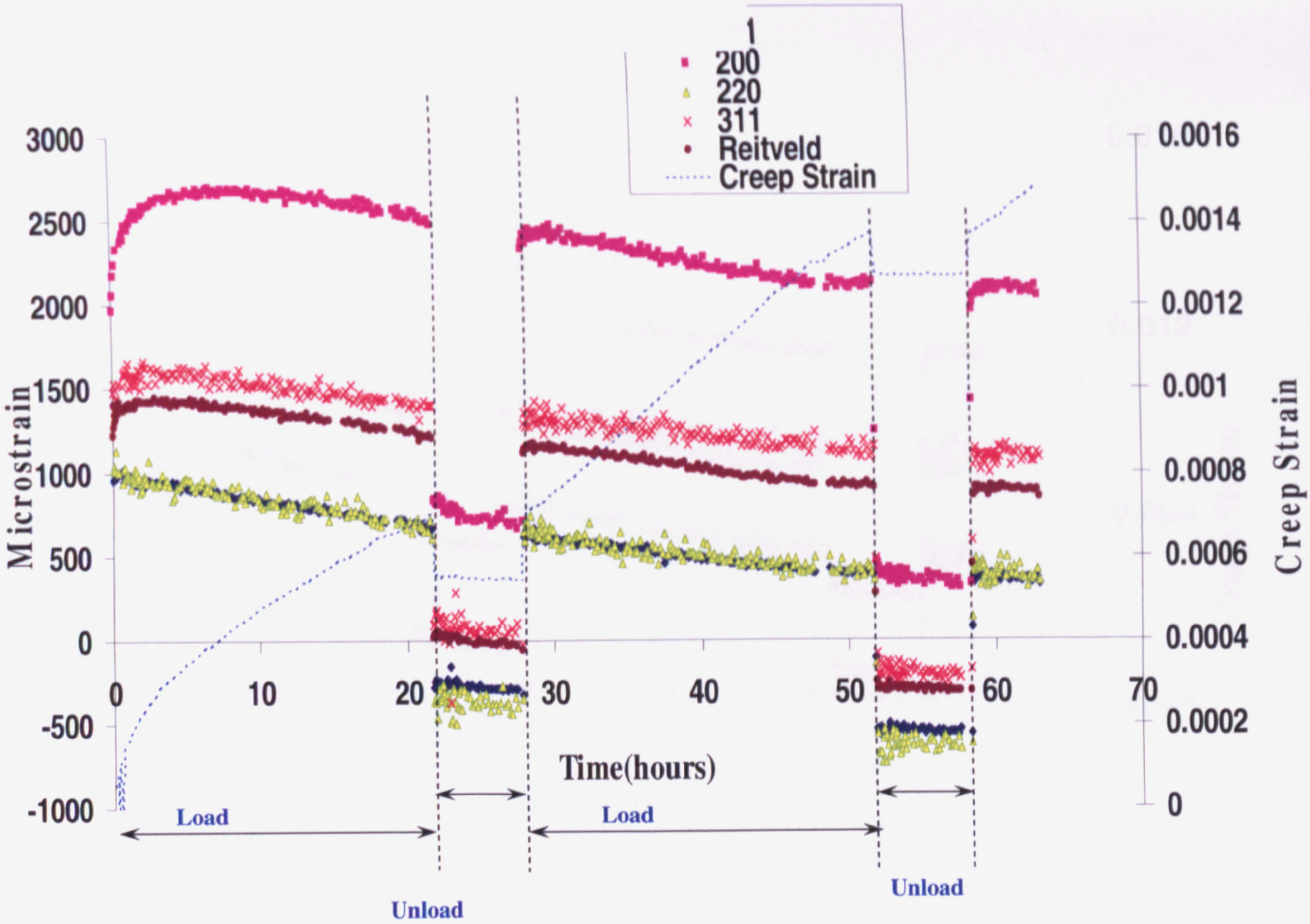

Fig. 7.5 Internal strain evolution for the whole experiment. The dotted blue line represents the macrostrain recorded by the strain gauge

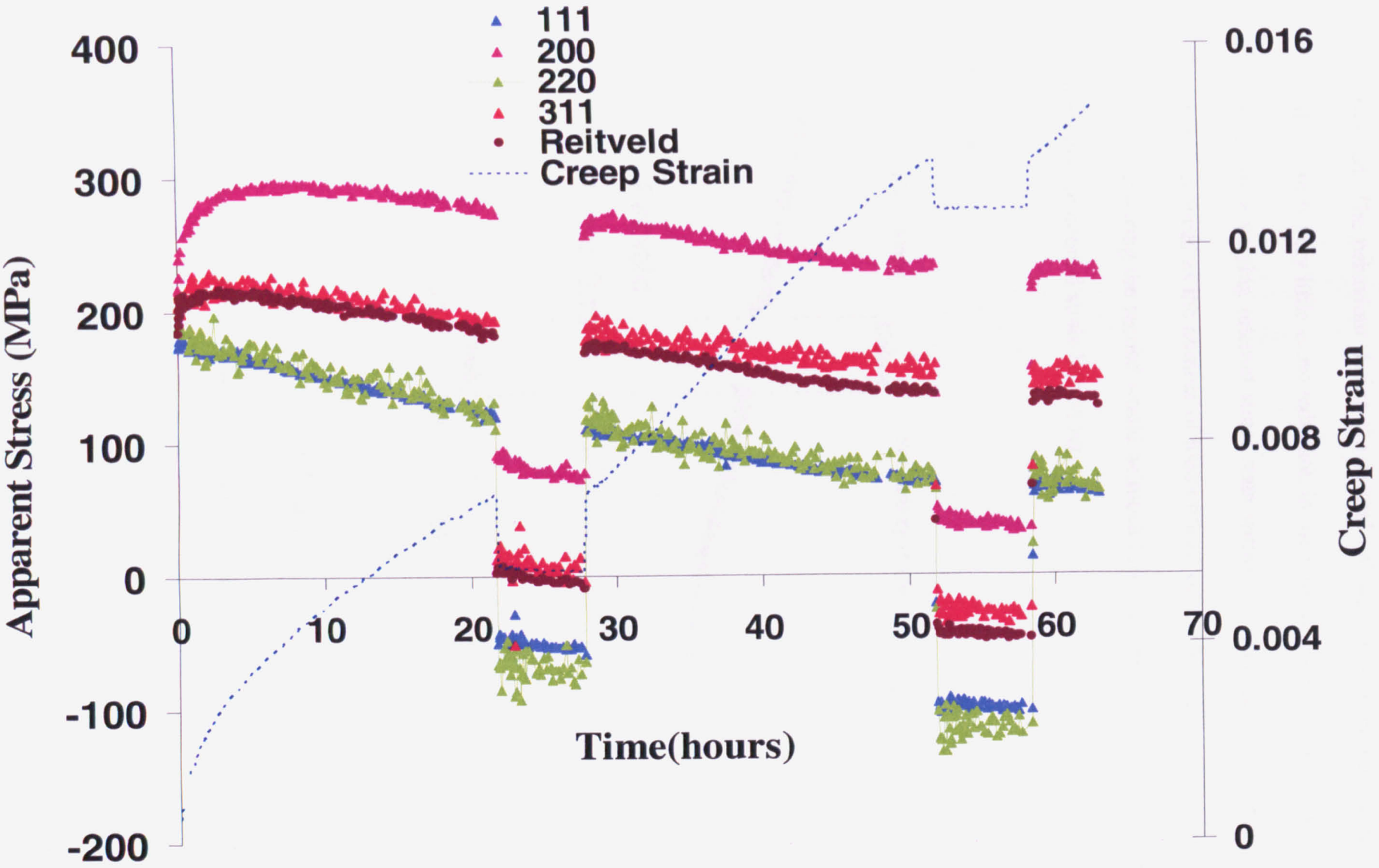

Fig. 7.6 Internal stress values calculated using the diffraction elastic constants.

follows the same trend as in the previous load cycle. A decrease in the internal strain can be observed. The behaviour during the second unload varies when compared to the first unload. There is very little or no reduction in the internal strain during the second unload. This suggests a varying internal stress state within the material. As reported previously, anelasticity reduces as the number of load-on/load off cycles increase. The overall plastic strain change during the second would be much less than the first which might be directly influencing the internal strain behaviour.

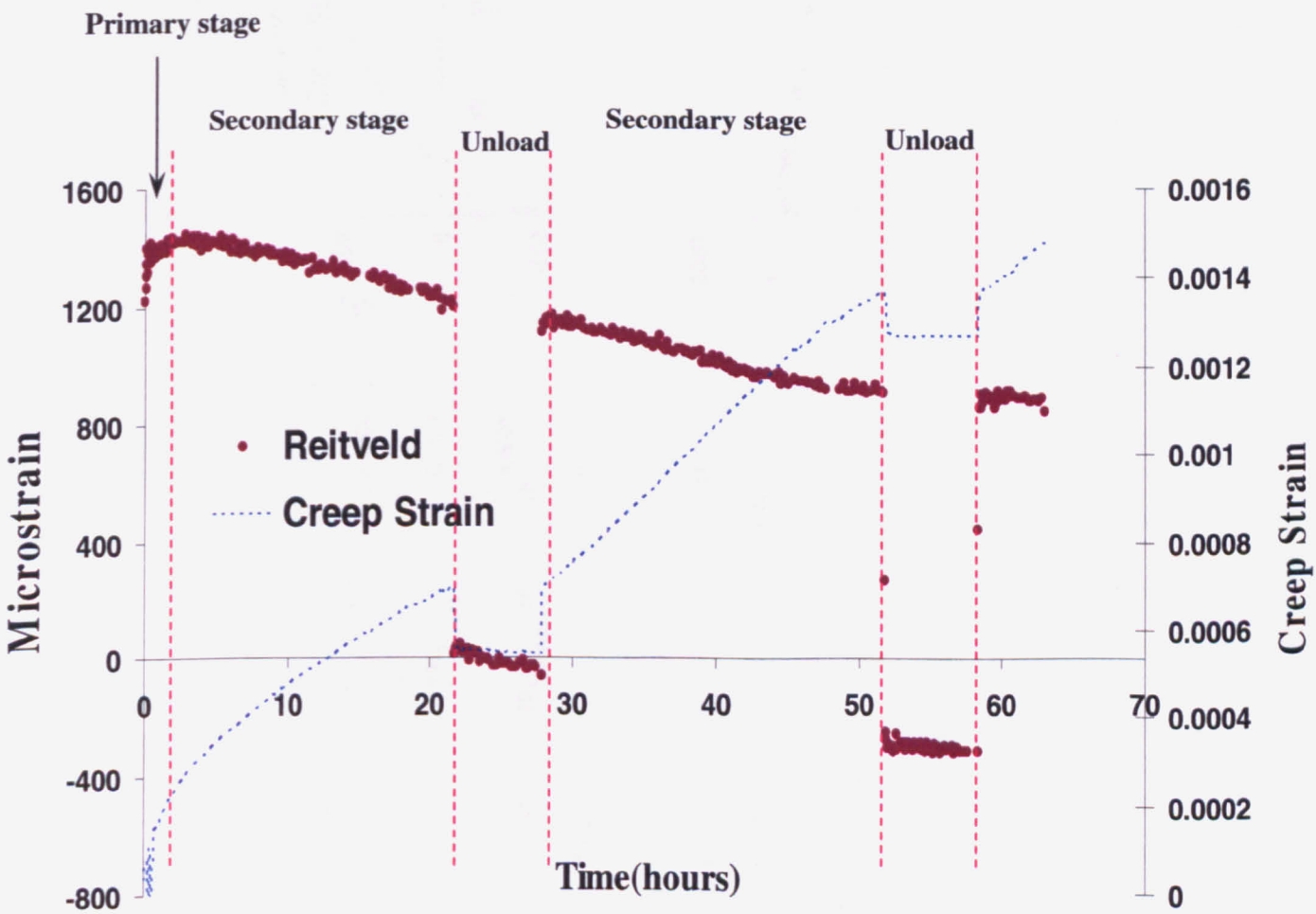

Fig. 7.7 Multi-peak data obtained using the Reitveld refinement technique

Fig. 7.8 shows the response of the individual lattice planes (111,200, 220 and 311). The behaviour of each of these varies when comparisons are done between themselves and also with the aggregate (Reitveld data). When the first grain orientations yield, the remaining

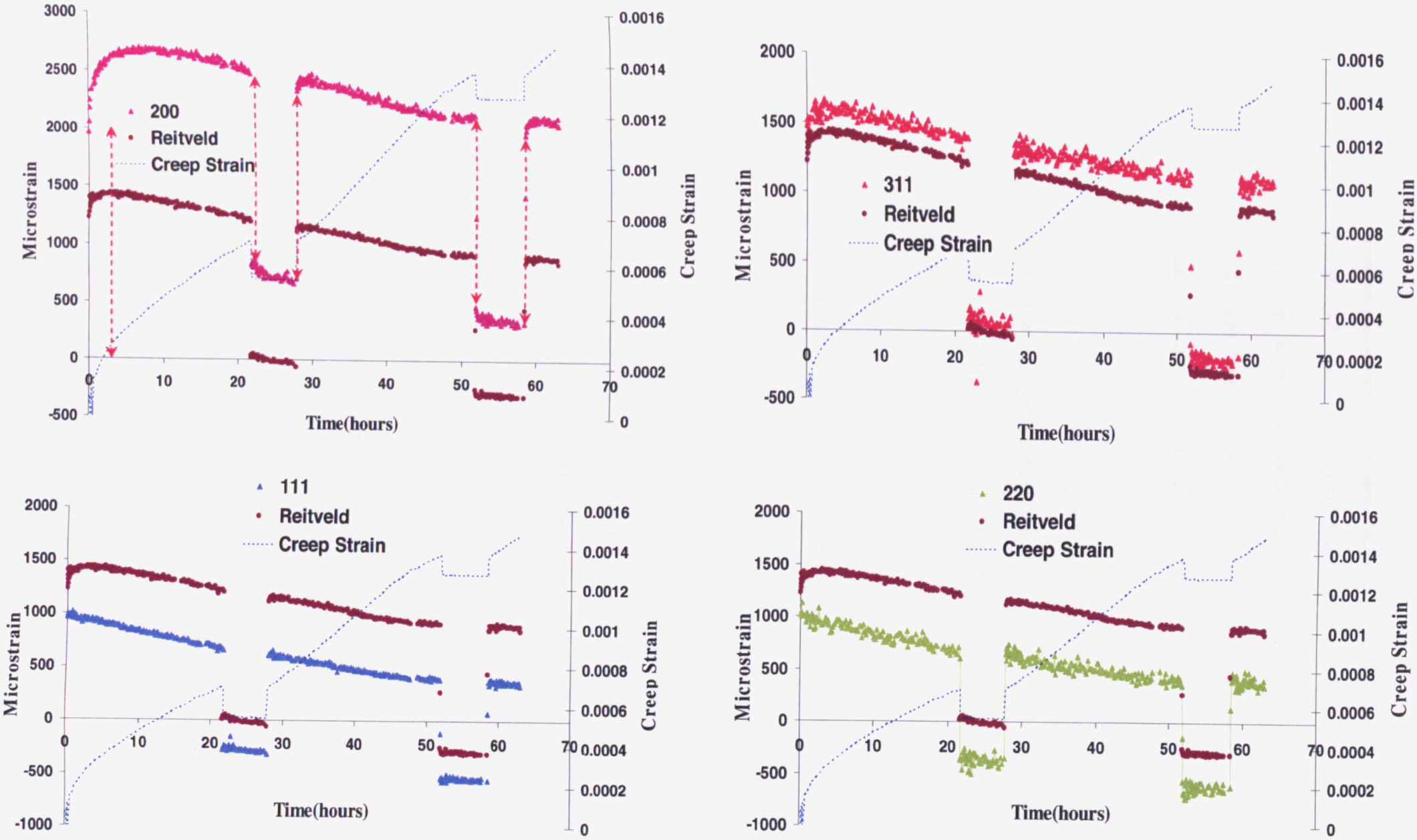

Fig. 7.8 Response of individual planes. Red arrows in the figure showing the behaviour of the {200} plane indicate the instantaneous elastic strains observed after loading/unloading

orientations that are still elastic will start bearing a larger load and will subsequently yield. The primary creep stage signals the start of an increasing plastic strain (macro) within the material. When all grains have become plastic, the behaviour will be a combination of the elastic and the plastic anisotropy of the material.

During the primary creep stage, grains oriented in the {200} plane strain in a more tensile manner compared to the multi-peak data. If the stress on this plane is calculated using the elastic modulus (section 7.4.2), it can be seen that (Fig. 7.6) the apparent stress on this plane is the highest. During the secondary creep stage(s), the strains decrease with time (tending towards compression). The behaviour during the unload periods follows a similar pattern as that during the load periods. The strain seems to decrease during the unload period.

The {311} plane follows the trend of multi-peak data throughout the test. Similar to the {200} plane, it strains in a tensile sense compared to the multi-peak data and tends towards compression as creep time increases. Compared to the multi-peak data, the recovery is higher in the unload cycle(s).

The {111} plane shows a different behaviour compared to the {200} and the {311}. It strains in a compressive sense to the multi-peak data. There is very little change in its behaviour when primary and secondary creep is compared. During the first unload, there is some evidence of recovery (straining in an opposite sense to that during load). This recovery is more prominent in the second unload cycle.

The behaviour of the {220} plane is similar to the {111} plane. It strains compressively compared to the multi-peak data. The major difference in its behaviour occurs during the

unload periods. The recovery is much more prominent in the first cycle itself. The strain increases by around 100-150 microstrain during the second unload period.

7.4.2 Elastic Behaviour and Estimation of Microstresses

The data presented in the previous sections contains the evolution of internal strains with both elastic and plastic loading. To understand the effects of creep and anelastic strains, the first step would be to subtract the instantaneous elastic strains observed when the load is applied or removed. The resultant data (Fig. 7.9) would then contain the effect due to inelastic strains only.

An example is shown for the {200} plane in Fig. 7.8. Hooke's Law can then be used to calculate the elastic modulus of that particular plane. The diffraction elastic moduli of each type will be the ratio between the strain drop when unloaded and the value of the stress removed (180MPa). The results are shown in Table 7.1. Using these elastic constants, an estimate can be made about the microstresses within the material. Although this will not be the local average residual stress, it can be considered as a far field homogenous stress required to produce the residual strain in a particular family of grains perpendicular to the loading direction.

Direction	I Unload	I Reload	II Unload	II Reload	III Unload
{111}	940	934	918	910	950
{200}	1650	1634	1666	1743	2130
{220}	971	996	955	1020	950
{311}	1300	1312	1300	1310	1440
Reitveld	1150	1145	1157	1160	1267

Table 7.1 Values of Instantaneous strain drops/ increases when the sample was unloaded/ reloaded

Table 7.2 shows the results. Comparisons have also been made with values of elastic moduli published in literature.

Direction	Estimated Elastic Moduli	Values of Elastic Moduli from Literature
{111}	181 GPa	180 GPa
{200}	109 GPa	90 GPa
{220}	183 GPa	165 GPa
{311}	138 GPa	125 GPa
Reitveld	156 GPa	140 GPa

Table 7.2 Comparison of estimated elastic moduli values of individual crystal planes at 650°C with literature

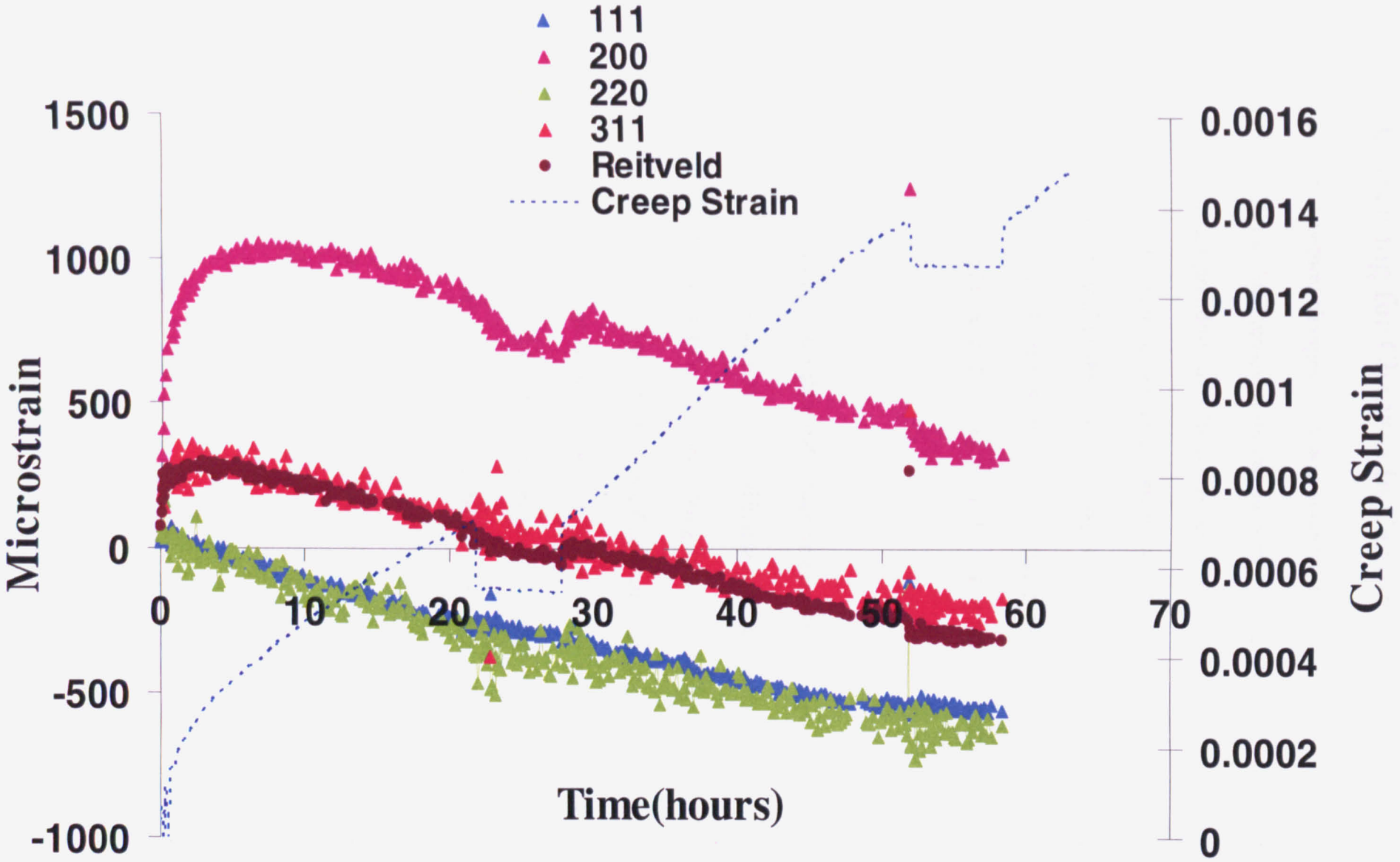

Fig. 7.9 Data after removal of instantaneous elastic strains

7.5 Correcting for Changes in Carbon Concentration

As mentioned before, changes in carbon concentration will affect the lattice spacing. To assess the effect of load removals on the microstrain behaviour, it is necessary to separate and subtract these pseudo-strains from the actual data. Separation of strains will require looking at the behaviour of one plane which will be least affected by the intergranular strains, and then assuming that all the changes seen in that plane is due to changes in carbon concentration. If the strain of one plane is made constant throughout the experiment, then relative differences with the other planes can be used to extract the overall behaviour.

The data obtained through the Reitveld refinement can be used for this purpose. Making an assumption that the refinement uses sufficient peaks, the behaviour of intergranular stresses on the data would be minimal. Using this hypothesis, the strain obtained using Rietveld refinement can be assumed to be a fixed value throughout the experiment and the relative differences of all other individual planes were calculated. The resultant data obtained is shown in Fig. 7.10. Alternatives to this method include using the {311} plane as the base plane and calculating all other strains relative to it [2].

The experiment can be split into four portions (Fig. 7.12) - First load, first unload, second load and second unload. Each of these has been examined individually.

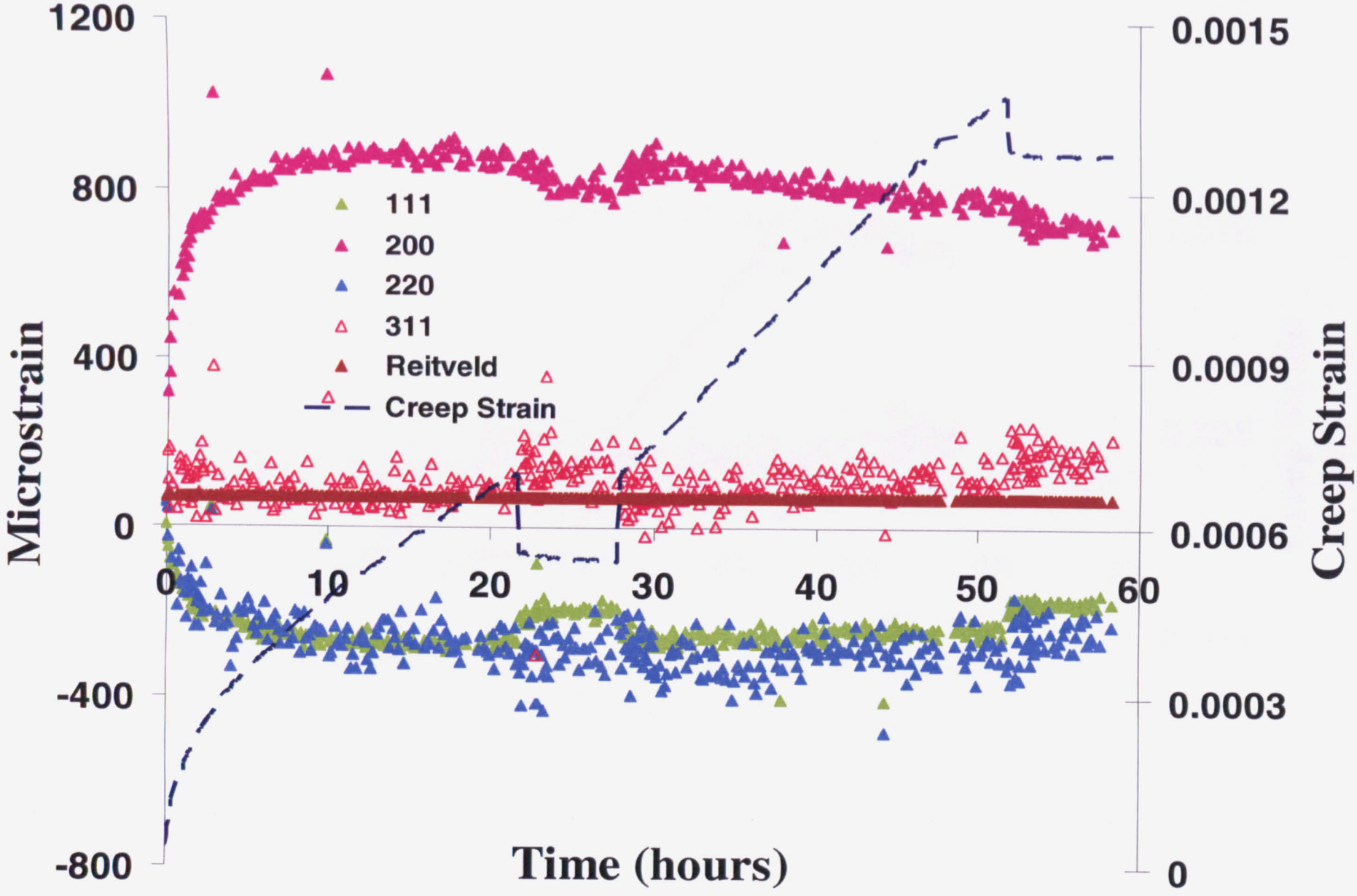

Fig. 7.10 Internal strain data after removal of elastic strains and correcting for changes in carbon concentration

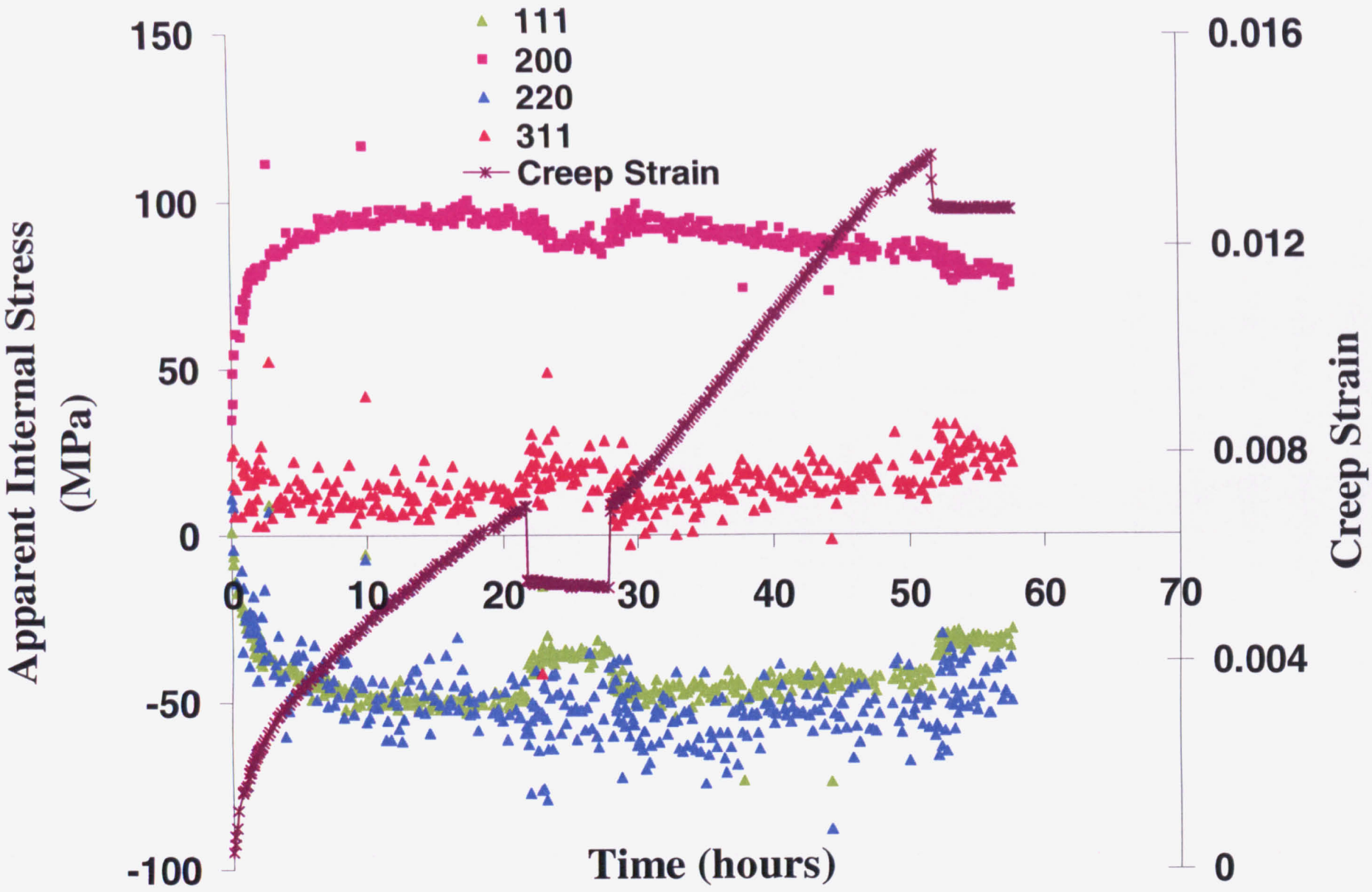

Fig. 7.11 Internal stress data after removal of elastic stresses and correcting for changes in carbon concentration

7.5.1 Behaviour during the First Load Cycle

The first loading is considered as the time period when the stress of 180MPa was applied to the specimen to the time it was unloaded. Creep strain will start from zero and then accumulates during this period. The material would first be in primary creep and then progress on to secondary creep. The increase in creep strain during this stage will result in changes to the intergranular strains and some amount of redistribution of strains will also occur.

Fig. 7.12 (a) shows the behaviour of the internal strains during the initial loading cycle. This, being the first loading cycle would consist of both primary and secondary creep contributions. The anisotropy seen in the behaviour of the individual planes would contain both elastic and plastic components. The {200} and {311} planes move towards a tensile direction whereas the {220} and the {111} planes move towards the compressive direction. The results obtained here are similar to results obtained by Daymond and Bouchard [2], where they conducted in-situ neutron diffraction tensile tests on 316 steel at various temperatures. Their results also show {111} and {220} again tend towards compression where as the {311} and the {200} move towards the tension.

The anisotropic behaviour observed during the initial loading is similar to that observed during plastic deformation which suggests similarities in the material behaviour when it is plastically strained by tensile deformation and creep deformation. At a grain scale, the response during primary creep is equivalent to plastic strain. Intergranular micro-stresses are introduced into the sample during primary creep. As the planes start to yield, the load now gets redistributed among the other planes and at the end of the primary creep, there is a tensile intergranular stress state in the {200} and the {311} planes, while a compressive state exists in the {220} and

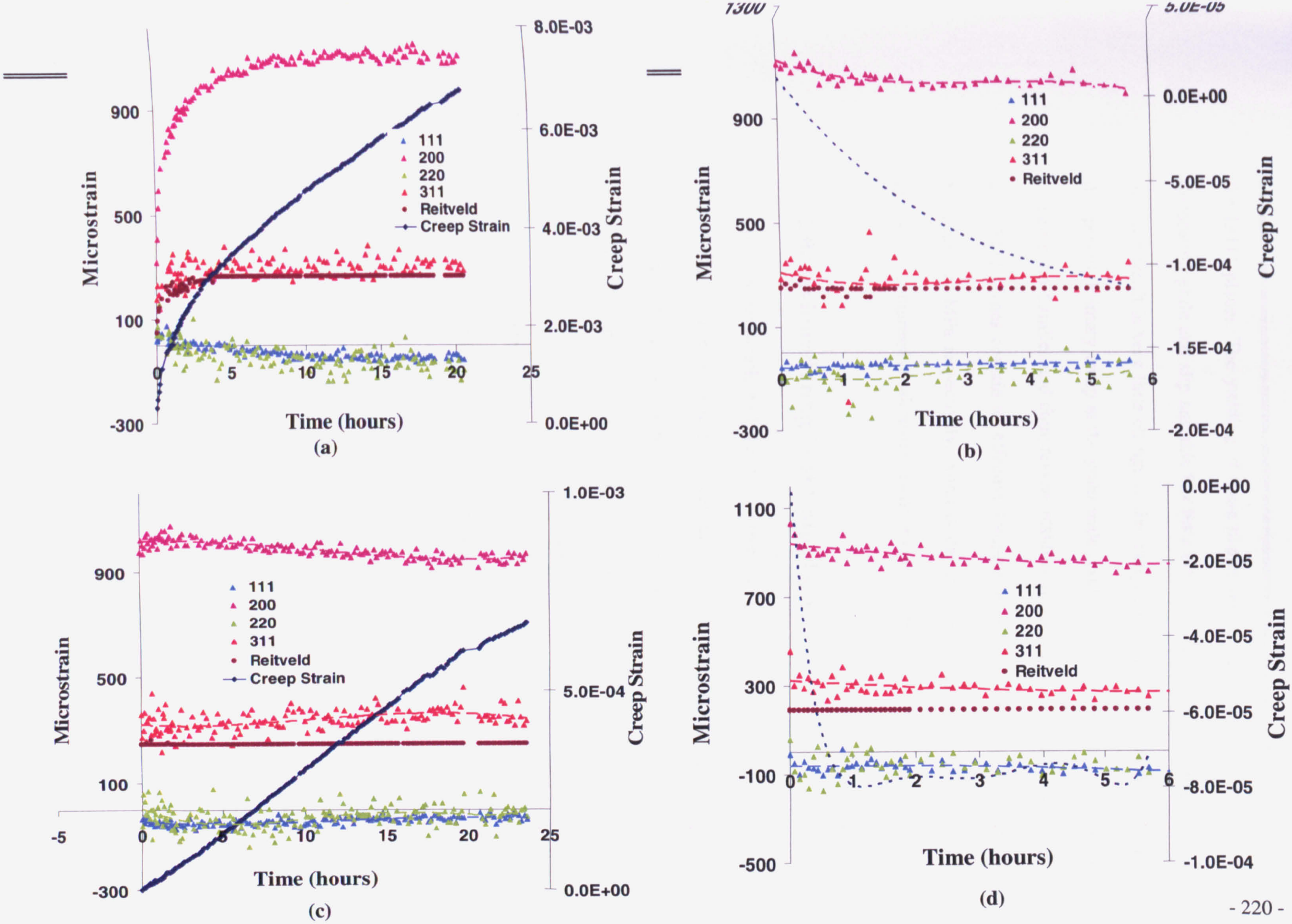

Fig. 7.12 Behaviour of crystal planes during (a) First load cycle (b) First unload cycle (c) Second load cycle (d) Second unload cycle

the {311} planes. The yielding of these planes results in deformation occurring through dislocation glide and slip and this has little effect on the elastic response of the material and as a result in very little change in the intergranular stress is seen in these planes post this period. Primary creep at the grain scale results in tensile residual strain generation in certain grain families and compressive residual strains in other grain families. The {200} and {311} planes contain an effective long-range tensile microstress level of around 80 MPa and 20 MPa respectively, whereas the creep-weak grains ({220} and {111}) are exposed to compressive microstresses of around -40 MPa.

7.5.2 Behaviour during First Unload Cycle

Unloading of the sample will start the recovery of plastic strain. The influence of anelastic creep on internal strain would be seen in this step. When the sample is unloaded, the stresses on all the planes are relaxed. This means the planes are unloaded from a plastic strain state. During the unload period, the driving force for each family of planes would be the relaxation of the stresses built up during the initial load period. The value of the strain after the instantaneous strain relaxation does not reach the value of the strain at the beginning of the test when the external stress on the sample was zero.

The behaviour of each crystal plane is different during the unload. The behaviour of the {200} plane follows the same trend as the macro-strain (i.e. moving towards compression). The {220} plane shows evidence of strain recovery. The lattice strains in this plane seem to be moving towards a tensile direction as compared to the first loading period when it moved towards a compressive direction. The {111} plane again shows a behaviour similar to the {220} plane, although the magnitude of recovery is much less.

The first loading increases the plastic strain, where-as the unloading will decrease the net creep strain by anelasticity. Anelastic strain can also be thought of as a strain which is being applied in the opposite direction (compressive) which will affect the overall macro-plastic strain state of the sample. This change in plastic strain will result in a redistribution of internal strains. When the load on the material is reduced, there is a tensile stress (accumulated in the previous load cycle) in the {200} plane and to a lesser extent in the {311} plane. Similarly, compressive stresses will exist in the {220} and the {111} planes. These compressive stresses will drive the dislocation motion and will cause anelastic creep during the unload period.

Section 5.10 presented results from tests where the sample was unloaded to stresses where anelastic recovery should be close to zero. The value of these macrostresses (≈45MPa) are similar to the values of the stresses in the {220} and the {111} planes. This suggests that residual stresses in these planes drive the anelastic deformation observed. The dislocations in grains oriented in the creep-hard planes under tensile stress will undergo no changes to their substructures as the total stress acting on that plane is less than the applied external load.

7.5.3 Behaviour during Second Load and Unload Cycle

The unloading of the material in the previous cycle influences the internal strains. Upon reloading, the behaviour of the crystal planes changes when compared to the behaviour during the first load cycle. The behaviour of the planes seems to suggest that after reloading there may be a very small period of primary creep like behaviour. This can be seen in the initial points of the {200} and the {220} planes (Fig. 7.12). The other planes also show similar behaviour but not as clearly. The load distribution among the different planes during this phase is different to that observed during the first loading cycle. The

{200} plane shows a bigger trend of internal stress relaxation. The {220} plane moves towards the tensile direction, something which is not seen in the first load cycle. The {111} plane shows a similar behaviour as the {220} plane but with lesser magnitude. There is a small change the internal strain behaviour of the {311} plane. The internal strains seem to move in a tensile direction whereas in the first cycle, the internal strain remains constant.

The behaviour of the planes in the second unload cycle is different to that observed in the first unload cycle. The strain evolution in the {311} plane seems to be similar to the behaviour observed in the previous unload cycle. The {220} plane shows a greater amount of strain recovery compared to the first unload cycle. Some amount of strain recovery (around 50 microstrain) can also be observed in the {111} plane.

To understand the effect of accumulated creep strain, internal strains can be plotted against absolute changes to the creep strain. Fig. 7.13 shows the comparisons in the behaviour of each plane during each load cycle. The {200} plane undergoes a much larger deformation during the initial stages of creep as compared to the second loading cycle when it would have reached secondary creep. The {111} plane again shows changes when the first and the second loading cycles are compared. During the first cycle, the plane tends to move towards a compressive direction but in the second cycle, the trend shows it moving towards a tensile direction. The {311} and the {220} planes do not show much change between the two loading cycles. However, in the {220} plane towards the end of the second loading cycle the planes seems to be moving towards the tensile direction.

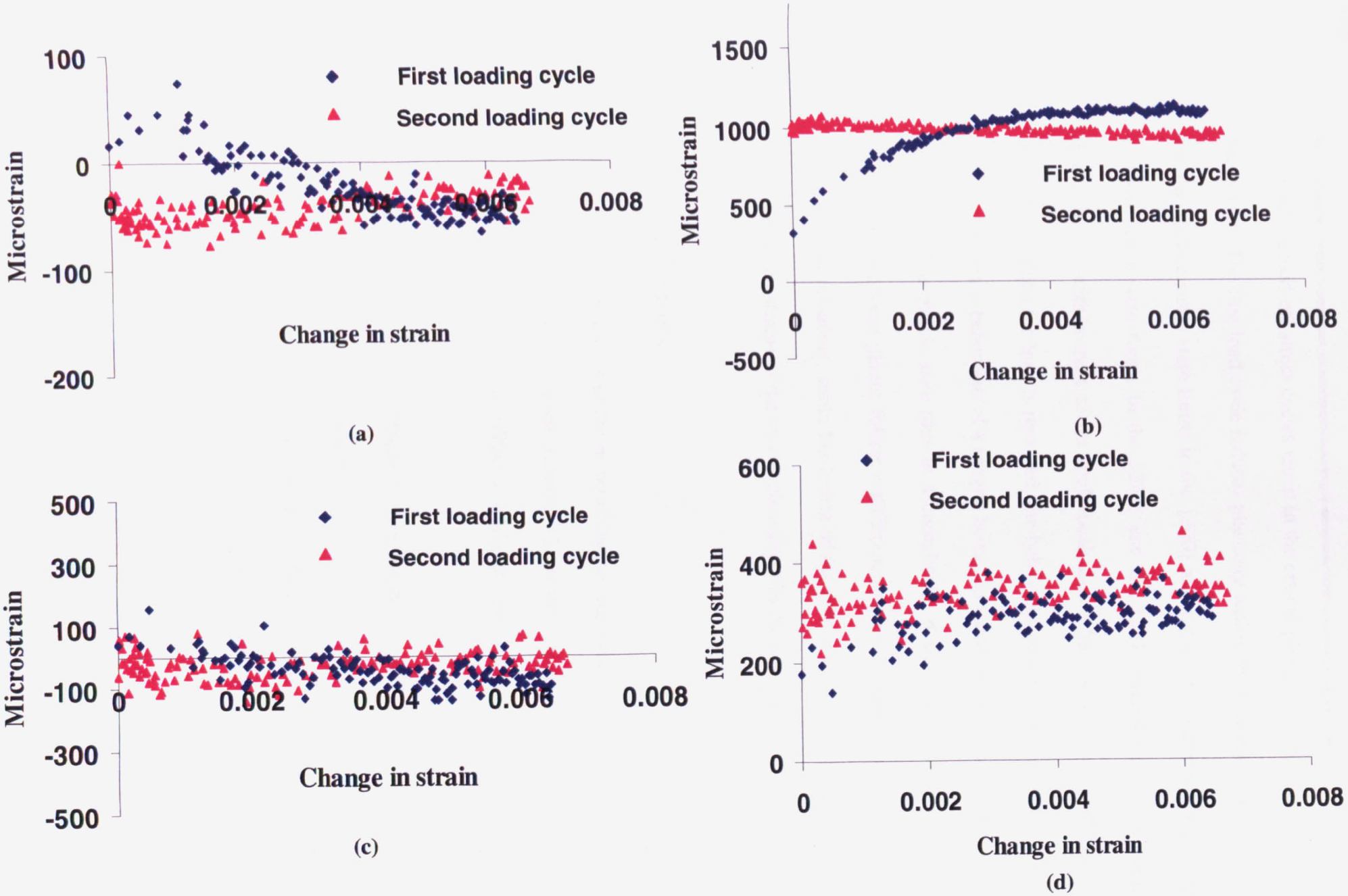

Fig. 7.13 Comparison of behaviour during the first and the second loading cycles (a) {111} plane (b) {200} plane (c) {220} plane (d) {311} plane

The load-on/load-off stress cycles result in the crystal planes displaying a strain ratcheting behaviour. The first load cycle induces plasticity within the material. During this cycle, a tensile residual stress state forms in the {200} and the {311} planes while a compressive residual stress state forms in the {220} and the {111} planes (tensile or compressive directions are with respect to the multi-peak data which would represent the aggregate behaviour). When the load is removed, the behaviour of the crystal planes can be equated to the stress-strain behaviour of a sample being unloaded during a conventional monotonic tensile test. The plastic state (due to accumulation of creep strain in the first load cycle) will make the crystal planes follow a different strain response to that seen during elastic loading. Upon reloading, strain hardening of the planes will result in very little change to the intergranular strains of the crystal planes within the material.

7.6 Conclusions

The changing plastic state of the material due to creep and anelasticity results in variations to the internal stress state of the material. Creep strain influences the manner in which the intergranular stresses are redistributed within the crystal planes.

- An in-situ neutron diffraction experiment which looked at the behaviour of the intergranular strains was conducted.
- The experiment showed anisotropy in the behaviour of the individual crystal planes which leads to the generation of intergranular stresses.
- Creep strain affects the way intergranular strains get redistributed during a material's lifetime. During the primary creep, it was found that the {200} plane is the main load bearing plane.
- The anisotropy results in tensile residual stresses being created in the {200} and the {311} planes and compressive stresses in the {220} and the {111} planes.

- When large load reductions occur, the residual compressive stresses present in the {220} and the {111} planes drives anelastic deformation.
- The anelastic strain rate generated due to the stresses in the planes with compressive residual stresses is similar to the strain rates observed when creep rupture tests were conducted at the same stress.

References

[1] P.J. Bouchard, D. George, J.R. Santisteban, G. Bruno, M. Dutta, L. Edwards, E. Kingston, and D.J. Smith, *Measurement of the residual stresses in a stainless steel pipe girth weld containing long and short repairs*, Int. J. Pressure Vessels. Piping, 2005, vol. 82 (4), pp. 299–310.

[2] M.R. Daymond, P.J.Bouchard, *Elastoplastic deformation of 316 stainless steel under tensile loading at elevated temperatures*, Metall. Mater. Trans. A, Vol. 37A, June 2006, pp.1863.

[3] M.R. Daymond and H.G. Priesmeyer, *Elastoplastic deformation of ferritic steel and cementite studied by neutron diffraction and self-consistent modelling*, Acta Mater., 2002, vol. 50 (6), pp. 1613–26.

[4] P.R. Dawson, A. Needleman, and S. Suresh, *Issues in the finite element modeling of polyphase plasticity*, Mater. Sci. Engineering, 1994, vol. A175, pp. 43–48.

[5] P.A. Turner, N. Christodoulou, and C.N. Tomé, *Modeling the mechanical response of rolled Zircaloy-2*, Int. J. Plasticity, 1995, vol. 11 (3), pp. 251–65.

[6] M.R. Daymond, M.A.M. Bourke, R.B. Von Dreele, B. Clausen, and T. Lorentzen, *Use of Rietveld refinement for elastic macrostrain determination and for evaluation of plastic strain history from diffraction spectra*, J. Appl. Phys., 1997, vol. 82 (4), pp. 1554–62.

[7] M.R. Daymond, *The determination of a continuum mechanics equivalent elastic strain from the analysis of multiple diffraction peaks*, J. Appl. Phys., 2004, vol. 96 (8), pp. 4263–72.

[8] S. MacEwen, J. Faber and A. Turner, *The use of time-of-flight neutron diffraction to study grain interaction stresses*, Acta Metall. 31 (1983) (5), pp. 657–676.

[9] T.M. Holden, R.A. Holt and A.P. Clarke, *Intergranular Strains in Inconel 600 and their Impact on the Interpretation of Stress Fields in Bent Steam-Generator Tubes*, Mater. Sci. Engineering, A 246 (1998), pp. 180–198

[10] E.C. Oliver, M.R. Daymond and P.J. Withers, *Interphase and intergranular stress generation in carbon steels*, Acta Mater. (2004), pp. 1937–1951

[11] D. Brown, M. Bourke, B. Clausen, T. Holden, C. Tomé and R. Varma, *A neutron diffraction and modeling study of uniaxial deformation in polycrystalline beryllium*, Metall. Trans. A 34A, 2003, pp.1439-1449.

[12] P. Dawson, D. Boyce, S. MacEwen and R. Rogge, *Residual strains in HY100 polycrystals: comparisons of experiments and simulations*, Metall. Mater. Trans. 31A (2000), p. 1543

[13] W. Boas and M. Hargreaves, Proc. Roy. Soc. 193 (1948) (1032), pp. 87–89.

[14] J.Quinta da Fonseca, E.C. Oliver, P.S. Bate, P.J. Withers, *Evolution of intergranular stresses during in situ straining of IF steel with different grain sizes* Mater. Sci. Engineering: A, Vol. 437, Issue 1, 10 November 2006, pp. 26.

[15] Z. Shen, R. Wagoner and W. Clark, *Dislocation and grain boundary interactions in metals*, Acta Metall. 36 (1988), pp. 3231–3242.

[16] H.M. Reitveld, *A profile refinement method for nuclear and magnetic structures*, J. Appl. Crystallogr. 2, 65 (1969).

[17] M.R. Daymond, M. A. M. Bourke, R. B. Von Dreele, B. Clausen and T. Lorentzen, *Use of Rietveld refinement for elastic macrostrain determination and for evaluation of plastic strain history from diffraction spectra*, J. Appl. Phys., Vol. 82, No. 4, 15 August 1997

[18] J. Quinta da Fonseca, E.C. Oliver, P. Bate, *Evolution of Internal Stresses during the Plastic Deformation of IF Steel and Their Correlation with Crystal Orientation*, Materials Science Forum 495-497, p. 1055-1060, 2005

[19] A. Korsunsky, M. Daymond, and K. James, *The Correlation Between Plastic Strain and Anisotropy Strain in Aluminium Alloy Polycrystals*, Mater. Sci Engineering A-Struct, 334(1-2):41–48, Jan 2002.

[20] C. Gaudin, X. Feaugas, *Cyclic creep process in AISI 316L stainless steel in terms of dislocation patterns and internal stresses*, Acta Materialia 52 (2004) 3097–3110

[21] L. Dickson, J. Boutin and L. Handfield, *A comparison of two simple methods for measuring cyclic internal and effective stresses*, Mater. Sci. Eng. 64 (1984), pp. L7–11.

[22] J.L. Dickson, L. Handfield and G. L'Esperance, *Cyclic softening and thermally activated deformation of titanium and zirconium*, Mater. Sci. Eng. 60 (1983), pp. L3–L7.

[23] X. Feaugas, *On the origin of the tensile flow stress in the stainless steel AISI 316L at 300 K: back stress and effective stress*, Acta Mater. 47 (1999), p. 3617.

[24] H.M.A Winand, P.J.Withers, *In situ phase strain monitoring during isothermal creep of metal matrix composites*, Physica B 234-236 (1997) 972-973.

[25] H.M.A Winand, A.F.Whitehouse, P.J.Withers, *An investigation of the isothermal creep response of Al-based composites by neutron diffraction*, Mater. Sci. Eng. A284, (2000) 103–113.

[26] R. Lin Peng, M. Odén, Y. D. Wang, S. Johansson , *Intergranular strains and plastic deformation of an austenitic stainless steel*, Mater. Sci. Eng. A334 (2002) 215–222.

[27] J. Pang, T. Holden, P. Turner and T. Mason, *Intergranular stresses in Zircaloy-2 with rod texture*, Acta Mater. 47 (1999), pp. 373–383.

[28] M.R.Daymond, M.E.Fitzpatrick, *Effect of cyclic plasticity on internal stresses in a metal matrix composite*, Metal. Mater. Trans. Vol 37A, 2006, pp.1985.

[29] B.Clausen, T. Lorentzen and T. Leffers, *Self-consistent Modelling of the Plastic Deformation of FCC Polycrystals and its Implications for Diffraction Measurements of Internal* Stresses, Acta mater. Vol.46, No. 9, pp. 3087-3098, 1998.

CHAPTER 8: MODELLING ANELASTICITY USING DAMAGE MECHANICS

The influence of loading conditions on the creep behaviour of 316H steel was examined in previous chapters. Experiments simulating power plant start-ups and shut downs showed a reduction in the ductility and an increase in the creep life. Microstructural examinations revealed changes in precipitate and dislocation densities during the unload phase. Neutron diffraction studies indicated corresponding changes in the internal strains, reflecting the role of internal stresses. This chapter looks at how changes in stress and temperature during a material's lifetime can be incorporated into a model representing the material's creep behaviour. Selected tests have been used for this purpose and microstructural inputs, such as changes in carbide densities, have been introduced. Due to time constraints, only a few tests have been modelled.

A damage mechanics approach has been employed to model the material behaviour. The following section gives a brief summary of other modelling techniques used to model creep behaviour and their limitations.

8.1 Prediction of Creep Behaviour

Prediction of creep behaviour can be performed using a number of techniques. Safe operation of power plants, often with conditions of variable load and temperature, places demands on the method(s) used to make safe and conservative estimates. In some cases, a limited material performance database must be used to extrapolate for longer times and for multi-axial/cyclic loading. This extrapolation requires a rational basis. To achieve this,

formalisms used must account for microstructural changes which can occur during the lifetime of a material.

If the precise stress-strain-time-temperature relationships were known for a material, these can be used to obtain material data for a range of conditions. Generally, this relationship is not known with sufficient confidence and a significant amount of subjectivity enters into any extrapolation procedure which potentially can lead to large errors when extrapolating. Logarithmic scales are sometimes used to represent a large range in data but this would result in higher errors in the real quantities for small errors in the extrapolated log quantities. For direct extrapolation, the stress-time plot is widely employed, usually in the form of stress-log time or log stress-log time.

8.1.1 Extrapolation of Creep Curves

This method was developed by Graham and Walles [16]. The creep strain of a material is described by a summation of terms of the form

$$\varepsilon = \sum_i C_i \sigma^{\beta i} \varphi^{Ki} \qquad 8.1$$

Where C, β and K are constants for any one term and φ is a function of time and temperature. σ and ε are the stress and strain respectively. The constant C can have dependencies on stress, temperature and φ

$$C = f(\sigma^{\alpha} \phi) \qquad 8.2$$

The values of C, α, β and K are found for each term using characteristics of the creep curve like secondary creep rate, time to failure and failure strain. These constants are then used to

extrapolate the terms individually to lower (or higher) stresses. The extrapolated values can then be recombined into the creep equations for those stresses.

8.1.2 Use of Time-Temperature Parameters

Creep deformation can be described using combined time-temperature laws. In effect, the four variables (time, temperature, stress and strain) can be split into two pairs and the resulting creep law can be written as:

$$f(\sigma,\varepsilon) = \phi(t,T) = U \qquad 8.3$$

Or for constant strain

$$f(\sigma) = \phi(t,T) = U \qquad 8.4$$

A single numerical value of U can be produced by any number of combinations of time and temperature. If the parameter is a correct representation for all times and temperatures, creep tests can be performed for short times at high temperatures to give a curve of σ against U. This same curve (the 'Master Curve') can then be used to predict the allowable stress for the same values of U given by long times and lower temperatures. The problem of extrapolation is then converted into one of interpolation of a master curve.

The three best known expressions are

$$f(\sigma) = U = te^{-\Delta H / RT} \qquad \text{Dorn [17]} \qquad 8.5$$

$$f(\sigma) = U = T(C_{LM} + \log t) \qquad \text{Larson Miller [18]} \qquad 8.6$$

$$f(\sigma) = U = (T - T_o)/(\log t - \log t_o) \qquad \text{Manson-Haferd [19]} \qquad 8.7$$

Where t is time, T is absolute temperature, K is the gas constant and ΔH, C_{LM}, T_o and t_o are constants for the material and the strain level, determined by experiment.

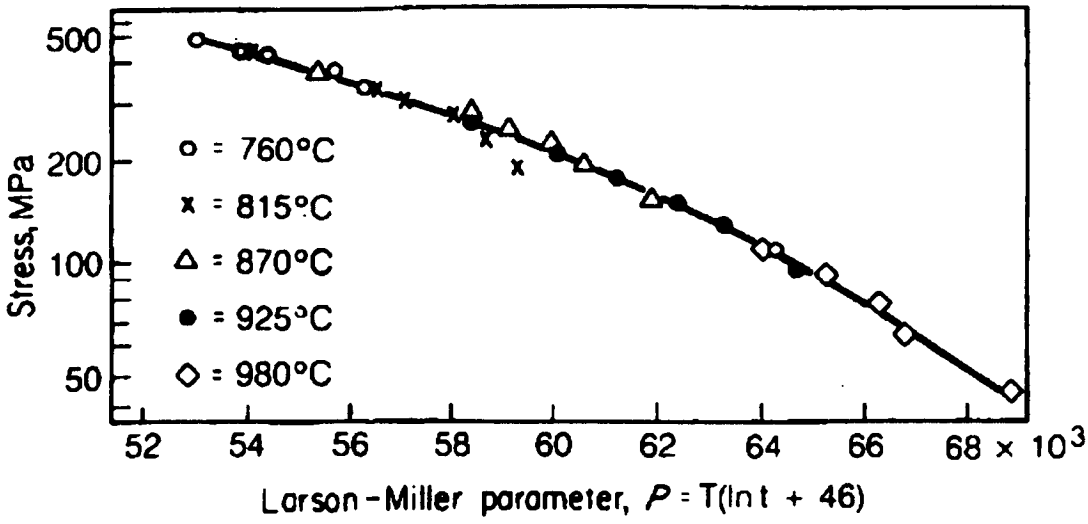

Fig. 8.1 Master curve for Larson-Miller parameter for Astroloy [20]

Creep is often considered to be dominated by secondary creep, with short primary and tertiary phases. Secondary creep rate ($\dot{\varepsilon}_{ss}$) can be represented using a power law equation with an Arrhenius temperature dependence

$$\dot{\varepsilon}_{ss} = A_o \sigma^n \exp(\frac{-Q}{RT}) \qquad 8.8$$

σ and T represent the stress and temperature, Q is the activation energy identical to self-diffusion of carbon in steels [11], n is the stress exponent, A_o is a material constant and K is the universal gas constant. However, material behaviour in practical situations can have dominant primary and tertiary creep components. Attempts have been made to model creep behaviour based on the shape of the entire creep curve. The theta projection approach uses this idea. For example, creep strain (ε) can be expressed as a function of stress, temperature and time [3- 5].

$$\varepsilon = \theta_1(1-\exp(-\theta_2 t)) + \theta_3(\exp(\theta_4 t) - 1) \qquad 8.9$$

$$\log\theta_i = a_i + b_i T + c_i \sigma + d_i \sigma T$$

where a_i, b_i, c_i, d_i are constants (i=1 to 4). For a particular test, the data can be fitted to obtain each individual θ_i.

If the variation in creep strain with time is given by 8.9, then the creep rate at any instant is

$$\dot{\varepsilon} = \theta_1\theta_2 \exp(-\theta_2 t) + \theta_3\theta_4 \exp(\theta_4 t) \qquad 8.10$$

And the rate of change of creep will be

$$\ddot{\varepsilon} = -\theta_1\theta_2^{\,2} \exp(-\theta_2 t) + \theta_3\theta_4^{\,2} \exp(\theta_4 t) \qquad 8.11$$

Equation 8.11 indicates that values of function $f\{\theta,t\}$will have a minimum gradient for positive values of θ_i and this minimum creep rate occurs at time t_m given by

$$t_m = \frac{1}{\theta_2 + \theta_4} \ln\left(\frac{\theta_1\theta_2^{\,2}}{\theta_3\theta_4^{\,2}}\right) \qquad 8.12$$

Thus, if θ_i is known at any set of testing conditions, it is possible to calculate t_m and the minimum creep rate. Although, this type of analysis would not define failure, it is also possible to rewrite equation 8.9 in terms of either failure time or failure strain.

One of the main drawbacks of this method is that a database of creep information is needed to establish the dependence of the model parameters on stress and temperature. Within a given creep database, this method can predict creep behaviour reasonably well. Extrapolation of longer term data from short term data can also be done with some degree of accuracy. However, if varying/multiaxial loading has to be predicted, there is a large increase in the number of model parameters required which increases the uncertainty in the analysis [6].

8.2 Introduction to Damage Mechanics Modelling

Large differences can be seen in the high temperature behaviour between different classes of material reflecting the operation of specific deformation mechanisms. The modelling technique used must allow the input of suitable physical mechanisms for different materials and different loading conditions [7]. Damage mechanics provides a framework within which it is possible to integrate the physical mechanisms responsible for material degradation and the subsequent effect on creep strain.

In this method, creep damage is represented by a series of rate equations which describe the evolution of strain along with state variables (S_1, S_2, etc) which influence the deformation.

$$\dot{\varepsilon} = f(\sigma, T, S_1, S_2 \ldots)$$

$$\dot{S}_1 = f(\sigma, T, S_1, S_2 \ldots) \qquad 8.13$$

$$\dot{S}_2 = f(\sigma, T, S_1, S_2 \ldots)$$

The main principle of the method is the assumption that creep behaviour is dominated by a progressively evolving creep rate caused by microstructural changes in the material that may be considered as 'damage' [7]. The method was first pioneered by Kachanov [8] and Rabotnov [9] who used purely empirical approaches where damage was described by a variable D that changes with creep strain:

$$\dot{\varepsilon} = \frac{\dot{\varepsilon}_i}{(1-D)^p} \qquad 8.14$$

$$\dot{D} = \frac{B\dot{\varepsilon}_i}{(1-D)^m}$$

where constants B, m, p and ε_i are adjusted fit to the creep data.

These concepts were further developed by Leckie and Hayhurst [10] to account for multiaxial loading. Damage mechanics has been applied to a wide range of metallic alloys. The complexity of the state variables used depends on the material and its applications.

Damage mechanics models which describe creep can be formed so that they incorporate the evolution of microstructure and development of creep cavitation. Damage can be classified into three categories [11]:

- Softening within the material due to changes in the microstructure. One of the main causes for this is the accumulation of mobile dislocations. Strain rate has a linear dependence on this type of damage.
- Cavitation and micro-cracking leading to a reduction in the load bearing area. Thus the stress on the remaining 'undamaged' area increases, which subsequently increases the strain rate.
- Changes in the material microstructure such as changes in particle densities.

Based upon this, equation sets can be developed which can be used to predict creep behaviour.

8.3 Selection of Model Used in this Study

To incorporate some of the microstructural observations seen during the unload period, a damage mechanics model was chosen. The ability to input microstructural details was one of the main selection criteria of the model. The model had to be such that it would allow

for changes in precipitate densities. Very few models exist which predict the behaviour of materials when unloaded during a creep test.

Certain simplifying assumptions were made when selecting the appropriate state variables for the current model. These were:

- Dislocations mainly move by glide or climb of dislocations over precipitates.
- Precipitates are spherical and the particle distribution is spatially homogenous.
- The motion of dislocations reflects the state of carbide distribution. A higher carbide density would mean a higher chance of dislocation pinning occurring.

Ghosh and Mclean have developed a model [11] which describes the strain rate as a function of various hardening and damage state variables.

$$\dot{\varepsilon} = A\sigma^n(1-H)\exp(\omega_1+\omega_2+\omega_3)$$

$$\dot{H} = H_1 A\sigma^n(1-H) - LH \qquad 8.15$$

$$\dot{\omega}_1 = c_1\dot{\varepsilon}$$

$$\dot{\omega}_2 = c_2\dot{\varepsilon}$$

$$\dot{\omega}_3 = c_3\dot{\varepsilon}$$

Here, state variable H represents the hardening behaviour of the material during primary creep and constant L is considered to be a recovery coefficient that leads to steady state value of internal stress [7]. ω_1, ω_2 and ω_3 are different 'damage' variables which can be used to describe the microstructural changes occurring during creep. H_1, c_1, c_2 and c_3 are

constants which depend on the material response during testing and the term $A\sigma^n$ is equivalent to the steady-state creep rate $\dot{\varepsilon}_{ss}$ given in equation 8.8 with $A=A_o exp(-Q/KT)$.

In this study, two other microstructural features were incorporated into the model described in 8.15. Creep cavitation and crack growth is generally considered the main mechanism during tertiary creep and this can be represented using one of the damage variables. A damage variable 'ω' was introduced to account for tertiary creep damage.

A second damage parameter 'S' described changes in precipitate densities. Dyson [6] has proposed that variation in particle spacing can be described using a softening parameter $S = 1 - \frac{p_i}{p}$, where p_i is the initial carbide spacing whose rate dependence can be written as

$$\dot{S} = K_c(1-S)^4 \qquad 8.16$$

where K_c is a material constant associated with particle coarsening and is related to the heat of solution of carbon in iron [21].

The variable describing stress rate can be written as $\dot{\sigma} = E(\dot{\varepsilon}_t - \dot{\varepsilon})$ according to Ghosh and Mclean [11]. Introducing the evolution of carbide spacing (8.16) into the general equation set (8.15) describing the strain response results in creation of a generalised equation set which can be used to describe high temperature deformation.

$$\dot{\sigma} = E(\dot{\varepsilon}_t - \dot{\varepsilon})$$

$$\dot{\varepsilon} = A\sigma^n(1-H)(1+S)(1+\omega)$$

$$\dot{H} = H_1 A\sigma^n(1-H) - LH \qquad 8.17$$

$$\dot{\omega} = c\dot{\varepsilon}$$

$$\dot{S} = K_c(1-S)^4$$

where ε_t is the total strain (elastic + creep) and $A=A_o exp(-Q/KT)$.

In summary, the above equation set describes creep rate $\dot{\varepsilon}$ in terms of

- Uniaxial stress σ.
- Internal hardening parameter H leading to primary creep. This simulates the accumulation of dislocations near carbides and other artefacts, leading to internal stress redistribution.
- Softening parameter S associated with carbide spacing.
- Damage parameter ω which causes tertiary creep and fracture.

During creep deformation, there will be a number of other microstructural changes occurring within the material. These include strain-induced mechanisms such as subgrain coarsening and mobile dislocation generation, environmentally-induced mechanisms such as internal oxidation and others. To incorporate all possible mechanisms will be extremely complex due to the interactions involved. Thus 8.17 can be considered as an equation set which represents material behaviour to a reasonable level.

The individual rate equations for the constituent state variables in the above equation set can be adjusted depending on experimental conditions. During a creep test, the applied load is kept constant and thus the stress rate ($\dot{\sigma}$) will be zero. However, when the sample is unloaded/loaded, there is a rate at which the sample is loaded which means $\dot{\sigma}$ has a finite value depending on the experimental procedure. Similarly, if only the primary and secondary parts of a creep curve are being modelled, then the state variable for tertiary creep (ω) can be made zero. The initial values of all variables (ε, H, S, ω) are zero.

8.4 Modelling of Experimental Data

This section describes the method developed to model unloading during a creep test. The first step in the procedure is to find the values of the activation energy Q and the stress exponent n. Equation 8.8 can be considered as:

$$\ln(\dot{\varepsilon}_{ss}) = \ln(A_o) + n\ln(\sigma) - \frac{Q}{RT} \qquad 8.19$$

Although, this is not an exact mathematical description of secondary creep (based on equation set 8.17), it provides a reasonable approximation.

Using an initial guess, this equation was used in an optimisation routine called *fminsearch* in MATLAB to find the values of Q and n_o. The routine uses a least-square approach to determine the values of the constants which will give the best fit to all the data. Details of the optimisation routine are given in Appendix II.

The strain rates presented in Table 4.5 were used in this optimisation procedure to obtain the stress exponent and the activation energy.

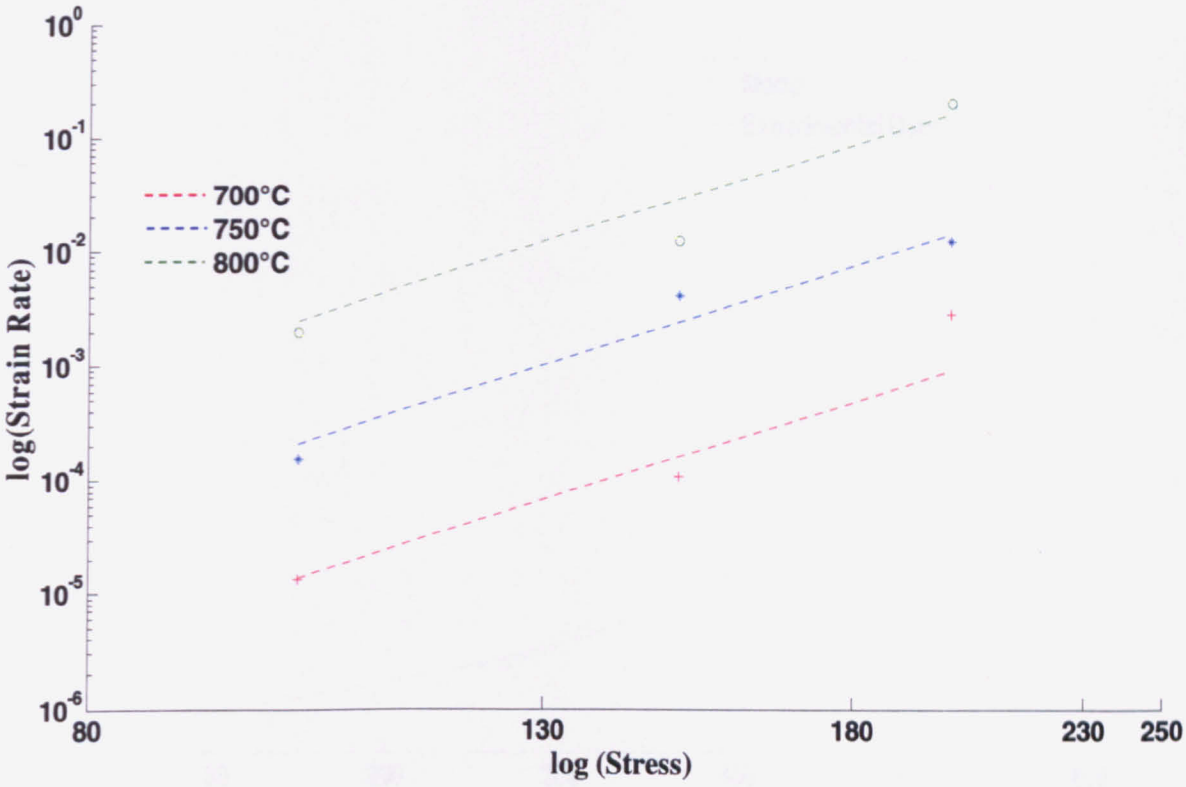

Fig. 8.2 Strain rate optimisation. Symbols represent experimental data. Dashed lines represent the results obtained after optimisation.

The values for n and Q were obtained as 5.5 and 450 kJ/mol respectively. The values are in the same range as those obtained by Dyson [22]. Fig. 8.2 shows comparisons of the predicted strain rates using the optimised values of n and Q with experimental data. These values for n and Q obtained using the optimisation procedure have been used throughout this chapter.

The next step was to check whether equation set 8.18 can be used to model conventional creep behaviour. The creep rupture test shown in Fig. 4.6 (test conditions 650°C and 180MPa) was chosen for this purpose. As this was a constant load creep test, the equation describing stress rate ($\dot{\sigma}$) can be assumed as zero.

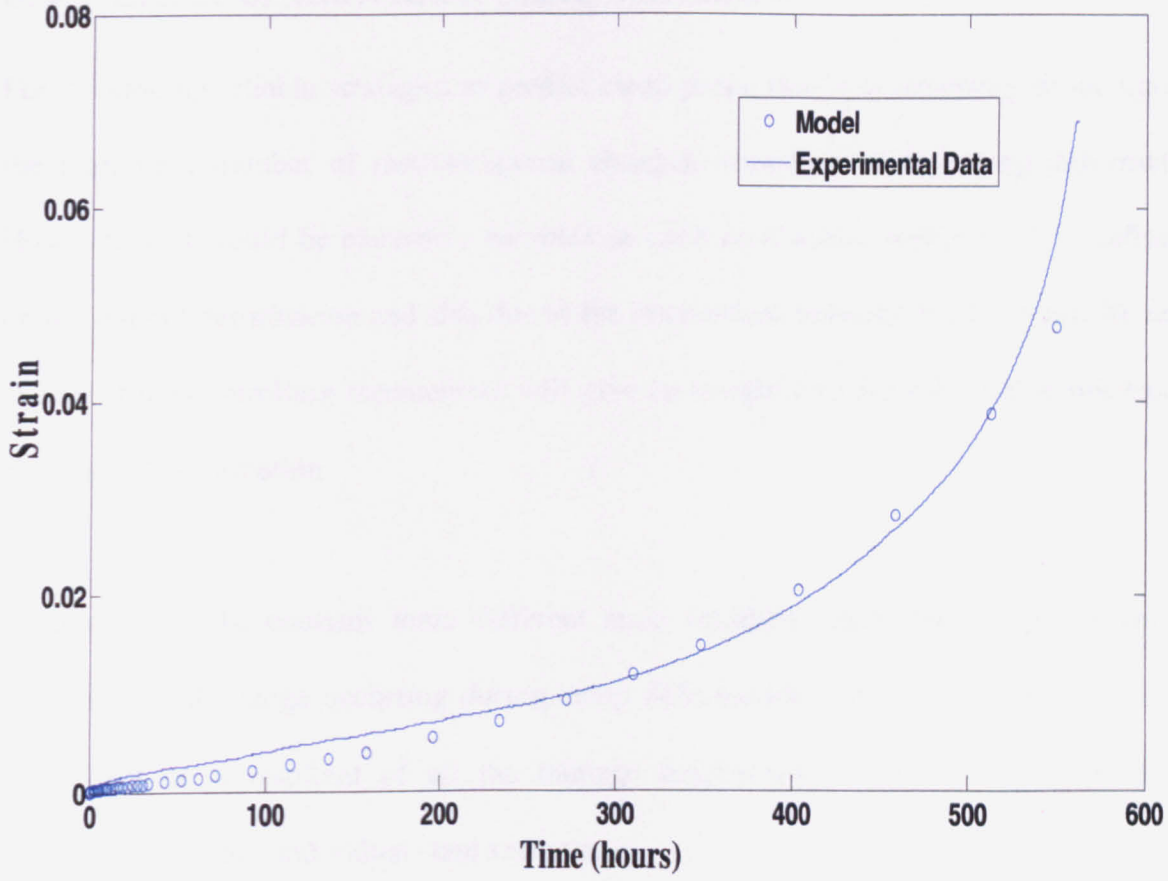

Fig. 8.3 Fitting of creep rupture data at 650°C 180 MPa

A_o $(Nm^{-2})^{-n}s^{-1}$	H_1(MPa)	L	c	K_c (h^{-1})
9.02×10^{9}	150.35	0.0054	401.20	0.021

Table 8.1 Values of constants for steady-load creep rupture curve (650°C 180MPa)

The equation set was optimised to fit to the experimental data. The result of the fitting that creep behaviour is shown in Fig. 8.3. This shows that creep behaviour can be modelled using this state-variable equation set. The values of the constants obtained are given in Table 8.1.

8.4.1 Effect of Individual State Variables

For developing reliable strategies to predict creep properties, it is necessary to incorporate the maximum number of microstructural changes occurring during creep deformation. However, this would be extremely complex as each mechanism would have an influence on the overall deformation and also due to the interactions between mechanisms. Removal of any of the controlling mechanisms will give an insight into the role of that mechanism on material deformation.

Equation set 8.18 contains three different state variables, each describing a particular microstructural change occurring during creep deformation. The final shape of the creep curve will be a resultant of all the damage mechanisms. This section looks at the contribution of each individual state variable.

A steady-load creep rupture test (test conditions 650°C 180MPa.-Fig. 8.3) was chosen for this purpose. The effect of tertiary creep was first examined (Fig. 8.4). This can be done by assuming c in equation set 8.18 as zero.

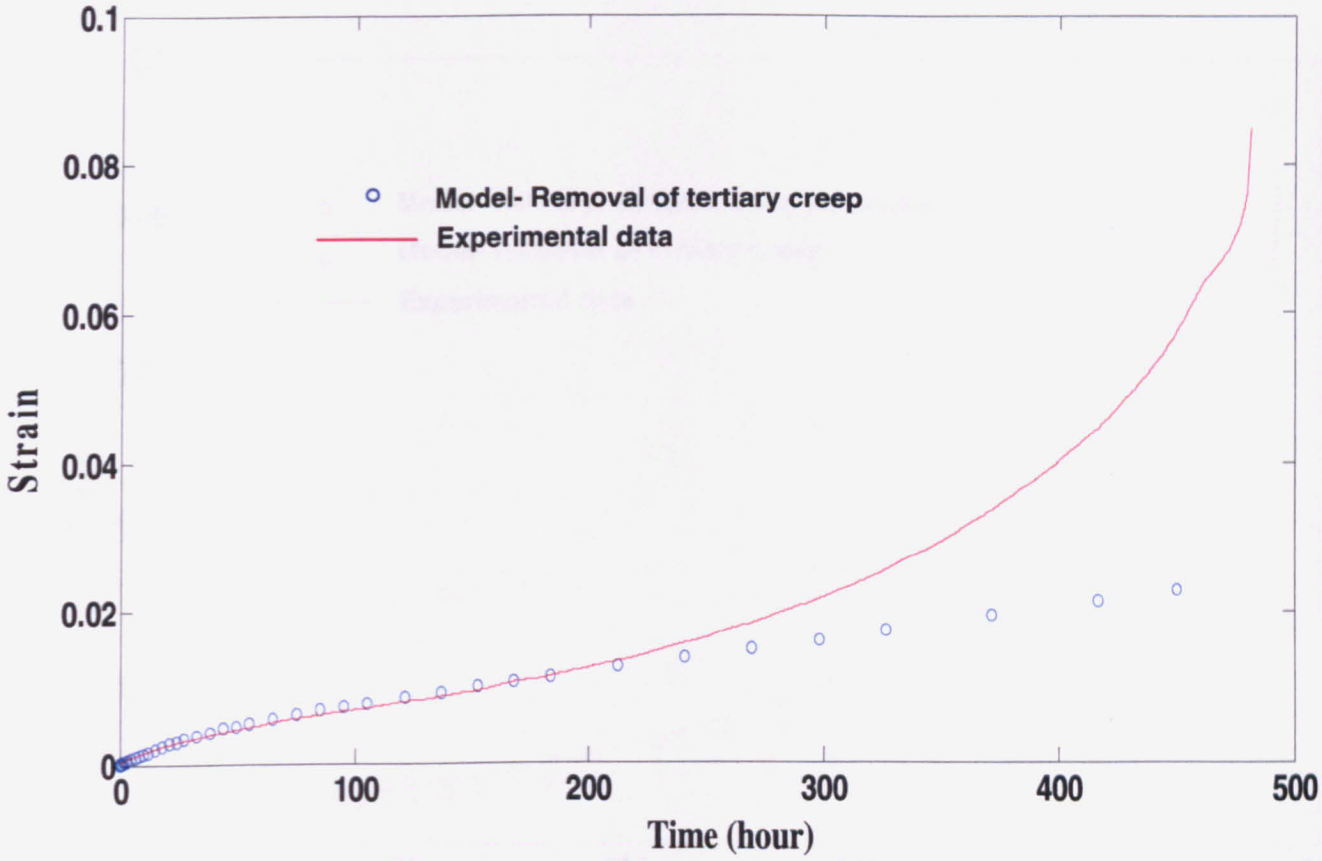

Fig. 8.4 Removal of tertiary creep damage

The constant set used is the same as that shown in table 8.1.

Using the above figure as a reference, removal of the particle coarsening state variable S was simulated. This was done by assuming K_c as zero.

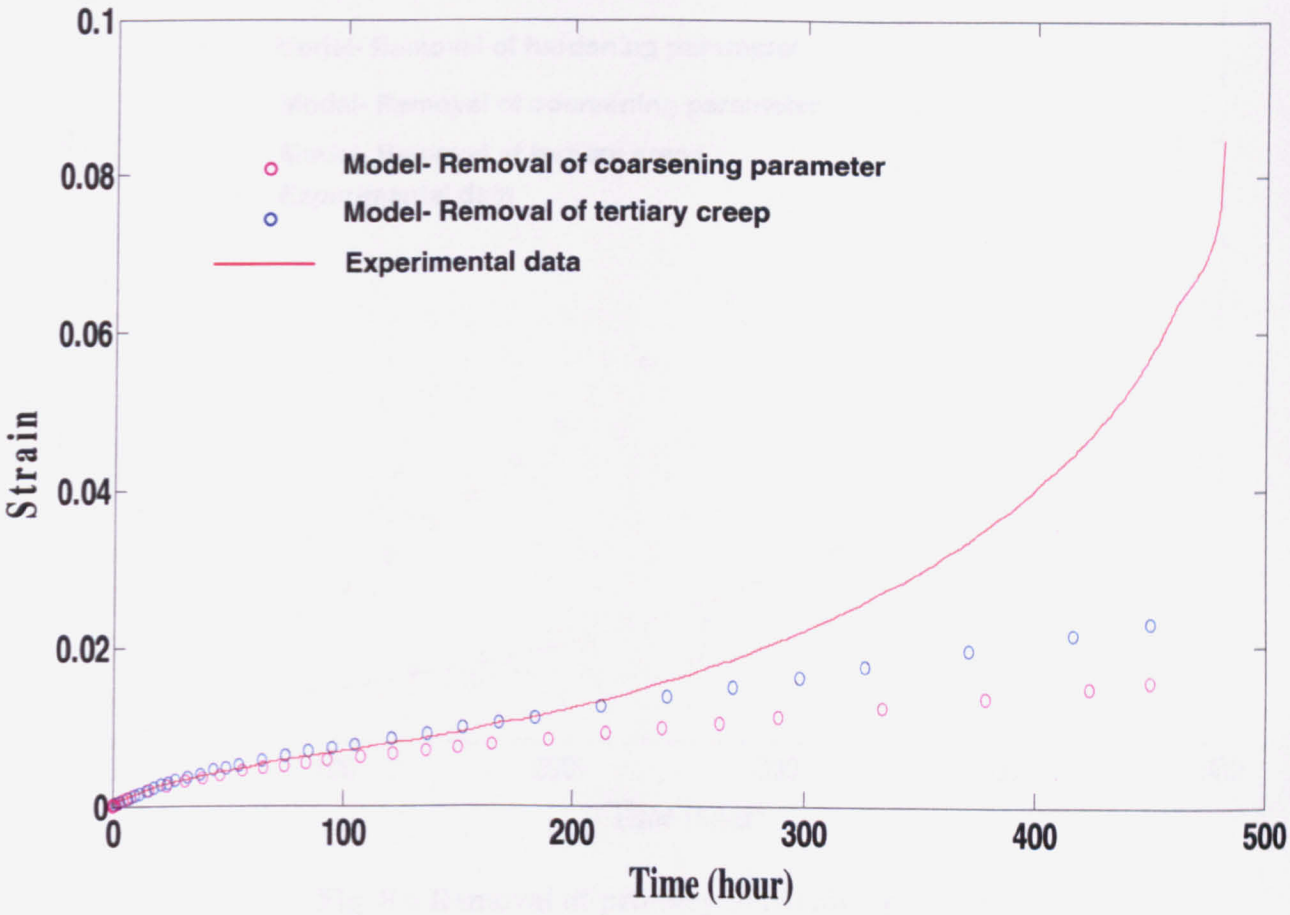

Fig. 8.5 Effect of removing coarsening parameter, *S*

The final step would be to remove the effect of the hardening parameter, H. This will result in the term describing the strain rate (ε) becoming a linear term which is described by $A\sigma^n$.

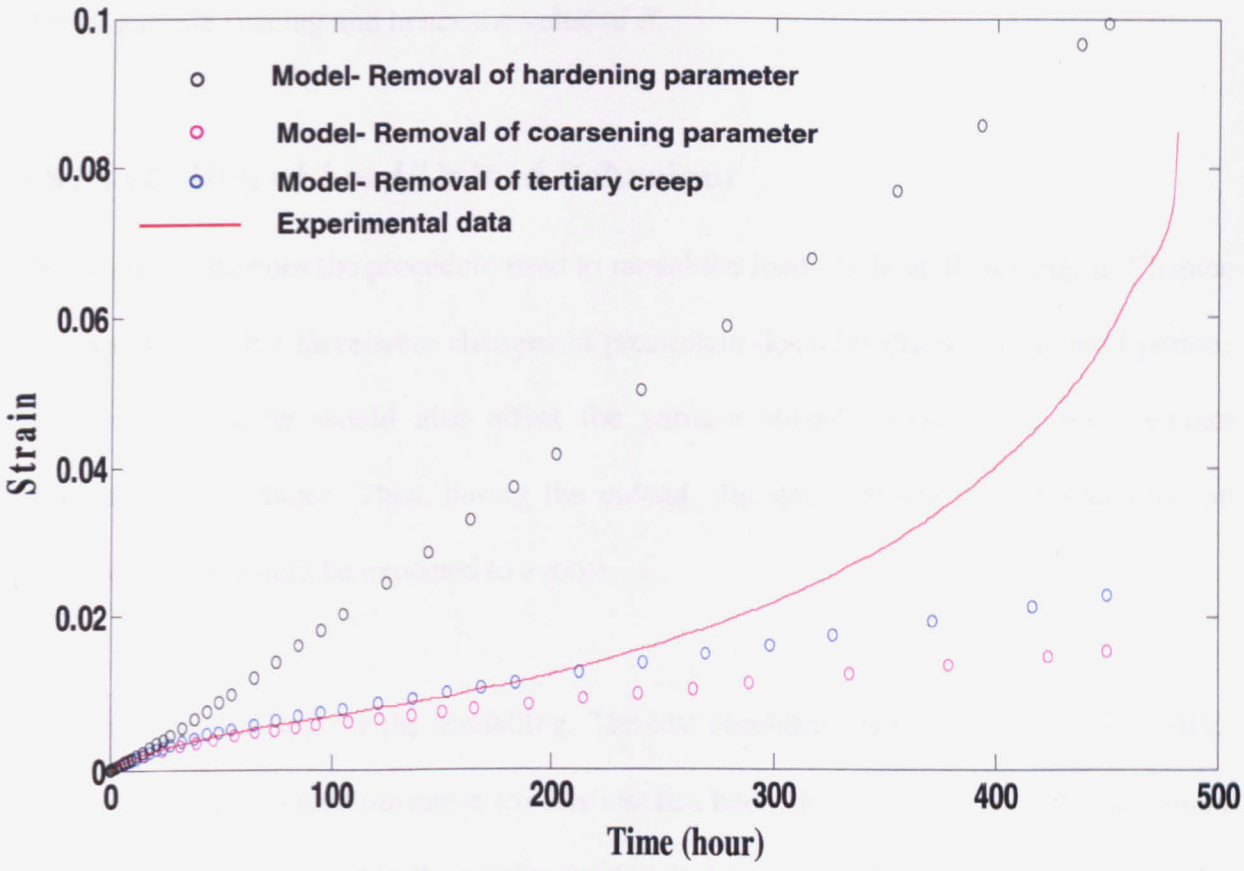

Fig. 8.6 Removal of primary hardening parameter

The above results show the extent to which each state variable influences the overall creep deformation. Some physical conclusions can be drawn from this: Cavity generation is a process which initiates during secondary creep (possibly in primary creep as well). However, as per Fig. 8.4, it becomes increasingly significant as the material approaches tertiary creep. Secondary creep again contains a number of other mechanisms such as subgrain formation, increase in mobile dislocations, etc. These mechanisms will influence the formation and propagation of cavities. Thus, tertiary creep behaviour of steady load creep tests and load-on/load off creep tests will be different which can cause changes to the state variable describing tertiary creep (ω). This will be reflected in the values of the constant 'c'. Unloading during secondary creep will affect the formation of precipitates

and dislocation networks. Changes in mechanisms which generate carbides will affect the overall carbide spacing and hence the value of K_c.

8.5 Modelling of Load/Unload Behaviour

This section describes the procedure used to model the load-on/ load off testing. In Chapter 6, it was found that there were changes in precipitate densities during the unload period. The density change would also affect the particle spacing assuming a homogenous distribution of carbides. Thus, during the unload, the state variable which accounts for particle spacing would be expected to evolve.

Test 1(a) was selected for the modelling. The test conditions were 650°C and 180 MPa. The experimental strain-time curve for this test has been shown in Fig. 8.7. The specimen was loaded for 48 hours and then unloaded for 48 hours. The first step was to model the load-on curve for this experiment. The load-unloading cycles would have influenced the overall behaviour when the sample was loaded. Thus using the same constants as in Table 8.1, it was expected that a good fit would not be obtained. For this reason, a new set of constants had to be found for the load-on curve.

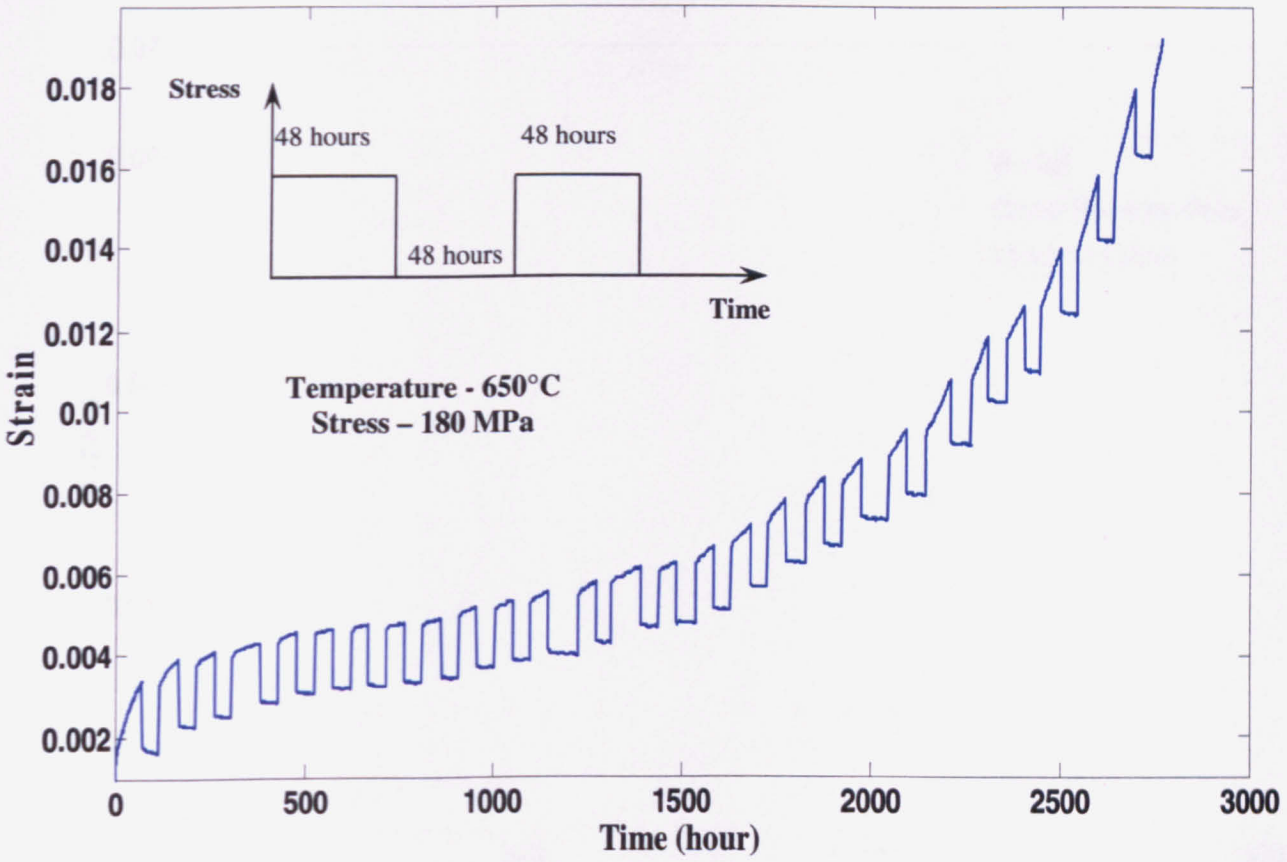

Fig. 8.7 Sample was loaded for 48 hours and unloaded for 48 hours

Fig. 8.8 shows the fit and Table 8.2 lists the values of the constants. The results of the model (values of constants A_o, H_1, L, c, K_c- Table 8.2) show distinct differences when compared to the results for the steady load creep rupture curve (Table 8.1). The constant c which is related to the tertiary creep behaviour shows the biggest variation. As explained in Section 5.6, upon reloading each time, there may be a small primary creep behaviour which can increase the density of dislocation networks resulting in decreased amount of tertiary creep behaviour. Unloading may also be changing the internal stress state which can result in cavity growth inhibition. A change in the value of K_c can also be observed which suggests that different processes may be influencing the carbide formation. This topic has been discussed further in section 9.2.

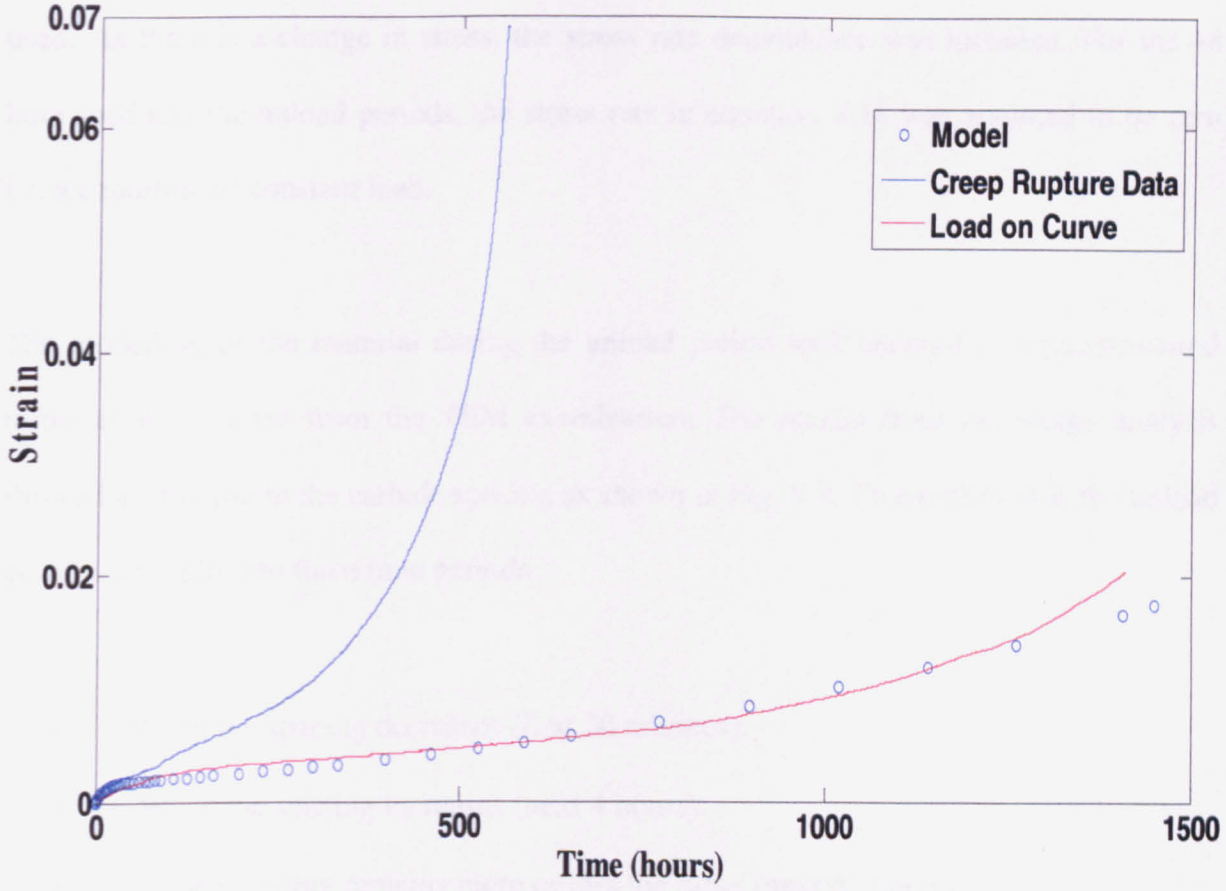

Fig. 8.8 Fitting of the load-on curve for test 1(a). Time refers to the duration the material spends in a 'loaded' condition

A_o $(Nm^{-2})^{-n}s^{-1}$	H_1(MPa)	L	c	K_c (h^{-1})
8.07×10^{9}	140.50	0.004	250	2.2×10^{-3}

Table 8.2 Values of constants for load-on curve for load-on/load off test shown in Fig. 8.3

Following this, modelling of a complete cycle was done. In this case, a complete cycle consisted of

- 48 hour load.
- 'Instantaneous' unload. The unload was estimated to occur in one minute.
- 48 hours of zero load. Anelastic recovery would occur during this period.
- 'Instantaneous' reload occurring in one minute.

For the instantaneous load/reload part of the curve, all equations in equation set 8.18 were used. As there is a change in stress, the stress rate dependence was included. For the 48 hour load and the unload periods, the stress rate in equation 8.18 was assumed to be zero i.e. a condition of constant load.

The modelling of the material during the unload period took account of microstructural information obtained from the TEM examination. The results from the image analysis showed a variation in the carbide spacing as shown in Fig. 8.9. To simplify this, the unload portion was split into three time periods:

- i- When the spacing decreases (first 30 minutes).
- ii- When the spacing increases (next 4 hours).
- iii- When spacing remains more or less the same (next 43 hours).

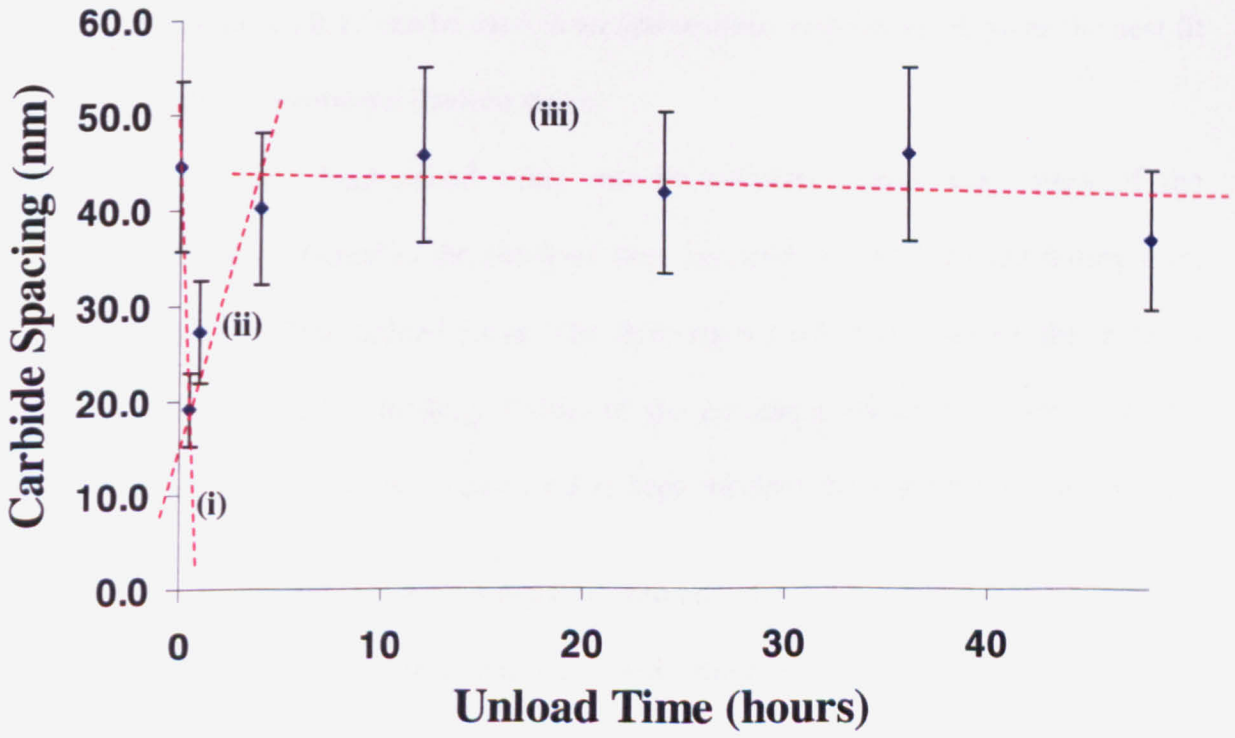

Fig. 8.9 Variation in carbide spacing with unload time. Red dotted lines are trend lines to the particle spacing data

Based on the variation in each period, the state variable $S = 1 - {}^{p_i}/_{p}$ would change.

During unloading, an assumption was made that the sample was unloaded to zero stress in a time of one minute. Once the stress reaches zero, the effect of anelasticity would begin which would mean changes in the carbide spacing would influence the overall strain rate term in equation 8.18. In this model, this influence can be considered as a softening parameter affecting the overall creep behaviour. Thus, the constants used for the load-on curve should fit the whole cycle to a reasonable degree.

The procedure for modelling a complete load-on/load-off test is described below:

1. The values of the stress exponent 'n' and activation energy 'Q' are obtained using the database of steady load creep tests.
2. Equation set 8.17 can be used to obtain values of constants A_o, H_I, L, c, K_c. Equation set 8.17 can be used in an optimisation routine which gives the best fit for the experimental load-on curve.
3. A complete load-unload cycle can be simulated using the values of the constants obtained in the previous step. Equation set 8.17 is used during each step of the load-unload curve. The first step would be to simulate the material behaviour during loading. Values of the constants obtained in Step 2 can be used for this purpose. Since load is kept constant throughout the test, the first term in equation set 8.17 is equal to zero ($\dot{\sigma} = 0$).
4. Upon unloading, an instantaneous elastic strain drop is observed. This drop can be modelled by providing a finite value to $\dot{\sigma}$. In this study, stress was applied and removed in a time of one minute.

5. The end of the strain drop signals the start of the anelastic recovery period. In Fig. 8.9, it was shown that particle spacing varies during the recovery period and there are three distinct phases where carbide spacing changes. This information can be provided as input to the state variable '*S*'.
6. At the end of the unload phase, the load is reapplied and a similar procedure described in step 4 can be used.

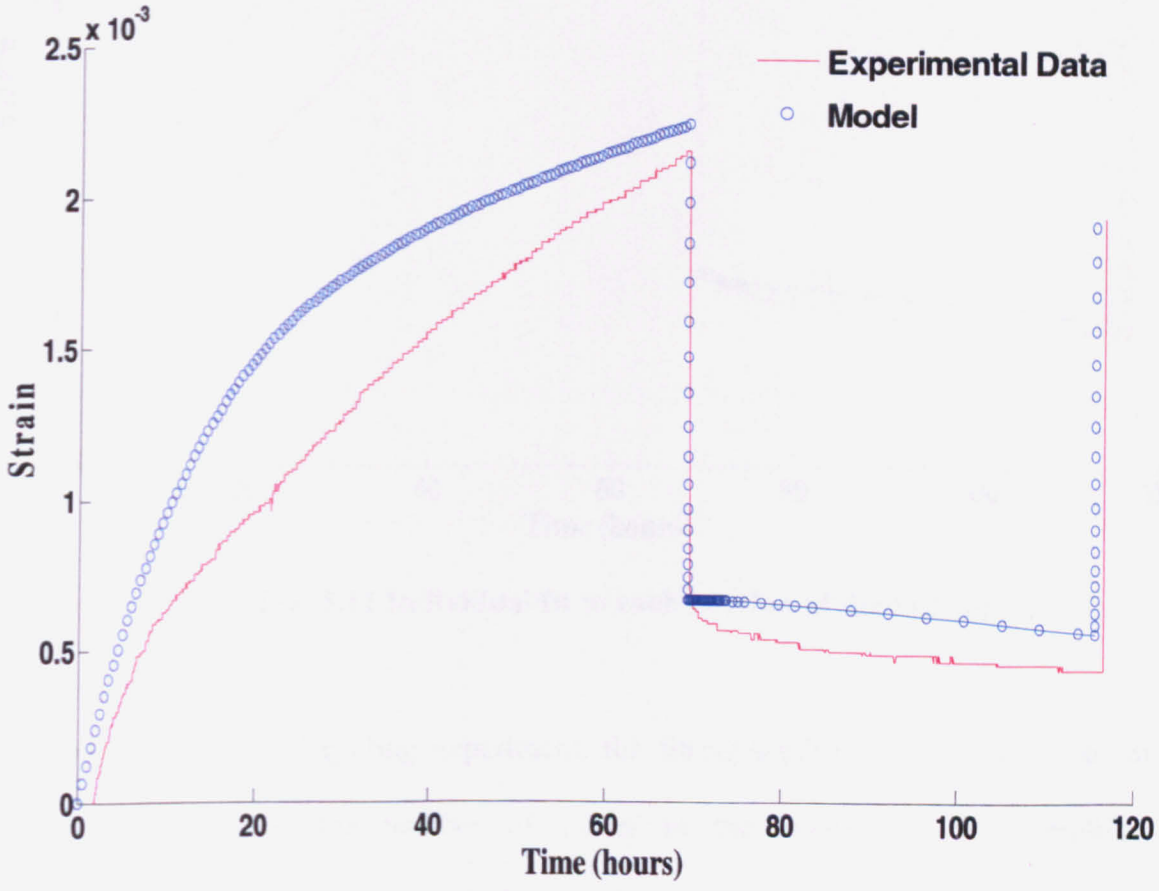

Fig. 8.10 Prediction of model for the first cycle of Test 1(a). Constants used are the same as those in Table 7.

The results from this analysis shown in Fig. 8.10 indicate a poor fit to the experimental data. The overall recovered strain as predicted by the model is less than the experimental data. Physically, this means that there may be mechanisms acting during the unload period which are unaccounted for. Optimising each part of the unload individually can improve

the fit as shown in Fig. 8.11 but this method would mean constants are required for each unload cycle which is also physically unrealistic.

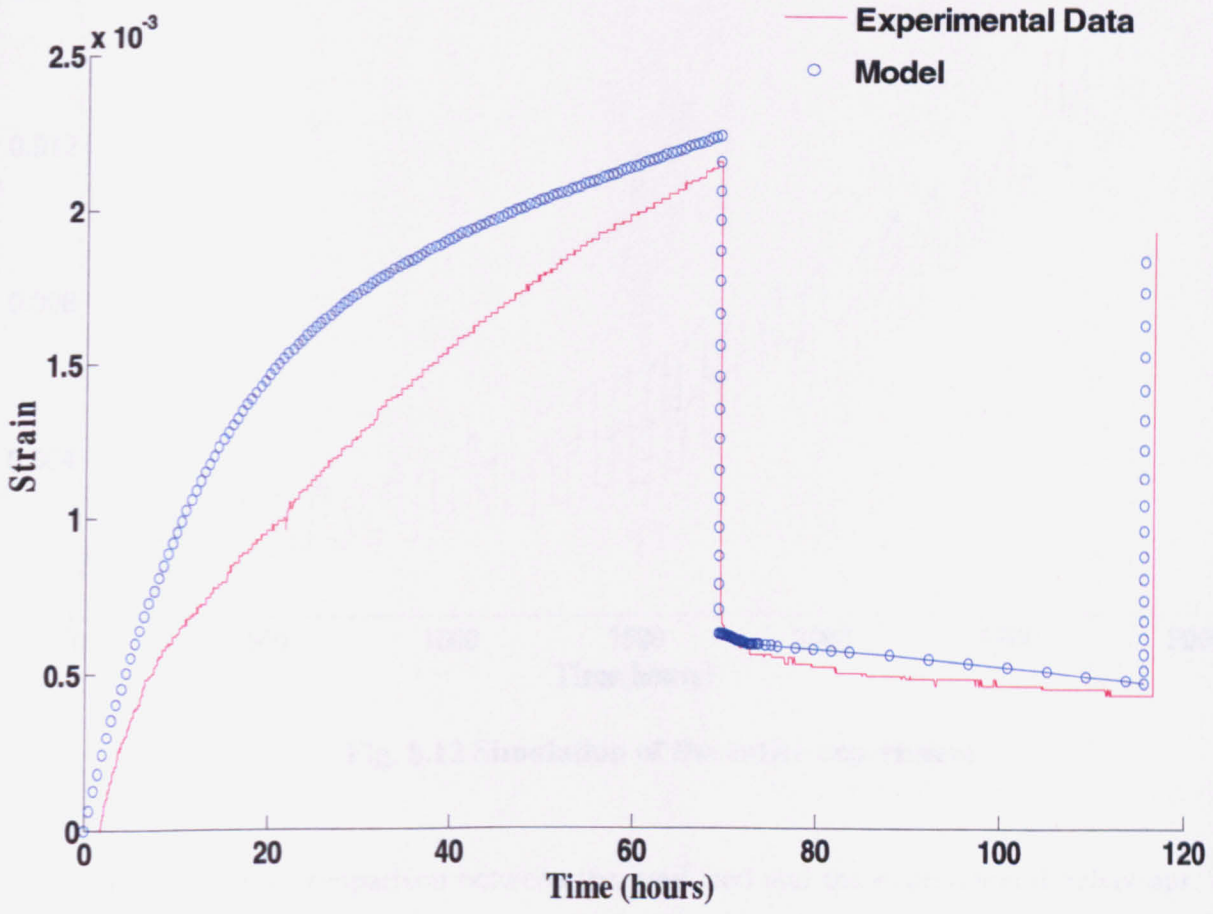

Fig. 8.11 Individual fit to each portion of the unload

To model the full load cycling experiment, the fitting applied to the first cycle can be looped depending on the number of cycles in the experiment. To simplify, the instantaneous strain drop was not modelled using the equation set but a set value for the elastic drop/increase was applied.

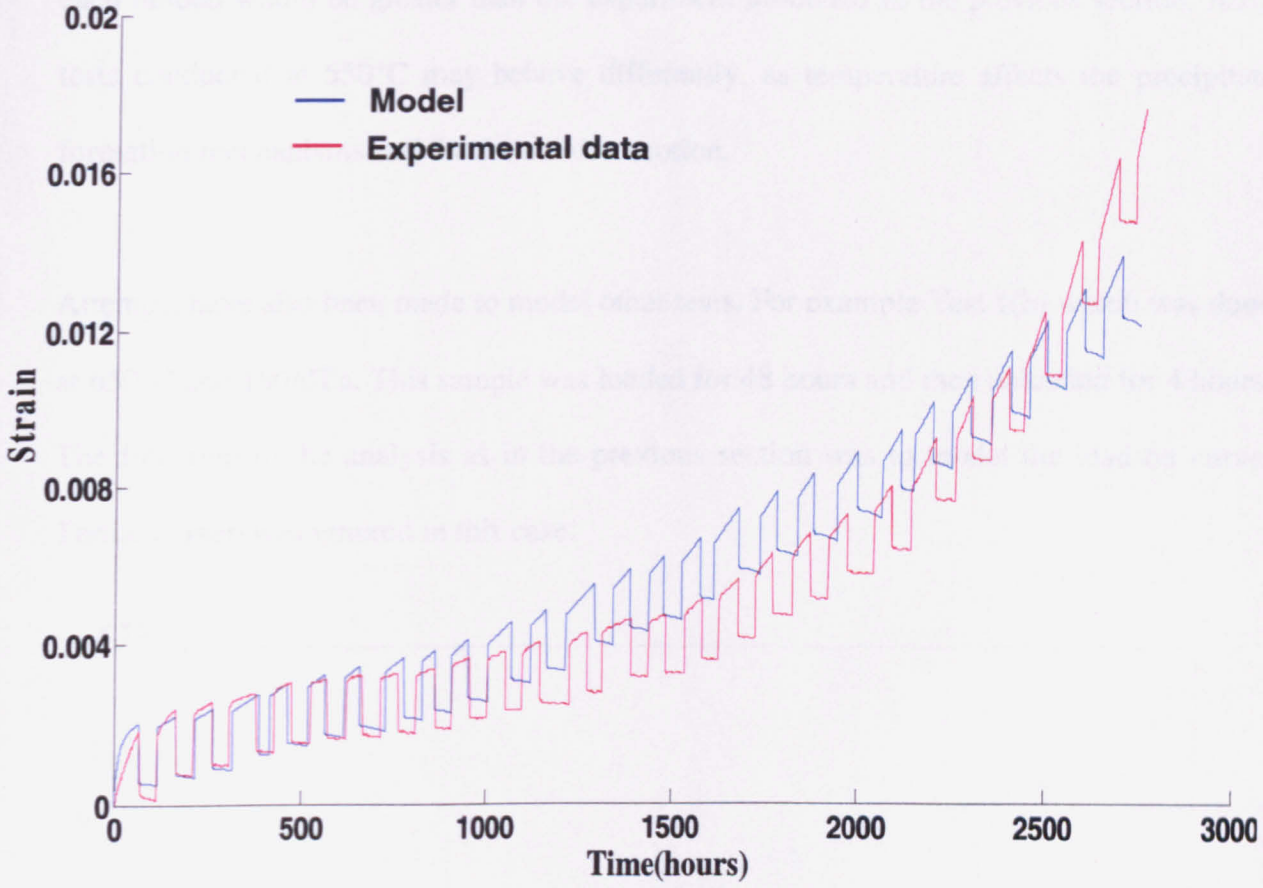

Fig. 8.12 Simulation of the entire experiment

Fig. 8.12 shows the comparison between the predicted and the experimental behaviour. A reasonable estimate of material behaviour can be given using the model. The model seems to be conservative in this case especially with regards to the rupture strain.

8.6 Modelling Other Experimental Conditions

8.6.1 Effect of Shorter Unload Periods

Depending on experimental loading conditions, the mechanisms responsible for creep/anelasticity will vary. For example, if a sample is unloaded for a very short duration (Fig. 5.8), it is possible that changes in particle spacing might be different compared to when the sample was unloaded for longer durations. If a specimen was unloaded after a longer initial on-load time (Fig. 5.9), then the amount of creep strain accumulated before

each unload would be greater than the experiment modelled in the previous section. Also, tests conducted at 550°C may behave differently, as temperature affects the precipitate formation mechanisms and the dislocation motion.

Attempts have also been made to model other tests. For example Test 1(b) which was done at 650°C and 180MPa. This sample was loaded for 48 hours and then unloaded for 4 hours. The first step in the analysis as in the previous section was to model the load-on curve. Tertiary creep was ignored in this case.

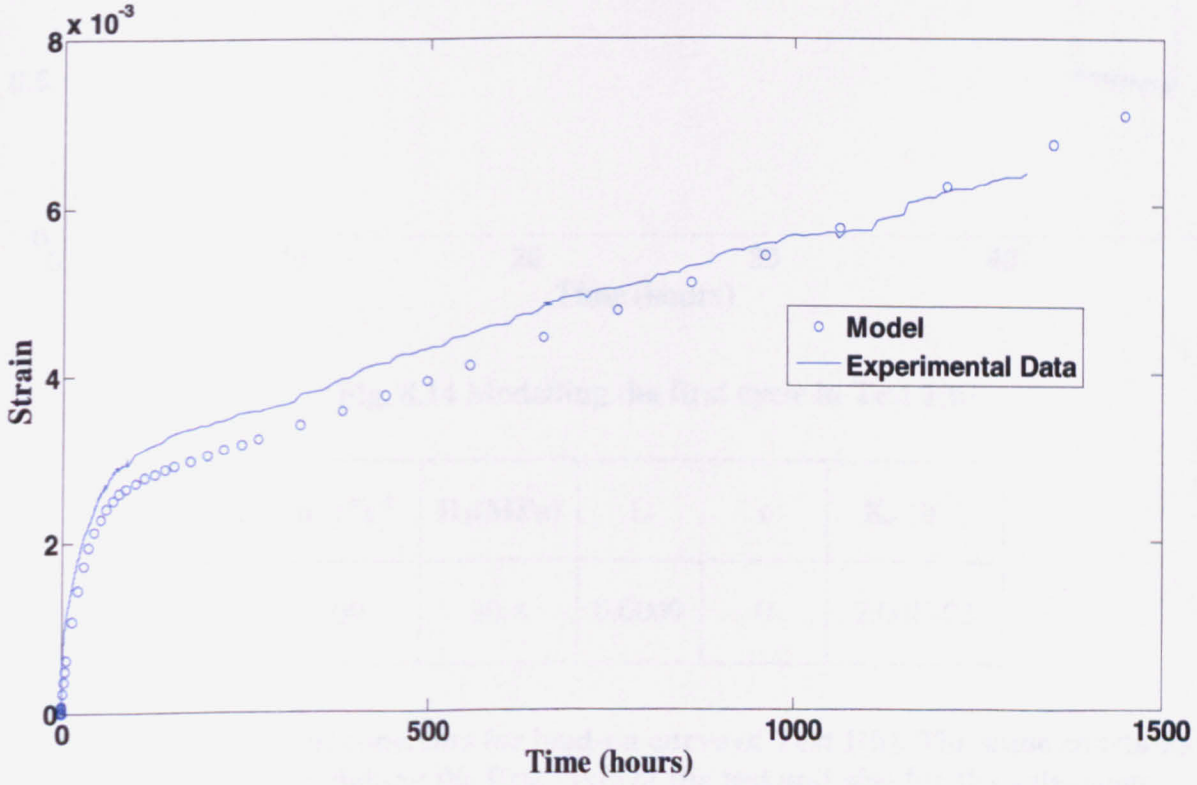

Fig. 8.13 Modelling the load-on curve for Test 1(b)

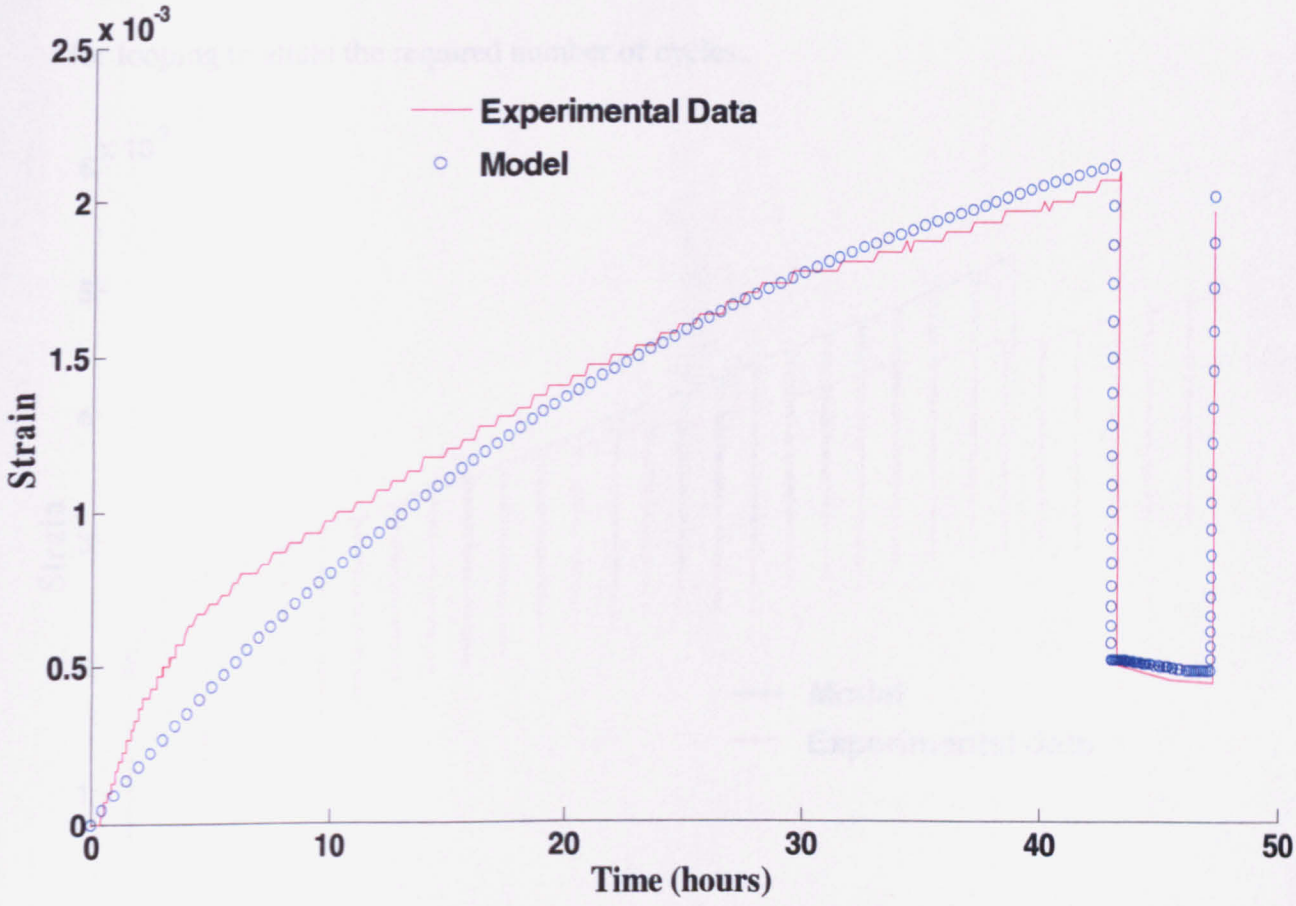

Fig. 8.14 Modelling the first cycle in Test 1(b)

A_o $(Nm^{-2})^{-n}s^{-1}$	H_1(MPa)	L	c	K_c (h^{-1})
6.00E+09	80.4	0.0009	0	2.00E-03

Table 8.3 Values of constants for load-on curve of Test 1(b). The same constants were used for modelling the first cycle of the test and also for the subsequent simulation of the entire experiment

The values of the constants used for fitting the load-on curve are given in Table 8.3. The fit is shown in Fig. 8.13. Using the same constants, the first cycle of the test was also simulated. As the duration of unload was only 4 hours, the latter stages of unload (when the carbide spacing remains same- stage iii in Fig. 8.6) would not be present. Consequently, the unload period was split into only two periods. The fit for the first cycle

has been shown in Fig. 8.14. As in the previous simulation, the same constants were used for looping to attain the required number of cycles.

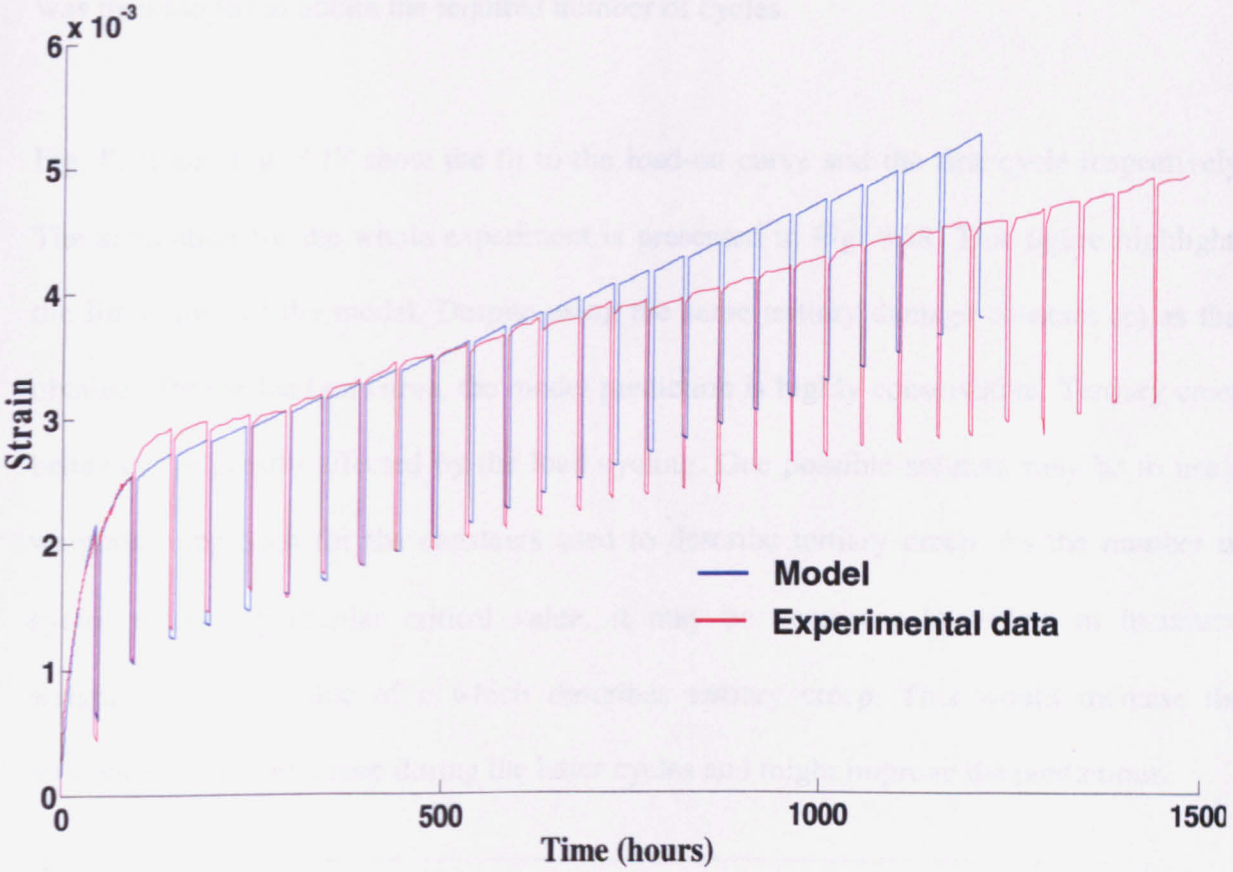

Fig. 8.15 Simulating the whole of test 1(b)

Fig. 8.15 shows the results of the simulation for the whole experiment. Looking at the primary and secondary behaviour, the model seems to over-predict the strains.

8.6.2 Modelling the Effect of Temperature

Tests conducted at temperatures other than 650°C can have different mechanisms operating which will affect the deformation. Precipitation formation in particular is affected by temperature so that the carbide spacing may vary significantly from that considered previously. To examine the effect of temperature, one further test was simulated. The test was Test 3(a) where the temperature was 550°C and the load was 335MPa. The sample was loaded for 48 hours and then unloaded for 48 hours.

As in the previous simulations, initially the load-on curve was fitted. The constants obtained from this process were used to fit the first cycle of the experiment. The first cycle was then looped to obtain the required number of cycles.

Fig. 8.16 and Fig. 8.17 show the fit to the load-on curve and the first cycle respectively. The simulation for the whole experiment is presented in Fig. 8.18. This figure highlights the limitations of the model. Despite using the same tertiary damage constant (c) as that obtained for the load on curve, the model prediction is highly conservative. Tertiary creep behaviour is greatly affected by the load cycling. One possible solution may be to use a weighting approach for the constants used to describe tertiary creep. As the number of cycles reach a particular critical value, it may be necessary to assign an increased weighting of the value of c which describes tertiary creep. This would increase the influence the tertiary creep during the latter cycles and might improve the predictions.

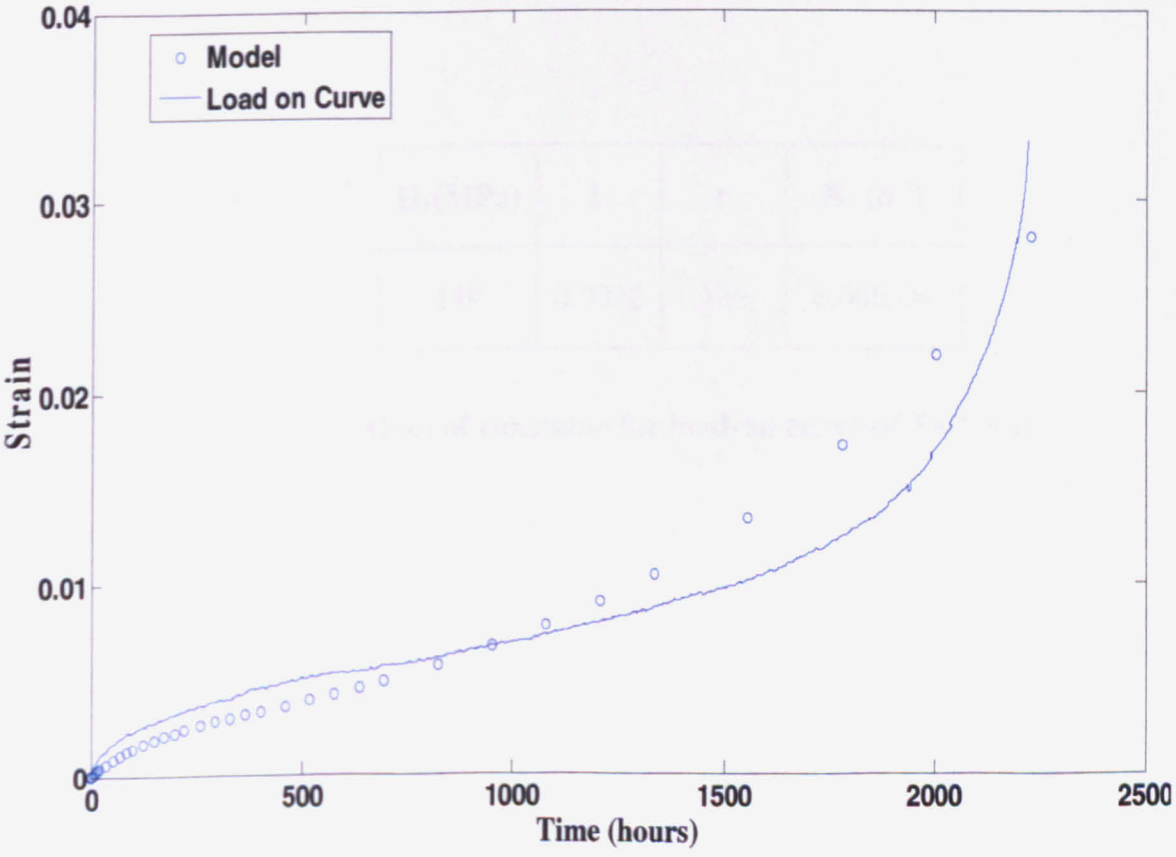

Fig. 8.16 Predicting the load-on curve for Test 3(a)

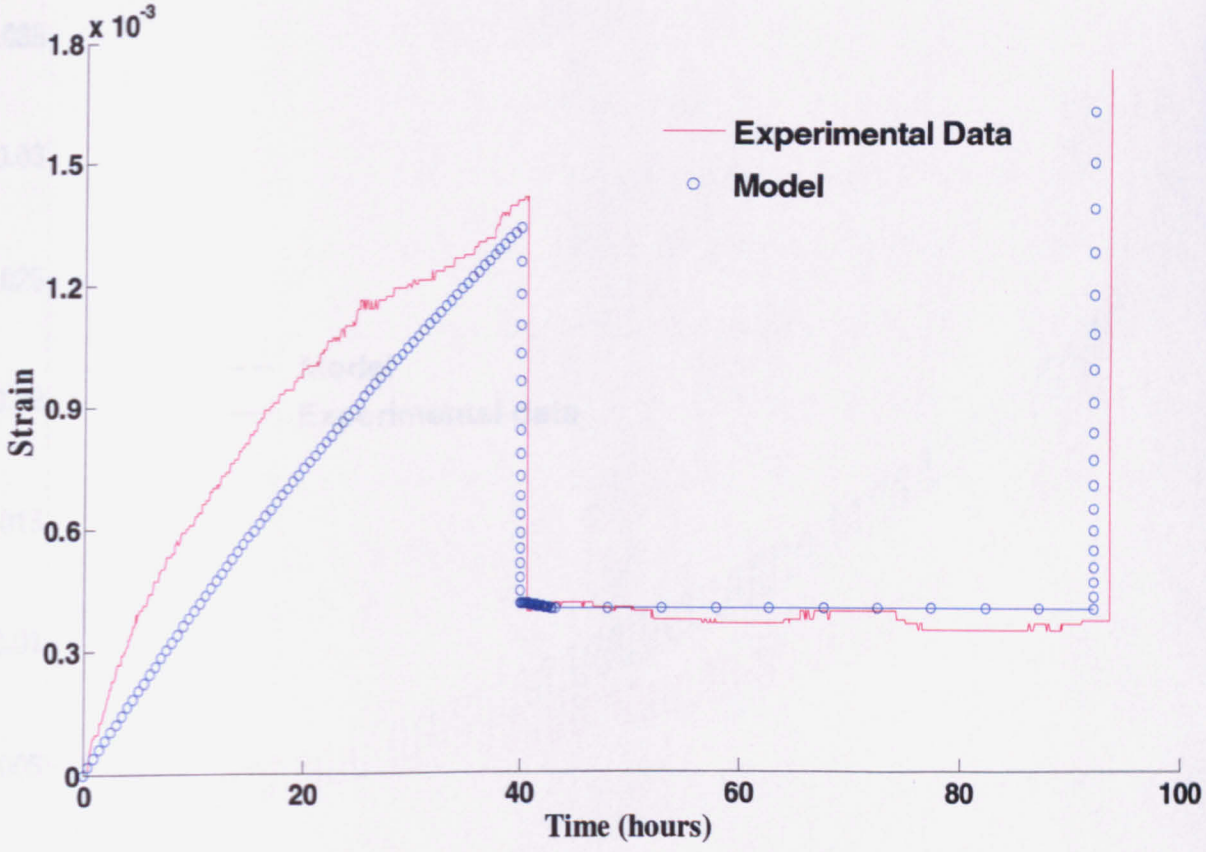

Fig. 8.17 Simulating the First Cycle for Test 3(a)

A_o $(Nm^{-2})^{-n}s^{-1}$	H_1(MPa)	L	c	K_c (h^{-1})
5.00E+10	139	0.0012	120	8.00E-04

Table 8.4 Values of constants for load-on curve of Test 3(a).

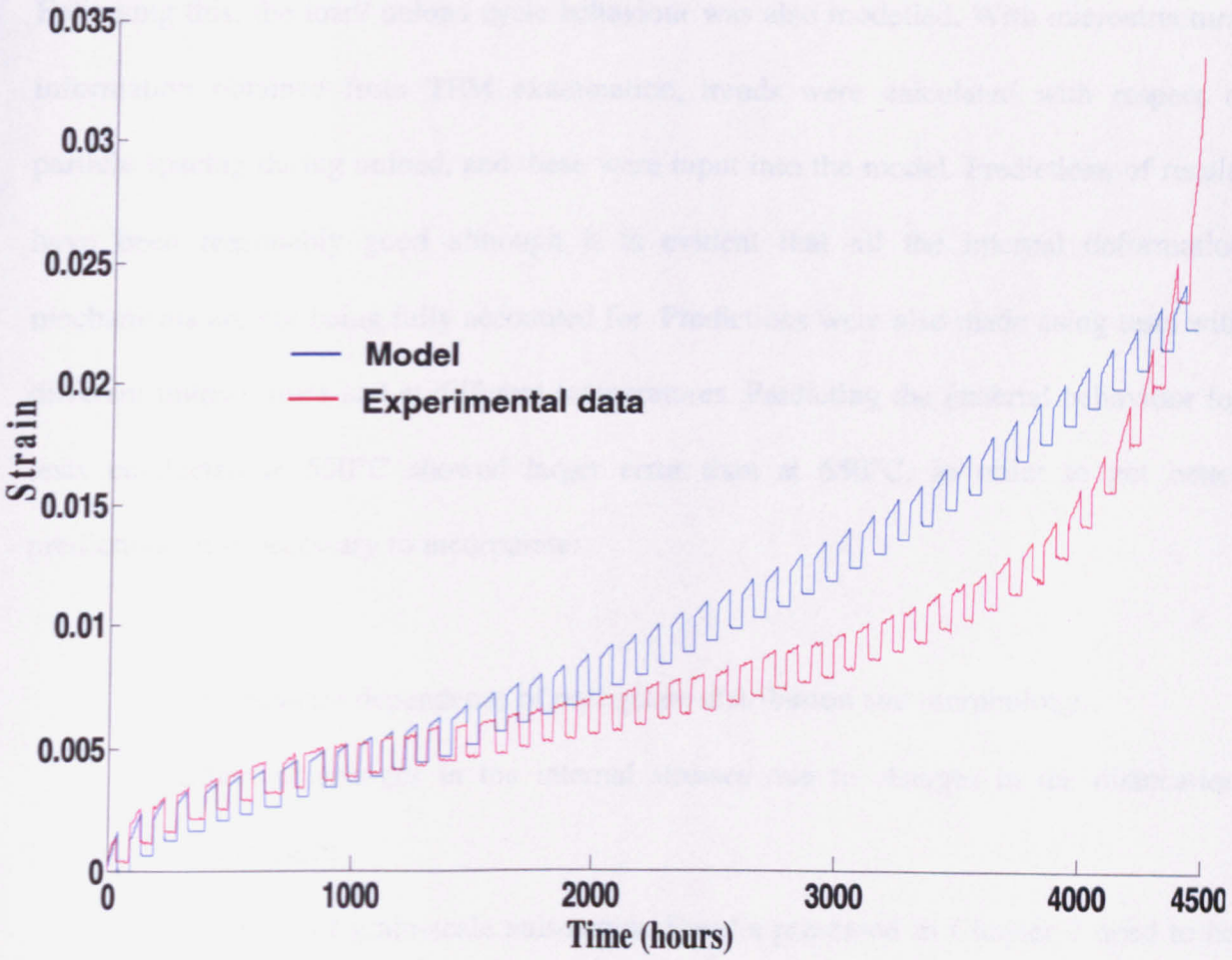

Fig. 8.18 Prediction for Test 3(a)

8.7 Discussions and Conclusions

The chapter has introduced the concept of state variable modelling and examined its efficiency in predicting creep behaviour using damage mechanics. Modelling of conventional creep behaviour is relatively straightforward using this method but the challenge lies in extending the method to model conditions for which little or no experimental data exists. A set of constants can be found using optimisation techniques which can predict the material's creep behaviour within certain limits.

In this chapter, a creep damage model was modified to include a state variable which described the evolution of particle spacing during creep of 316H. The ability to add

specific material mechanisms is one of the main advantages of using damage mechanics. Following this, the load/ unload cycle behaviour was also modelled. With microstructural information obtained from TEM examination, trends were calculated with respect to particle spacing during unload, and these were input into the model. Predictions of results have been reasonably good although it is evident that all the internal deformation mechanisms are not being fully accounted for. Predictions were also made using tests with different unload times and at different temperatures. Predicting the material behaviour for tests conducted at 550°C showed larger error than at 650°C. In order to get better predictions, it is necessary to incorporate:

- Temperature dependence of precipitate distribution and morphology.
- Effect of changes in the internal stresses due to changes in the dislocation substructure.
- Influence of grain-scale anisotropy. Results presented in Chapter 7 need to be incorporated into the model used.
- Better description of tertiary creep behaviour.

References

[1] E.N.Andrade, *The viscous flow in metals and allied phenomena*, Proc. R. Soc. London, Ser. A, 84 (1910), pp-1-12.

[2] A.Graham., K.F.A.Walles, *Relationships Between Long and Short Time Creep and Tensile Properties of a Commercial Alloy*, Met. Sci., 3 (1955), pp.221.

[3] R.W.Evans, I.Beden, B.Wilshire, "*Creep of Metals and alloys*", The Institute of Metals, (1985)

[4] R.W. Evans, J.D. Parker and B. Wilshire, *An extrapolation procedure for long-term creep strain and creep life prediction with special reference to ½ Cr ½ Mo 1/4V ferritic steels*. In: B. Wilshire and D.R.J. Owen, Editors, Recent Advances in Creep and Fracture of Engineering Materials and Structures, Pineridge Press, Swansea (1982), pp. 135–184.

[5] R.W. Evans, B.Wilshire "*Introduction to creep*" The Institute of Metals, Swansea (1983).

[6] M. Mclean, B.F.Dyson, *Modeling the Effects of Damage and Microstructural Evolution on the Creep Behavior of Engineering Alloys*, Jour. of Engg. Mater. and Tech., Vol. 122 (2000), 273.

[7] B.F.Dyson, M.Mclean, *Creep Deformation of Engineering Alloys: Developments from Physical Modelling*, ISIJ International, Vol. 30 (1990), No. 10, pp. 802-811.

[8] L.M.Kachanov, *The time of failure under conditions of creep*, IZV. Akad. Nauk SSSR, (1958), No. 8, 26.

[9] Yu.N.Rabotnov, *Creep Problems in Structural Members*, Proc of XII IUTAM Congress, Stanford, ed. By H.Hetenyi and W.G.Vincenti, Springer-Verlag, Berlin, (1969)

[10] F.A.Leckie, D.R.Hayhurst, *Constitutive equations for creep rupture*, Acta metall., 25(1977), 1059.

[11] R.N.Ghosh, M.Mclean, *High temperature deformation in engineering alloys control*, Acta metall. Vol. 40 (1992), No.11, pp. 3075.

[12] D.Bammann and R.D. Krieg, *'Unified Constitutive Equations for Creep and Plasticity'*, p. 303, Elsivier Applied Science, Amsterdam (1987).

[13] M.Hatterstrand, H.O.Andren, *Influence of strain on precipitation reactions during creep of an advanced 9% chromium steel*, Acta Metal. 49. (2001), pp. 2123-2128

[14] R.W.Bailey, *Utilization of Creep Test Data*, Proc. Inst. Mech. Eng., Vol. 131 (1935), pp. 131-349.

[15] P.Brozzo, *A Method for the Extrapolation of Creep and Stress-Rupture Data of Complex Alloys*, Proc. Joint Int. Conference on Creep, Inst. Mech. Eng., New York-London, pp. 6.77-6.85, (1963)

[16] K.F.A Walles, A.Graham, *On the Extrapolation and Scatter of Creep Data*, A.R.C.C.P. No. 680, (1961)

[17] R.L.Orr, O. D. Sherby, J. E. Dorn, *Correlations of Rupture Data for Metals at Elevated Temperatures*, Trans. ASM, Vol. 46, p. 113, (1954)

[18] F.R.Larson, J.Miller, *A Time-Temperature Relationship for Rupture and Creep Stresses*, Trans. ASME, Vol. 74, pp, 765-775, (1952)

[19] S.S.Manson, A.M.Haferd, *A Linear Time-Temperature Relation for Extrapolation of Creep and Stress Rupture Data*, National Advisory Committee for Aeronautics, Technical Note 2890, (1953).

[20] G.E.Dieter, Mechanical Metallurgy. McGraw-Hill series in Materials Science and Engineering. McGraw Hill, 3rd edition, 1986.

[21] B. F. Dyson, P. Hirsch, M. McLean, R. C. Thomson, M. S. Loveday, *Mechanical Testing of High-Temperature Materials: Modelling Data-Scatter*, Phil. Trans: Phys. Sci. and Eng., Vol. 351, No. 1697, High -Temperature Structural Materials (Jun. 15, 1995), pp. 579-594

[22] B.F.Dyson and M.Mclean, *Particle Coarsening, σ_o and Tertiary Creep*, Acta Metall. Vol.31, pp.17-27, 1983.

CHAPTER 9: DISCUSSION AND CONCLUSIONS

The aim of this study was to develop an understanding of the impact of load reductions on the creep behaviour of austenitic stainless steels used in nuclear power plants. This research has focussed on the material response of AISI type 316H when loading conditions similar to reactor shut-downs and start-ups are applied.

Experiments were performed to understand the creep behaviour of the material under such situations, with results showing significant changes in the material's properties. Unloading during a creep test resulted in some of the plastic strain being recovered (anelasticity). When the material underwent a number of such unload/reload cycles, its creep life increased but a decrease in its creep ductility was also observed.

Anelasticity affects the deformation characteristics of every stage of creep. There is a strong relationship between the material's plastic strain state and the dislocation substructures present within the material. If the net plastic strain of the material changes, dislocation substructures will reorder themselves in order to accommodate this change. A change in the dislocation substructures will also impact the intergranular stresses present between grains and the intragranular stresses present within each grain. This relationship between a changing plastic strain state, dislocation structures and the internal stresses (both intergranular and intragranular) presents a complex scenario where changes in any of the three will influence the other two.

Fig. 9.1 is a schematic diagram showing the effect of anelasticity on the different creep mechanisms. Load reductions when the material is in its primary creep stage will induce

changes in the dislocation substructure. Anelasticity can also influence the formation of precipitates as described in section 6.5. Most load-removals in this study were implemented once the material had reached secondary creep. Thus, the role of anelasticity during primary creep can only be theorised. However, the changing plastic strain state due to the unload will introduce intergranular stresses which can affect material properties.

Secondary creep behaviour will also be influenced by anelasticity. The load-on/load-off experiments showed large reductions in strain rate when compared to steady-load creep tests at the same conditions. The anelastic deformation will be driven by the compressive residual stresses generated in the primary creep stage in some of the grain families and alter the dislocation structures. Upon reloading, the accumulation of intergranular stresses can be very different to that observed in previous cycles. This is clearly seen in Fig. 7.12. Load reductions during tertiary creep will also affect the formation and propagation of creep cavities. This has been discussed in sections 9.4 and 9.5 of this chapter.

9.1 Saturation in Anelastic Strain

Upon unloading, the anelastic behaviour of the sample follows an exponential decay. The amount of plastic strain recovery was found to be high during the first hour of the unload, and then saturated as the unload time increased. The amount of recovered strain also decreased as the number of cycles increased. This behaviour has also been observed in other studies by different researchers. Some of these experiments involved unloading to zero load whereas others involved unloading to specific stress levels, but in all cases wherever anelastic strain was observed, it saturated with time.

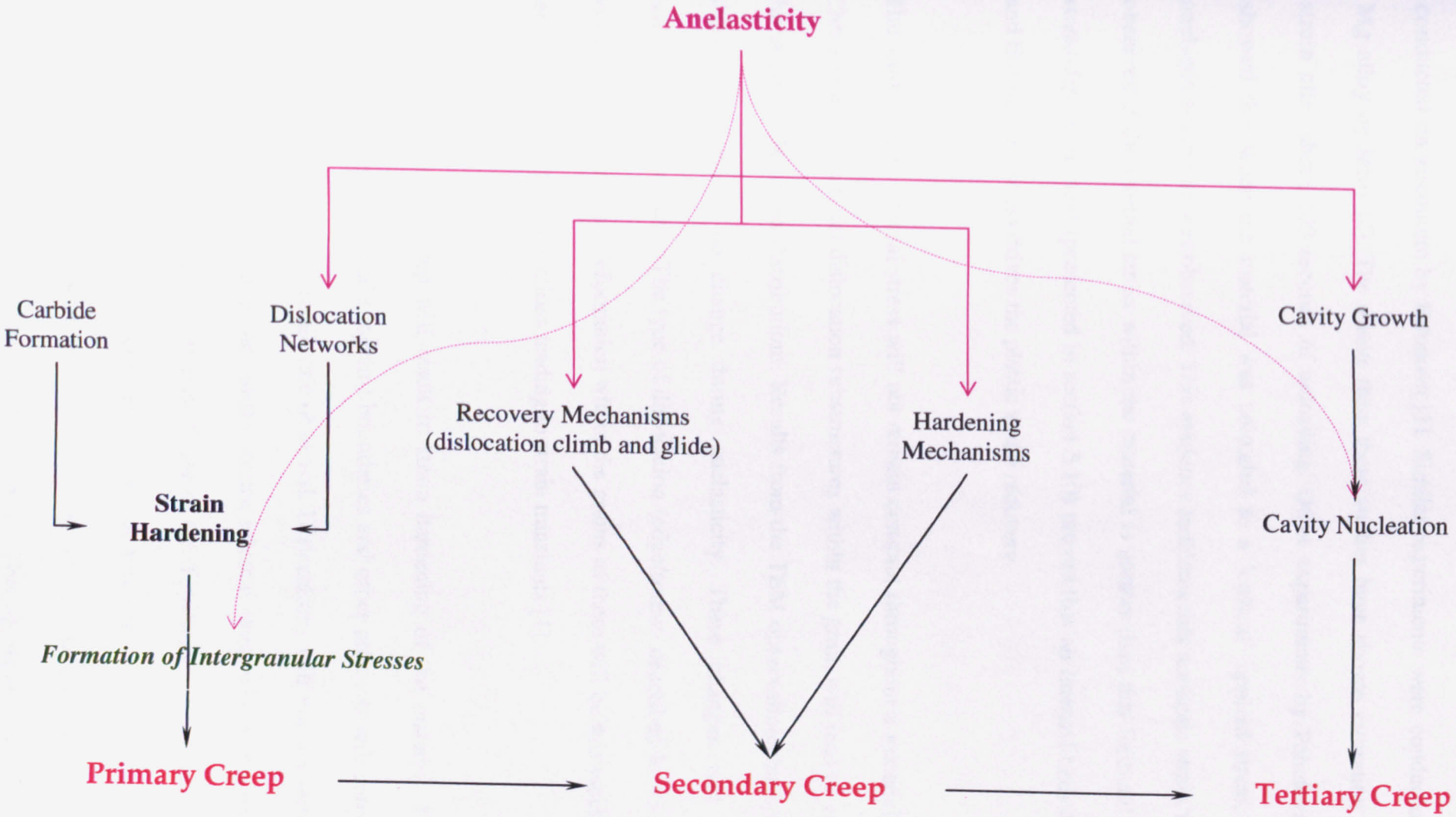

Fig. 9.1 Schematic showing the effect of anelasticity on the different stages of creep. Pink solid lines show the deformation mechanisms which will be directly affected by the changing strain state due to anelasticity. Dotted pink lines show mechanisms which will be indirectly affected due to anelasticity.

Creep experiments, where the load was reduced to 5MPa from 60MPa, have been conducted on zirconium by Pahutova [1]. Similar experiments were conducted on an Al-Mg alloy by Mills [2]. The results from these studies have shown saturation in anelastic strain after about 100 seconds of unloading. Other experiments by Pahutova and Mills showed that when the material was unloaded to a 'critical' applied stress, a net zero anelastic strain rate was observed. This evidence indicates that anelastic strain will only be observed if the internal stress within the material is greater than this 'critical' stress. The stress-dip experiment (presented in section 5.10) proved that an internal backstress exists, and this internal stress drives the plastic strain recovery.

The value of this internal stress will not remain constant throughout a material's lifetime. Changes in the material dislocation substructures within the grain will lead to variations in the intragranular stress distributions. Results from the TEM observations have shown that dislocation densities do change during anelasticity. These changes will affect the dislocation substructures. The type of dislocation (edge/screw- described in Appendix VI) will also affect the local deformation within the grains as there will be mismatches in their behaviour during load reductions leading to strain transients [1].

The onset of primary creep will result in strain hardening of the material. Dislocation accumulation near grain (and subgrain) boundaries and other artefacts will cause pile-ups leading to a reduction in the strain rate observed. Dislocations will interact with carbides and become pinned. As soon as the unload occurs, internal stress will be the only driving force for deformation within the material. Some of the dislocations which are pinned will move to a configuration which is relatively less stressed than that observed during the load period. Depending on the local stress fields, one can infer that the internal stress will drive this motion to a reasonably unstressed arrangement. This springback in the dislocation

motion is reflected in the high plastic strain recovery during the initial stages of the unload period. Once this unstressed state is reached, all further motion of the dislocation will be to balance its strain energy (or line tension) with the stress of its surroundings. The net macro-effect is the saturation seen in the latter periods of an unload cycle.

The magnitude of anelastic strain observed in each cycle decreased as the number of load/unload cycles increased. Changes in mobile dislocation densities can be used to explain this. As the creep test begins, dislocation densities start to increase. The proportion of mobile dislocations is quite high, which is seen in the strain increase during primary creep [5], [6]. However, work hardening effects lead to dislocations becoming immobile as they start to form tangles. Dislocations interacting with carbides and grain boundaries will also reduce the proportion of mobile dislocations. Thus, as creep strain increases a reduction in the proportion of mobile dislocations will occur. The rate of recovery mechanisms will determine the evolution of dislocation substructures as creep time increases. This is turn will be reflected in the mobility of dislocations. Using a similar analogy, as the number of load/unload cycles increases, the overall changes in plastic strain will affect the balance between recovery and hardening mechanisms. If, hardening mechanisms are more dominant, then the availability of mobile dislocations decrease which will lead to saturation in anelastic strain.

9.2 Changes in Dislocation and Precipitate Densities during the Unload Phase

As creep deformation progresses, the material will contain a mix of mobile and immobile dislocations. Prior to load removal, a large number of dislocations will be a part of networks and pile-ups. The mobility of such dislocations will be minimal. When the

material is unloaded, some of these dislocations can free themselves from the tangles by executing a climb motion. The surrounding internal stress state may provide the extra energy required for this climb mechanism. This increases the ratio of mobile dislocations and will assist in deformation of the material. Temperature will also influence this mechanism as described in chapter 6.

This process continues and the densities increase up to a point where dislocation spacing becomes smaller. As a result, dislocations have opportunities to interact with other dislocations. This interaction, depending on the direction of dislocation motion, can result in annihilation which can explain the decrease during the next stage.

Explaining changes in carbide densities is a more complicated problem as formation of precipitates is a temperature-dominated mechanism. Diffusion of carbon from the lattice will not account for the apparent rapid increase observed in samples obtained during unload. Different studies [7], [10] have proposed that the mechanism of 'pipe diffusion' can be used to explain the increase in carbides. Pipe diffusion is an accelerated diffusion process which occurs along the grain boundaries and dislocation networks. It plays an important role in many metallurgical processes and often can affect properties of polycrystalline materials [11].

Pipe diffusion consists of diffusion mechanisms where the solute diffuses from the cluster of dislocations along the core of a mobile dislocation [12]. Other theories for pipe diffusion include diffusion along the core of a partial dislocation and diffusion along the stacking fault of a mobile dislocation. For this mechanism, a driving force must exist [10]. A difference between the concentration gradients along the dislocation length is another example of a driving force for pipe diffusion [13]. It is estimated that the activation energy

for this process is about 20-50% less than that of 'conventional' diffusion [8, 22]. The greater density of mobile dislocations during the initial period (>2 hours) of the unload available will enhance the probability of precipitates forming due to pipe diffusion.

Thus, it is possible to explain the apparent increase in carbides during the initial stages of the unload. However, a more thorough investigation is required to ascertain if the observed precipitate density changes are real.

9.3 Influence of Residual Stresses

When a creep test specimen was loaded beyond its absolute limit at elevated temperature, neutron diffraction measurements presented in Chapter 7 showed the development of large intergranular stresses. Tensile strains developed in the {200} and {311} planes normal to the loading direction, compared with the Reitveld response (bulk response). The {111} and {220} developed compressive strains. The behaviour of the crystal planes in terms of magnitudes and directions (tensile or compressive) is similar to that observed during in-situ tensile experiments [18], [21].

Conclusions can also be drawn from work carried out examining the creep behaviour of pre-strained materials. Plastic pre-straining generally reduces ductilities and creep strain rates while the rupture life sees an increase [14]. If anelasticity is considered as an applied negative plastic strain, then the overall plastic strain of the material changes. During primary creep, dislocation densities increase. Recovery processes such as cross slip and climb allow the dislocations to get to lower energy states. This process leads to changes in the dislocation substructures. The stress-dip experiments have shown the presence of an internal stress from which it can be concluded that deformation within the material occurs

to a greater extent in some areas. Long range stresses will be developed as a consequence of elastic strain set up to accommodate the plastic strains.

9.3.1 Effect on Tertiary Creep Behaviour- Explaining the Increase in Creep Life

Creep cavitation processes are affected the plastic strain. Cavity nucleation and cavity growth mechanisms are both influenced by the creep strain rate [23]. The dependence of failure time on creep strain rate demonstrates that the rates of cavity development and times to eventual failure are governed by the rates of creep strain accumulation.

The extent of damage due to creep cavitation will depend on the deformation characteristics of grain boundaries as grain boundaries are the areas which are most susceptible to cavity nucleation and growth. Compared with the grain interiors, grain boundary zone deformation is relatively unaffected by plastic strain, possibly as dislocation recovery processes are more rapid within the boundary zones [20]. As a result, intragranular microstresses can originate between the grain interior and the grain boundary which again will affect the way dislocations move locally within a grain. In the absence of mechanical or microstructural instabilities, the tertiary stage of creep will begin when the numbers and sizes of the cavities are sufficient to cause a creep rate acceleration.

When the 'on-load' curves of the load-on/load-off tests are considered, there is still a prominent tertiary stage suggesting creep cavitation is the prime mechanism responsible for fracture. The changing plastic strain state due to conventional creep and anelastic deformation accumulation restricts grain interior deformation but boundary zone

deformation remains relatively unaffected, and therefore the tertiary creep and fracture characteristics are comparatively unchanged.

Dislocation behaviour will be different when the grain boundary and grain interiors are compared. Anisotropy in the material will result in different states of internal stresses for each family of grains when the sample goes through a load-unload cycle. On a microscopic level, each grain will experience a different stress level compared to its neighbours depending on their orientations. Using this as a basis, cavitation will only occur if the intergranular stress reaches a critical value. Depending on the intragranular stress levels within the subgrains, it is possible that, the critical stress for cavitation to initiate is higher. The effect of the net plastic strain within the material will also play a role in determining where the cavities originate.

Stress fields present at/near the boundaries will also influence the tertiary creep mechanisms. Cavity and micro-crack propagation will only occur if the stress field in front of the crack is greater than the surrounding stress fields. Due to dislocation tangles, it is possible that a very high stress field is created which acts to impede the motion of these microcracks. With these reasons, it is possible to explain the extended rupture life seen in the material.

9.3.2 Explaining Loss in Ductility

The load-on/load-off experiments have shown that material ductilities can be greatly affected by the loading conditions. If, for design and assessment procedures, steady state creep data is utilised, this might lead to significant errors. Creep ductility can be affected by processes occurring during all the three stages of creep. Mechanisms which are

responsible for dislocation motion and formation of dislocation tangles will influence the amount of strain seen.

Formation of dislocation substructures occurs through different mechanisms which will depend on the prevalent creep state (primary, secondary or tertiary). Stress reductions during any of these stages will result in changes to the dislocation substructure formation. Data from the in-situ neutron diffraction experiment show prevalence of a compressive residual stress in the {220} and the {111} planes during anelasticity. Dislocations in the grains oriented along these planes may be driven to form tangles and pile-ups. For deformation to occur, the material must display a suitable number of mobile dislocations. The formation of tangles and pile-ups will capture the mobile dislocations and unless these captured dislocations execute a climb motion, deformation strain rates will decrease. Over a number of cycles, if the formation of tangles decreases the total ratio of mobile dislocations, then a reduction in the creep ductility is bound to occur.

9.7 Conclusions

This research has shown that experiments, which are more realistic simulations of material behaviour in-service, need to be conducted to ascertain the effects of interacting deformation modes. The introduction of load cycling induces a type of fatigue loading, and interactions of such cycles with creep deformation will lead to large deviations from steady-load creep behaviour.

- A series of uniaxial load-controlled creep tests have been undertaken on austenitic stainless steel at 550°C and 650°C. The effect of removal of load and temperature has been studied using standard extensometry, neutron diffraction, optical, SEM and TEM microscopy.

- It was found that some forward creep strain was recovered during the unload cycle. This phenomenon is termed anelasticity. Results from these tests showed that creep ductilities were reduced by around 50% and creep rupture lives increased by a factor of 2-3 times when compared to uniaxial creep tests under identical conditions.

- The amount of creep strain recovered during each unload period followed an exponential decay. The anelastic strain is high during the first 1-2 hours of the unload and seems to saturate after 10-12 hours. As the number of load/unload cycles increase, the recovered strains decreases exponentially and saturates.

- Removal of temperature resulted in a much higher recovered strain compared with tests where only the load was removed. An increase in the creep life was also observed in these tests. Temperature removal affects the precipitation mechanics of $M_{23}C_6$ which seems to be causing an increased amount of creep strain recovery.

- TEM observations of samples which were stopped at different points on the unload curves showed changes in the dislocation substructures. Dislocation densities increased in the initial 1-2 hours of the unload and then decreased post that period. Fewer dislocation tangles were observed during the initial stages of the unload.

- An increase in carbide densities was observed in samples stopped during the initial periods of the unload (<2 hours). One probable mechanism which can explain this

occurrence is pipe diffusion. In this process, carbon atoms from solution escape using dislocations as conduits. This increased concentration of carbon available to precipitates results in an increase in carbide numbers.

- An in-situ neutron diffraction experiment was conducted to understand how intergranular stresses can drive this observed creep recovery. The results showed that anisotropies in the behaviour of the individual crystal planes lead to formation of intergranular stresses. During primary creep, the behaviour of the crystal planes is similar to that observed during uniaxial tensile plastic deformation. A tensile residual stress is developed in the {200} and the {311} planes while a compressive state is developed in the {220} and the {111} planes. When unloaded, the relaxation of the planes in compression is a plausible mechanism which is providing a driving force responsible for anelasticity.

- The neutron diffraction results can also be used to explain the reasons for reduced ductilities and increased creep life. The accumulation of intergranular stresses changes the stress fields around the grain boundaries. For cavitation to proceed, this stress barrier needs to be broken. Thus the critical stress after which cavities form and propagate may be higher than those observed during steady-load creep tests which can explain the higher lifetimes observed. The loss in ductility could be due to a higher proportion of dislocations becoming immobile (dislocation tangles, pile-ups, pinning with precipitates). The mobile dislocation proportion thus gets reduced which will result in reduced ductilities.

- Some of the microstructural observations were incorporated into a model based on damage mechanics. Simulation of selected tests showed reasonable agreements with experimental behaviour.

9.8 Scope for Future Work

This work has answered some key questions but there remain areas where further research is needed.

Material behaviour should be examined under lower stresses which are more representative of loads seen in power plants. A lower applied stress will result in diffusion-creep deformation mechanisms exerting a greater influence on the material deformation.

Experimental studies also need to be carried out on determining the material behaviour when smaller stress reductions happen. Research also needs to be conducted to understand the effect of smaller temperature reductions (less than 50°C) on creep deformation.

TEM work carried out indicated changes in the dislocation densities during the unload periods. Further careful observations are desirable to confirm the findings. The evolution of dislocations along individual crystal planes also need to be researched.

Further work needs to be done on the relationship between plastic strain and the development of intergranular stresses. A material can plastically deform from a number of methods (e.g. creep, fatigue, etc.). The role each of these individual modes play needs to be looked at. This work can be supplemented by modelling using finite element methods and self consistent modelling techniques.

Comparisons have to be carried out examining the behaviour of the crystal planes during steady-load creep experiments. The data presented in chapter 7 can only be used to ascertain the residual stress state until the unload. Steady-load neutron diffraction experiments will provide information about the behaviour of the crystal planes during the three stages of creep. It will also give an insight on how the load-bearing behaviour of the planes change as plastic or creep strain increases.

The role of deformation modes also needs to be studied. In austenitic steels, slip is the most important deformation mode. Dislocation climb starts to dominate at higher temperatures. Peng [18] has proposed that large plastic strains (>30%) may cause a shift from slip to twinning in the deformation mode. The ductility of stainless steels decreases as temperature increases. Thus the strain required to initiate twinning may be much lower by 20-30% at higher temperatures.

An important aspect that needs to be incorporated into material modelling techniques is the backstress generation due to internal stresses originating from crystal anisotropy. Design and assessment codes and procedures need to be validated against observed material behaviour. More realistic simulations of material behaviour observed during service will help in making these codes more robust and accurate.

References

[1] Pahutova, J. Cadek and P. Rys, *Some stress change experiments on creep in a zirconium*,Mater. Sci. Eng. 39 (1979), pp. 169–174

[2] M.J.Mills, J.C. Gibeling, W.D. Nix, *Measurement of anelastic creep strains in Al-5.5 at.% Mg using a new technique: Implications for the mechanism of class I creep*, Acta. Metall. Vol. 34 No.5 (1986), pp. 915-925.

[3] J. Friedel, '*Dislocations*', Pergamon Press, 1964.

[4] Cottrell AH, '*Dislocations and plastic flow in crystals*', Oxford University Press, 1953.

[5] Hayakawa.H, Satoshi Nakashima, Junichi Kusumoto, Akihiro Kanaya and Hideharu Nakashima, *Creep deformation characterization of heat resisant steel by stress change test*, Int. J. Pressure Vessels and Piping 86 (2009), pp.556

[6] H. Yoshinaga, S. Matsuo and H. Kurishita, *Dislocation density and internal stress in an Al-5.7 at% Mg alloy deformed at high temperatures*, Japan Inst. Metals 48 (1984), pp. 35.

[7] D.G.Morris, *Anelasticity and creep transients in an austenitic steel*, Mat. Sci. J. 13 (1978), pp. 1849-1854

[8] D.G.Morris, *Creep in type 316 stainless steel*, Acta. Metall. 26 (1978), pp. 1143-1151.

[9] D.G.Morris, D.R.Harries, The *cyclic creep behaviour of Type 316 stainless steel*, Mat. Sci. J. 13, 1978, pp. 985-996.

[10] R.C. Picu, D. Zhang, *Atomistic study of pipe diffusion in Al-Mg alloys*, Acta Mater. 52 (2004), pp. 161–171

[11] I. Kaur, Y. Mishin, and W. Gust, *Fundamentals of Grain and Interphase Boundary Diffusion*, Wiley, Chichester, 1995.

[12] L.Klinger, E.Rabkin, *Interface Science 6* (1998), pp. 197–203.

[13] D. Zhang, R. C. Picu, *Solute clustering in Al-Mg binary alloys*, Modelling Simul. Mater. Sci. Eng., Vol. 11 p. 1-12.

[14] B.Wilshire, M.Willis, *Mechanisms of strain accumulation and damage development during creep of prestrained 316 stainless steels*, Metal. Mater. Trans. A, Vol. 35A Feb 2004, pp. 563.

[15] P.H.Hunenberger, J.A.McCammon, M.Willis, McDonaugh-Smith A, R.Hales, *Prestrain effects on creep ductility of a 316 stainless steel light forging*, Int. Journ. of Pressure Vessels and Piping, Volume 76, Number 6, May 1999 , pp. 355-359(5)

[16] K. Enami, *The effects of compressive and tensile prestrain on ductile fracture initiation in steels*, Engineering Fracture Mechanics 72, (2005), pp.1089–1105.

[17] Fujiwara M, Uchida H, Ohta S., *Effect of boron and carbon on creep strength of cold-worked type 316 stainless steel*, Journal of Materials Science Letters 1994; pp.13

[18] R. Lin Peng, M. Odén, Y. D. Wang, S. Johansson , *Intergranular strains and plastic deformation of an austenitic stainless steel*, Mater. Sci. Eng. A334 (2002) 215–222.

[19] B.Wilshire, M.T.Whittaker, *Grain boundaries: their influence on creep strain accumulation*, J. Inst. Met., 1961, vol. 90, pp.431

[20] J.D. Parker and B. Wilshire, *The effects of prestrain on the creep and fracture behavior of polycrystalline copper*, Mater. Sci. Eng., 1980, vol. 43, pp. 271-80.

[21] M.R. Daymond, P.J.Bouchard, *Elastoplastic deformation of 316 stainless steel under tensile loading at elevated temperatures*, Metall. Mater. Trans. A, Vol. 37A, June 2006, pp.1863.

[22] R. W. Balluffi, Cornell University Materials Science Centre Report NYO-3504-42, March (1970).

[23] M. E. Kassner, *Creep cavitation in metals*, International Jour. of Plasticity, Vol. 19, Issue 10, October 2003, pp.1715-1748.

APPENDIX

APPENDIX I- EXPERIMENTAL ERROR ANALYSIS

Sources of Error in the Creep Testing Equipment

All the experimental creep data which has been presented in this study will have some error. Thus it is important to find potential sources of errors and estimate values of errors occurring. For the equipment used to conduct the creep rupture and the load-on/ load-off testing, errors can be from various sources: load train, strain measurement system and errors in the sample environment.

Errors in the Load Train Assembly

The load-train assembly consists of three main parts- the weights, lever arm and the actual specimen mounting assembly. All of these are potential sources of errors.

Errors due to Differences between Actual and Assumed Weights

To apply the load on the specimen, different weights were used. During loading and unloading of a specimen, it is possible that some material from these weights might get chipped which will lead to an error. To minimise this, a load cell was used on all frames to determine the actual force the weight would apply on the specimen. The load cell reading was then taped on to the weight and this weight was used for that particular frame only. This procedure was repeated once a every six months. Using this procedure helps to reduce the error involved in determining the actual load on the specimen. In worst case scenario, it is estimated that error due to this would be around 1N for every 100N. Thus while applying a stress of 200MPa (5.6KN or 0.560KN due to the lever arm ratio), the total error would be about 5N (0.17MPa).

Errors due to the Lever-arm not being Horizontal

The lever arm used to amplify the load has to be horizontal in order for the exact load to be applied. The creep frame uses an automatic balancing mechanism for levelling the lever arm. When the load is applied on a specimen, the lever arm will deviate from the horizontal. Limit switches were used, which if tripped would move the load train assembly to make the lever arm horizontal. These limit switches were adjusted so that, if the lever at an angle greater than 5° from the horizontal, they would make the necessary corrections. A 5° angle results in an error of 0.5% in the stress applied.

Errors due to Specimen Bending During a Creep Test

When the sample is loaded, small deviations in the load train can result in bending stresses. This potentially can cause errors in the measured strain. The strain measuring system used two LVDT's to measure the strain along one diameter which reduces the error. The most effective way to eliminate this problem would be to measure strain all along the diameter of the sample. This, however practically would be difficult. The error due to bending in the experimental system described in section 3.2 will be minimal due to the use of the knife edges and the universal joints.

Errors in the Strain Measurement System

The LVDT used to measure the displacements are also sources of error. Data sheets for the part used mention errors of up to 0.5% in the displacement measurement. Another problem would be drift in the instrument. To account for this, the LVDT were calibrated once a year. Changes in the temperature of the environment of the laboratory can also cause some errors in the displacements.

Errors in Sample Environment

Changes in the sample temperature can lead to variation in the material behaviour. Testing standards recommend that a maximum variation of 3°C should exist across the gauge length and the test temperature should be within ±2°C of the target temperature. Temperature measurement was done through thermocouples. Despite sufficient care being taken during setting up of a creep test, it is possible that during a test, the tips of the thermocouples would not be touching the sample completely which can lead to some variation in the temperature reading. Drift of the equipment can also lead to some errors. Thermocouples were changed after they were used for one year to reduce this effect.

Appendix II- Sampling of Dislocation Densities

Test Condition	Unload Time(hours)	Line Length (nm)	No of dislocation intersections	Total number of dislocations sampled	Dislocation density ($/m^3$)	Average dislocation density ($/m^3$)
650°C-180MPa	Zero	600	225	**873**	6.26E+12	**1.02×10^{13}**
650°C-180MPa	Zero	600	207		5.71E+12	
650°C-180MPa	Zero	600	228		8.66E+12	
650°C-180MPa	Zero	600	213		2.02E+13	
650°C-180MPa	0.5	800	156	**1116**	1.82E+13	**1.52×10^{13}**
650°C-180MPa	0.5	800	284		1.90E+13	
650°C-180MPa	0.5	800	240		1.77E+13	
650°C-180MPa	0.5	800	144		1.60E+13	
650°C-180MPa	0.5	800	140		7.77E+12	
650°C-180MPa	0.5	800	152		1.28E+13	
650°C-180MPa	1	500	530	**2380**	3.77E+13	**3.01×10^{13}**
650°C-180MPa	1	500	462		2.79E+13	
650°C-180MPa	1	200	582		2.66E+13	
650°C-180MPa	1	500	374		2.95E+13	
650°C-180MPa	1	500	432		2.83E+13	
650°C-180MPa	1	500	511	**1621**	6.75E+13	**4.12×10^{13}**

650°C-180MPa	1	500	355		3.63E+13	
650°C-180MPa	1	500	324		2.38E+13	
650°C-180MPa	1	500	431		3.71E+13	
650°C-180MPa	4	500	661	**1699**	4.49E+13	**3.67×10^{13}**
650°C-180MPa	4	500	453		3.23E+13	
650°C-180MPa	4	500	585		3.29E+13	
650°C-180MPa	12	500	503	**1719**	1.33E+13	**2.09×10^{13}**
650°C-180MPa	12	1000	576		1.40E+13	
650°C-180MPa	12	500	640		3.54E+13	
650°C-180MPa	24	500	522	**1667**	2.78E+13	**2.01×10^{13}**
650°C-180MPa	24	500	534		2.02E+13	
650°C-180MPa	24	500	257		3.00E+10	
650°C-180MPa	24	500	354		3.24E+13	
650°C-180MPa	36	500	552	**1613**	2.58E+13	**2.73×10^{13}**
650°C-180MPa	36	1000	627		1.13E+13	
650°C-180MPa	36	500	434		4.48E+13	
650°C-180MPa	48	500	486	**2208**	3.05E+13	**2.13×10^{13}**
650°C-180MPa	48	1000	462		1.26E+13	
650°C-180MPa	48	1000	344		1.72E+13	
650°C-180MPa	48	500	370		2.60E+13	

650°C-180MPa	48	500	546		2.01E+13	
550°C-335MPa	Zero	500	490	**2410**	1.23E+13	**1.32×10^{13}**
550°C-335MPa	Zero	1000	424		1.35E+13	
550°C-335MPa	Zero	1000	572		1.06E+13	
550°C-335MPa	Zero	1000	366		1.90E+13	
550°C-335MPa	zero	1000	558		1.06E+13	
550°C-335MPa	4	500	481	**2015**	2.15E+13	**2.7×10^{13}**
550°C-335MPa	4	500	384		4.39E+13	
550°C-335MPa	4	500	557		1.89E+13	
550°C-335MPa	4	500	593		2.38E+13	
550°C-335MPa	24	1000	643	**2385**	1.65E+13	**2.44×10^{13}**
550°C-335MPa	24	1000	651		2.55E+13	
550°C-335MPa	24	500	577		2.99E+13	
550°C-335MPa	24	1000	514		2.56E+13	
550°C-335MPa	48	500	507	**2185**	1.33E+13	**1.49×10^{13}**
550°C-335MPa	48	1000	510		1.38E+13	
550°C-335MPa	48	1000	397		5.49E+12	
550°C-335MPa	48	2000	520		2.46E+13	
550°C-335MPa	48	1000	251		1.73E+13	

Appendix III- Sampling of Precipitate Densities

Test Condition	Unload Time (hours)	Preparation Method	Area (nm^2)	No of carbides sampled	Total number of carbides sampled	Carbide density ($/m^3$)	Average carbide density ($/m^3$)
650°C-180MPa	Zero	Ion-polishing	526054.7	120	**336**	1.26E+21	**1.37×10^{21}**
650°C-180MPa	Zero	Ion-polishing	350703.1	112		1.77E+21	
650°C-180MPa	Zero	Ion-polishing	526054.7	104		1.05E+21	
650°C-180MPa	0.5	Ion-polishing	349752.1	148	**346**	9.40E+21	**6.24×10^{21}**
650°C-180MPa	0.5	Ion-polishing	661250	88		2.95E+21	
650°C-180MPa	0.5	Ion-polishing	349752.1	110		6.35E+21	
650°C-180MPa	1	Ion-polishing	932672.2	144	**312**	3.43E+21	**3.12×10^{21}**
650°C-180MPa	1	Ion-polishing	621781.5	72		2.57E+21	
650°C-180MPa	1	Ion-polishing	634800	96		3.36E+21	
650°C-180MPa	12	Ion-polishing	1125000	76	**224**	1.50E+21	**1.19×10^{21}**
650°C-180MPa	12	Ion-polishing	1580247	68		9.56E+20	
650°C-180MPa	12	Ion-polishing	1580247	80		1.12E+21	
650°C-180MPa	24	Ion-polishing	1692800	88	**276**	1.15E+21	**1.45×10^{21}**
650°C-180MPa	24	Ion-polishing	2098512	124		1.31E+21	
650°C-180MPa	24	Ion-polishing	752355.6	64		1.89E+21	

650°C-180MPa	36	Ion-polishing	540562.5	50	**166**	2.05E+21	**2.26×10^{21}**
650°C-180MPa	36	Ion-polishing	540562.5	61		2.46E+21	
650°C-180MPa	36	Ion-polishing	540562.5	55		2.26E+21	
650°C-180MPa	48	Ion-polishing	690976.6	68	**524**	2.18E+21	**2.08×10^{21}**
650°C-180MPa	48	Ion-polishing	690976.6	88		2.83E+21	
650°C-180MPa	48	Ion-polishing	690976.6	96		3.08E+21	
650°C-180MPa	48	Ion-polishing	690976.6	100		3.21E+21	
650°C-180MPa	48	Ion-polishing	2702813	88		7.23E+20	
650°C-180MPa	0.5	Electro-polishing	3394329	212	**764**	4.63E+21	**9.61×10^{21}**
650°C-180MPa	0.5	Electro-polishing	1122250	316		1.25E+22	
650°C-180MPa	0.5	Electro-polishing	1122250	236		1.17E+22	
650°C-180MPa	1	Electro-polishing	7014063	264	**828**	2.09E+21	**3.62×10^{21}**
650°C-180MPa	1	Electro-polishing	7014063	328		3.46E+21	
650°C-180MPa	1	Electro-polishing	2463100	236		5.32E+21	
650°C-180MPa	4	Electro-polishing	10624852	360	**904**	2.51E+21	**2.37×10^{21}**
650°C-180MPa	4	Electro-polishing	10624852	320		2.23E+21	
650°C-180MPa	4	Electro-polishing	7014063	224		2.37E+21	
550°C-335MPa	Zero	Electro-polishing	14400000	588	**1492**	9.07E+21	**5.38×10^{21}**
550°C-335MPa	Zero	Electro-polishing	22141440	280		2.81E+21	
550°C-335MPa	Zero	Electro-polishing	14400000	288		4.44E+21	

550°C-335MPa	Zero	Electro-polishing	14400000	336		5.19E+21	
550°C-335MPa	0.5	Electro-polishing	3844000	268	**2044**	1.55E+22	**1.21×10^{22}**
550°C-335MPa	0.5	Electro-polishing	28591736	904		7.03E+21	
550°C-335MPa	0.5	Electro-polishing	6539887	436		1.48E+22	
550°C-335MPa	0.5	Electro-polishing	8649000	436		1.12E+22	
550°C-335MPa	1	Electro-polishing	13514063	416	**2072**	6.84E+21	**1.68×10^{22}**
550°C-335MPa	1	Electro-polishing	4745679	668		3.13E+22	
550°C-335MPa	1	Electro-polishing	5535360	468		1.88E+22	
550°C-335MPa	1	Electro-polishing	11296653	520		1.02E+22	
550°C-335MPa	4	Electro-polishing	31379592	348	**1392**	2.46E+21	**3.83×10^{21}**
550°C-335MPa	4	Electro-polishing	15376000	468		6.76E+21	
550°C-335MPa	4	Electro-polishing	15376000	244		3.53E+21	
550°C-335MPa	4	Electro-polishing	28591736	332		2.58E+21	

APPENDIX IV OPTIMISATION OF MATERIAL CONSTANTS

Modelling of material constants presented in chapter 8 involved comparing the best fits of the model with experimental values. This section some of the concepts used in the optimisation process.

Optimisation was carries out using an objective function that calculates the least squares difference between the experimental data and the modelled output i.e.

$$F(\bar{x}) = \sum_{j=1}^{u} (\sigma_j - \sigma_j(\bar{x}))^2 \qquad \text{A.4.1}$$

Where σ_j is the experimental value and $\sigma_j(\bar{x})$ is the values from the model.

If an exact solution is unavailable for the non-linear function, the minimisation will be achieved by adjusting the unknown parameters in the equation set of the model. There are a number of techniques which can be used for the optimisation. These methods make use of functional value alone during the iterative process, to those that compute first and second order derivatives to expedite optimisation. The higher order methods are computationally expensive and can lead to instability in the computing program used. The iterative algorithm will terminate when the computed value of equation A3.1 reaches a pre-determined condition.

In this thesis, an optimisation function called 'fminsearch' which is available within MATLAB was used. fminsearch uses the simplex search method of [1]. This is a direct search method that does not use numerical or analytic gradients. If n is the length of x, a simplex in n-dimensional space is characterized by the n+1 distinct vectors that are its vertices. In two-space, a simplex is a triangle; in three-space, it is a pyramid. At each step of the search, a new point in or near the current simplex is generated. The function value at the new point is compared with the function's values at the vertices of the simplex and, usually, one of the vertices is replaced by the new point, giving a new simplex. This step is repeated until the diameter of the simplex is less than the specified tolerance.

References

[1] Lagarias, J.C., J. A. Reeds, M. H. Wright, and P. E. Wright, "Convergence Properties of the Nelder-Mead Simplex Method in Low Dimensions," *SIAM Journal of Optimization*, Vol. 9 Number 1, pp. 112-147, 1998.

APPENDIX V- REPEAT EXPERIMENTS

Some of the experiments shown in chapter were repeated to check the scatter in the data. The experiments were not taken to failure.

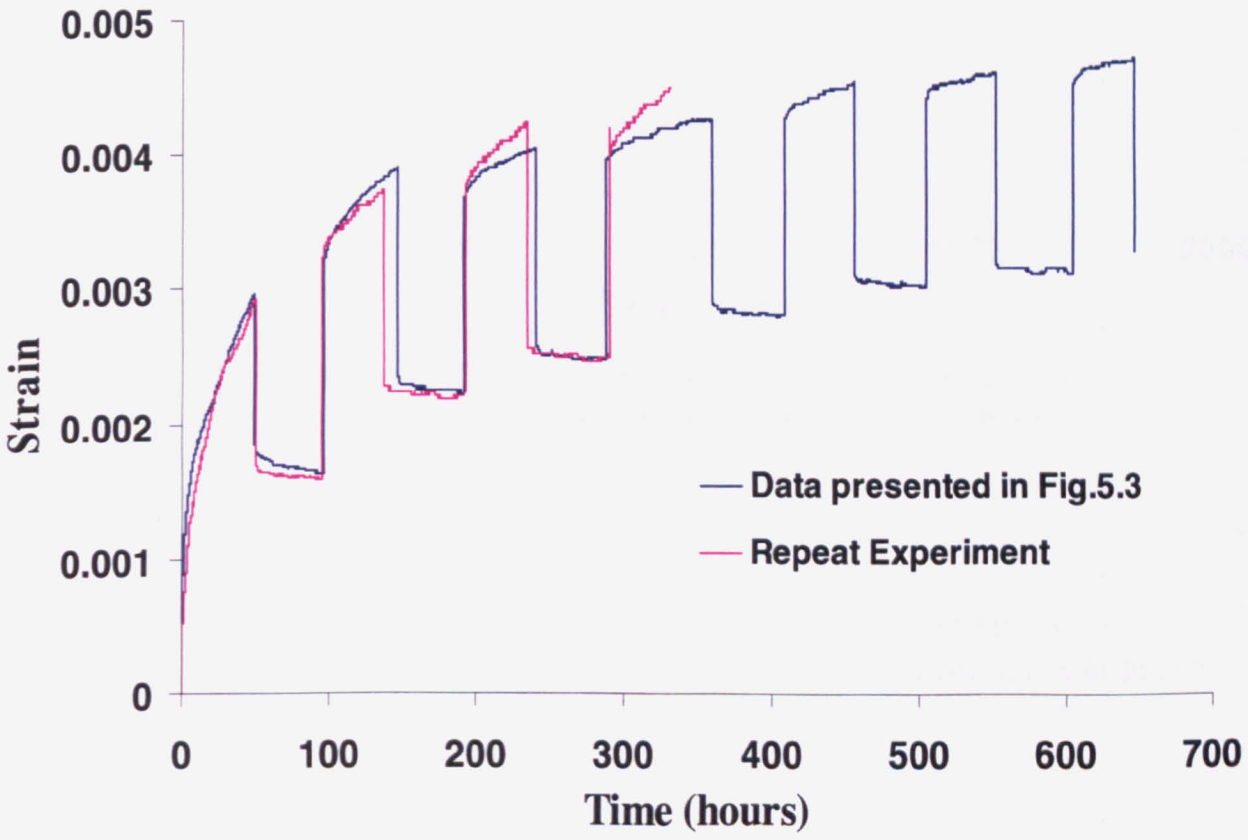

Fig. A.4.1 Test conditions- 650°C 180MPa. Sample was loaded for 48 hours and then unloaded for 48 hours

The results show good correlation between the two sets of data.

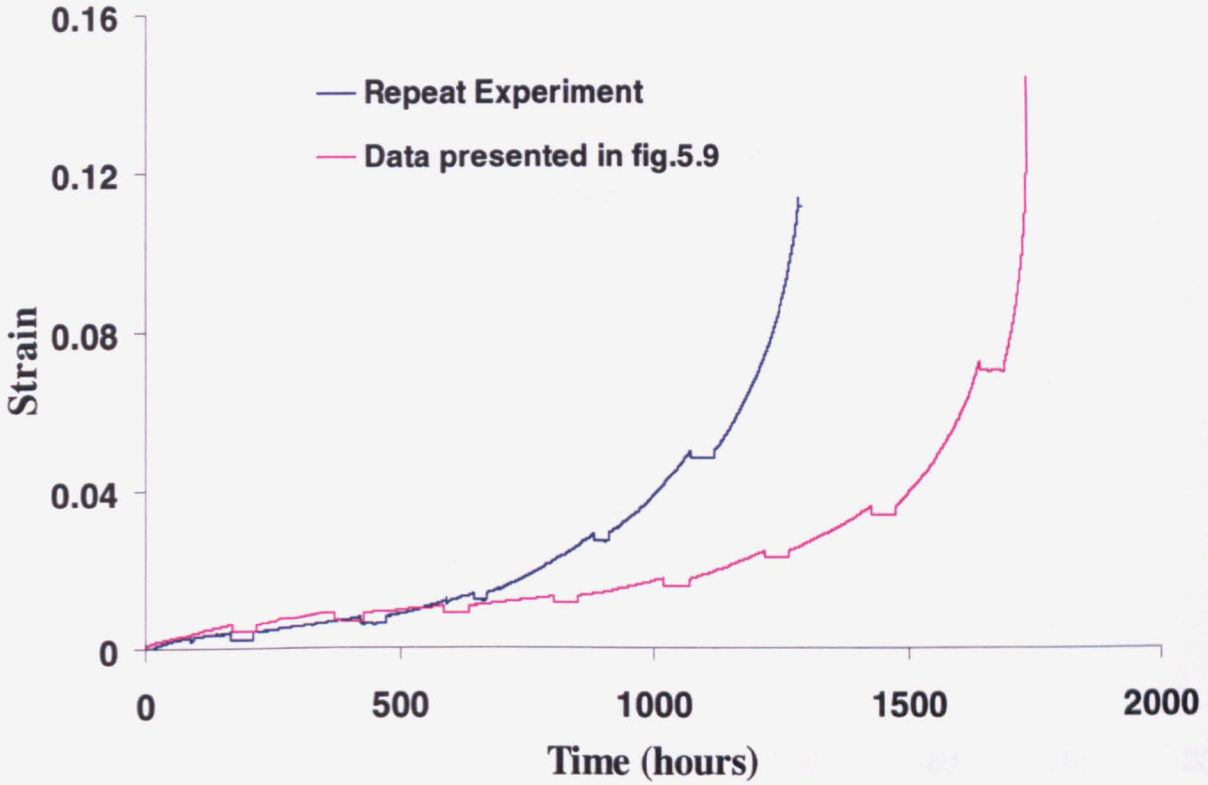

Fig. A.4.2 Test Conditions- 650°C 180MPa. Sample was loaded for 7 days and then unloaded for 48 hours

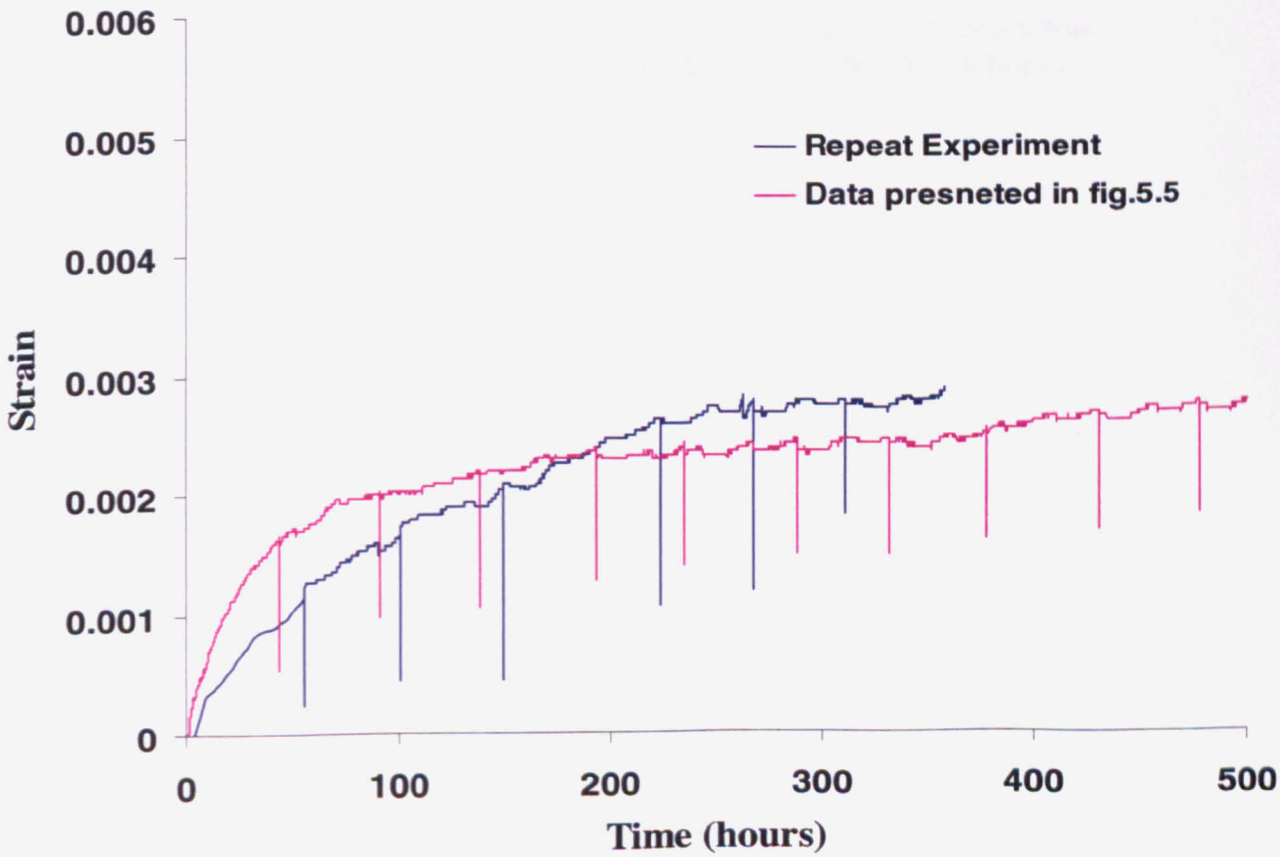

Fig. A.4.3 Test Conditions- 650°C 180MPa. Sample was loaded for 48 hours and then unloaded for 5 seconds

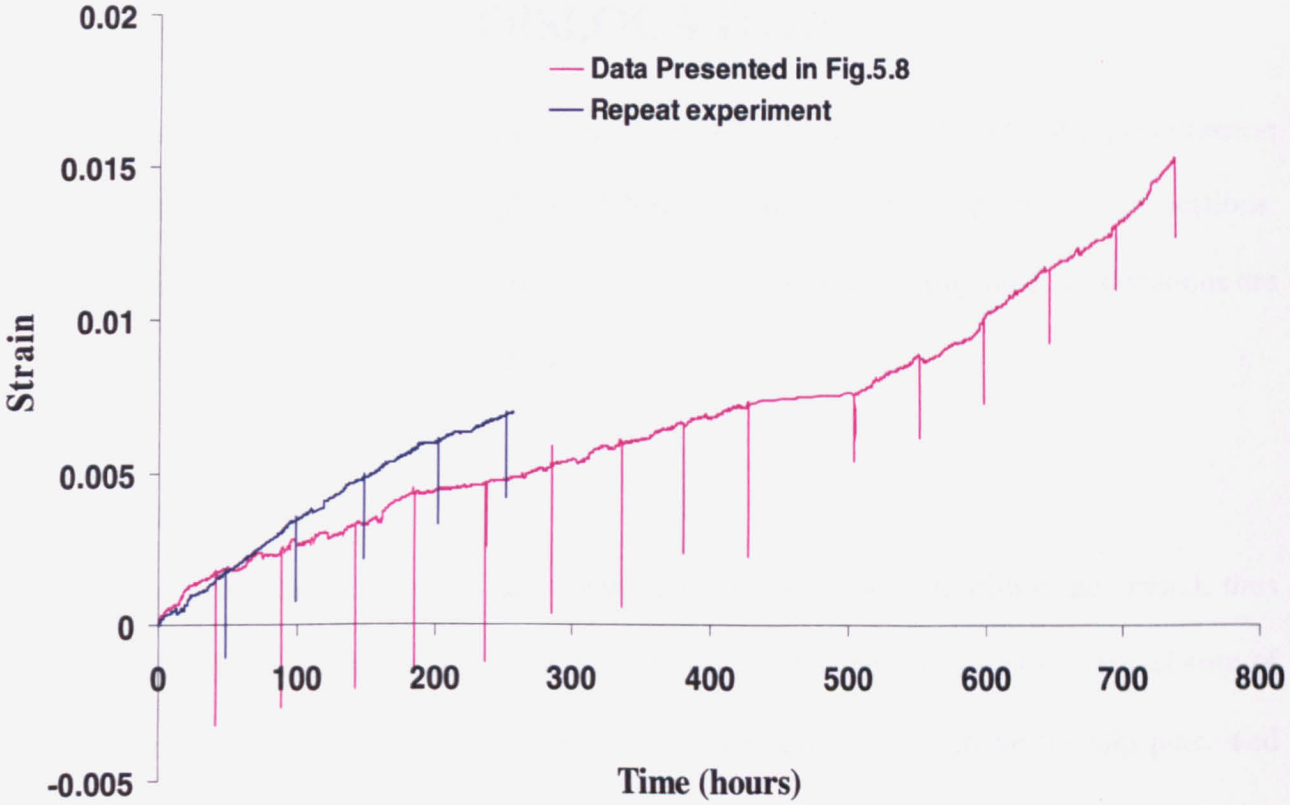

Fig. A.4.4 Test Conditions- 550°C 335MPa. Sample was loaded for 48 hours and then unloaded for 48 hours

APPENDIX- VI EDGE AND SCREW DISLOCATIONS

Dislocations are the most important line defects found in crystals. The slip phenomenon which is largely responsible for plastic deformation occurs through motion of dislocations. Dislocation motion will occur through resolved shear stresses acting on it. Dislocations are categorised into two: Edge and Screw

Edge Dislocations

In these dislocations, an extra half-plane of atoms is introduced within the crystal, thus distorting the surrounding atoms. In Fig. shown below, there is an extra vertical row of atoms above the slip plane. This results in compressive stresses above the slip plane and tensile stress below the slip plane. By convention, such an arrangement is termed positive (symbol- ⊥). The Burgers vector of such dislocations is perpendicular to the dislocation line.

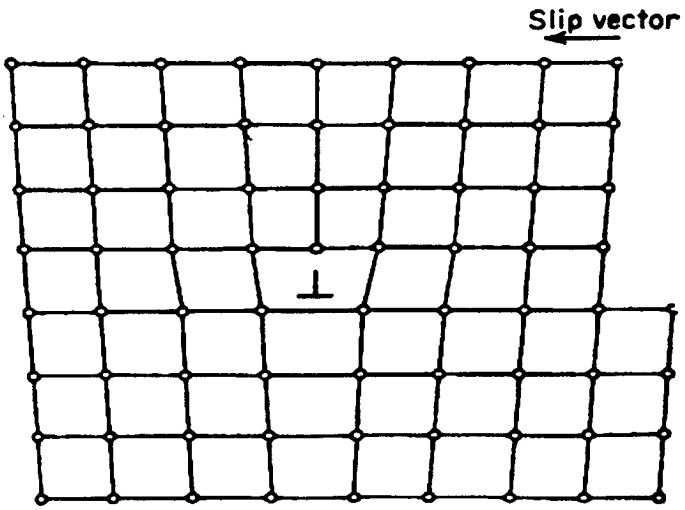

Fig.A.6.1 Atomic Arrangement in a Plane Normal to an Edge

Edge dislocations can move through the crystal either by glide, slip and climb. Fig. A.6.1 shows a schematic diagram of an edge dislocation moving through the lattice using the glide motion. The dislocation line can move through the crystal in the direction of the

applied stress by breaking only one line of bonds at a time. This process requires far less energy than breaking a number of bonds simultaneously and hence the material can deform under a much lower applied stress

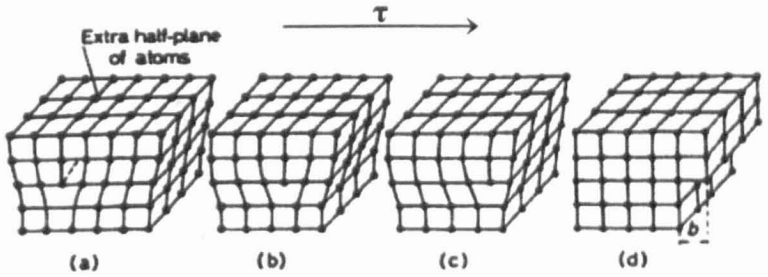

Fig. A.5.2 Motion of an Edge Dislocation. τ indicates the net shear stress acting on the crystal

Screw Dislocations

The Burger's vector of these dislocations are parallel to the dislocation line. A schematic diagram of this dislocation type is shown in Fig. A.5.2 A screw dislocation does not have a preferred slip plane. As a result, the motion of such dislocations are less restricted than edge dislocations. Also, screw dislocations cannot execute the climb motion.

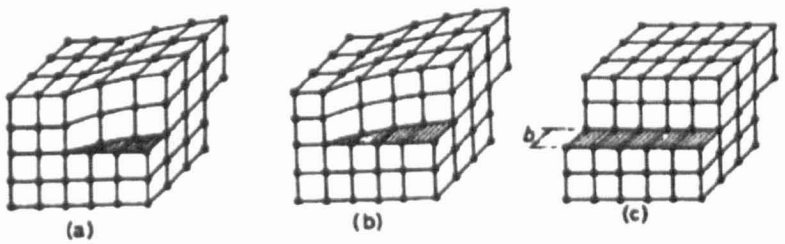

Fig. A.6.2 Motion of an Edge Dislocation. τ indicates the net shear stress acting on the crystal

References

1. R. E. Smallman and R J Bishop, *Modern Physical Metallurgy and Materials Engineering: Metals and Materials,* 6th edition, 1999, pg. 92

APPENDIX- VII EDS ANALYSIS

Chapter 6 has described the effect of strain/load on precipitate numbers. The next step was to confirm whether any chemical changes had occurred in the precipitates. This can be verified using the EDS (Energy Dispersive Spectroscopy) technique. For the duration of the test, most of the precipitates seen would be of type $M_{23}C_6$. Standard spectra exist with which the resultant EDS spectra can be compared.

EDS is a technique used for chemical characterisation of materials. It works on the principle that any material when hit by a ray of protons, electrons or X-rays will emit a characteristic radiation. Each element within the material will have a unique atomic and electronic structure which assists in identifying the elements when bombarded with electrons or X-rays. In the system, a beam of electrons was focussed on the sample. When unexcited, the electrons in the material will sit in discrete shells but when excited, these electrons can move to a higher orbit and electrons from a higher orbit will occupy the vacant site releasing energy in the form of electro-magnetic radiation. These wavelengths can be measured using a spectrometer. The emitted electrons are characteristic of the difference in energy between the two shells. Using this, the elemental composition can be determined.

EDS can be performed in either the SEM or the TEM. Some examples are shown. The first step would be to get the spectrum from the bulk of the material. This is shown in Fig. 6.23. Characteristic spectra of different precipitates are given in [16]. The spectra from the samples show the existence of $M_{23}C_6$ carbides predominantly.

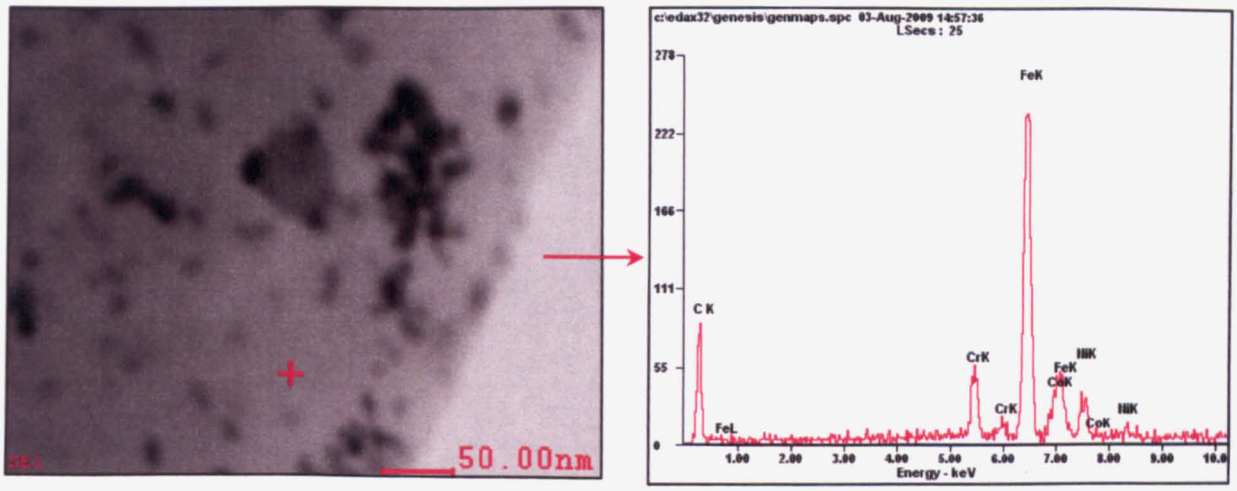

Fig. A.7.1 EDS spectrum from specimen bulk

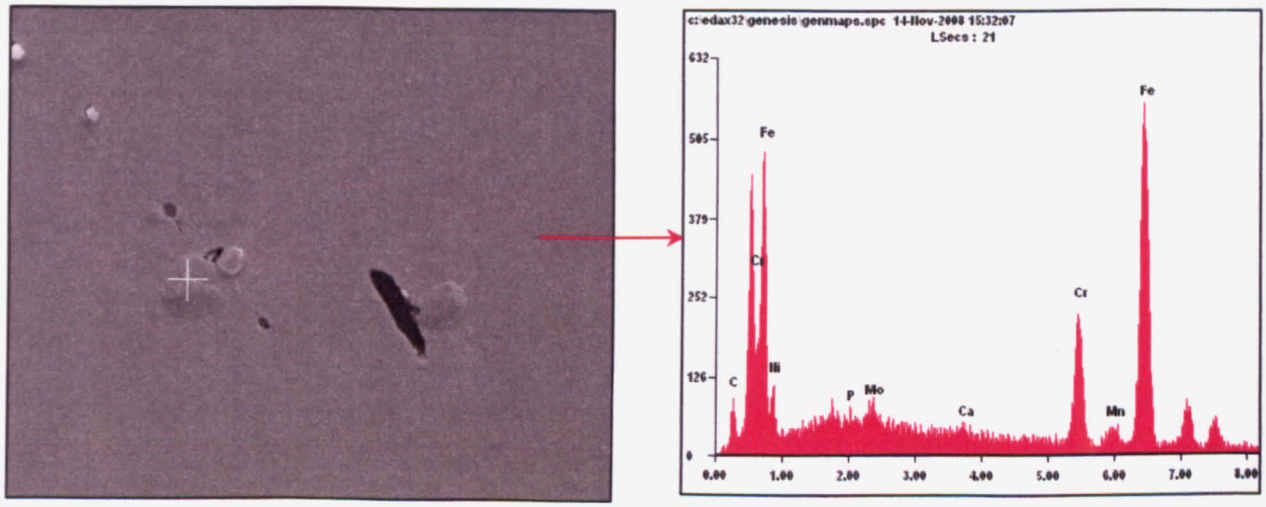

Fig. A.7.2 EDS spectrum of an $M_{23}C_6$ carbide

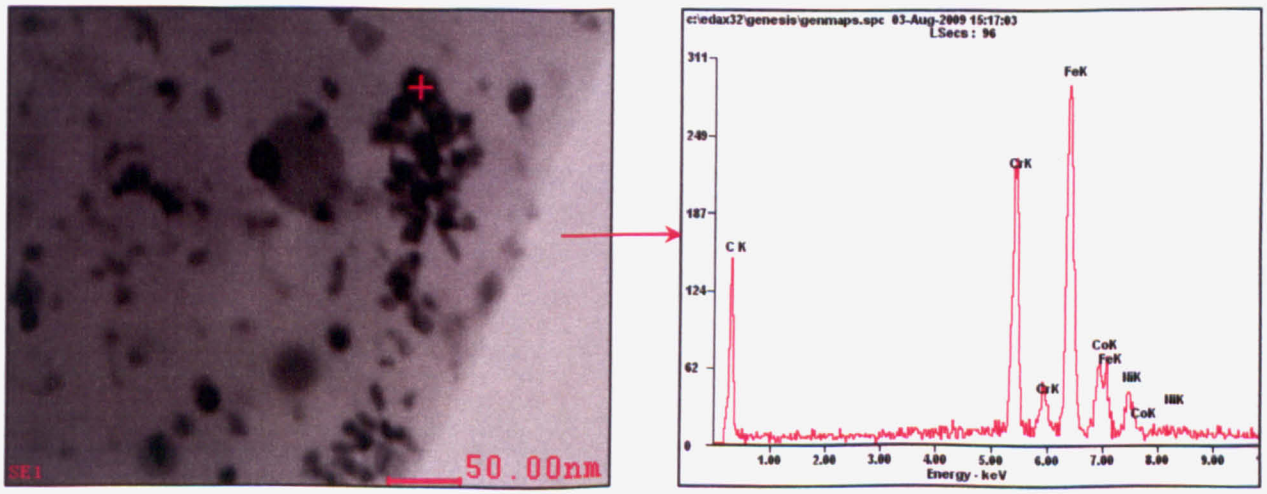

Fig. A.7.3 EDS Spectrum of a $M_{23}C_6$ carbide. Taken from a specimen that was stopped half hour into unload